

Understanding metal-organic frameworks for photocatalytic solar fuel production

Garcia Santaclara, Jara

DOI

[10.4233/uuid:3ed6dcb1-4865-46bf-b03f-c37f5fb3f743](https://doi.org/10.4233/uuid:3ed6dcb1-4865-46bf-b03f-c37f5fb3f743)

Publication date

2017

Document Version

Final published version

Citation (APA)

Garcia Santaclara, J. (2017). *Understanding metal-organic frameworks for photocatalytic solar fuel production*. [Dissertation (TU Delft), Delft University of Technology]. <https://doi.org/10.4233/uuid:3ed6dcb1-4865-46bf-b03f-c37f5fb3f743>

Important note

To cite this publication, please use the final published version (if applicable). Please check the document version above.

Copyright

Other than for strictly personal use, it is not permitted to download, forward or distribute the text or part of it, without the consent of the author(s) and/or copyright holder(s), unless the work is under an open content license such as Creative Commons.

Takedown policy

Please contact us and provide details if you believe this document breaches copyrights. We will remove access to the work immediately and investigate your claim.

Understanding metal-organic frameworks for photocatalytic solar fuel production

Proefschrift

ter verkrijgen van de graad van doctor
aan de Technische Universiteit Delft,
op gezag van de Rector Magnificus prof. *[titels, naam]*;
voorzitter van het College voor Promoties,
in het openbaar te verdedigen op
26 oktober 2017 om 12:30 uur

door

Jara GARCIA SANTA CLARA

scheikundig ingenieur

Universidade de Santiago de Compostela, Spain

geboren te Bueu, Pontevedra, Spain

This dissertation has been approved by the promotor:

Prof. dr. F. Kapteijn

Prof. dr. J. Gascon

Dr. M. van der Veen

Composition of the doctoral committee:

Rector Magnificus

Chairperson

Prof. dr. F. Kapteijn

Delft University of Technology, promotor

Prof. dr. J. Gascon

Delft University of Technology, promotor

Dr. M. van der Veen

Delft University of Technology, copromotor

Independent members:

Prof. dr. L. Siebbeles

Delft University of Technology, promotor

Prof. dr. J. Reek

University of Amsterdam

Prof. B. Civalleri

University of Torino

Dr. C. Hendon

University of Oregon

Prof. dr. B. Dam

Delft University of Technology (reserve)

The research reported in this thesis was conducted in the Catalysis Engineering section of the Chemical Engineering Department, Faculty of Applied Sciences (TNW) of the Delft University of Technology.

Proefschrift, Technische Universiteit Delft

Met samenvatting in het Nederlands

@2017 Jara Garcia Santaclara

All rights reserved

Printed by

Content

Introduction	2
Organic linker defines kinetics the excited-state decay of photocatalytic MIL-125-type materials	17
Electronic origins of photocatalytic activity in d^0 metal organic frameworks	47
Revisiting the incorporation of Ti(IV) in UiO-type metal-organic frameworks: metal exchange versus grafting and their implications for photocatalysis	80
Harvesting the photoexcited holes in a photocatalytic proton reduction metal-organic framework	97

Introduction

The fascinating chemical and physical properties of MOFs have recently stimulated exploration of their application for photocatalysis. Despite the intense research effort, the efficiencies of most photocatalytic MOFs for solar fuel generation are still very modest. In this introduction we analyse the current status of the field and stress the potential of advanced spectroscopic techniques to gain structural and mechanistic insight, and hence supporting future development of MOFs to harvest and store solar energy.

This chapter is based on the following publication:

Revisiting the incorporation of Ti(IV) in UiO-type metal-organic frameworks: metal exchange versus grafting and their implications for photocatalysis

J. G. Santaclara, A. I. Olivos-Suarez, A. Gonzalez-Nelson, D. Osadchii, M. A. Nasalevich, M. A. van der Veen, F. Kapteijn, A. M. Sheveleva, S. L. Veber, M. V. Fedin, A. T. Murray, C. H. Hendon, A. Walsh and J. Gascon (submitted)

Introduction

It is no wonder that mankind has been intrigued for quite long by the effect of light on materials. Inspired by natural photosynthesis as the greatest chemical factory of mother Earth, photocatalysis has been studied by several generations of scientists as a promising method for energy production, the so-called artificial photosynthesis. It was already more than a century ago when Ostwald, the founder of modern catalysis, stressed the relevance of these photocatalytic processes in nature identifying them as the “mill of life”.¹

However, it was not until 1972 when the first example of photocatalytic energy generation, namely photocatalytic water splitting, was reported.² Since then, different kinds of materials, i.e. semiconductors, metal-doped zeolites and metal complexes, have been intensively studied to boost artificial photosynthesis.³⁻⁶ Still, most known catalysts are based on expensive noble metals, the activities in the visible range of the spectrum achieved so far are low, and problems like fast back-electron transfer and recombination considerably decrease their efficiency. Therefore, artificial photosynthesis, where light absorption, charge funnelling, and subsequent utilization in redox reactions are performed by different sets of molecules arranged in a complex system, stands at the intersection between the urgent drive for sustainable energy sources and state-of-the-art nanomaterials engineering.

Metal–organic frameworks (MOFs) are newly emerged functional inorganic–organic hybrid materials. MOFs consist of long range ordered crystalline lattices built up of organic linkers and inorganic secondary building units (metal ions or clusters). Early enthusiasm about MOFs took advantage of their molecular nature and extreme porosity, focussing on applications, considered nowadays “classical”, like gas storage and separation.⁷⁻¹⁰ More recently, increasing attention is paid to the electronic nature of MOFs, and the opportunities to use them as light-harvesting mimics of natural photosynthesis for solar fuel production. The resemblances between MOFs and bulk transition metal oxides encouraged more than a decade ago the first examples of photocatalytic MOFs.¹¹⁻¹⁵ Since then, frameworks based on Ti,¹⁶⁻¹⁸ Zr,¹⁹⁻²⁴ Fe,^{25, 26} etc. have been reported for different artificial photosynthetic reactions (i.e. hydrogen evolution, carbon dioxide reduction and organic oxidations).²⁷⁻²⁹ In this context, different approaches have been recently followed: from the use of MOFs as containers for encapsulating light absorbing photocatalysts,^{22, 24, 30} to exploiting ligand-to-metal charge transfer (LMCT) within the MOF or even inducing charge transfer from the MOF to encapsulated catalysts.^{29, 31} Regardless of the promising discoveries made in the past years, a lot of progress is still needed.

A proof of the interest in this application of MOFs is the unprecedented number of reviews (almost as many as the number of papers on the topic) that have appeared in the literature over the last two years.³¹⁻³⁶ In this highlight article, we do not intend to again review the state of the art, but rather to encourage research in this field towards understanding MOF properties from an optoelectronics point of view. We

make here special emphasis on recent advances in this direction and finally outline future directions for the design of more efficient MOFs for solar fuel production.

Electronic structure of the main photocatalytic MOFs

Semiconductor versus insulator nature

Based on their optical transitions and prospective electro/photochemical activity, MOFs have been labelled for many years as semiconductors. However, it is nowadays well accepted that, in general, they are insulator materials.^{32, 37, 38} This is due to, on one hand, the inadequate energy levels alignment of ligand and metal orbitals. Typically, organic ligands possess HOMO-LUMO gaps above 3 eV. This makes it less likely that a metal centre will have energy levels that align with those of the ligand. On the other hand, the metal and ligand orbital symmetry mismatch results often in an electronic structure analogous to that only of the linker or the metal. Therefore, the way that organic molecules link metal centres in the majority of MOFs results in localized electronic states, which typically prevents efficient charge transport through the framework. Accordingly, MOFs should be seen as an array of self-assembled molecular entities, which are best defined in terms of the crystal equivalent of molecular orbitals -HOCO (highest occupied crystal orbital) and LUCO (lowest unoccupied crystal orbital)- rather than band-like states (conduction and valence bands).

Despite the fact that stimulating examples on conductor MOFs have been very recently reported,³⁹ none of those have been applied yet in photocatalysis for solar fuels production. This infers that so far the MOFs studied for this application are insulators. Hence, we discuss their properties further within that frame.

Applying “push-pull” principles by ligand engineering

Many attempts have been made to push MOFs' light absorption into the visible region of the spectrum targeting efficient solar energy utilization. Since one of the most appealing properties of MOFs for photocatalysis is the easy tuneability of their light harvesting properties, ligand engineering has been intensively used to alter their electronic structure by modifying the orbital composition (Figure 1.1), and, consequently, the chemistry of the HOCO-LUCO band edges.^{14, 40, 41} Considering that in most MOFs at least one these frontier bands (HOCO and LUCO) is centred on the ligand, and that this is usually an organic conjugated molecule, their electron energies are tuneable and certainly influenced by the electron donating/withdrawing character of additional substituents (push-pull effect). Initially predicted by Civalleri,⁴² this effect was, for the first time, experimentally demonstrated with different organic bidentate ligands in the isorecticular IRMOF series.¹⁴ Afterwards, the introduction of primary amines has been also reported as a powerful strategy to sensitize various frameworks to visible light. Amino substituents on the ligand provide in many cases the lone pair of nitrogen for the interaction with the π^* -orbitals of the benzene ring, donating electron density to the antibonding orbitals.⁴³ In this context, the amino

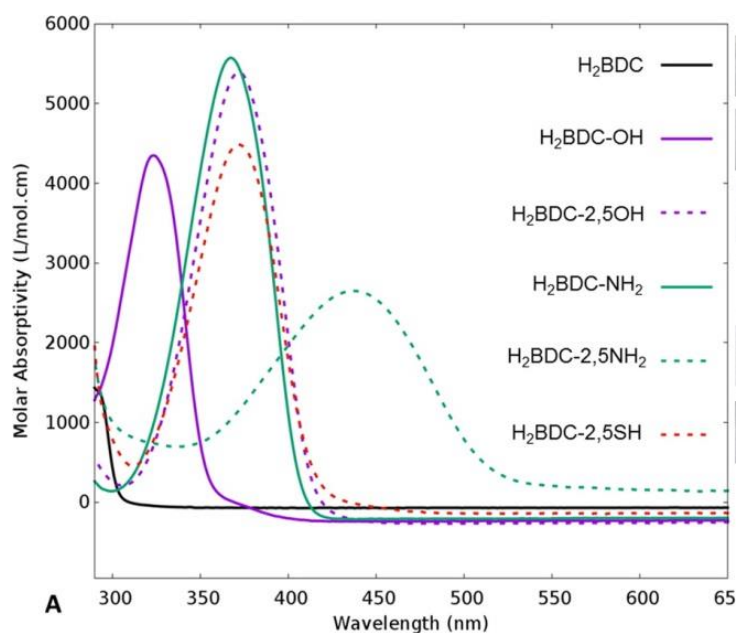


Figure 1.1. Experimental linker spectra. Different UiO-66 were synthesized using these linkers, and different band gaps were obtained. Adapted with permission from 41. Copyright 2015 American Chemical Society.

functionalization of MIL-125(Ti) and UiO-66(Zr), two originally deep-UV absorbing MOFs, resulted in an enhancement of electron density and a lowering of the ionization potential, by raising the HOCO energy level, and bringing absorption to the visible region.^{27, 44} The addition of a second amino-group in the linker of MIL-125(Ti) was calculated to follow a similar trend.⁴⁰ However, introducing the desired functionalization in a framework of choice is not always synthetically feasible,⁴⁵ therefore post-synthetic modification strategies were required and successfully employed.^{46, 47}

HOCO/LUCO gap estimation

Notably, enhancing sunlight uptake is only worth when the photogenerated charges meet two fundamental requirements: 1) possessing sufficient redox potentials for driving the desired chemistry and 2) located on atoms or molecule fragments that facilitate the charge transfer. Regarding the former requisite, the HOCO/LUCO gap estimation is often obtained from UV/VIS absorption spectroscopy. However, it does not provide with the absolute energy level of HOCO and LUCO. Importantly, electrochemical experiments are capable at giving this vital information. By definition, electrochemistry comprises the transfer or storage of electrons at the interface of the electrode-electrolyte. Withal, due to their poor electron-conductivity, MOFs are rarely used as electrode materials,⁴⁸ and the interpretation and discovery of the active sites nature from electrochemical measurements is not trivial.⁴⁹ Conversely, MOFs in which charge and mass transport, and active-site density are precisely controlled offer new avenues for electrochemistry and electrocatalysis. An excellent example was reported for electrocatalytic CO₂ reduction, where MOFs porous thin films were integrated onto a conductive support.⁵⁰

In general, an electrochemical experiment entails the measurement of current when a potential difference is applied between two metal electrodes (working electrode, sensitive to the analyte concentration, and counter electrode, which closes the circuit) immersed in a chemical solution. Via a reference electrode (whose potential remains constant) the potential of the working electrode can be measured.⁵¹

However, few electrochemical studies have been reported up to date in photocatalytic MOFs, due to their insulating nature. Normally, deposition on conducting material (e.g. ITO, indium tin oxide/ FTO, fluorine doped tin oxide) is necessary and the choice of the right electrolyte (and buffer solution) is not trivial.

An indirect way to obtain electrochemical insights on insulating photocatalytic MOFs is by the study of the redox potentials of its molecular components: organic linker and metal oxocluster.⁵² Obviously, this is just an approximate estimation, and detailed experimental protocols should be described for electrochemistry with MOFs. In addition, DFT calculations have also proven to be effective in shedding light on this issue.⁵³⁻⁵⁵

Electronic properties of d^0 MOFs

Apart from a few reports on MOFs based on Cu or Fe metal ions, the vast majority of studies for solar fuels production feature d^0 MOFs, which are very often based on Ti^{4+} and Zr^{4+} . Here, we provide a photophysical understanding of their electronic properties.

In general, MOFs featuring ligand-to-metal charge transfer (LMCT) as the lowest energy electronic transition are desired for photocatalysis. This is due to the expected more efficient charge separation, versus frameworks where, for example, only the metals⁵⁶ or the ligands⁵⁷⁻⁵⁹ contribute to the photoexcitation process. MIL-125(Ti)-type materials (HOCO LUCO is represented in Figure 1.2) are a well-known example, where LMCT has been clearly demonstrated by EPR,^{16, 29} flash photolysis,⁶⁰ theory⁶¹ and ultrafast spectroscopy combined with spectroelectrochemistry.⁵² However, demonstrating LMCT in photoactive MOFs is often overlooked. As a matter of fact, the mechanism behind light-excitation in the case of UiO-66(Zr) has been debated by several researchers.^{16, 28, 62, 63} It is now resolved that both the HOCO and the LUCO are defined by organic orbitals, and that this framework does not feature LMCT, since there is no contribution during photoexcitation from the metal (both for Zr and Hf-based UiO-66, Figure 1.3), as it will be discussed in Chapter 3 of this Thesis. The fact that this transition is solely ligand based, results in a short lifetime of excited state and, therefore, a poor photocatalytic performance. Thus, organic functionalization could be used to modify the chemistry of band edges and try to realize LMCT in this material. It has already been reported that the simple NH_2 functionalization is not sufficient for this purpose, thus other ligands should be used.⁶⁴ Moreover, non-carboxylate linkers should also be studied for improving the orbital overlap in the UiO-66 frameworks, for instance, by employing porphyrin based ligands.^{20, 65-67}

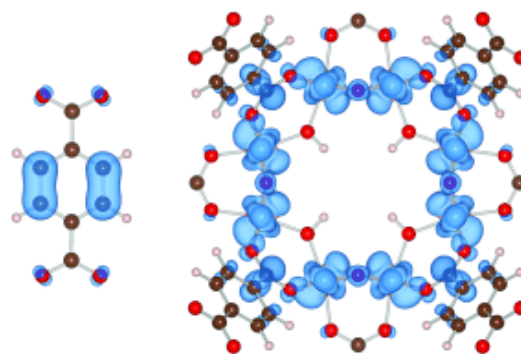


Figure 1.2. Highest occupied states (HOCO) are localized on the aromatic organic group, while the lowest unoccupied states (LUCO) are localized on the octameric TiO_2 units for $\text{NH}_2\text{-MIL-125(Ti)}$.⁶¹ Reproduced with permission from Wiley.

Electron paramagnetic resonance (EPR) and DFT calculations were crucial to determine the electronic origins of photocatalytic activity in $\text{NH}_2\text{-UiO-66(Zr)}$ and $\text{NH}_2\text{-UiO-66(Hf)}$. On the one hand, the detection of paramagnetic $\text{Zr}^{+3}/\text{Hf}^{+3}$ should be straightforward, being a key experimental proof for LMCT. On the other hand, DFT calculations can give insights into the composition, energy, and distribution of the frontier orbitals.^{53, 56, 59} It is noteworthy that concepts like matching electronic energy levels and orbital symmetry are still rarely applied in MOF chemistry; however, knowing the electronic structure of a material can provide very valuable guidelines for their design in photocatalysis.

Kinetics of photoexcited state defined by the organic linker

Apart from the thermodynamic requirement that implies that LUCO and HOCO positions need to be appropriate in order to run the desired redox half reaction, as mentioned briefly above, the kinetics of the photoexcited states critically influence efficiency in photocatalysis. Accordingly, the lifetime of the charge separated state(s)

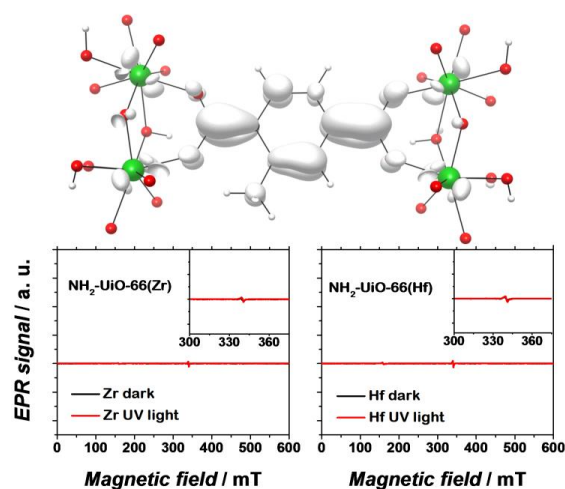


Figure 1.3. EPR spectra of dark (black) and UV-illuminated (red) $\text{NH}_2\text{-UiO-66(Zr)}$ (left) and $\text{NH}_2\text{-UiO-66(Hf)}$ (right). The photoexcited electron is primarily centred on the organic linker. Adapted with permission from Nasalevich *et al.*⁵⁹.

is of paramount importance, since it needs to be sufficiently long, such that catalytic conversion can compete with the charge separated state decay. These kinetic considerations are often not explicitly considered in examples of photocatalytic MOFs in literature. Thus, it is highly recommended to profit from the advanced spectroscopic techniques we have nowadays available for the understanding of the photocatalytic reaction mechanisms and for a better design of MOFs photocatalytic systems.

In this context, time-resolved absorption spectroscopy (TAS), is a widely employed technique in photocatalysts to study the formation, decay, recombination, and transfer processes of photogenerated charge carriers.⁶⁸ In this technique samples are excited by a laser pulse, and the absorption of the photogenerated intermediates are detected by time-resolved optical spectroscopy, usually in the UV/VIS/NIR region, employing white light for the analysis (Figure 1.4).

The type of dynamics that one wants to follow determines the required temporal resolution of the laser system. For dynamic processes from nanosecond to millisecond time scales, the most common tool is laser flash photolysis, where a sample is first excited by an intense pulse laser, populating the excited state. This change is spectroscopically monitored applying a synchronized probe light (i.e. intense flash xenon lamp) by measuring the transmittance for transparent samples or the reflectance for opaque samples, respectively, before and after the laser excitation.⁶⁹

However, when the efficiency of the photoexcitation process is limited by the fast decay (within a few picoseconds) of the photogenerated charges, the fact that the remaining charges have a microsecond lifetime makes no difference, and unravelling the dynamics at short time scales becomes crucial. Thus, in order to capture the entire extent of the photoexcited state decays and the fast dynamics of photocatalytic systems, subpicosecond time resolution is needed. Ultrafast pump-probe spectroscopies allows us to get direct information on the MOFs excited redox-active states and to study their decay profiles from sub-picoseconds up to several nanoseconds time resolution.⁷⁰

In the case of very weak absorbance, but reasonable fluorescence, this is usually done in an emission fashion.^{71, 72} Here, time-correlated single-photon counting (TCSPC) is the most popular method, measuring picosecond emission decays.

For the case of femtosecond emission transients the fluorescence up-conversion technique is often used.^{73, 74} Regarding ultrafast measurements in absorbance mode, the ultrafast study done on the MIL-125(Ti) series is one of the most clear examples.⁵² Here, MOF suspensions were excited them at their wavelength absorption maxima. By separating the large MOF particles (>100 nm) from the suspension, the experiments could be done in transmittance fashion, avoiding light scattering and following the decay kinetics with a picosecond time resolution. In this way, the kinetics of the photoexcitation process were elucidated for two titanium

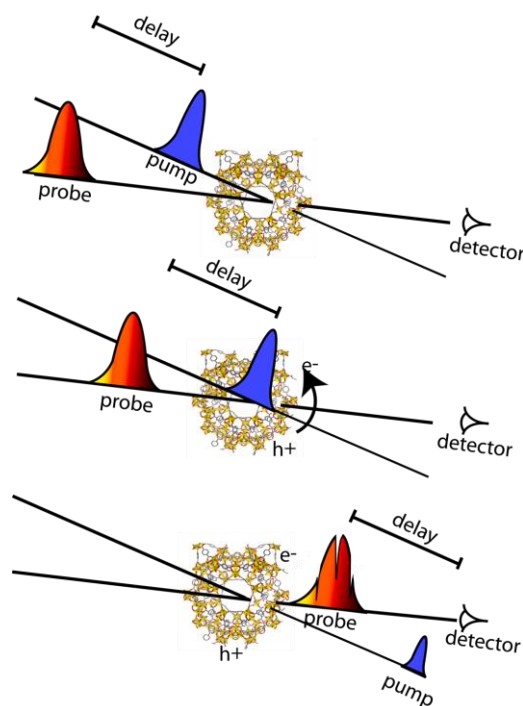


Figure 1.4. Scheme of pump-probe experiment Systematic variation of the delay between pump and probe beams allows for a time window from ~100 fs to several ns.

MOFs, MIL-125(Ti) and NH₂-MIL-125(Ti). Even though both MOFs undergo a ligand to metal charge transfer transition, it was found that NH₂-MIL-125(Ti) has a remarkably longer lifetime due to the electron-donating primary amine on the benzene ring, as it is demonstrated in Chapter 2 of this Thesis. Analogous comprehensive studies should be included more often in reported photocatalytic systems, in order to enable the creation of more design guidelines for photocatalytic MOFs.

respectively. Indeed these charges need to be able to be easily transferred to reactants in order to achieve catalytic conversion. The most unambiguous way to assess this issue experimentally in MOFs photocatalytic systems is by spectro-electrochemistry (SEC). In general, this technique consists in recording the *in situ* absorption spectra upon electrochemical oxidation/reduction of a material, allowing for the detection of unknown intermediates or products created by the redox reaction.⁷⁵ However, its potential on the localization of charges carriers resides in the direct comparison of the MOF SEC spectra with the one of its building units. Moreover, and despite the different time resolution of both techniques, this also allows for a better understanding of the TA spectra obtained by ultrafast spectroscopy.

Localization of the photogenerated electrons and holes

In addition to the charge recombination rates, the localization of photogenerated electrons and holes is critical for the design of reduction and oxidation catalysts,

Typically SEC experiments (Figure 1.5) are performed on transparent thin

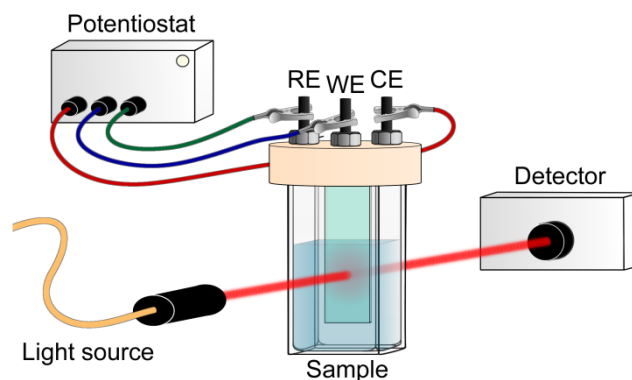


Figure 1.5. Scheme of SEC experiment. RE, WE and CE refers to reference, working and counter electrode, respectively.

glass tubes or flat cells with incorporated electrodes (i.e. working electrode, counter electrode and, frequently, reference electrode).⁷⁵ In order to observe the changes in the analyte, optical cells are usually made from conducting transparent materials (i.e. ITO), or on somewhat transparent noble metal grids.

Despite the fact that SEC can potentially assist in unravelling the photoexcitation process, these measurements on photocatalytic MOFs are not straightforward and often not possible to carry out due to, once again, MOFs' insulating character. Moreover, a compromise in concentration is necessary when cyclic voltammetry is linked to SEC results for MOFs. Often, higher MOF concentrations are required than commonly used in electrochemical measurements for a sufficient spectroscopic response. This toughens the electrochemical part of the measurement, due to the increased probability of MOF falling from the electrode where it is deposited.

Coming back to the earlier discussed titanium-MOF example, SEC could only be performed on the soluble models of the organic and inorganic $\text{NH}_2\text{-MIL-125(Ti)}$ constituents. SEC analysis gave strong evidence for the LMCT character of the $\text{NH}_2\text{-}$

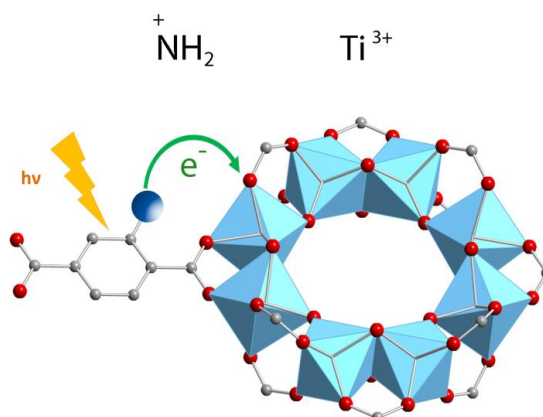


Figure 1.6. Ligand-to-metal charge transfer (LMCT) and location of photogenerated charges in $\text{NH}_2\text{-MIL-125(Ti)}$.⁵² Reproduced with permission from Wiley.

MIL-125(Ti) photoexcited state, through the detection of the absorption fingerprints of linker radical cation and reduced Ti-oxocluster.

A more elaborate way to precisely localize the photoexcited charges is by employing VIS-pump mid-IR-probe spectroscopy. By using this ultrafast technique electrons and holes can be traced through the different organic groups of the framework. For instance, mid-IR transient spectra were measured in the NH₂-MIL-125(Ti) material by placing a very thin layer of concentrated MOF suspension in a mid-IR transparent solvent on a cell made from CaF₂ windows. This measurements revealed that the photogenerated hole resides on the amino group in NH₂-MIL-125(Ti) (Figure 1.6).

The state-of-the-art spectroscopy is not limited to the aforementioned techniques. VIS-pump X-ray-probe spectroscopy allows recording X-ray absorption spectra, both for X-ray diffraction and EXAFS spectra, with a time resolution of tens of microseconds at free electron laser and synchrotron facilities, respectively. This powerful technique can be used to unravel the mechanisms behind photocatalytic reactions, especially when dealing with multicomponent arrangements.⁷⁶ It has not yet been applied in any photocatalytic MOF, nonetheless future studies using these tools will definitely allow for a better understanding on the field.

Moreover, charge transfer is another crucial piece of the artificial photosynthetic scheme. Once more, by using ultrafast spectroscopic techniques charge transfer from photoexcited MOFs to occluded molecules (i.e. reactants) can be studied.

Strategies for photocatalysis by guest inclusion

In contrast to classical semiconductor materials, where tuneability is commonly limited to the modification of surfaces by noble metal nanoparticles or, occasionally, transition metal complexes, in the case of MOFs different approaches can be followed in order to induce photocatalytic activity (Figure 1.7). The first one, described in the previous section, uses the organic linker as antenna for light sensitizing and charge transfer to the inorganic cluster, by exploiting ligand-to-metal charge transfer (LMCT). We have earlier emphasized that photocatalytic MOFs that feature LMCT are ideal due to the efficient charge separation. Moreover, by tuning the organic linker (introducing additional substituents, using mixed linkers¹⁹ or even capping additional metal ions), the oxidative power of these MOFs can be affected. The same analogy can be extended towards reductions: since metal orbitals in such MOFs define the position of LUCO, the reductive power can be altered by choosing metal ions that possess appropriate orbitals. Alternatively, the optical response can be modified by tuning the cluster-forming metal or even by using mixed metal clusters. The latter has been used as an approach to create mid-gap metal-centred states that result in the MOF featuring a LMCT transition, clusters that cannot be formed via direct synthesis. For instance, it has been proposed that in the UiO-66 framework Ti⁴⁺ could substitute Zr⁴⁺ in the oxocluster. However, it remains unclear whether the metals truly exchange or are just anchored to the node. In this sense,

Chapter 4 of this Thesis aims to understand Ti-incorporation in $\text{NH}_2\text{-UiO-66(Zr)}$ framework.

Even if such manipulations on their electronic properties lead to improvements in the MOFs photocatalytic performance, so far the activity of reported MOFs for artificial photosynthesis is very modest. Since tuning the optical absorption does not appear to be the issue, active site engineering is certainly the path to follow in order to improve their catalytic activity.

Accordingly, a second strategy is to employ MOFs as a passive container for the encapsulation of a light absorbing photocatalyst.^{30, 31} These active species are often homogeneous catalysts based on precious metals, and by encapsulating²⁹ or covalently bonding them to the framework, leaching has been successfully prevented.²² This strategy was also employed on an UiO-66 framework, using a $\text{Ru}(\text{bpy})_3$ as photosensitizer. Inspired by nature, the authors selected an organometallic Fe_2 complex for hydrogen evolution.²⁴ Fortunately, MOFs are not solely limited to being a static scaffold, thus promoting synergistic and cooperative interactions among the MOF and the encapsulated catalyst is a more stimulating third approach, where charge transfer between MOF and guest is achieved.²⁹ This method was applied, for example, on a UiO-67 framework consisting of biphenyl-4,4'-dicarboxylic acid combined with Ir-based ligands. When loaded with Pt nanoparticles,¹⁹ it showed remarkable activity for hydrogen evolution, due to the efficient electron transfer from the Ir-complex to Pt. Despite its good stability under photocatalytic conditions, this example relies on noble metals, limiting the applicability. Thus, new prospects for enhancing MOFs hydrogen evolution was outstanding.²⁹ This work revealed the potential of modular design in photocatalytic MOFs, and the importance of cooperativity between the MOFs photoactive matrix and a catalytically active encapsulated guest. This work encouraged other researchers to use different ligands in a surprisingly similar manner.⁷⁷

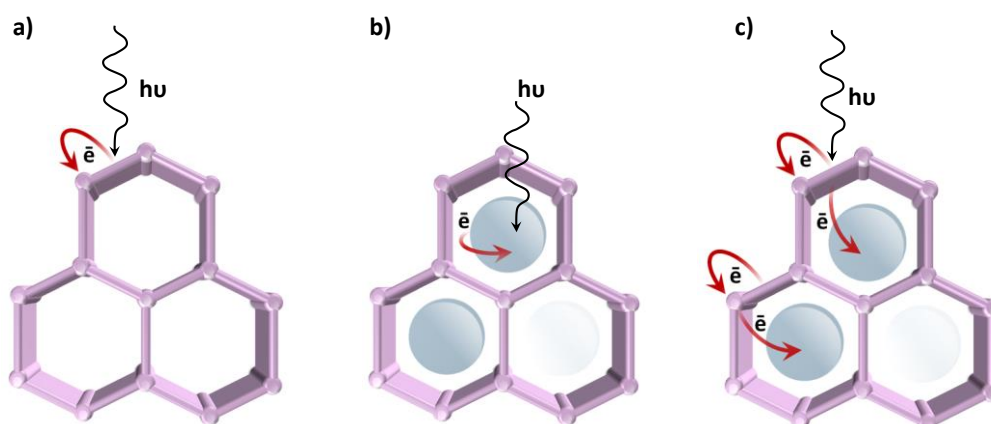


Figure 1.7. Approaches for promoting photocatalytic activity in MOFs: a) the organic linker harvest the light and LMCT is promoted; b) the MOF is used as a container of a light absorbing catalyst; c) charge transfer occurs between the MOF and the encapsulated catalyst.

photocatalytic performances appear by using redox- and photoactive and inexpensive metals, such as Fe and Co.

In this line, the “ship-in-a-bottle” technique for assembling a cobalt-based electrocatalyst in the NH₂-MIL-125(Ti) framework was reported. Although the precise structure of the catalyst remains unknown, the achieved performance for visible light

Outlook

MOFs provide an attractive matrix to achieve solar energy conversion by hierarchically organizing light-harvesting antennae and catalytic centres. Nonetheless so far, photocatalytic MOFs also show several drawbacks. Indeed, it is fair to admit that, despite some advances in the field during the last years, photocatalytic MOF performance is still far from the state of the art.

It is noteworthy that while most reports focus on the hydrogen evolution or CO₂ reduction reaction, there are only few MOF examples on water oxidation. This is not surprising, since most MOFs are built up from carboxylate linkers, and typically do not possess enough oxidation power to perform water oxidation. Moreover, the use of buffer solutions and strong oxidants typically used for water oxidation results in extreme environments where MOFs are unstable. Consequently, every study focusses on hydrogen evolution by means of a sacrificial electron donor (usually triethanolamine or trimethylamine) to provide an oxidative half reaction to close the catalytic cycle. It is vital to understand the role of these sacrificial electron donors⁷⁸ such that we can replace them by recyclable electron donors.^{79, 80} Then, by combining this system with a water oxidation catalyst, sustainable solar fuel generation can be achieved, as it is discussed through Chapter 5 of this Thesis.²⁷

Low charge mobility is another limitation in most photocatalytic MOFs.³⁷ Fortunately, MOFs' porous nature can compensate for it and allows for the diffusion of reactants and redox carriers throughout the crystallite. In addition, limitations by light penetration and light scattering should be also considered in MOFs photocatalytic systems. Accordingly, and combining the former with the lack of photogenerated charge mobility, different reaction rates can be obtained at the external surface and in the bulk of the MOF photocatalyst.⁸¹

Thus, conducting properties are very attractive for improved efficiencies, potentially allowing for higher electron/hole separation, and for physical separation of charges (in photo-electrochemical cells, PEC). Despite the fact that an exciting new field on conductor MOFs has emerged,^{39, 48} insights in the electronic transport properties of MOFs are still lacking. Moreover, we would like to encourage the application of conductive MOFs in photocatalysis for solar fuels generation.

We have emphasized that strong visible light absorption, long lifetime of excited states and high yield of charge-separated states are the main requirements for an excellent photocatalyst. Accordingly, matching reactant conversion times with the lifetime of photogenerated charges is the key for minimizing charge recombination

and maximizing the energy utilized for the photochemical reaction. We believe that the combination of innovative spectroscopic techniques and the appropriate photocatalytic testing⁸² will advance this field greatly.

Even when achieving a high quantum yield is the ultimate goal, the future growth of MOF-based photocatalysts requires deeper understanding of the operation of current systems and their advantages over other photocatalytic materials. The different ultrafast spectroscopies that have been outlined in this highlight are highly powerful tools to unravel MOFs functioning and to develop design guidelines for these materials in photocatalysis.

Scope and outline of the thesis

This thesis focuses on exploiting through understanding the potential of metal-organic frameworks in photocatalysis. Metal-organic frameworks (MOFs) are porous ordered materials consisting of metal centres connected by organic linkers. The great compositional variety in terms of metals and ligands has yielded more than 20.000 unique structures. Recently, an exciting new area in MOFs has emerged centred around controlling their electronic and optical properties to achieve artificial photosynthesis. MOFs provide an attractive, highly interesting matrix in which light-harvesting antennae and catalytic centres are hierarchically organized, and that facilitates the diffusion of reactants and products. The future growth of MOF-based photocatalysis requires deeper understanding of their underlying photo-physical processes, and of the benefits they offer over other photocatalytic materials.

In brief, the aim of this thesis is to gain structural and mechanistic insight for further development of photocatalytic MOFs. The choice of studying d^0 metal-organic frameworks was driven by a high photocatalytic activity (i.e. $\text{NH}_2\text{-MIL-125(Ti)}$), framework robustness and stability (i.e. $\text{NH}_2\text{-UiO-66}$) and the vast amount of research done on these structures.

The thesis starts with this Chapter 1 as an introduction to metal-organic frameworks as photocatalysts, and to some advanced spectroscopic techniques, which can help developing design guidelines of MOFs for this application.

MOFs are well known for their versatility via functionalization of their organic counterpart. In this context, chapter 2 compares the photoexcitation of MIL-125(Ti) -type structures containing different linkers, and reveals that the choice of the linker has a profound effect in the lifetime of the photoexcited state. This chapter highlights the importance of electron donating moieties at the linker for accomplishing efficient charge separation, which hinders recombination and allows chemical reactions to take place.

Chapter 3 describes the role of d^0 metal ions in $\text{NH}_2\text{-MIL-125}$ and $\text{NH}_2\text{-UiO-66}$ frameworks, and the implication of the choice of the metal (Ti, Zr and Hf) in photocatalytic hydrogen production. It was found that the photocatalytic proton reduction by $\text{NH}_2\text{-MIL-125(Ti)}$ is much more efficient than by the Zr/Hf UiO-66s ,

despite their structural similarities. This chapter shows that only in the case of the Ti-based MOF the highest occupied and lowest unoccupied orbitals promote a long lived ligand-to-metal charge transfer (LMCT) upon photoexcitation, making this material suitable for photocatalytic applications.

In chapter 4 the incorporation of Ti(IV) into the Zr-based NH₂-UiO-66 as a shortcut to improve its poor photocatalytic performance is revisited. The location of binding Ti(IV) is at linker defect sites and Ti is not incorporated into the inorganic secondary building unit through metal exchange. The choice of the titanium source is critical in the generation of an active hydrogen evolution photocatalyst.

Chapter 5 deals with the challenging search for a recyclable electron donor that enables the coupling of water oxidation and reductive half reactions into the Z-scheme. Through a combined study of multicomponent oxidation potentials and the dynamics at ultrafast time scales, charge transfer from the excited NH₂-MIL-125(Ti) to three different candidate charge acceptors is revealed.

Note that all chapters are based on published work and can be read independently. Therefore, some overlap may be present.

References

1. W. Ostwald, *Die Mühle des Lebens*, Leipzig, 1911.
2. A. Fujishima and K. Honda, *Nature*, 1972, **238**, 37-38.
3. Z. Jiang, Y. Tang, Q. Tay, Y. Zhang, O. I. Malyi, D. Wang, J. Deng, Y. Lai, H. Zhou, X. Chen, Z. Dong and Z. Chen, *Advanced Energy Materials*, 2013, **3**, 1368-1380.
4. A. Corma and H. Garcia, *Chemical Communications*, 2004, DOI: 10.1039/B400147H, 1443-1459.
5. T. Hisatomi, J. Kubota and K. Domen, *Chemical Society Reviews*, 2014, **43**, 7520-7535.
6. X. Li, J. Yu and M. Jaroniec, *Chemical Society Reviews*, 2016, **45**, 2603-2636.
7. H. Furukawa, K. E. Cordova, M. O'Keeffe and O. M. Yaghi, *Science*, 2013, **341**.
8. H.-C. Zhou, J. R. Long and O. M. Yaghi, *Chemical Reviews*, 2012, **112**, 673-674.
9. M. P. Suh, H. J. Park, T. K. Prasad and D.-W. Lim, *Chemical Reviews*, 2012, **112**, 782-835.
10. J.-R. Li, J. Sculley and H.-C. Zhou, *Chemical Reviews*, 2012, **112**, 869-932.
11. S. Bordiga, C. Lamberti, G. Ricchiardi, L. Regli, F. Bonino, A. Damin, K. P. Lillerud, M. Bjorgen and A. Zecchina, *Chemical Communications*, 2004, DOI: 10.1039/B407246D, 2300-2301.
12. M. Alvaro, E. Carbonell, B. Ferrer, F. X. Llabrés i Xamena and H. Garcia, *Chemistry – A European Journal*, 2007, **13**, 5106-5112.
13. F. X. Llabrés i Xamena, A. Corma and H. Garcia, *The Journal of Physical Chemistry C*, 2007, **111**, 80-85.
14. J. Gascon, M. D. Hernández-Alonso, A. R. Almeida, G. P. M. van Klink, F. Kapteijn and G. Mul, *ChemSusChem*, 2008, **1**, 981-983.
15. Y. Kataoka, K. Sato, Y. Miyazaki, K. Masuda, H. Tanaka, S. Naito and W. Mori, *Energy & Environmental Science*, 2009, **2**, 397-400.
16. Y. Horiuchi, T. Toyao, M. Saito, K. Mochizuki, M. Iwata, H. Higashimura, M. Anpo and M. Matsuoka, *The Journal of Physical Chemistry C*, 2012, **116**, 20848-20853.
17. T. Toyao, M. Saito, S. Dohshi, K. Mochizuki, M. Iwata, H. Higashimura, Y. Horiuchi and M. Matsuoka, *Chemical Communications*, 2014, **50**, 6779-6781.
18. D. Sun, L. Ye and Z. Li, *Applied Catalysis B: Environmental*, 2015, **164**, 428-432.
19. C. Wang, K. E. deKrafft and W. Lin, *J. Am. Chem. Soc.*, 2012, **134**, 7211-7214.
20. H.-Q. Xu, J. Hu, D. Wang, Z. Li, Q. Zhang, Y. Luo, S.-H. Yu and H.-L. Jiang, *Journal of the American Chemical Society*, 2015, **137**, 13440-13443.

21. T. Toyao, M. Saito, S. Dohshi, K. Mochizuki, M. Iwata, H. Higashimura, Y. Horiuchi and M. Matsuoka, *Research on Chemical Intermediates*, 2016, **42**, 7679-7688.
22. C. Wang, Z. Xie, K. E. de Krafft and W. Lin, *J. Am. Chem. Soc.*, 2011, **133**, 13445-13454.
23. H. Zhang, J. Wei, J. Dong, G. Liu, L. Shi, P. An, G. Zhao, J. Kong, X. Wang, X. Meng, J. Zhang and J. Ye, *Angewandte Chemie International Edition*, 2016, **55**, 14310-14314.
24. S. Pullen, H. Fei, A. Orthaber, S. M. Cohen and S. Ott, *J. Am. Chem. Soc.*, 2013, **135**, 16997-17003.
25. D. Wang, R. Huang, W. Liu, D. Sun and Z. Li, *ACS Catalysis*, 2014, **4**, 4254-4260.
26. D. Wang, M. Wang and Z. Li, *ACS Catalysis*, 2015, **5**, 6852-6857.
27. Y. Fu, D. Sun, Y. Chen, R. Huang, Z. Ding, X. Fu and Z. Li, *Angew. Chem., Int. Ed.*, 2012, **51**, 3364-3367.
28. D. Sun, Y. Fu, W. Liu, L. Ye, D. Wang, L. Yang, X. Fu and Z. Li, *Chemistry – A European Journal*, 2013, **19**, 14279-14285.
29. M. A. Nasalevich, R. Becker, E. V. Ramos-Fernandez, S. Castellanos, S. L. Veber, M. V. Fedin, F. Kapteijn, J. N. H. Reek, J. I. van der Vlugt and J. Gascon, *Energy & Environmental Science*, 2015, DOI: 10.1039/C4EE02853H.
30. J. He, Z. Yan, J. Wang, J. Xie, L. Jiang, Y. Shi, F. Yuan, F. Yu and Y. Sun, *Chem. Commun. (Cambridge, U. K.)*, 2013, **49**, 6761-6763.
31. J.-L. Wang, C. Wang and W. Lin, *ACS Catalysis*, 2012, **2**, 2630-2640.
32. T. Zhang and W. Lin, *Chemical Society Reviews*, 2014, **43**, 5982-5993.
33. A. Dhakshinamoorthy, A. M. Asiri and H. Garcia, *Angewandte Chemie International Edition*, 2016, **55**, 5414-5445.
34. S. Wang and X. Wang, *Small*, 2015, **11**, 3097-3112.
35. L. Zeng, X. Guo, C. He and C. Duan, *ACS Catalysis*, 2016, **6**, 7935-7947.
36. Y. Horiuchi, T. Toyao, M. Takeuchi, M. Matsuoka and M. Anpo, *Phys. Chem. Chem. Phys.*, 2013, **15**, 13243-13253.
37. M. A. Nasalevich, M. van der Veen, F. Kapteijn and J. Gascon, *CrystEngComm*, 2014, **16**, 4919-4926.
38. M. A. Nasalevich, M. G. Goesten, T. J. Savenije, F. Kapteijn and J. Gascon, *Chem. Commun.*, 2013, **49**, 10575-10577.
39. L. Sun, M. G. Campbell and M. Dincă, *Angewandte Chemie International Edition*, 2016, **55**, 3566-3579.
40. C. H. Hendon, D. Tiana, M. Fontecave, C. Sanchez, L. D'Arras, C. Sassoie, L. Rozes, C. Mellot-Draznieks and A. Walsh, *J. Am. Chem. Soc.*, 2013, **135**, 10942-10945.
41. K. Hendrickx, D. E. P. Vanpoucke, K. Leus, K. Lejaeghere, A. Van Yperen-De Deyne, V. Van Speybroeck, P. Van Der Voort and K. Hemelsoet, *Inorganic Chemistry*, 2015, **54**, 10701-10710.
42. B. Civalleri, F. Napoli, Y. Noel, C. Roetti and R. Dovesi, *CrystEngComm*, 2006, **8**, 364-371.
43. P. M. Wojciechowski, W. Zierkiewicz, D. Michalska and P. Hobza, *The Journal of Chemical Physics*, 2003, **118**, 10900-10911.
44. J. H. Cavka, S. Jakobsen, U. Olsbye, N. Guillou, C. Lamberti, S. Bordiga and K. P. Lillerud, *Journal of the American Chemical Society*, 2008, **130**, 13850-13851.
45. M. G. Goesten, F. Kapteijn and J. Gascon, *CrystEngComm*, 2013, **15**, 9249-9257.
46. M. A. Nasalevich, M. G. Goesten, T. J. Savenije, F. Kapteijn and J. Gascon, *Chemical Communications*, 2015, **51**, 961-962.
47. S. M. Chavan, G. C. Shearer, S. Svelle, U. Olsbye, F. Bonino, J. Ethiraj, K. P. Lillerud and S. Bordiga, *Inorganic Chemistry*, 2014, **53**, 9509-9515.
48. I. Hod, P. Deria, W. Bury, J. E. Mondloch, C.-W. Kung, M. So, M. D. Sampson, A. W. Peters, C. P. Kubiak, O. K. Farha and J. T. Hupp, *Nature Communications*, 2015, **6**, 8304.
49. A. Morozan and F. Jaouen, *Energy & Environmental Science*, 2012, **5**, 9269-9290.
50. N. Kornienko, Y. Zhao, C. S. Kley, C. Zhu, D. Kim, S. Lin, C. J. Chang, O. M. Yaghi and P. Yang, *Journal of the American Chemical Society*, 2015, **137**, 14129-14135.
51. A. J. Bard, Faulkner, L. R., *Electrochemical Methods: Fundamentals and Applications*, Wiley, 2001.
52. J. G. Santaclara, M. A. Nasalevich, S. Castellanos, W. H. Evers, F. C. M. Spoor, K. Rock, L. D. A. Siebbeles, F. Kapteijn, F. Grozema, A. Houtepen, J. Gascon, J. Hunger and M. A. van der Veen, *ChemSusChem*, 2016, **9**, 388-395.
53. K. T. Butler, C. H. Hendon and A. Walsh, *Journal of the American Chemical Society*, 2014, **136**, 2703-2706.

54. K. T. Butler, C. H. Hendon and A. Walsh, *ACS Applied Materials & Interfaces*, 2014, **6**, 22044-22050.
55. A. Walsh, K. T. Butler and C. H. Hendon, *MRS Bulletin*, 2016, **41**, 870-876.
56. C. H. Hendon and A. Walsh, *Chemical Science*, 2015, **6**, 3674-3683.
57. H.-J. Son, S. Jin, S. Patwardhan, S. J. Wezenberg, N. C. Jeong, M. So, C. E. Wilmer, A. A. Sarjeant, G. C. Schatz, R. Q. Snurr, O. K. Farha, G. P. Wiederrecht and J. T. Hupp, *Journal of the American Chemical Society*, 2013, **135**, 862-869.
58. C. Zou, M.-H. Xie, G.-Q. Kong and C.-D. Wu, *CrystEngComm*, 2012, **14**, 4850-4856.
59. M. A. Nasalevich, C. H. Hendon, J. G. Santaclara, K. Svane, B. van der Linden, S. L. Veber, M. V. Fedin, A. J. Houtepen, M. A. van der Veen, F. Kapteijn, A. Walsh and J. Gascon, *Scientific Reports*, 2016, **6**, 23676.
60. M. de Miguel, F. Ragon, T. Devic, C. Serre, P. Horcajada and H. Garcia, *ChemPhysChem*, 2012, **13**, 3651-3654.
61. A. Walsh and C. R. A. Catlow, *ChemPhysChem*, 2010, **11**, 2341-2344.
62. J. Long, S. Wang, Z. Ding, S. Wang, Y. Zhou, L. Huang and X. Wang, *Chem. Commun. (Cambridge, U. K.)*, 2012, **48**, 11656-11658.
63. D. Sun, W. Liu, M. Qiu, Y. Zhang and Z. Li, *Chemical Communications*, 2015, **51**, 2056-2059.
64. M. Gutierrez, F. Sanchez and A. Douhal, *Physical Chemistry Chemical Physics*, 2016, **18**, 5112-5120.
65. A. Fateeva, P. A. Chater, C. P. Ireland, A. A. Tahir, Y. Z. Khimyak, P. V. Wiper, J. R. Darwent and M. J. Rosseinsky, *Angewandte Chemie International Edition*, 2012, **51**, 7440-7444.
66. Y. Liu, Y. Yang, Q. Sun, Z. Wang, B. Huang, Y. Dai, X. Qin and X. Zhang, *ACS Applied Materials & Interfaces*, 2013, **5**, 7654-7658.
67. M.-H. Xie, X.-L. Yang, C. Zou and C.-D. Wu, *Inorganic Chemistry*, 2011, **50**, 5318-5320.
68. J. Schneider, M. Matsuoka, M. Takeuchi, J. Zhang, Y. Horiuchi, M. Anpo and D. W. Bahnemann, *Chemical Reviews*, 2014, **114**, 9919-9986.
69. J. Schneider, K. Nikitin, R. Dillert and D. W. Bahnemann, *Faraday Discussions*, 2016, DOI: 10.1039/C6FD00193A.
70. R. Berera, R. Grondelle and J. T. M. Kennis, *Photosynth. Res.*, 2009, **101**, 105-118.
71. M. Gutierrez, B. Cohen, F. Sanchez and A. Douhal, *Physical Chemistry Chemical Physics*, 2016, **18**, 27761-27774.
72. M. Gutiérrez, F. Sánchez and A. Douhal, *Chemistry – A European Journal*, 2016, **22**, 13072-13082.
73. M. A. Ratner, *International Journal of Quantum Chemistry*, 1987, **31**, 989-989.
74. X.-X. Zhang, C. Würth, L. Zhao, U. Resch-Genger, N. P. Ernsting and M. Sajadi, *Review of Scientific Instruments*, 2011, **82**, 063108.
75. W. Kaim and J. Fiedler, *Chemical Society Reviews*, 2009, **38**, 3373-3382.
76. G. Smolentsev, A. Guda, X. Zhang, K. Haldrup, E. S. Andreiadis, M. Chavarot-Kerlidou, S. E. Canton, M. Nachtegaal, V. Artero and V. Sundstrom, *The Journal of Physical Chemistry C*, 2013, **117**, 17367-17375.
77. Z. Li, J.-D. Xiao and H.-L. Jiang, *ACS Catalysis*, 2016, **6**, 5359-5365.
78. T. Morimoto, T. Nakajima, S. Sawa, R. Nakanishi, D. Imori and O. Ishitani, *Journal of the American Chemical Society*, 2013, **135**, 16825-16828.
79. B. C. M. Martindale, E. Joliat, C. Bachmann, R. Alberto and E. Reisner, *Angewandte Chemie International Edition*, 2016, **55**, 9402-9406.
80. R. D. Richardson, E. J. Holland and B. K. Carpenter, *Nat Chem*, 2011, **3**, 301-303.
81. M. Motegh, DOI: 10.4233/uuid:8e9ed02f-2fee-4613-8d85-4ed12b54fa52, Delft University of Technology, 2013.
82. M. Qureshi and K. Takanabe, *Chemistry of Materials*, 2016, DOI: 10.1021/acs.chemmater.6b02907.

Organic linker defines kinetics the excited-state decay of photocatalytic MIL-125-type materials

Recently, MIL-125(Ti) and NH₂-MIL-125(Ti), two titanium based metal-organic frameworks, have attracted significant research attention in the field of photocatalysis for solar fuel generation. This work reveals that the differences between these structures are not only based on their light absorption range but also on the decay profile and topography of their excited states. In contrast to MIL-125(Ti), NH₂-MIL-125(Ti) shows markedly longer lifetimes of the charge separated state, which improves photoconversion by the suppression of competing decay mechanisms. Using spectroelectrochemistry and ultrafast spectroscopy we demonstrate that upon photoexcitation in NH₂-MIL-125(Ti) the electron is located in the Ti-oxoclusters and the hole resides on the aminoterephthalate unit, specifically on the amino group. The results highlight the role of the amino group in NH₂-MIL-125(Ti), the electron donation of which extends the lifetime of the photoexcited state substantially.

This chapter is based on the following publication:

Organic linker defines kinetics of the excited-state decay of photocatalytic MIL-125-type materials

J. G. Santaclara, M. A. Nasalevich, S. Castellanos, W. H. Evers, F. C. M. Spoor, L. D. A. Siebbeles, F. Kapteijn, F. Grozema, A. Houtepen, J. Gascon, J. Hunger, M. A. van der Veen, *ChemSusChem*. 9, 2016, 388

Introduction

Our society is currently facing the challenge of fossil fuel depletion. Moreover, the utilization of such fuels also results in CO₂ emissions, which leads to climate change. In this context, solar-driven hydrogen production from water is very attractive to provide a long-term solution for sustainable solar energy conversion and storage,¹ yet efficiencies are still too low for practical application.^{2, 3}

Metal-Organic Frameworks (MOFs) are promising materials for gas separation and storage,⁴ drug delivery,^{5, 6} chemical sensing⁷ or membrane technologies.⁸ Recently, they emerged as prospective alternative photocatalysts to more traditional materials such as TiO₂ or other semiconductors.^{9, 10} The unprecedented tunability of MOFs, typically characteristic of molecular (photo)catalysts, combined with the durability and recyclability of heterogeneous systems shows potential for a bright future in photocatalysis.

Notably, the number of reported MOFs based on earth abundant elements that demonstrate photocatalytic activity is still increasing. To date, a variety of photocatalytic reactions, which include the most relevant for environmental concerns such as CO₂ reduction,^{11, 12} H₂ evolution^{13, 14} and the oxidation of various pollutants,¹⁵ have been catalyzed by frameworks based on metals such as Ti,¹⁶ Zr,^{17, 18} Zn,^{19, 20} Fe²¹ etc. However, their performance is limited compared to that of state-of-the-art photocatalysts.²² A fundamental understanding of photocatalysis by MOFs has the potential to advance this field significantly. If we consider that the oxygen half reaction is the kinetic bottleneck in the water splitting reaction,^{23, 24} it would be particularly interesting to unravel the pathway experienced by the photogenerated holes of MOFs such that more efficient oxidation catalysts for this reaction can be designed. This has remained elusive so far.

In this work, we focus on two MOFs based on titanium, MIL-125(Ti) and NH₂-MIL-125(Ti) (Figure 2.1). These two frameworks are isorecticular, which means that their structure and the crystallographic topology are not affected by the difference in the organic linkers that constitute the MOF. NH₂-MIL-125(Ti) is of great interest as it is one of the most reported MOFs in this field because of its successful application in visible-light photocatalysis.^{11, 13, 25}

MIL-125(Ti) was reported for the first time by Férey and co-workers in 2009.²⁶ In their first publication, the authors assessed the catalytic activity of MIL-125(Ti) in oxidation of alcohols prompted by the analogy between the Ti-based MOF and the most studied photocatalyst TiO₂. However, the catalyst is only active under UV irradiation, which restricts its applicability in solar-driven photocatalysis. Later, the remarkable tunability of MOFs came into play: MIL-125(Ti) was synthesized using 2-aminoterephthalic acid (ATA) instead of terephthalic acid as the linker.^{11, 27} The additional NH₂ group in the aromatic system of the linker yielded a framework sensitive to visible-light irradiation, named NH₂-MIL-125(Ti). Although the two MOFs are isorecticular, they possess some distinct properties, such as surface area and light

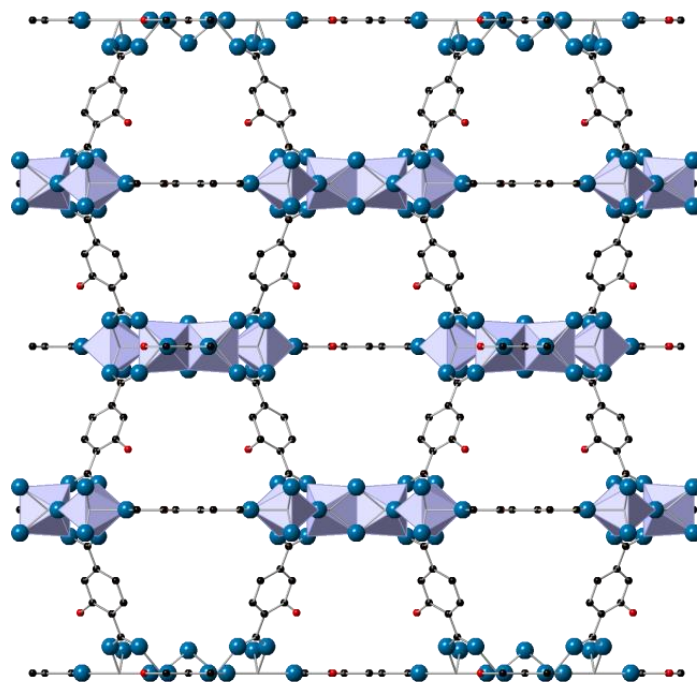


Figure 2.1. Crystal structure of X-MIL-125(Ti) metal-organic framework. The (100) view: red balls denote X, MIL-125(Ti) X = H; NH₂-MIL-125(Ti) X = NH₂. The orientation of the NH₂-groups with respect to each other cannot be determined by XRD.

absorption (Figures 2.9 and 2.2a). It is often assumed that from a photocatalytic point of view the biggest difference between both systems is that the NH₂-functionalized version of the MOF is able to absorb lower-energy photons. However, in this work we demonstrate that the difference in photoexcitation is much more profound and is not limited to the light absorption profiles.

To exploit the rich potential of NH₂-MIL-125(Ti), in this study we address a set of fundamental questions related to how the presence of the amino group modifies the excited states promoted by light absorption compared to the non-aminated analogue.

It is commonly accepted that photoexcitation in MIL-125(Ti) proceeds through ligand-to-metal charge transfer (LMCT).^{13, 16, 28} This implies that the highest occupied crystal orbital (HOCO) of MIL-125(Ti) resides on the organic linker, whereas the lowest unoccupied crystal orbital (LUCO) is localized largely on the titanium oxo cluster.²⁹ Such excitation promotes an electron from the linker to the metal to reduce it to Ti³⁺. These species have been detected by EPR spectroscopy.^{13, 16, 26} However, although the localization of photogenerated holes is critical to design oxidation catalysts for reactions (i.e., water splitting) the pathway experienced by the photogenerated hole is less evident. Walsh and Catlow modelled photoexcitation in MIL-125(Ti) and found that the removal of an electron from the organic-defined HOCO is likely to result in the formation of hydroxyl radicals or an oxygen vacancy by O₂ release.²⁹ The oxygen atom involved in both processes is most probably the bridging oxydo ligand of the titanium oxo clusters.

A different process might occur in the case of NH₂-MIL-125(Ti). The NH₂ group of ATA carries a lone pair that can donate an electron relatively easily. Amines are well-known donors, and formation of N-centred radical cations is not uncommon.^{30, 31}

In the present study, we resolve the localization of the photogenerated holes in the NH₂-MIL-125(Ti) by a combination of spectroscopic techniques. The presence of the amino groups leads to a drastically slower decay of the photoexcited state with respect to that of MIL-125(Ti). The increase of the lifetime if electron-donating substituents are used on the organic linker is of great importance for the rational design of MOFs as photocatalysts. Moreover, the localization of the hole in the amine group provides knowledge upon which to base this rational design of MOF-based catalysts that fully exploit their oxidative power.

Experimental

Materials and reagents

All chemicals were purchased from Sigma Aldrich and used without further purification.

Synthesis

MIL-125(Ti) was synthesized according to a method reported previously.²⁷ Typically, terephthalic acid (3.53 g) and anhydrous DMF (56 mL) were mixed and placed in a round-bottomed flask. The mixture was heated at 105 °C for 1 h to dissolve the acid and remove the residual water. With the temperature of the solution kept at 105 °C, anhydrous methanol (14 mL) was added, and a reflux condenser was fitted. The solution was heated under stirring for 1 h, after which titanium isopropoxide (4.2 mL) was added. The resulting mixture was heated to reflux with stirring for 72 h at 100 °C. After cooling to RT and filtration of the mixture, a white solid was isolated, which was washed with DMF for 24 h at 155 °C and then methanol at 100 °C. The white product was dried in air at 100 °C to remove methanol from the pores.

NH₂-MIL-125(Ti) was synthesized using a protocol reported by Walsh and co-workers.²⁸ Typically, 2-aminoterephthalic acid (0.5 g, 2.76 mmol) was dissolved in a mixture anhydrous DMF (16 mL) and anhydrous methanol (4 mL) at RT in a glovebox. Titanium isopropoxide (0.55 mL, 1.93 mmol) was added, and the mixture was placed in an autoclave. The autoclave was sealed and heated for 72 h at 110 °C. The obtained yellow solid was collected by filtration, dispersed in fresh DMF, and heated at 110 °C overnight to remove residual linker. Then, the same procedure was repeated using methanol for 6 h at 80 °C. Finally, the solid was dried in air at 80 °C.

Characterization and methods

Powder X-Ray diffraction patterns were recorded using Bruker-AXS D5005 with CoK α radiation.

Nitrogen physisorption measurements were performed using a Tristar II 3020 Micromeritics unit at 77 K. Before the experiment, the samples were degassed for 16

h at 423 K under vacuum. The BET areas were calculated using intervals to allow positive BET constants.³² The total pore volumes were calculated at a relative pressure of 0.9.

Thermogravimetric analysis (TGA) was performed by using a Mettler Toledo TGA/SDTA851 system under an air flow (60 mL min⁻¹) at a heating rate of 10 K min⁻¹ to 1073 K.

Diffuse reflectance UV/Vis spectra were collected by using a PerkinElmer Lambda 900 spectrophotometer equipped with an integrating sphere (“Labsphere”) in the $\lambda=200\text{--}800$ nm range. BaSO₄ was used as a white standard.

Spectroelectrochemistry. The optical setup comprised a Deuterium-Halogen lamp DH-2000 as light source, a USB2000 UV-VIS spectrometer, and a NIRQUEST NIR spectrometer, all from Ocean Optics Inc. The potential was applied by using CH Instruments Analyser CHI832B as the potentiostat. An optically transparent thin-layer electrochemical (OTTLE) cell fabricated by Spectroelectrochemistry Reading (University of Reading)^{33, 34} provided with a three-electrode set that consisted of a Pt minigrid working electrode (32 wires cm⁻¹), Pt minigrid auxiliary electrode, and Ag wire pseudo-reference electrode melt-sealed in a modified polyethylene spacer (≈ 0.2 mm thickness) was used as the measuring cell. LiClO₄ in acetonitrile (0.1 M) and (N^tBu₄)BF₄ in dichloromethane (0.1 M) were used as electrolytes for aminoterephthalate dimethyl ester and Ti₈O₈(OCC(CH₃)₃), respectively. All solutions were prepared under glovebox conditions to avoid the presence of oxygen.

Femtosecond transient absorption spectroscopy. Samples for visible (Vis)-pump visible-probe measurements were excited by 180 fs pulses at $\lambda=400$ nm generated by using a YKGBW oscillator (Light Conversion, Pharos SP) at $\lambda=1028$ nm through nonlinear frequency mixing in an optical parametric amplifier (OPA) and second harmonics module (Light Conversion, Orpheus). A small fraction of the $\lambda=1028$ nm fundamental beam was split off to generate the broadband probe spectrum in a sapphire (500 - 1600 nm) crystal. The probe pulse was delayed relative to the pump using a delay stage with maximum delay of 3 ns. The pump and probe pulses overlap on the sample position at an angle of $\sim 8^\circ$, after which the probe light is led to a detector suitable for the probe spectrum selected (Ultrafast Systems, Helios). To prevent multiple photons absorption processes, the pump fluence was set sufficiently low to allow us to study single exciton dynamics. Typically, MOF (50 mg) was dispersed in the solvent (14 mL) and sonicated for 30 min. To separate large particles (>100 nm), the suspension was then centrifuged for 30 min at 6000 rpm. The supernatant was placed in a 2 mm stirred quartz cuvette for the measurements.

Vis-pump infrared (IR)-probe experiments were performed by using a regenerative Ti:Sapphire amplified laser system (Spitfire Ace, Spectra Physics) to provide pulses at $\lambda=800$ nm with a duration of 35 fs and a pulse energy of 5 mJ at a repetition rate of 1 kHz. Commercial optical parametric amplifiers (TOPAS-C, Spectra-Physics) were pumped with 1.5 mJ of the $\lambda=800$ nm pulses. The signal and idler pulses from one TOPAS-C were used in a difference frequency mixing process in a silver gallium

disulfide (AgGaS₂) crystal, resulting in ~8 μJ tuneable IR pulses with a full width at half maximum (FWHM) of 300 cm⁻¹. A wedged CaF₂ window was used to generate a probe and a reference pulse from the output of the OPA, and the reflection of the front side was used as the probe pulse and a reference pulse from the back-reflection. A second portion of the λ=800 nm pulses was frequency-doubled in a β-barium borate crystal to yield visible pump pulses with a central wavelength of 400 nm. A translational stage was used to control the timing of the Vis-pump pulses relative to the IR probe pulses. A mechanical chopper was used to block every second pump pulse, which allows active background subtraction. The pump, probe, and reference pulses were focused into the sample, and the pump and the probe pulses were spatially overlapped. The probe and the reference pulses were recollimated and spectrally dispersed with an imaging spectrograph (Horiba Triax 180). The intensities *I* were detected on two separate lines of a 3x32 mercury-cadmium-telluride (MCT, Infrared Associates) detector array. The pump-induced absorption change were thus given as $\Delta A = -\ln[I_{probe} \cdot I_{reference,0} / (I_{probe,0} \cdot I_{reference})]$, in which the subscript 0 refers to the IR intensities recorded without pump excitation. For all the measurements, NH₂-MIL-125(Ti) (40 mg) was dried overnight at 423 K then dispersed in solvent (800 μL) and sonicated for 15 min.

Results and discussion

MIL-125(Ti) and NH₂-MIL-125(Ti) were synthesized according to protocols reported elsewhere.^{27, 35} We obtained MIL-125(Ti) and NH₂-MIL-125(Ti) that appear white and yellow, respectively, and possess large total pore volumes in line with previous reports (Figure A2.9).²⁷ Powder XRD showed that the MOFs have a high crystallinity, and no crystalline impurities were detected (Figure A2.10). The structures of MIL-125(Ti) and NH₂-MIL-125(Ti) are illustrated in Figure 2.1. These frameworks consist of octameric Ti₈O₈(OH)₄ clusters as nodes that are interconnected by the corresponding linkers to form a centered cubic structure.²⁶ Despite the identical crystal structure, some of the properties are remarkably different as a result of the additional substituent in the aromatic system of the terephthalate in the case of NH₂-MIL-125(Ti). The presence of the -NH₂ group, which holds a lone electron pair on the N atom, implies changes in hydrophilicity and basicity compared to the bare aromatic linker. Importantly for photocatalysis, the lowest-energy optical absorption bands differ by circa 100 nm: MIL-125(Ti) has λ_{max} of 290 nm, whereas NH₂-MIL-125(Ti) absorbs visible light at λ_{max} = 380 nm (Figure 2.2a).

Efforts have been made to push the absorption of photocatalytic systems into the visible region of the spectrum to utilize solar energy efficiently.^{36, 37} Clearly, an enhancement of the uptake of sunlight is only worthwhile if the redox potentials of the photogenerated charges are sufficient to drive the desired chemistry.

Apart from this requirement, the kinetics of the photoexcited states in MIL-125(Ti)-type MOFs have a profound effect on the efficiency of the photocatalysis. For an effective transfer of the light-induced charges to a reactant, the lifetime of the charge-

separated state needs to be sufficiently long to compete with other decay mechanisms of the photoexcited state. To assess the decay profiles of both MOFs, we performed ultrafast transient absorption (TA) spectroscopy.

In a typical TA experiment, an excitation laser pulse (pump) promotes a fraction of chromophores to an electronically excited state. After a certain delay (τ), a weak probe pulse is sent through the excited sample, from which the transmission spectrum is detected. By subtracting the unpumped transmission spectrum of the probe, a difference absorption spectrum $\Delta A(\lambda, \tau)$ for the time delay τ is obtained. We used pulses of ~ 150 fs to obtain difference spectra $\Delta A(\lambda, \tau)$ with a sub-picosecond time resolution. This ultrafast time scale allows us to collect information on the dynamic processes that occur in the exposed system³⁸ and to probe the very first dynamics of the photoexcited state.

In general, the difference spectra contain contributions from the following processes: a) depletion of the ground state to lead to a negative ΔA called “ground state bleach”; b) redshifted from the ground state bleach, a negative ΔA may be caused by stimulated emission; c) a positive ΔA caused by excited state absorption; d) a positive ΔA caused by reactions of the excited state to result in charge-separated states, triplet states, among others.³⁸

Two types of probe beams were employed in this study. The type 1 probe assesses visible-light absorption. The TA in this configuration is ideally suited to follow charge transfer to/from the metal centre because it provides direct information on the excited redox-active states of the MOFs. The type 2 probe provides a mid-IR absorption spectrum. Transient IR absorption spectroscopy is able to trace motion of photogenerated charge carriers through various functional organic groups of modular materials.³⁹

The transient absorption spectra of MIL-125(Ti) and NH₂-MIL-125(Ti) are presented in Figure 2.2 b and c, respectively. With the application of water splitting in mind, we selected water as the solvent. TA spectra of NH₂-MIL-125(Ti) were also measured in DMF to compare the obtained results in a solvent of different polarity (Figure A2.13). The MOFs were excited at wavelengths as close as possible to their respective absorption maxima ($\lambda=315$ and 400 nm).

In the case of MIL-125(Ti), the observed transient signal covers the whole $\lambda=500-750$ nm range and decays rapidly to the ground state after pump pulse excitation. We also detected stimulated emission that leads to negative absorption (below $\lambda=525$ nm). In contrast, NH₂-MIL-125(Ti) shows a substantially different behaviour. The excitation results in an intense transient signal with a maximum at $\lambda=570$ nm, a shoulder at $\lambda=530$ nm, and a somewhat broad additional band at $\lambda=500 - 750$ nm. The excited state absorption of NH₂-MIL-125(Ti) exhibits much slower decay than observed for MIL-125(Ti) (Figure 2.3). Indeed, more than 70% of the signal intensity for NH₂-MIL-125(Ti) remains after 3 ns, the time window of the measurement, versus

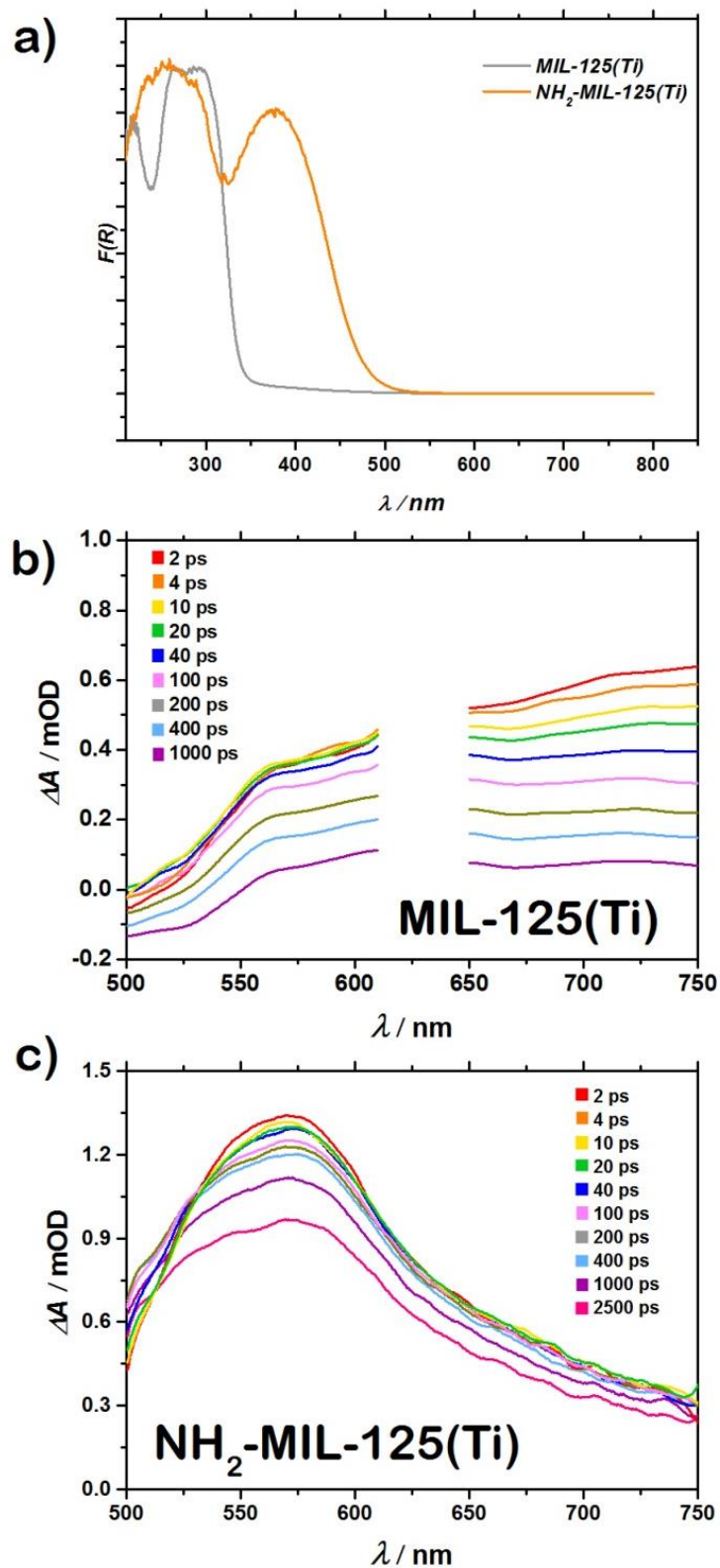


Figure 2.2. a) Diffuse reflectance UV/Vis spectra of the two catalysts: MIL-125(Ti) (grey), NH₂-MIL-125(Ti) (orange); b) Transient spectra of MIL-125(Ti) in water upon excitation at 315 nm pump and c) NH₂-MIL-125(Ti) in water upon excitation at 400 nm pump. The remnant of the 630 nm light used to generate 315 nm light via second-harmonic generation in the pump beam overwhelms the transient spectra between 610-650 nm, hence this part of the spectra is omitted. A fast Fourier transform filter was applied to the experimental data and it is shown as a trend for a more clear visualization.

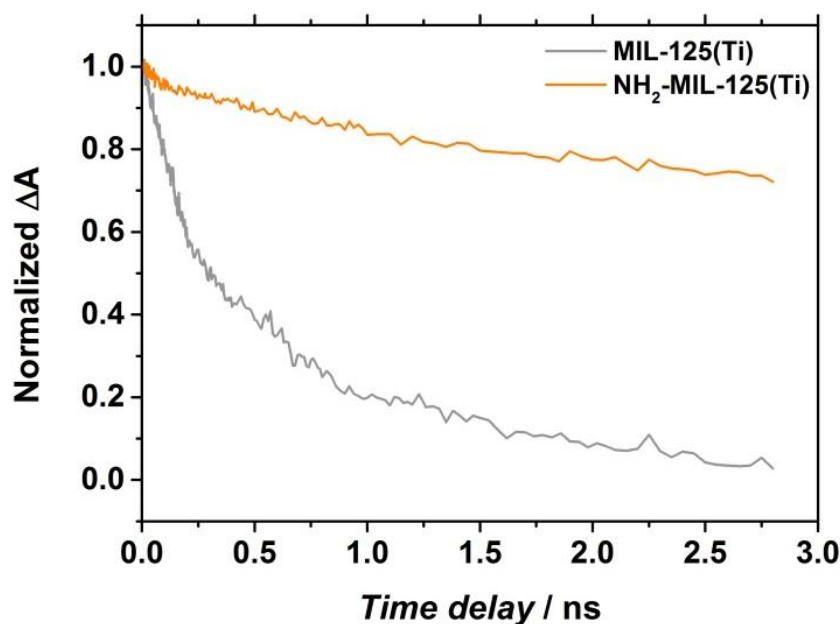


Figure 2.3. Comparison of the time traces of MIL-125(Ti) (grey) and NH₂-MIL-125(Ti) (orange) in water in the range $\lambda=560-610$ nm.

10% for MIL-125(Ti).

Notably, the information extracted from the TA analysis is of great relevance as the kinetics of the excited state decay can have a profound impact on the photocatalytic performance. More efficient photocatalysis is expected if the photoexcited charges have a longer lifetime, whereas the lifetime of the excited state of MIL-125(Ti) may be too short to allow the efficient utilization of the generated charge carriers.

In addition to the charge recombination rates, the localization of the photogenerated charge carriers in MIL-125(Ti) and NH₂-MIL-125(Ti) is critical for the rational design of photocatalysts. It is accepted that in both MOFs the photogenerated electron is mainly centered on Ti.¹³ Moreover, LMCT in MIL-125(Ti)-type materials has been demonstrated clearly by EPR spectroscopy,^{13, 16} flash photolysis⁴⁰ and theory.²⁹ The detection of Ti⁺³ is straightforward because of its paramagnetic nature and the clear signatures of these species in the visible-light region, regardless of the surrounding structure.^{26, 28, 41-43} However, the localization of the hole remains rather unclear. As discussed above, with the help of DFT, Walsh and Catlow revealed the importance of the organic linker in the photogeneration of the hole for MIL-125(Ti).²⁹ To the best of our knowledge, no such information has been reported for NH₂-MIL-125(Ti). Indeed, inducing a LMCT implies that the positively charged hole is localized mainly on the organic linker, yet there is no clear evidence for this. Here this issue is addressed through the analysis of the different spectral features of the photoexcited states obtained from TA by spectroelectrochemistry.

Along with the slower decay kinetics, TA spectra of NH₂-MIL-125(Ti) differ from those of its nonaminated counterpart in the clear dominance of a peak centred at $\lambda=570$ nm. If we assume that LMCT occurs in both MOFs, the differences in their respective TA spectra might arise from the distinct absorption features of the holes

localized in the two different linkers. To detect the optical changes associated with the injection of a hole in the NH₂-MIL-125(Ti) amino linker, a model molecule was used in spectroelectrochemistry experiments. *In situ* absorption spectra of aminoterephthalate dimethyl ester were recorded upon its electrochemical oxidation (Figure 2.4a). Immediately after the anodic current starts, the bleaching of the bands at $\lambda=250$ and $\lambda=365$ nm is recorded together with the growth of new bands at $\lambda=300$ and 530 nm. We assign these initial changes, which exhibit clear isosbestic points at $\lambda=402$, 334 and 267 nm, to the initial formation of the aminoterephthalatic radical cation.⁴⁰ Such radical species further react, most likely through dimerization,⁴⁴⁻⁴⁶ to lead to irreversible oxidation and permanent alterations of the optical spectrum (Figure A2.30). Notably, if the linker is incorporated in the MOF lattice, such dimerization reactions between radical cations cannot occur and allow for a reversible cycle of the charge separation/recombination to lead to photocatalytic activity.

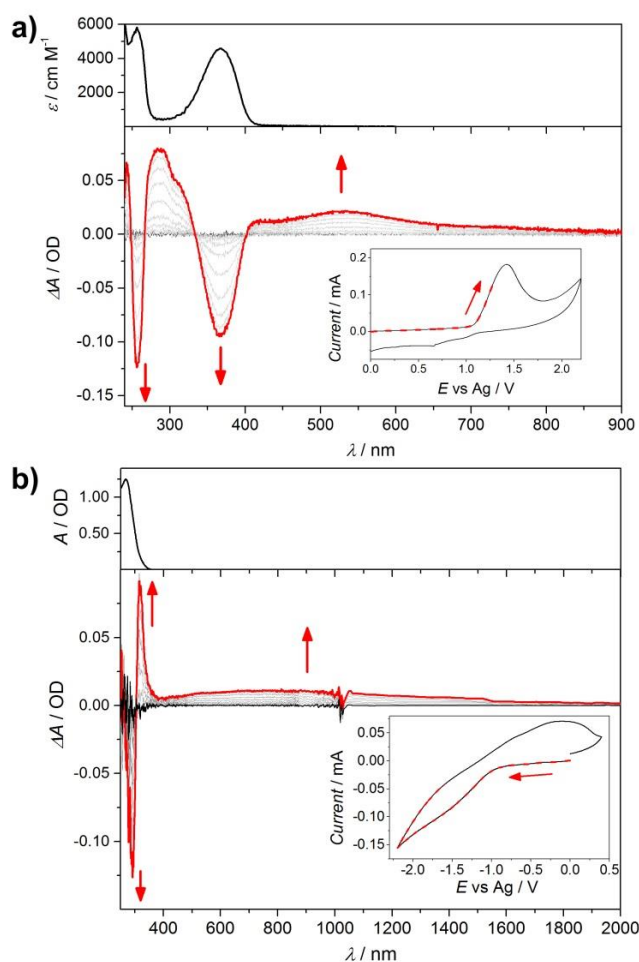


Figure 2.4. Absorption spectral changes of a) aminoterephthalate dimethyl ester in acetonitrile and b) $\text{Ti}_8\text{O}_8(\text{OOCC}(\text{CH}_3)_3)_{16}$ soluble oxoclusters in dichloromethane upon oxidation and reduction, respectively. Ground state absorption spectra are shown on top of each spectroelectrochemical measurement. Insets display the registered cyclic voltammogram and highlighted in red dashes the voltage range corresponding to the shown spectra.

The spectral features of the aminoterephthalate radical cation can be recognized clearly in the TA spectrum of NH₂-MIL-125(Ti) (Figure 2.2c and 2.31). The redshift of the maximum (from $\lambda=530$ nm in the linker to $\lambda=570$ nm in the MOF) is in line with that observed in the ground-state spectra of the MOF (Figure 2.2a) and the linker (Figure 2.4a top). Thus, we conclude that a hole is located on the linker in the excited state.

To unequivocally find the optical fingerprint of the Ti³⁺ species in these MOFs, we performed the same experiment with inverted bias and with soluble titanium oxo clusters. Such oxo clusters, with molecular formula Ti₈O₈(OCC(CH₃)₃)₁₆, consist of well-defined ring-shaped Ti octamers linked by the carboxylic groups of pivalic acid ligands and are used as precursors in the synthesis of MIL-125(Ti).²⁸

Upon the application of negative potentials, the generation of cathodic current was accompanied by the appearance of a broad band with a smooth maximum around $\lambda=750$ nm and a tail that covers the near-IR region together with the bleaching of the band at $\lambda=268$ nm (Figure 2.4b). Such changes were fully reversible upon reversing the applied potential (see Figure A2.31). Thus, in line with previous studies where Ti^{3+/4+} mixed valence states are identified by the detection of broad bands that cover range of $\lambda=400$ nm to near-IR,^{26, 41, 47} we assign the $\lambda=400$ -2000 nm positive ΔA in Figure 2.4b to the reduced species of the titanium oxo clusters.

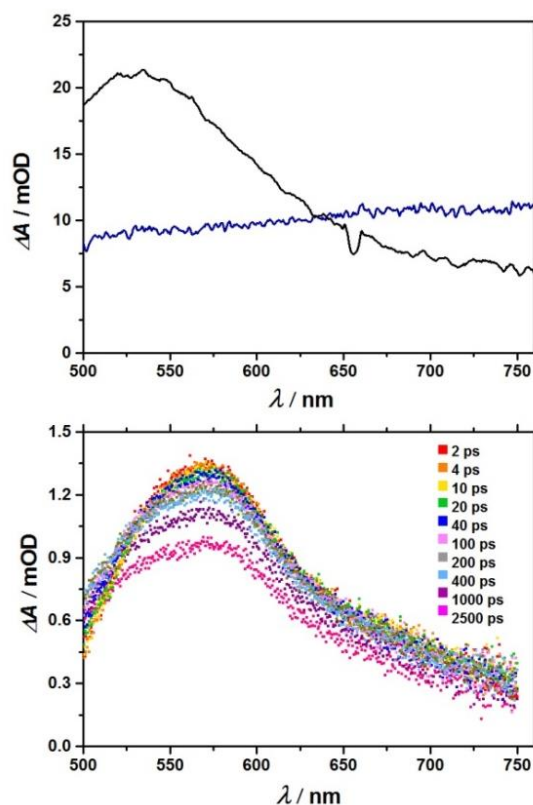


Figure 2.5. Top the absorption spectra of oxidised linker (dimethyl aminoterephthalate) (*black*) and reduced oxocluster (Ti₈O₈(OCC(CH₃)₃)₁₆) (*blue*) from the spectroelectrochemical measurements presented in Figure 2.4. Here these figures are zoomed in to the same wavelength range as the TA spectra (bottom) of NH₂-MIL-125(Ti) in water (Figure 2.2c).

Such a different absorption profile is also present in the TA spectra of MIL-125(Ti) (Figure 2.2b) and overlaps with the radical cation absorption band in NH₂-MIL-125(Ti) (Figure 2.2c). This indicates that electrons are indeed injected into the inorganic scaffolds in the nonaminated and aminated MIL-125(Ti), although they exhibit different decays. Thus spectroelectrochemical analysis gives strong evidence for the LMCT character of the NH₂-MIL-125(Ti) photoexcited state through the detection of the linker radical cation ($\lambda=570$ nm peak) and the reduced Ti-oxo cluster ($\lambda=500-750$ nm broad band) absorption fingerprints (Figure 2.5). This demonstrates that the behaviour observed in the MOF is a clear combination of the behaviour shown by its main components, once again suggests that MOFs should be considered as an array of self-assembled molecular catalysts rather than as classical semiconductors.

To understand how the photogenerated oxidative power of the NH₂-MIL-125(Ti) framework may be harnessed and more precisely localize the photoexcited hole on the organic linker, a mid-IR probe was used. Indeed, the region of the mid-IR that we examined ($\sigma=1250$ to 3620 cm⁻¹; Figure 2.6) solely probes the organic vibrations of the structure. For this purpose, the MOF was immersed in an IR-transparent solvent and assessed by a mid-IR probe after an excitation pulse at $\lambda=400$ nm, again with a sub-picosecond time resolution. Polar (D₂O, $\sigma=1350$ to 1610 cm⁻¹) and apolar (C₂H₂Cl₄, $\sigma=1250$ to 3620 cm⁻¹) solvents were used. Except for solvochromatic shifts, similar transient spectra and time dynamics are observed in both media (Figures 2.7, Figures 2.15-2.29). Hence, it is likely that the spectra of NH₂-MIL-125(Ti) are representative of the situation in water, also for the ranges for which C₂H₂Cl₄ was the sole transparent solvent for the IR probe. Although we expected to obtain different spectra and kinetics if we used solvents with different polarities (generally, more polar media facilitate charge-transfer processes)⁴⁸ our results may be associated with the less efficient solvation of the porous material compared to that of discrete molecules.

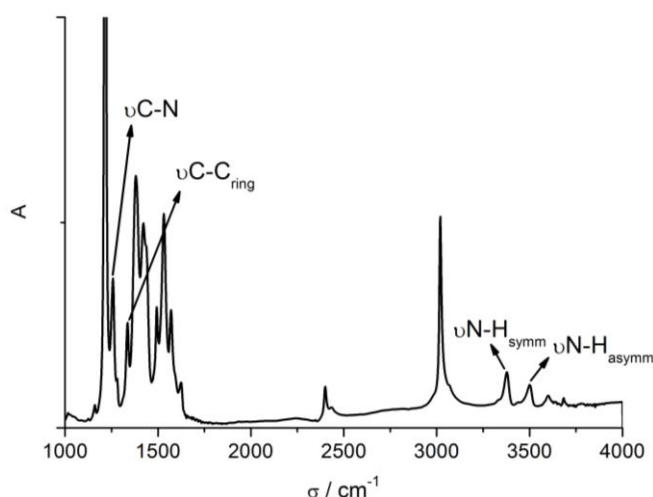


Figure 2.6. Fourier transform infrared spectrum of NH₂-MIL-125(Ti) in CHCl₃. Vibrations discussed in the main text are shown in the figure.[†] This is most likely a combination band of vibrations, for better visualization only the contribution of the ν C-N is shown. All the assignments can be found in Table A1 in the Appendix 1.

The transient mid-IR probe spectra specifically for the regions that corresponds to the amino group are shown in Figure 2.7 [see Figure 2.6 for the ground state mid-IR absorbance spectrum of NH₂-MIL-125(Ti)]. The N-H and the C-N bond stretching vibrations show pronounced bleaching in the TA spectra. The transient spectra at $\sigma=3000-3610\text{ cm}^{-1}$ (Figures 2.7 b and c, Figures 2.26 and 2.27) show a flat featureless induced absorption, which likely originates from the broad visible-light absorbance that extends far into the near-IR with the presence of Ti³⁺ in the Ti-oxo clusters (Figure 2.4b).

Along the different spectral regions, we find strong coupling of the excited state to molecular vibrations associated with the amine group of the MOF structure. At $\sigma=3485\text{ cm}^{-1}$, which corresponds to the characteristic frequency of the N-H asymmetric stretching vibration (Figure 2.7c), a long-lived bleaching signal is observed, which can be explained by a reduction of the transition dipole moment of the vibration upon photoexcitation. In contrast, at the N-H symmetric frequency ($\sigma=3380\text{ cm}^{-1}$; Figure 2.7b) a redshifted induced absorption is observed adjacent to the bleaching signal at the fundamental frequency indicative of a redshift of the N-H stretching band.

Notably, for the oxidized aniline radical with respect to neutral aniline, a more pronounced redshift of the symmetrical N-H stretch is reported than for the asymmetrical N-H stretch ($\sigma=40\text{ cm}^{-1}$ vs. 20 cm^{-1}), in addition to a higher IR intensity of the symmetrical N-H stretch than the asymmetrical N-H stretch of the radical. In the positive radical of aniline, the reduced electron density is most pronounced on the N atom.⁴⁹ This is in line with the transient mid-IR spectra obtained and a first indication of reduced electron density on the N atom of NH₂-MIL-125(Ti). A significant bleach can be seen in the spectra shown in Figure 2.7a that corresponds to the bleach of the ground state vibration of the combination band dominated by the C-N stretching vibration at $\sigma=1257\text{ cm}^{-1}$ (Figure 2.7) and a bleach that corresponds to the ground state $\nu\text{C-C}_{\text{ring}}$ vibration at $\sigma=1334\text{ cm}^{-1}$, which indicated the ground-state depletion of these vibrations.

Remarkably, at most resonances in the IR spectra the associated dynamics equilibrated on a timescale of $\sim 20\text{ ps}$ and the associated transient spectra remain constant within the time frame of the experiment (e.g., the band at $\sigma=1325\text{ cm}^{-1}$ in Figure 2.8 and Figures 2.15-2.17). This indicates that the MOF structure is relaxing on rather fast timescales because of vibrational cooling. Remarkably, only the vibrations that are related to the C-N-H₂ group show adjacent slower dynamics: the bands in the transient spectra at $\sigma=3485$, 3380 and 1256 cm^{-1} (N-H asymmetric stretch, N-H symmetric stretch, and C-N stretch) do not plateau within 1 ns, the experimentally accessible delay time range (e.g. the band at $\sigma=1256\text{ cm}^{-1}$ in Figure 2.8 and Figure A2.15). If we compare this with the time dependency of the transient visible spectra (Figure 2.8), we see a similar slower time dynamics. As we were able to assign the band around $\lambda=570\text{ nm}$ to the hole previously, this is a clear indication

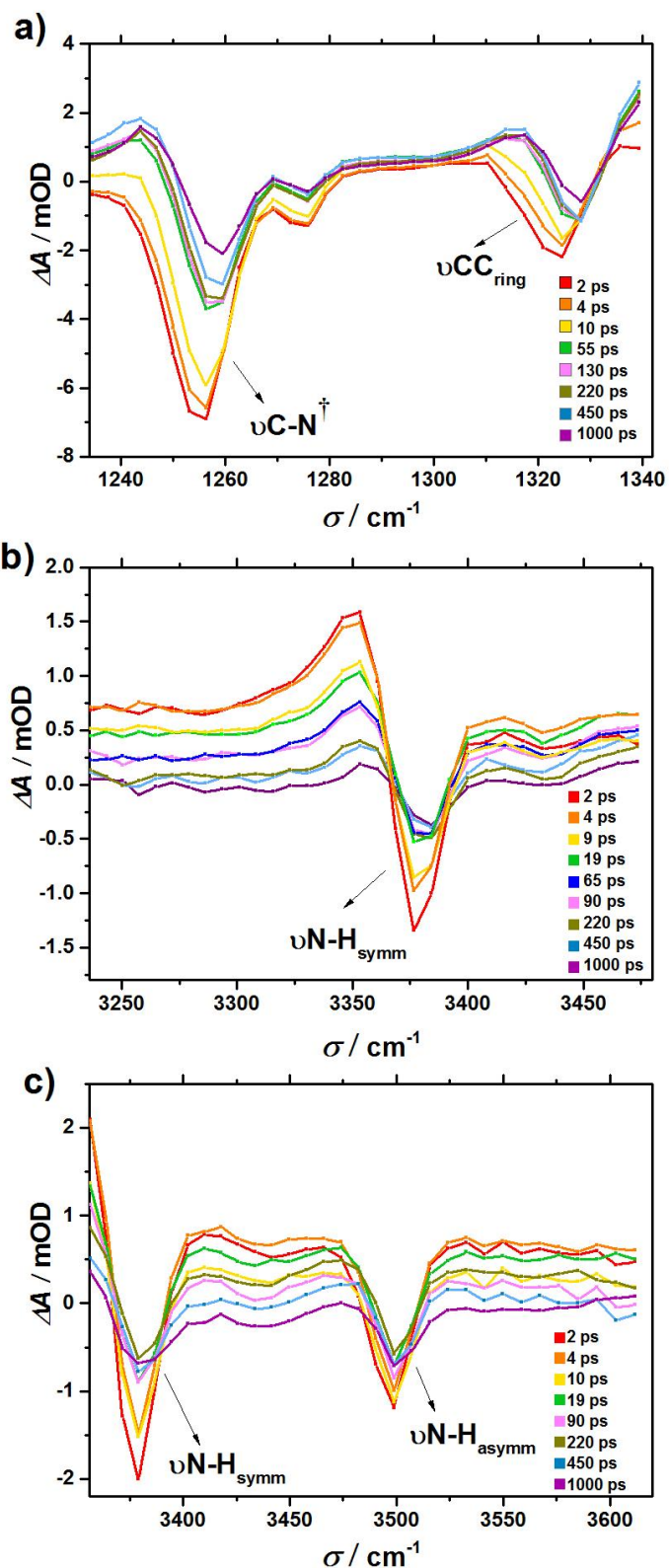


Figure 2.7. Differential transient absorption spectra for $\text{NH}_2\text{-MIL-125(Ti)}$ in $\text{C}_2\text{H}_2\text{Cl}_4$ as solvent upon excitation at 400 nm: a) C-N stretching vibration region, b) in the N-H and c) N-H symmetric stretching vibration region. Lines are depicted for a better visualization of the data. Although the ΔA is different for b) and c), the N-H symmetric vibration is depicted in both graphs.[†] This is most likely a combination band of vibrations, for better visualization only the contribution of the $\nu\text{C-N}$ is shown. The complete assignment can be found in Table 1 in the Appendix 1.

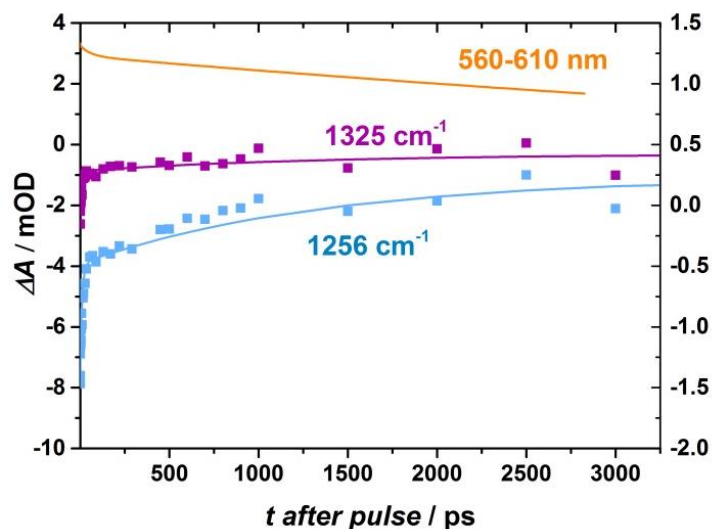


Figure 2.8. Representative time traces of NH₂-MIL-125(Ti) upon excitation at 400 nm in C₂H₂Cl₄ recorded at 1256 cm⁻¹ (blue), 1325 cm⁻¹ (purple): experimental data (squares) and model fit (line). The orange line (corresponding to the right y axis) represents the time traces in the λ=560-610 nm range in water (Figure 2.3 orange, experimental data). The graph starts at 1 ps to remove the points related to the coherent artefact.

that the C-N-H₂ related vibrations are associated with the hole. After 5 ns, the resonances associated with C-N-H₂ are also equilibrated (Figure A2.16). This longer-lived state is potentially caused by intersystem crossing to a triplet state, which is common for aniline derivatives.^{50, 51} The resemblance of the time dynamics between the resonances of the C-N-H₂ vibrations and the visible transient spectrum associated with the hole and the resemblance of the transient mid-IR spectra with that of the aniline radical reveal a positively charged vacancy most likely localized on the NH₂ group of the aminoterephthalate. Therefore, the electron-donating character of the amino group contributes to the stabilization of the photoexcited state with respect to MIL-125(Ti).

Conclusions

The kinetics of the photoexcitation process of two titanium metal-organic frameworks [MOFs; MIL-125(Ti) and NH₂-MIL-125(Ti)] were elucidated. These MOFs show, apart from their thermodynamic differences that lead to dissimilar light absorption profiles, a vast contrast in their kinetic behaviour. The excited state, which results from a LMCT transition, has a remarkably longer lifetime in NH₂-MIL-125(Ti).

Our results clarify the contributions of the organic and inorganic subunits to the formation of the charge-separated state. Spectroelectrochemistry performed on the soluble models of the organic and inorganic NH₂-MIL-125(Ti) constituents gave further insights into the transient absorption experiments. The results point to the localization of the hole on the aminoterephthalate unit and of the electron on the Ti-oxo clusters. Furthermore, ultrafast mid-IR spectra evidenced that the photogenerated hole resides on the amino group.

Thus, the amino group, which acts as a hole stabilizer in NH₂-MIL-125(Ti), prolongs the lifetime of the photoexcited state considerably compared to that of MIL-125(Ti). The NH₂ group sensitizes the MIL-125(Ti) to visible light and enables the capture of a larger fraction of solar light without the use of expensive noble metal while also improving the kinetics of the photoexcitation. To allow photogenerated charges to be used effectively in photocatalytic reactions, such as solar fuel generation, their lifetime needs to be sufficient. These results provide us with important insight into how to improve photocatalytic metal-organic frameworks. In particular, our findings encourage the design of MIL-125(Ti)-type structures with one or multiple strong electron donor groups to improve their photocatalytic performance. Moreover, the knowledge that the hole resides on the amino group allows us to create a rational design scheme to harness these holes for the oxygen evolution half reaction.

References

1. C. Acar and I. Dincer, *International Journal of Energy Research*, 2015, **39**, 1757-1768.
2. W. J. Youngblood, S.-H. A. Lee, K. Maeda and T. E. Mallouk, *Accounts of Chemical Research*, 2009, **42**, 1966-1973.
3. G. F. Moore and G. W. Brudvig, *Annu Rev Condens Ma P*, 2011, **2**, 303-327.
4. S. Ma and H.-C. Zhou, *Chemical Communications*, 2010, **46**, 44-53.
5. K. M. L. Taylor-Pashow, J. Della Rocca, Z. Xie, S. Tran and W. Lin, *Journal of the American Chemical Society*, 2009, **131**, 14261-14263.
6. R. C. Huxford, J. Della Rocca and W. Lin, *Current Opinion in Chemical Biology*, 2010, **14**, 262-268.
7. C. Wang, D. Liu and W. Lin, *Journal of the American Chemical Society*, 2013, **135**, 13222-13234.
8. T. Rodenas, I. Luz, G. Prieto, B. Seoane, H. Miro, A. Corma, F. Kapteijn, F. X. Llabrés i Xamena and J. Gascon, *Nat Mater*, 2015, **14**, 48-55.
9. T. Zhang and W. Lin, *Chemical Society Reviews*, 2014, **43**, 5982-5993.
10. M. Nasalevich, M. A. van der Veen, F. Kapteijn and J. Gascon, *CrystEngComm*, 2014, DOI: 10.1039/C4CE00032C.
11. Y. Fu, D. Sun, Y. Chen, R. Huang, Z. Ding, X. Fu and Z. Li, *Angewandte Chemie - International Edition*, 2012, **51**, 3364-3367.
12. D. Sun, Y. Fu, W. Liu, L. Ye, D. Wang, L. Yang, X. Fu and Z. Li, *Chemistry – A European Journal*, 2013, **19**, 14279-14285.
13. M. A. Nasalevich, R. Becker, E. V. Ramos-Fernandez, S. Castellanos, S. L. Veber, M. V. Fedin, F. Kapteijn, J. N. H. Reek, J. I. van der Vlugt and J. Gascon, *Energy & Environmental Science*, 2015, **8**, 364-375.
14. D. Sun, W. Liu, Y. Fu, Z. Fang, F. Sun, X. Fu, Y. Zhang and Z. Li, *Chemistry – A European Journal*, 2014, **20**, 4780-4788.
15. C.-C. Wang, J.-R. Li, X.-L. Lv, Y.-Q. Zhang and G. Guo, *Energy & Environmental Science*, 2014, **7**, 2831-2867.
16. Y. Horiuchi, T. Toyao, M. Saito, K. Mochizuki, M. Iwata, H. Higashimura, M. Anpo and M. Matsuoka, *Journal of Physical Chemistry C*, 2012, **116**, 20848-20853.
17. J. Long, S. Wang, Z. Ding, S. Wang, Y. Zhou, L. Huang and X. Wang, *Chemical Communications*, 2012, **48**, 11656-11658.
18. C. Wang, Z. Xie, K. E. deKrafft and W. Lin, *Journal of the American Chemical Society*, 2011, **133**, 13445-13454.
19. J. Gascon, M. D. Hernandez-Alonso, A. R. Almeida, G. P. M. van Klink, F. Kapteijn and G. Mul, *ChemSusChem*, 2008, **1**, 981-983.
20. M. Alvaro, E. Carbonell, B. Ferrer, F. Xamena and H. Garcia, *Chemistry-A European Journal*, 2007, **13**, 5106-5112.
21. K. G. M. Laurier, F. Vermoortele, R. Ameloot, D. E. De Vos, J. Hofkens and M. B. J. Roelfaers, *Journal of the American Chemical Society*, 2013, **135**, 14488-14491.
22. S. Wang and X. Wang, *Small*, 2015, **11**, 3097-3112.

23. D. Gust, T. A. Moore and A. L. Moore, *Accounts of Chemical Research*, 2009, **42**, 1890-1898.
24. J. P. McEvoy and G. W. Brudvig, *Chemical Reviews*, 2006, **106**, 4455-4483.
25. M. A. Nasalevich, M. G. Goesten, T. J. Savenije, F. Kapteijn and J. Gascon, *Chemical Communications*, 2013, **49**, 10575-10577.
26. M. Dan-Hardi, C. Serre, T. Frot, L. Rozes, G. Maurin, C. Sanchez and G. Férey, *Journal of the American Chemical Society*, 2009, **131**, 10857-10859.
27. M. A. Moreira, J. C. Santos, A. F. P. Ferreira, J. M. Loureiro, F. Ragon, P. Horcajada, P. G. Yot, C. Serre and A. E. Rodrigues, *Microporous and Mesoporous Materials*, 2012, **158**, 229-234.
28. C. H. Hendon, D. Tiana, M. Fontecave, C. Sanchez, L. D'arras, C. Sassoey, L. Rozes, C. Mellot-Draznieks and A. Walsh, *Journal of the American Chemical Society*, 2013, DOI: 10.1021/ja405350u.
29. A. Walsh and C. R. A. Catlow, *ChemPhysChem*, 2010, **11**, 2341-2344.
30. J. Hu, J. Wang, T. H. Nguyen and N. Zheng, *Beilstein Journal of Organic Chemistry*, 2013, **9**, 1977-2001.
31. M. Jonsson, J. Lind, T. E. Eriksen and G. Merenyi, *Journal of the American Chemical Society*, 1994, **116**, 1423-1427.
32. M. F. De Lange, T. J. H. Vlugt, J. Gascon and F. Kapteijn, *Microporous and Mesoporous Materials*, 2014, **200**, 199-215.
33. E. Hashem, J. A. Platts, F. Hartl, G. Lorusso, M. Evangelisti, C. Schulzke and R. J. Baker, *Inorganic Chemistry*, 2014, **53**, 8624-8637.
34. J. Tory, B. Setterfield-Price, R. A. W. Dryfe and F. Hartl, *ChemElectroChem*, 2015, **2**, 213-217.
35. C. H. Hendon and A. Walsh, *Chemical Science*, 2015, **6**, 3674-3683.
36. X. Chen, S. Shen, L. Guo and S. S. Mao, *Chemical Reviews*, 2010, **110**, 6503-6570.
37. A. Kudo and Y. Miseki, *Chemical Society Reviews*, 2009, **38**, 253-278.
38. R. Berera, R. Grondelle and J. T. M. Kennis, *Photosynth. Res.*, 2009, **101**, 105-118.
39. J. B. Asbury, E. Hao, Y. Wang, H. N. Ghosh and T. Lian, *J. Phys. Chem. B*, 2001, **105**, 4545-4557.
40. M. De Miguel, F. Ragon, T. Devic, C. Serre, P. Horcajada and H. García, *ChemPhysChem*, 2012, **13**, 3651-3654.
41. A. I. Kuznetsov, O. Kameneva, N. Biturin, L. Rozes, C. Sanchez and A. Kanaev, *Physical Chemistry Chemical Physics*, 2009, **11**, 1248-1257.
42. C. Creutz and M. H. Chou, *Inorganic Chemistry*, 2008, **47**, 3509-3514.
43. P. Jeske, G. Haselhorst, T. Weyhermueller, K. Wieghardt and B. Nuber, *Inorganic Chemistry*, 1994, **33**, 2462-2471.
44. M. Kirchgessner, K. Sreenath and K. R. Gopidas, *The Journal of Organic Chemistry*, 2006, **71**, 9849-9852.
45. E. T. Seo, R. F. Nelson, J. M. Fritsch, L. S. Marcoux, D. W. Leedy and R. N. Adams, *Journal of the American Chemical Society*, 1966, **88**, 3498-3503.
46. S. Sumalekshmy and K. R. Gopidas, *Chemical Physics Letters*, 2005, **413**, 294-299.
47. G. K. Ramesha, J. F. Brennecke and P. V. Kamat, *ACS Catalysis*, 2014, **4**, 3249-3254.
48. J. D. Megiatto, A. Antoniuk-Pablant, B. D. Sherman, G. Kodis, M. Gervaldo, T. A. Moore, A. L. Moore and D. Gust, *Proceedings of the National Academy of Sciences*, 2012, **109**, 15578-15583.
49. P. M. Wojciechowski, W. Zierkiewicz, D. Michalska and P. Hobza, *The Journal of Chemical Physics*, 2003, **118**, 10900-10911.
50. H. Shimamori and A. Sato, *The Journal of Physical Chemistry*, 1994, **98**, 13481-13485.
51. X.-J. Hou, P. Quan, T. Höltzl, T. Veszprémi and M. T. Nguyen, *The Journal of Physical Chemistry A*, 2005, **109**, 10396-10402.
52. J. Hunger, T. Sonleitner, L. Liu, R. Buchner, M. Bonn and H. J. Bakker, *The Journal of Physical Chemistry Letters*, 2012, **3**, 3034-3038.
53. M. Karabacak, M. Cinar, Z. Unal and M. Kurt, *Journal of Molecular Structure*, 2010, **982**, 22-27.
54. Z. Su, J. H. Chen, X. Sun, Y. Huang and X. Dong, *RSC Advances*, 2015, **5**, 99008-99017.
55. S. Hu, M. Liu, K. Li, Y. Zuo, A. Zhang, C. Song, G. Zhang and X. Guo, *CrystEngComm*, 2014, **16**, 9645-9650.
56. H. R. Abid, J. Shang, H.-M. Ang and S. Wang, *International Journal of Smart and Nano Materials*, 2013, **4**, 72-82.

Appendix 1

Nitrogen physisorption

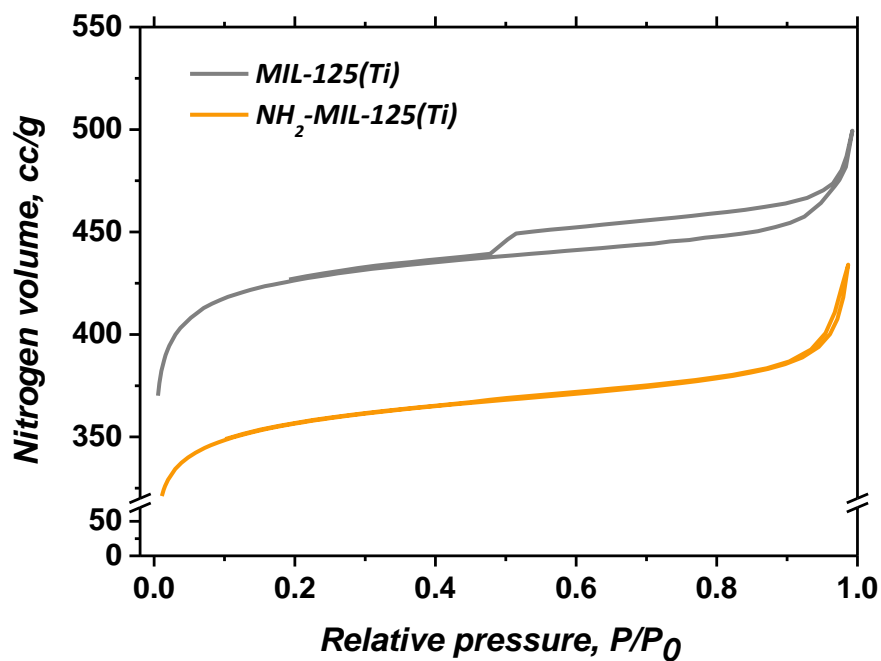


Figure A2.9. Nitrogen physisorption isotherms for the catalysts used in this work. Top to bottom: MIL-125(Ti) (*grey*), NH₂-MIL-125(Ti) (*orange*).

Powder X-ray diffraction

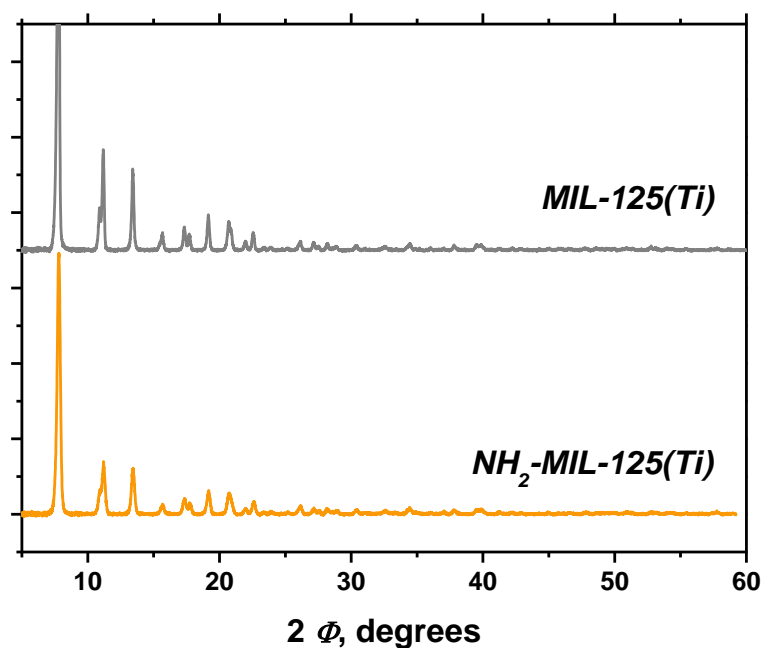


Figure A2.10. Powder X-Ray diffraction patterns of the catalysts used in this work.

Vis-pump Vis-probe spectroscopy

In order to determine whether multiple photons absorption processes are being observed, we check whether the pump power and the change in absorption follow a linear correlation. With that purpose, a region of the data is selected for every measurement, containing the data at the highest intensity. It is averaged for each pump power and then fitted by a linear fit. The resulting correlations are referred to as linearity checks.

MIL-125(Ti) in water

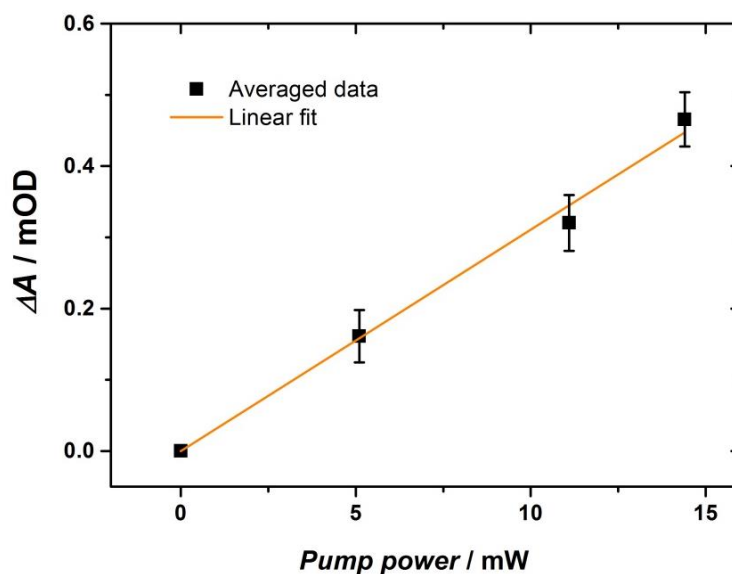


Figure A2.11. Linearity check for MIL-125(Ti) in water.

NH₂-MIL-125(Ti) in water

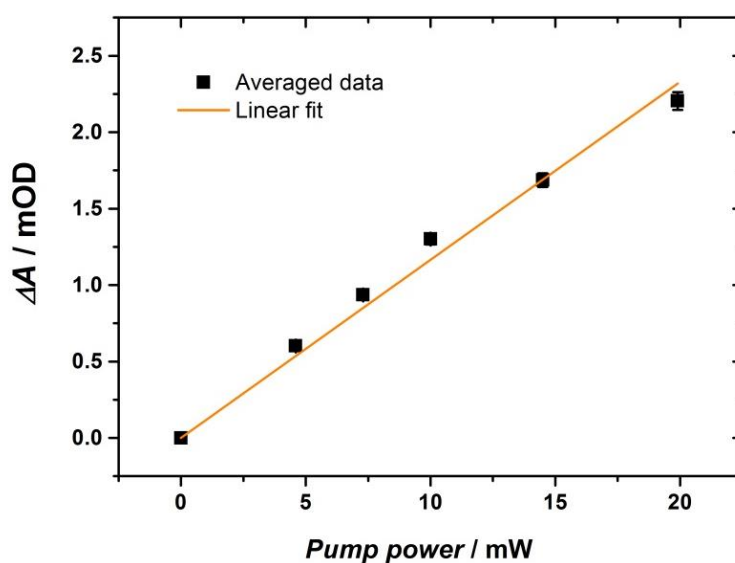


Figure A2.12. Linearity check for NH₂-MIL-125(Ti) in water.

NH₂-MIL-125(Ti) in DMF

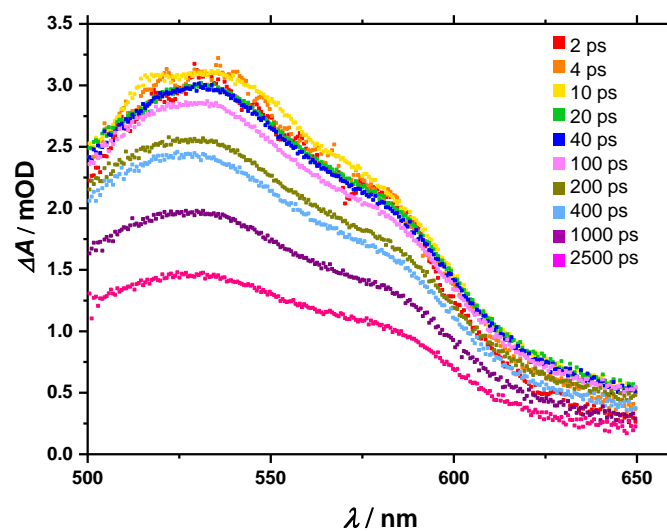


Figure A2.13. Differential transient absorption spectra for $\text{NH}_2\text{-MIL-125(Ti)}$ in DMF upon excitation at 400 nm and 10.9 mW pump power.

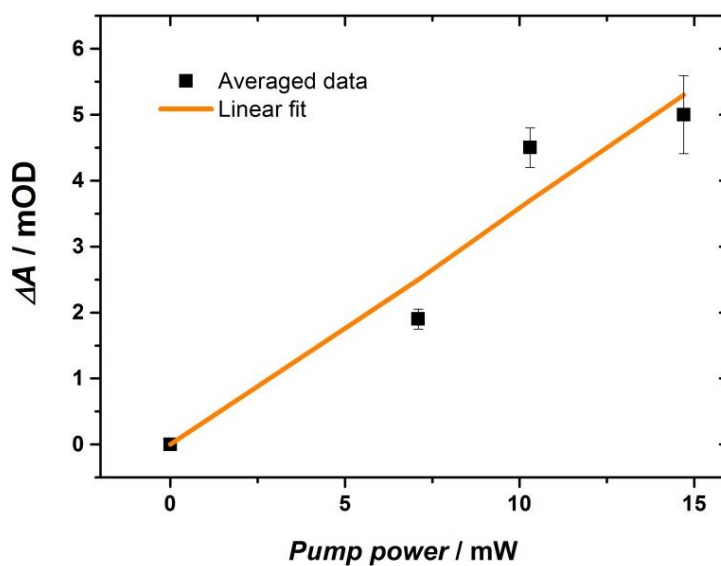


Figure A2.14. Linearity check for MIL-125(Ti) in DMF.

Vis-pump mid-IR-probe spectroscopy

Range 1235-1340 cm^{-1}

$\text{NH}_2\text{-MIL-125(Ti)}$ in $\text{C}_2\text{H}_2\text{Cl}_4$

A transient-kinetic model with three decaying states was used to obtain the fit for the experimental data.⁵² Three lifetimes were necessary: 10 ps, 1.3 ns and 200 ns.

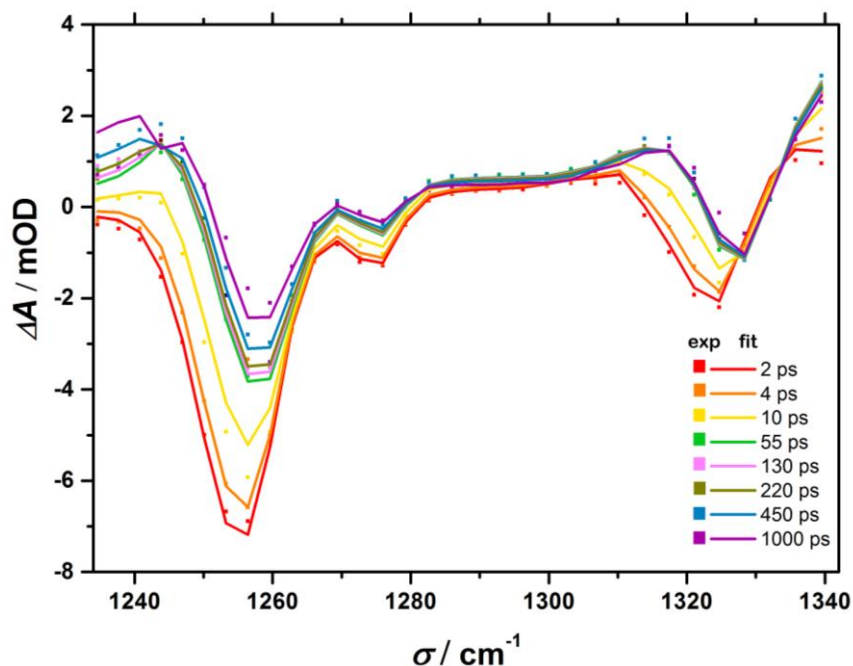


Figure A2.15. Differential transient absorption spectra for $\text{NH}_2\text{-MIL-125(Ti)}$ in $\text{C}_2\text{H}_2\text{Cl}_4$ upon excitation at 400 nm in the range 1235-1340 cm^{-1} : experimental data (*squares*) and model fit (*line*).

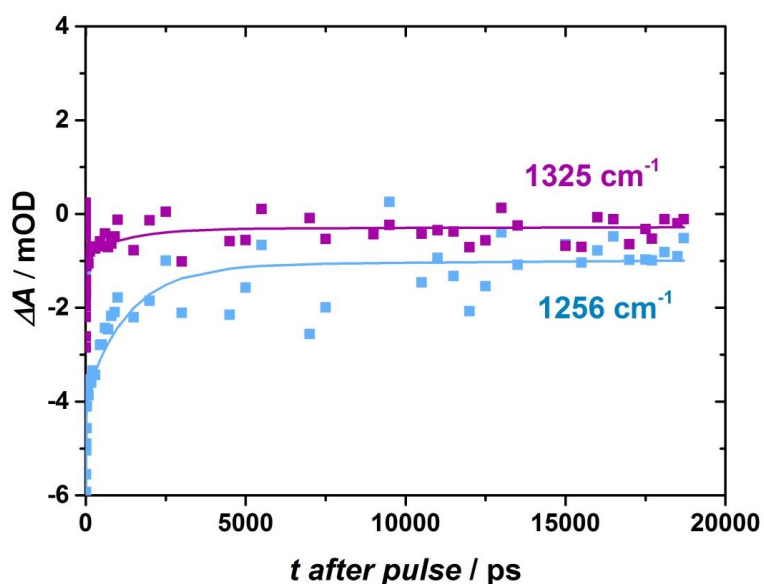


Figure A2.16. Representative time traces of $\text{NH}_2\text{-MIL-125(Ti)}$ in $\text{C}_2\text{H}_2\text{Cl}_4$ recorded at 1256 cm^{-1} (*blue*) and 1325 cm^{-1} (*purple*) upon excitation at 400 nm with excitation power of 2 μJ : experimental data (*squares*) and model fit (*line*).

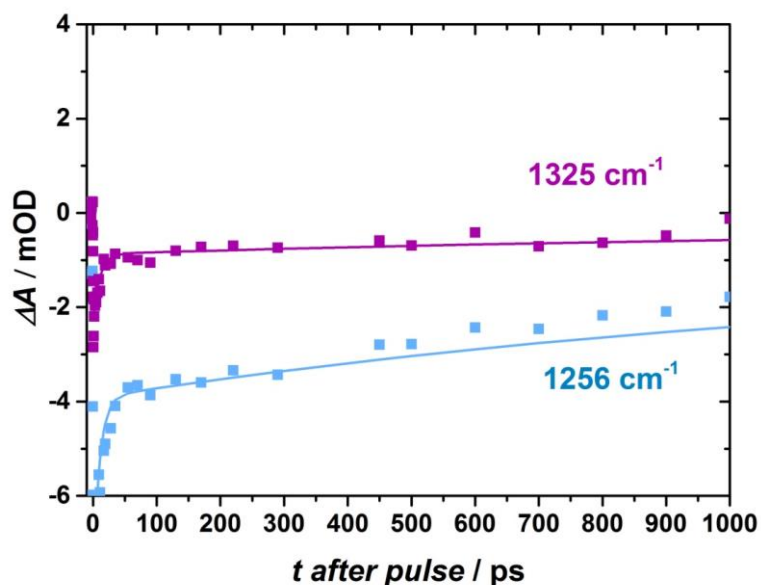


Figure A2.17. Representative time traces up to 1000 ps of $\text{NH}_2\text{-MIL-125(Ti)}$ in $\text{C}_2\text{H}_2\text{Cl}_4$ recorded at 1256 cm^{-1} (blue) and 1325 cm^{-1} (purple) upon excitation at 400 nm with excitation power of $2\text{ }\mu\text{J}$: experimental data (squares) and model fit (line).

Range $1350\text{-}1470\text{ cm}^{-1}$

$\text{NH}_2\text{-MIL-125(Ti)}$ in D_2O

A transient-kinetic model with two decaying states was necessary to obtain a reasonable fit for the experimental data.⁵² Thus, one lifetime was obtained: 10 ps.

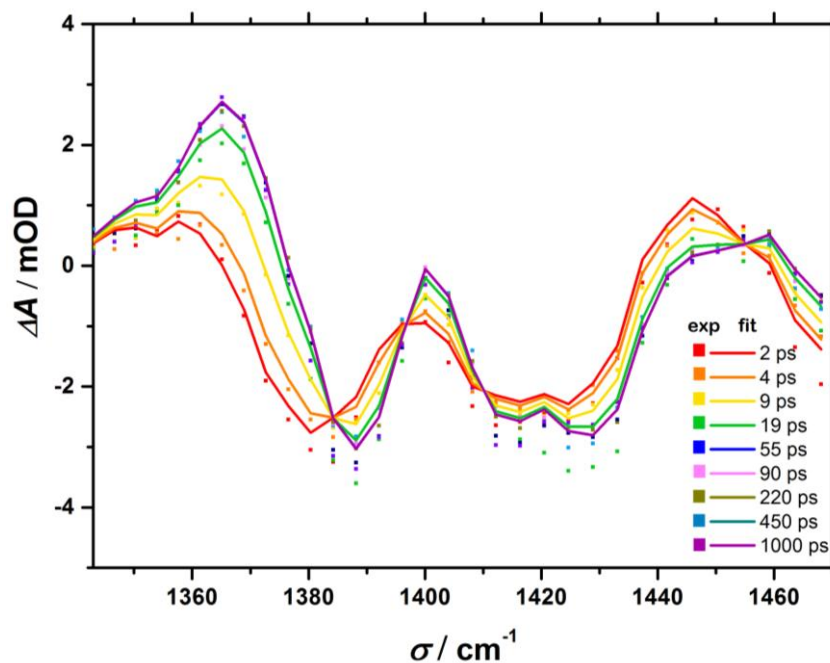


Figure A2.18. Differential transient absorption spectra for $\text{NH}_2\text{-MIL-125(Ti)}$ in D_2O upon excitation at 400 nm with excitation power of $2\text{ }\mu\text{J}$ in the range $1350\text{-}1470\text{ cm}^{-1}$: experimental data (squares) and model fit (line).

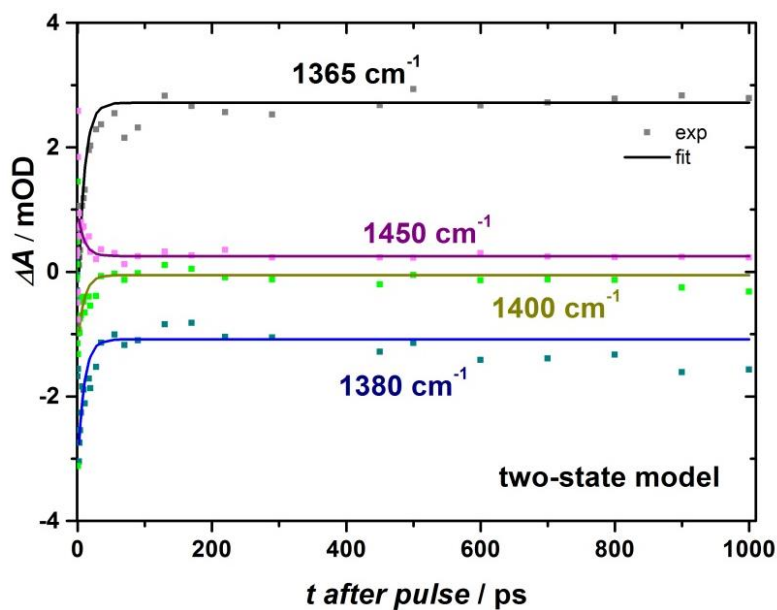


Figure A2.19. Representative time traces of $\text{NH}_2\text{-MIL-125(Ti)}$ in D_2O recorded at 1365 cm^{-1} (black), 1380 cm^{-1} (blue) and 1450 cm^{-1} (purple) upon excitation at 400 nm with excitation power of $2\text{ }\mu\text{J}$: experimental data (squares) and model fit (line).

$\text{NH}_2\text{-MIL-125(Ti)}$ in $\text{C}_2\text{H}_2\text{Cl}_4$

A transient-kinetic model with two decaying states was necessary to obtain a reasonable fit for the experimental data.⁵² Thus, one lifetime was obtained: 11 ps .

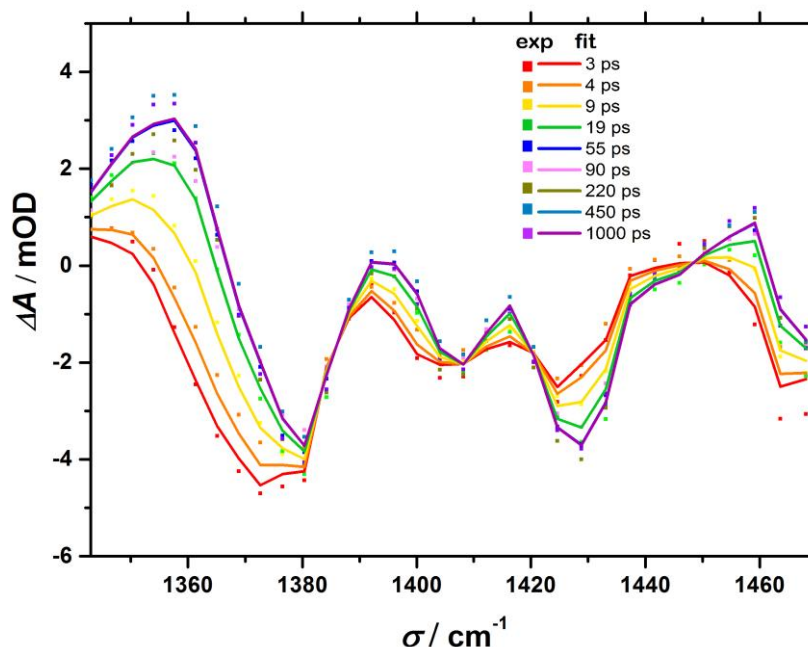


Figure A2.20. Differential transient absorption spectra for $\text{NH}_2\text{-MIL-125(Ti)}$ in $\text{C}_2\text{H}_2\text{Cl}_4$ upon excitation at 400 nm with excitation power of $2\text{ }\mu\text{J}$ in the range $1350\text{-}1470\text{ cm}^{-1}$: experimental data (squares) and model fit (line).

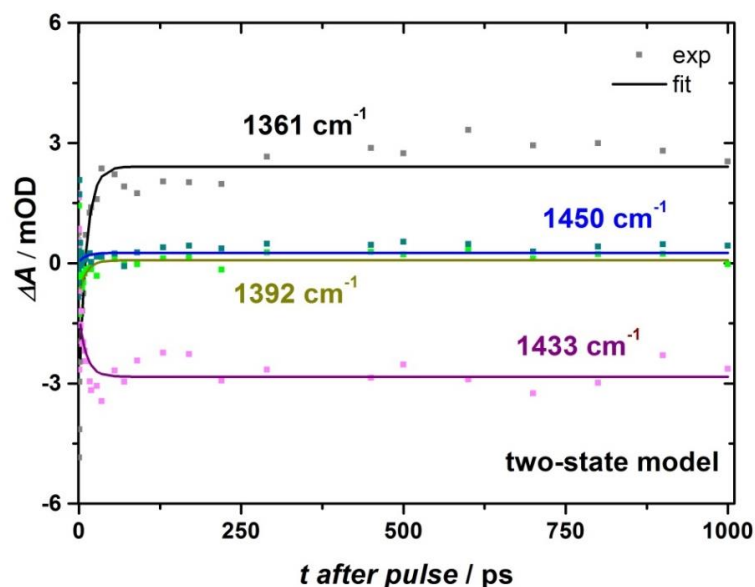


Figure A2.21. Representative time traces of NH₂-MIL-125(Ti) in C₂H₂Cl₄ recorded at 1361 cm⁻¹ (black), 1450 cm⁻¹ (blue) and 1433 cm⁻¹ (purple) upon excitation at 400 nm with excitation power of 2 μJ: experimental data (squares) and model fit (line).

Range 1420-1610 cm⁻¹

NH₂-MIL-125(Ti) in D₂O

A transient-kinetic model with two decaying states was necessary to obtain a reasonable fit for the experimental data.⁵² Thus, one lifetime was obtained: 22 ps.

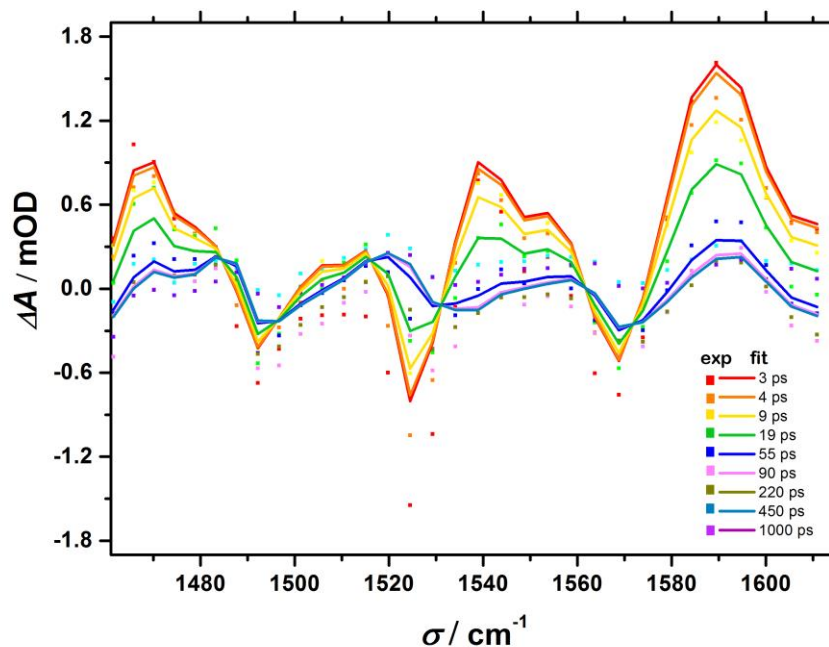


Figure A2.22. Differential transient absorption spectra for NH₂-MIL-125(Ti) in D₂O upon excitation at 400 nm with excitation power of 2 μJ in the range 1420-1610 cm⁻¹: experimental data (squares) and model fit (line).

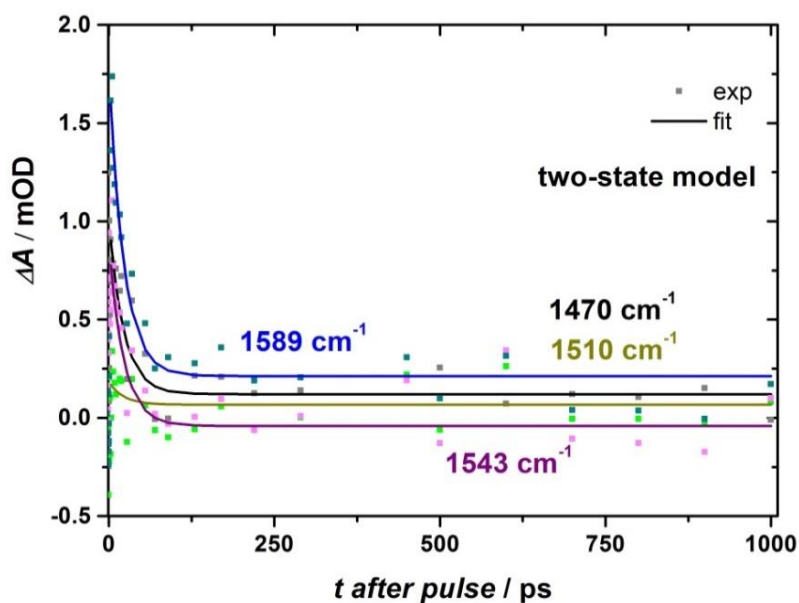


Figure A2.23. Representative time traces of $\text{NH}_2\text{-MIL-125(Ti)}$ in D_2O recorded at 1470 cm^{-1} (black), 1589 cm^{-1} (blue), 1510 cm^{-1} (dark yellow) and 1543 cm^{-1} (purple) upon excitation at 400 nm with excitation power of $2\text{ }\mu\text{J}$: experimental data (squares) and model fit (line).

$\text{NH}_2\text{-MIL-125(Ti)}$ in $\text{C}_2\text{H}_2\text{Cl}_4$

A transient-kinetic model with two decaying state was necessary to obtain a reasonable fit for the experimental data.⁵² Thus, one lifetime was obtained: 7 ps .

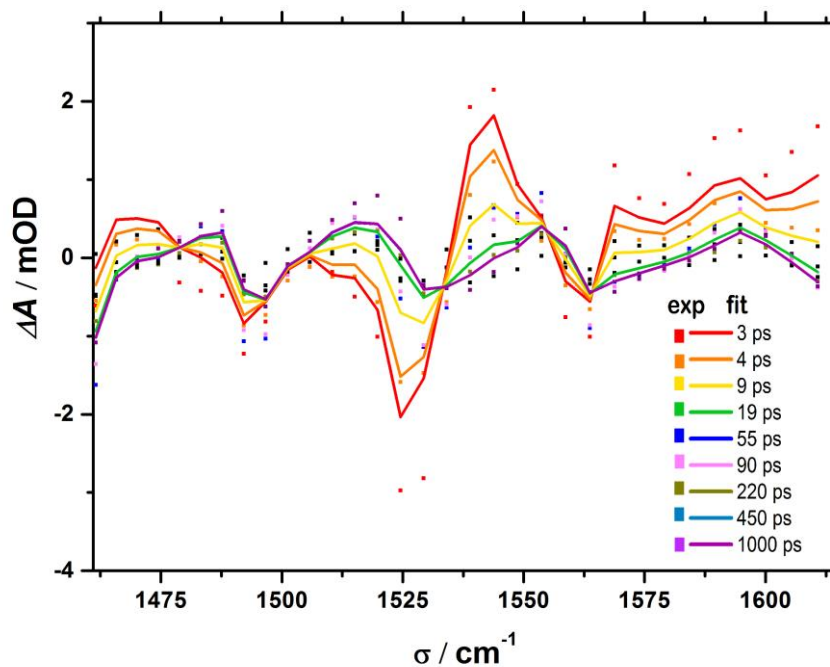


Figure A2.24. Differential transient absorption spectra for $\text{NH}_2\text{-MIL-125(Ti)}$ in D_2O upon excitation at 400 nm with excitation power of $2\text{ }\mu\text{J}$ in the range $1420\text{-}1610\text{ cm}^{-1}$: experimental data (squares) and model fit (line).

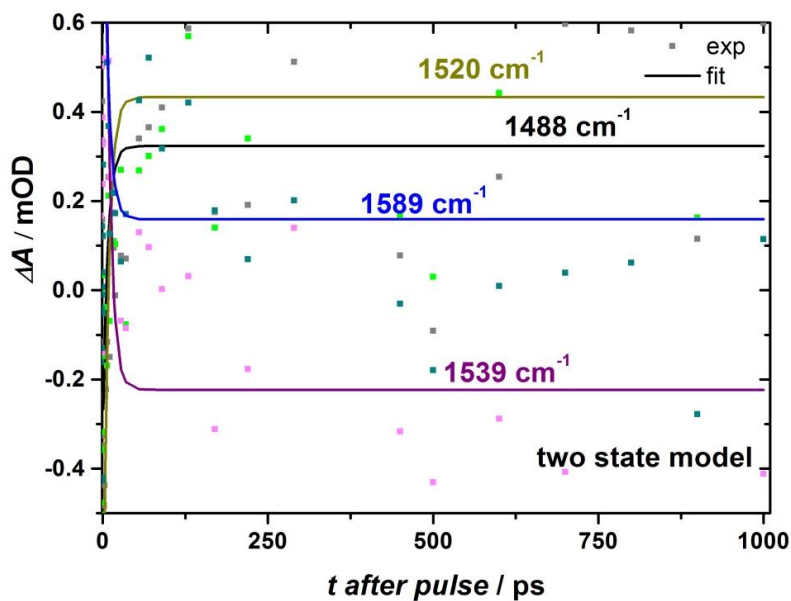


Figure A2.25. Representative time traces of NH₂-MIL-125(Ti) in C₂H₂Cl₄ recorded at 1488 cm⁻¹ (black), 1589 cm⁻¹ (blue), 1520 cm⁻¹ (dark yellow) and 1539 cm⁻¹ (purple) upon excitation at 400 nm with excitation power of 2 μJ: experimental data (squares) and model fit (line).

Range 3000-3200 cm⁻¹

NH₂-MIL-125(Ti) in C₂H₂Cl₄

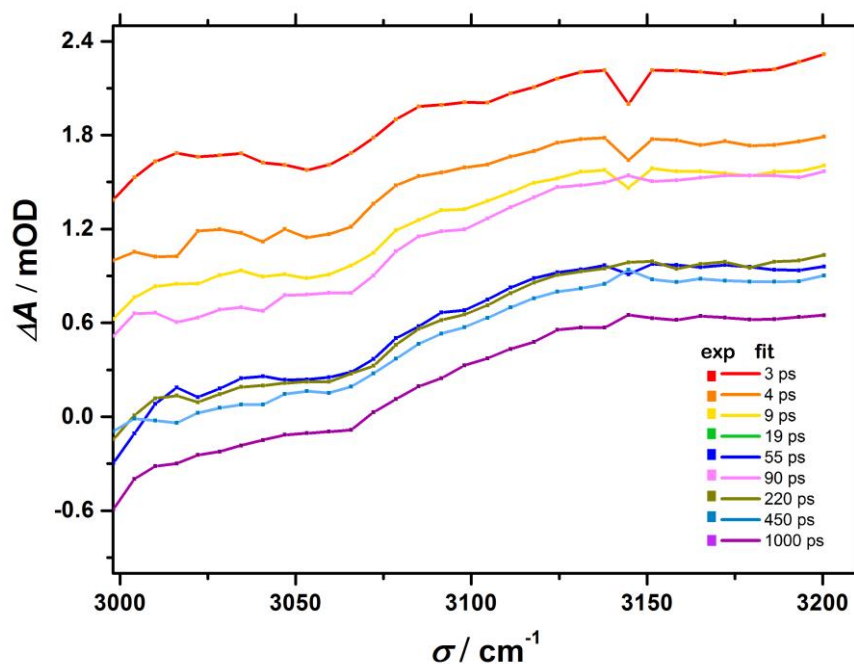


Figure A2.26. Differential transient absorption spectra for NH₂-MIL-125(Ti) in D₂O upon excitation at 400 nm with excitation power of 19.5 μJ in the range 3000-3200 cm⁻¹.

Range 3150-3380 cm⁻¹

NH₂-MIL-125(Ti) in C₂H₂Cl₄

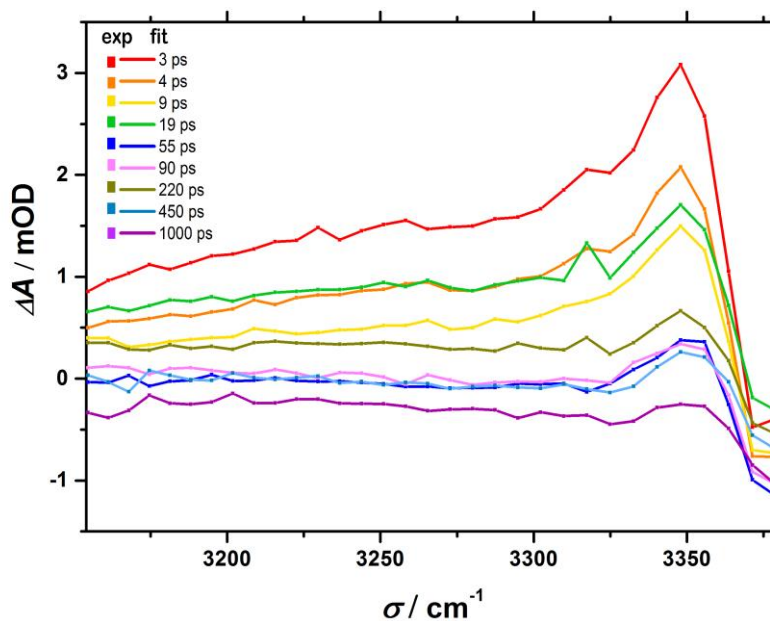


Figure A2.27. Differential transient absorption spectra for NH₂-MIL-125(Ti) in C₂H₂Cl₄ upon excitation at 400 nm with excitation power of 15.7 μJ in the range 3150-3380 cm⁻¹.

Range 3350-3610 cm⁻¹

NH₂-MIL-125(Ti) in C₂H₂Cl₄

A transient-kinetic model with three decaying states was necessary to obtain a reasonable fit for the experimental data.⁵² Thus, two lifetimes were obtained: 4 ps and 620 ps.

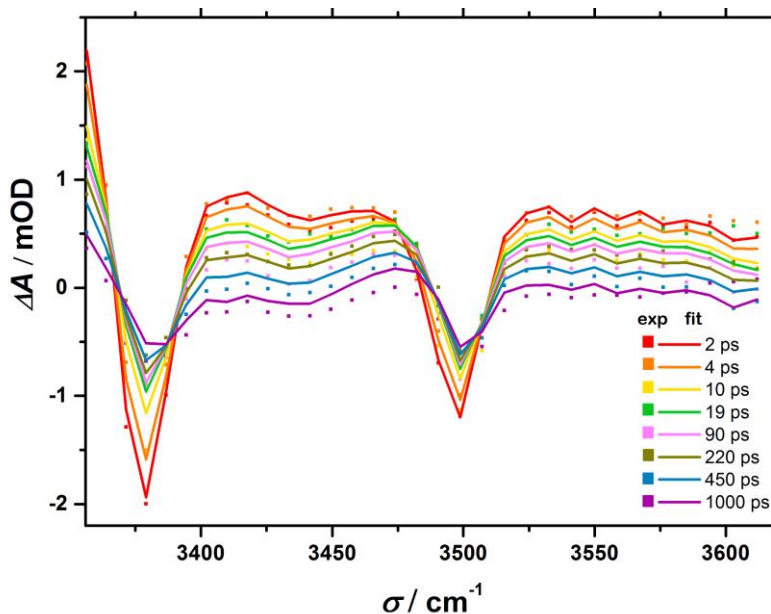


Figure A2.28. Differential transient absorption spectra for NH₂-MIL-125(Ti) in C₂H₂Cl₄ upon excitation at 400 nm in the range 3350-3610 cm⁻¹: experimental data (*squares*) and model fit (*line*).

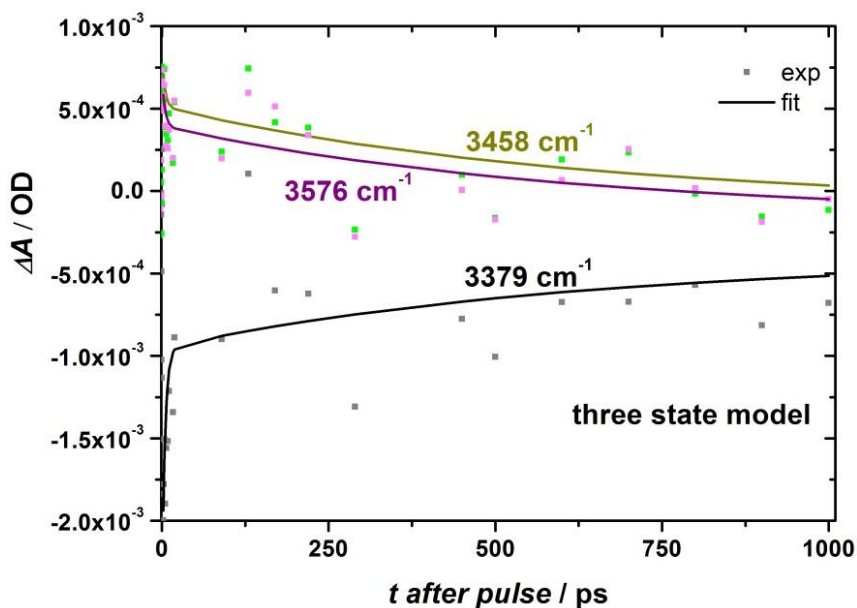


Figure A2.29. Representative time traces of NH₂-MIL-125(Ti) in C₂H₂Cl₄ recorded at 3379 cm⁻¹ (black), 3458 cm⁻¹ (dark yellow) and 3576 cm⁻¹ (purple) upon excitation at 400 nm with excitation power of 6.3 μJ: experimental data (squares) and model fit (line).

Table 1. Assignments of ground state IR vibrations from Figure 2.6 and the respective lifetimes of the transient spectra at these wavenumber for NH₂-MIL-125(Ti) in different solvents.

Peak	Assignment	T in C ₂ H ₂ Cl ₄	T in D ₂ O
1215 cm ⁻¹	Solvent peak (CHCl ₃)	-	-
1257 cm ⁻¹	ν C-NH ₂ , ν CC _{ring} , β CH ^{49, 53-55}	10 ps, 1.3 ns, 200 ns	-
1334 cm ⁻¹	ν CC _{ring} ^{49, 53}	7 ps	-
1380 cm ⁻¹	β C-H ⁴⁹	11 ps	10 ps
1423 cm ⁻¹	ν CC _{ring} , ν C-C, ν_{sym} C=O ⁵³⁻⁵⁶	7 ps	22 ps
1495 cm ⁻¹	β CH, ν CC _{ring} ^{49 53}		
1533 cm ⁻¹	ν_{asym} C=O ⁵⁴⁻⁵⁶		
1572 cm ⁻¹	ρ NH ₂ , ν CC _{ring} , ^{49, 53}		
1622 cm ⁻¹	ν CC _{ring} , ρ NH ₂ ^{49,53}	-	-
3020 cm ⁻¹	ν CH ^{49, 53}	4 ps, 620 ps	-
3376 cm ⁻¹	ν_{sym} NH ₂ ^{49, 54 13, 55, 56}		
3500 cm ⁻¹	ν_{asym} NH ₂ ^{49, 53-56}		
3598 cm ⁻¹	ν OH ⁵³	-	-
3683 cm ⁻¹	ν OH ⁵⁶	-	-

ν_{sym} - ν_{asym} : symmetric-asymmetric stretching

β : in-plane bending

ρ : scissoring

Spectroelectrochemistry

Spectroelectrochemistry experiments consisted on the registration of the sample absorption spectra (plotted as ΔOD) upon the application of positive (leading to sample oxidation) or negative potentials (leading to sample reduction). The optical setup comprised a Deuterium-Halogen lamp DH-2000 as light source, a USB2000 UV-VIS Spectrometer and a NIRQUEST NIR spectrometer, all components purchased from Ocean Optics Inc. The potential was applied using CH Instruments Analyser CHI832B as potentiostat. An OTTLE cell fabricated by Spectroelectrochemistry Reading (University of Reading) provided with a three-electrode set consisting of a Pt minigrad working electrode (32 wires/cm), Pt minigrad auxiliary electrode and Ag wire pseudo-reference electrode melt-sealed in a modified polyethylene spacer (ca 0.2 mm thickness) was used as measuring cell. $LiClO_4$ in acetonitrile (0.1 M) and $(N^iBu_4)BF_4$ in dichloromethane (0.1 M) were used as electrolytes for aminoterephthalate dimethyl ester and $Ti_8O_8(OOCC(CH_3)_3)_3$,²⁸ respectively. All solutions were prepared in glove-box conditions to avoid the presence of oxygen.

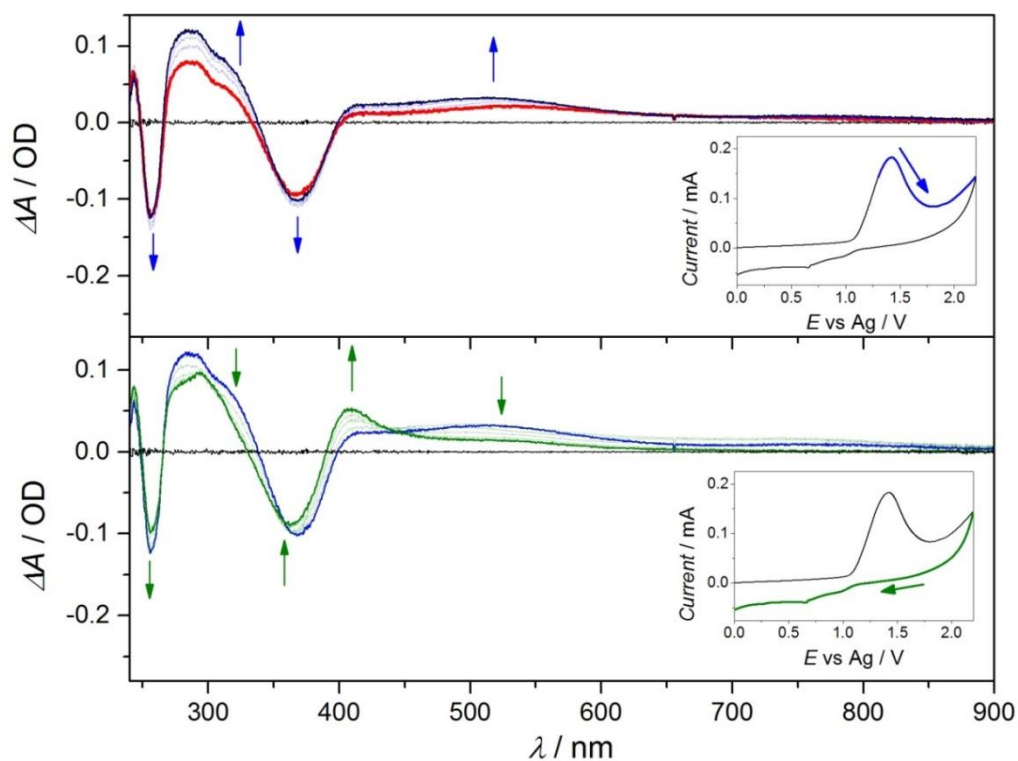


Figure A2.30. Evolution of the absorption spectrum of dimethyl aminoterephthalate in acetonitrile (1×10^{-3} M) during the irreversible oxidation process. Inset displays the registered cyclic voltammogram and highlights the current ranges corresponding with the shown spectra.

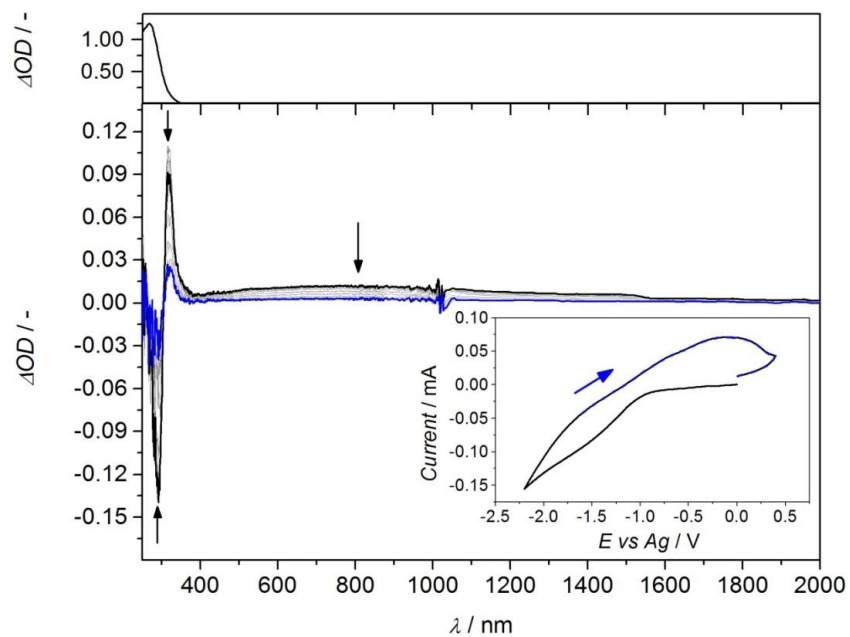


Figure A2.31. Absorption spectral changes of $\text{Ti}_8\text{O}_8(\text{OOCC}(\text{CH}_3)_3)_{16}$ soluble oxoclusters in dichloromethane ($2 \times 10^{-3} \text{ M}$) upon closure of the reduction cycle ($\text{Ti}^{3+} \rightarrow \text{Ti}^{4+}$). Steady absorption spectrum is shown on top. Inset displays the registered cyclic voltammogram and highlights in blue the anodic current range corresponding to the shown spectra.

Electronic origins of photocatalytic activity in d^0 metal organic frameworks

Metal-organic frameworks (MOFs) containing d^0 metals such as $\text{NH}_2\text{-MIL-125(Ti)}$, $\text{NH}_2\text{-UiO-66(Zr)}$ and $\text{NH}_2\text{-UiO-66(Hf)}$ are among the most studied for photocatalytic applications. Despite structural similarities, we demonstrate that the electronic properties of these MOFs are markedly different. As revealed by quantum chemistry, EPR measurements and transient absorption spectroscopy, the highest occupied and lowest unoccupied orbitals of $\text{NH}_2\text{-MIL-125(Ti)}$ promote a long-lived ligand-to-metal charge transfer upon photoexcitation, making this material suitable for photocatalytic applications. In contrast, in case of UiO materials, the d -orbitals of Zr and Hf, are too low in binding energy and thus cannot overlap with the π^* orbital of the ligand, making both frontier orbitals localized at the organic linker. This electronic reconfiguration results in short exciton lifetimes and diminishes photocatalytic performance. These results highlight the importance of orbital contributions at the band edges and delineate future directions in the development of photo-active hybrid solids.

This chapter is based on the following publication:

Electronic origins of photocatalytic activity in d^0 metal organic frameworks

M. A. Nasalevich, C. H. Hendon, J. G. Santaclara, K. Svane, B. van der Linden, S. L. Veber, M. V. Fedin, M. A. van der Veen, F. Kapteijn, A. Walsh, J. Gascon, , Sci. Rep. 6, 2016, 23676

Introduction

Metal-organic frameworks (MOFs) have attracted a great deal of interest during the last decades due to their unprecedented surface area, remarkable tuneability and the fascinating variety of possible combinations of constituting blocks. Several applications have been suggested, such as separation of gases,^{1, 2} catalysis,³ drug delivery and sensing.⁴ Photocatalysis was proposed in the early 2000s inspired by an intuitive analogy between them and their corresponding oxides, often being semiconductors.^{5, 6} Despite the fact that the early reports of semiconducting properties of MOFs have been disputed,^{7, 8} this initial misconception led to the application of frameworks based on Zn, Ti and other transition metals in a variety of photocatalytic reactions such as oxidation of organic compounds,^{9, 10} reduction of metal ions¹¹ and synthesis of solar fuels.¹² NH₂-MIL-125(Ti) and NH₂-UiO-66(Zr) clearly stand out as the most researched among the different MOF structures tested in photocatalysis to date. While these two MOFs are based on the same linker, namely 2-aminoterephthalate, and crystallize in a rather similar topology, the metal ions constituting the inorganic nodes in the framework are different: Ti⁴⁺ forms octameric Ti₈O₈(OH)₄ rings¹³ in NH₂-MIL-125(Ti) and Zr⁴⁺ or Hf⁴⁺ form the M₆O₄(OH)₄ clusters in the UiOs.¹⁴

Intuitively, the light absorption properties of MOFs are determined by the synergy between the organic ligand and the metal ion. In this case, the addition of the primary amine group to terephthalate alters the electronic properties and promotes absorption in the visible region of the solar spectrum.¹⁵ It has been assumed that the three *d*⁰ metals (Ti, Zr and Hf) feature similar electronic properties; accepting electrons in their unoccupied *d* orbitals. Thus, one would expect that a photo-generated electron in this series of MOFs would result in ligand-to-metal charge transfer (LMCT). Although understanding the nature of the excited states and the redox levels of these MOFs is crucial for the rational design of new photo-active frameworks,¹⁶ these important aspects still need to be clarified. The electronic origin of the photocatalytic activity is the focus of this chapter.

LMCT is generally accepted in the MIL-125(Ti)-type materials and was clearly demonstrated by EPR,^{17, 18} flash photolysis¹⁹ and theory²⁰ by a number of groups. The highest occupied crystalline orbital (HOCO) of NH₂-MIL-125(Ti) is localized at the organic linker and the lowest unoccupied crystalline orbital (LUCO) is centred at the Ti *d*-orbitals.²¹ Furthermore, the photoexcitation process results in the formation of Ti³⁺ species that are paramagnetic and have a very evident visible light absorption, making the detection straightforward.

The mechanism behind light-excitation in UiO-66(Zr) materials raises more questions and has been debated by several researchers. Matsuoka and co-workers reported the absence of both photocatalytic activity towards hydrogen evolution and EPR signatures of paramagnetic Zr³⁺ in NH₂-UiO-66(Zr).¹⁷ They attributed this observation to the very negative redox potential of Zr⁴⁺-centred clusters that cannot be accessed by the photoexcited state of aminoterephthalate, thus electron transfer to the

inorganic cluster does not occur. At the same time, Garcia and co-workers claimed the semiconducting behaviour of NH₂-UiO-66(Zr) based on flash photolysis spectroscopy.²² Li *et al.* and Wang *et al.* ascribed the lowest in energy absorption band to LMCT analogously to NH₂-MIL-125(Ti) and reported EPR spectra as the evidence.^{9, 23, 24}

The LUCO positions determine the ability of these MOFs to perform photo-driven reduction processes such as H₂ evolution and/or CO₂ reduction. Walsh and co-workers computed the HOCO-LUCO levels of MIL-125(Ti) and found, in line with previous experimental results, that hydrogen evolution is indeed feasible by using X-MIL-125(Ti) because the LUCO potential is more negative than the redox potential of normal hydrogen electrode (NHE).²⁵ The analysis of the electronic density of states revealed that C, N and O contribute to the HOCO while LUCO is composed of Ti *d* and O *p*-orbitals. They also reported a set of MOFs adopting the MIL-125(Ti) topology that contain different substituents in the aromatic ring of the terephthalate. From simple Hammett arguments,²⁶ the band gap was tuned precisely as low as ca. 1.3 eV in the case of diaminoterephthalic acid.²¹

Although this synthetic strategy is very powerful and gives a remarkable flexibility to tune light absorption properties, the fact that the HOCO localizes at the organic linker implies that the HOCO-LUCO gap becomes smaller at the cost of reducing the oxidative power of the photocatalyst. Conceptually, the LUCO stays unperturbed and the choice of linkers has little influence on the reductive potential of the excited MOF.

In this study we focus on the electronic properties of NH₂-MIL-125(Ti), NH₂-UiO-66(Zr) and NH₂-UiO-66(Hf) and their influence on the photocatalytic performance in hydrogen evolution reaction (HER). For a fair comparison between MOFs containing these metals, the crystalline topology of the different structures should be identical. These three structures were selected because of their clear similarities and the interest raised in the recent literature on their photocatalytic performance. In contrast to what has been recently reported, we demonstrate that only the Ti-based MOF exhibits appreciable catalytic activity while the frameworks of Zr and Hf are hardly active and exhibit nearly identical catalytic performance. Based on transient absorption spectroscopy, EPR and density functional theory (DFT), this difference is attributed to the nature of the excited states in these MOFs and emphasizes the importance of orbital contributions at the electronic 'band' edges.

Experimental

Materials and reagents

All chemicals were purchased from Sigma Aldrich and used without further purification. Methanol and dimethylformamide (DMF) were additionally dried over molecular sieve (zeolite 5Å).

Synthesis

NH₂-MIL-125(Ti): The MOF was synthesized using the protocol reported by Moreira and co-workers.²⁷ In a typical synthesis, 2.86 g (15.8 mmol) 2-aminoterephthalic acid were dissolved in a mixture of 40 mL dry N, N-dimethylformamide (DMF) and 10 mL dry methanol (at room temperature). Then 2.86 mL (9.7 mmol) titanium isopropoxide were added and the mixture was placed in an autoclave. The autoclave was sealed and the mixture was heated for 72 h at 110 °C. The obtained yellow solid was filtered, dispersed in fresh DMF and kept under stirring overnight (50 mL DMF per g of product) in order to remove residual linker. Then, the same procedure was repeated twice using methanol instead of DMF to exchange the DMF within the pores. The solid was finally dried under air at 100 °C.

NH₂-UiO-66(Zr/Hf) 'defective': The protocol is based on the procedure reported by Farha and co-workers.²⁸ For the synthesis of NH₂-UiO-66(X), where X = Zr or Hf, ZrCl₄ (250 mg) or HfCl₄ (346 mg) were dissolved in DMF (10 mL) in the presence of concentrated HCl (2 mL) upon sonication. Additional DMF (15 mL) and 2-aminoterephthalic acid (268 mg) were introduced and the mixture was placed in an autoclave and heated overnight at 80 °C. The pale yellow solids were filtered off, suspended in DMF and sonicated for 10 min. This procedure was repeated twice with DMF and then twice with methanol. The solid was dried under air at 100 °C.

NH₂-UiO-66(Zr/Hf) 'ideal': These MOFs were synthesized following the protocol reported by Lillerud *et al.*²⁹ ZrCl₄ (945 mg) or HfCl₄ (1.308 g) were dissolved in DMF (24.4 mL) in the presence of concentrated HCl (0.7 mL) upon sonication. 1.467 g of 2-aminoterephthalic acid were introduced and the mixture was then heated for 20 h at 220 °C in an autoclave. The pale yellow precipitate was filtered off and washed twice with DMF at 100 °C (10 h each), then methanol at 100 °C (10 h each).

Characterization and methods

Powder X-Ray diffraction patterns were recorded using Bruker-AXS D5005 with CoK α radiation.

N₂-physisorption experiments were carried out at 77 K in a TriStar II unit gas adsorption analyser (Micrometrics). Prior to the measurements the samples were degassed at 423 K under vacuum for 16 h. The BET areas were calculated using intervals allowing positive BET constants. The total pore volumes were calculated at 0.9 relative pressure.³⁰

Scanning electron microscopy (SEM). Scanning electron microscopy (SEM) was carried out using a JEOL JSM-6010LA InTouchScope microscope.

Thermogravimetric analysis was performed by means of Mettler Toledo TGA/SDTA851e, under an air flow of 60 ml min⁻¹ at heating rates of 10 K min⁻¹ up to 1073 K.

Diffuse reflectance UV/Vis spectra were collected using a Perkin–Elmer Lambda 900 spectrophotometer equipped with an integrating sphere (“Labsphere”) in the 200–800 nm range. BaSO₄ was used as a white standard.

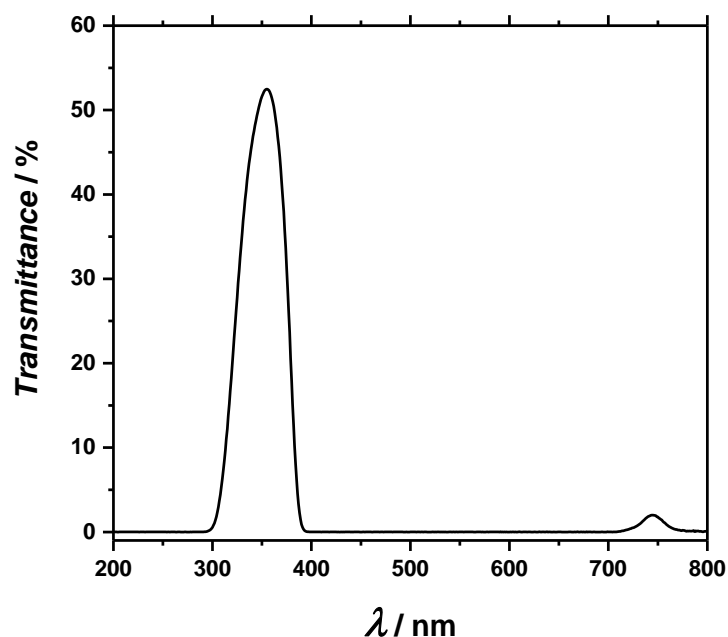


Figure 3.1. Transmittance of the UFS6 filter used in the CW EPR experiments.

EPR spectroscopy. Steady-state EPR measurements were carried out at X-band (9.52 GHz) using a commercial EPR spectrometer Bruker Elexsys E580 equipped with an Oxford Instruments temperature control system ($T = 4 - 300$ K). All spectra were acquired at 80 K. Samples were prepared by suspending 25 mg of a MOF in a solution of electron donor triethylamine (TEA)/CH₃CN/H₂O = 1/5/0.1 (total volume 200 μ L). The volume of suspension placed into the EPR resonator was 50-60 μ L. Each sample was degassed by several freeze-pump-thaw procedures and then sealed in an EPR quartz tube (OD 3.8 mm, ID 2.8 mm). When needed, the samples were exposed to a 500 W mercury lamp equipped with an IR filter (H₂O, 7 cm optical path) and a UFS6 filter (see Figure 3.1) for 30 min. After this period the sample tube was placed into liquid nitrogen. The cool-down time to frozen state was ~ 10 -15 s. Then it was inserted into EPR cryostat.

Femtosecond Transient Absorption Spectroscopy. Samples were excited using 180 fs pulses at 400 nm for NH₂-MIL-125(Ti) and 370 nm for NH₂-UiO-66(Zr) and NH₂-UiO-66(Hf) generated in a YKGBW oscillator (Light Conversion, Pharos SP) at 1028 nm through nonlinear frequency mixing in an OPA and second harmonics module (Light Conversion, Orpheus). A small fraction of the 1028 nm fundamental beam was split off to generate the broadband probe spectrum in a sapphire (500 – 1600 nm) crystal. The probe pulse was delayed relative to the pump using a delay stage with maximum delay of 3 ns. The pump and probe pulses overlap on the sample position under an angle of ~ 8 degrees, after which the probe light is led to a detector suitable for the probe spectrum selected (Ultrafast Systems, Helios). In order to prevent multiple photons absorption processes, the pump fluence was set sufficiently low, allowing us to study single exciton dynamics. In a typical experiment 2.7 mg of a MOF were dispersed in acetonitrile (700 μ L) and sonicated for 30 min. In order to separate large particles (> 100 nm), the suspension was then centrifuged for 8 min

at 10000 rpm. The supernatant was placed in a 2 mm stirred quartz cuvette for the measurements. Transient data were analysed using a global fitting routine in which the spectral evolution of the time-dependent absorption difference spectra is fitted to a sequential model yielding evolution-associated difference spectra (EADS).³¹ In the case of the NH₂-MIL-125(Ti) and NH₂-UiO-66(Zr/Hf) 'defective' a three-state kinetic model was used to fit the experimental data.³² An additional state was used to force the system to go to the ground state. All time traces were fitted with three time constants and a non-decaying component giving satisfactory results. For the NH₂-UiO-66(Zr/Hf) 'ideal' one excited state (which population's decay is defined by $\exp(-kt)$) that goes to the ground state (described by $1 - \exp(-kt)$) was sufficient for a good fit.

Computational Methods

All calculations were performed within the framework of density functional theory with electron exchange and correlation treated with the semi-local PBEsol functional (for structure relaxation) and the non-local screened HSE06 functional (for quantitative electronic structure information). The crystalline MOFs were described within periodic boundary conditions are implemented in the VASP computational chemistry package.³³ A 500 eV planewave cutoff and Gamma point sampling of the first Brillouin zone was found to be sufficient for energy convergence within 0.01 eV per atom. Starting with experimentally collected crystallographic structures, lattice parameters and atomic positions were relaxed with PBEsol to equilibrium structures, which are available in an external data repository: https://github.com/WMD-Bath/Crystal_Structures. The optimized structures were then computed with HSE06 to recover the electronic structure. Electron energies were aligned to the vacuum level using a procedure developed by Butler, Hendon and Walsh, and the code is freely available.²⁵ A model of the triplet state (*i.e.* a first excited state) was obtained by fixing the total spin moment in the crystallographic unit cell (NUPDOWN = 2 in VASP). Images were made in VESTA.³⁴

Photocatalysis

Photocatalytic experiments were carried out using a home-built set-up equipped with a 500 W Xe/Hg lamp (66983, Newport). It consists of a custom-made Pyrex-glass reactor, a CP 9001 gas chromatograph (Chrompack) for analysis of the headspace, a KSLA gas pump and the light source. Light intensity was measured with AvaSpec-3648-2-USB2 (Avantes, the Netherlands). The reactor has a volume of 42.1 mL and is equipped with a water jacket to allow for precise temperature control. The light emitted by the lamp passes through a lens assembly (77330, Newport) focussing the beam on the reactor window, an H₂O filter (61945, Newport) and a 385 nm cut-off optical filter. The pump is applied to ensure a sufficient mixing of gases in the headspace of the reactor and the stainless steel tubes (2.5 mL/min continuous operation). Every 60 min a probe of the headspace is analyzed by the GC. In a typical experiment 30 mg of a MOF were suspended in 23.5 mL CH₃CN, 4.7 mL TEA and 0.5 mL H₂O. The suspension was then placed in the reactor and deoxygenated

by an argon flow of 30 mL/min applied for 30 min at 25 °C. The oxygen concentration was monitored by the GC analysis. Once the system became free of oxygen, the illumination was applied followed by the GC analysis. All the visible light photocatalytic experiments were carried out at 40 °C monitored by a thermocouple. The heat was supplied in order to maximize the hydrogen production allowing the detection of H₂ gas in the case of samples with the lowest activity.

Calculation of external quantum efficiency

External quantum efficiencies of catalysts employed in this work were calculated using the following equation:

$$\Phi = \frac{E(t)}{P(t)} \quad (\text{eq. 1}),$$

where $E(t)$ is the number of electrons carrying out a redox reaction per unit of time; $P(t)$ is a photon flux per unit of time. The incident photon flux was determined with the help of the photon counter. The spectrum was taken at the conditions of the photocatalytic reactions: 385 nm cut-off filter, liquid filter on, the distance 5.5 cm. Then the curve was integrated with the lower boundary being 350 nm, where the flux goes to 0. The upper boundary for the integration was determined by using the *Tauc* plot (Figure 3.8) and converting the HOMO-LUMO gaps back to nm using the relation $\lambda = 1240/E(\text{eV})$. The integration yielded the following photon fluxes: 16815, 6839, 6839, 6582 and 6438 $\mu\text{mol}(\text{photons}) \cdot \text{s}^{-1} \text{m}^{-2}$. The spot size of the beam reaching the reactor window was 2.27 cm². Details of the calculation for the case of Ti are given below:

$$\begin{aligned} P_{Ti}(t) &= \int_{350}^{451} P(t, \lambda) d\lambda \cdot 0.000227 \text{ m}^2 = 16815 \mu\text{mol}(\text{photons}) \cdot \text{s}^{-1} \text{m}^{-2} \cdot 0.00027 \text{ m}^2 = \\ &= 3.817 \mu\text{mol}(\text{photons}) \cdot \text{s}^{-1} \end{aligned} \quad (\text{eq. 2})$$

To account for the number of photons required to assemble one hydrogen molecule (2) the reaction rates must be multiplied by 2 and converted to appropriate units to obtain the number of electrons:

$$E(t) = r(\text{H}_2) \cdot 2 = 1.484 \mu\text{mol} \cdot \text{h}^{-1} \cdot 2 = 2.968 \mu\text{mol} \cdot \text{h}^{-1} = 8.244 \cdot 10^{-4} \mu\text{mol} \cdot \text{s}^{-1} \quad (\text{eq. 3})$$

$$\Phi_{Ti} = \frac{E(t)}{P(t)} = \frac{8.244 \cdot 10^{-4} \mu\text{mol} \cdot \text{s}^{-1}}{3.817 \mu\text{mol} \cdot \text{s}^{-1}} = 2.16 \cdot 10^{-4} = 0.0216 \% \quad (\text{eq. 4})$$

All the other EQEs were calculated in the same manner.

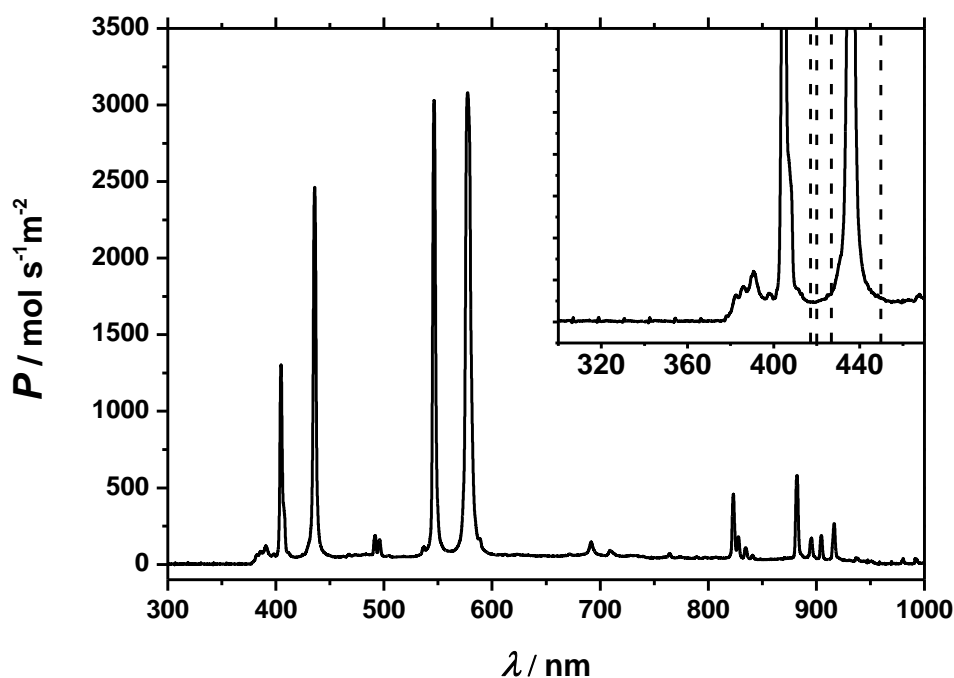


Figure 3.2. Incident photon flux as a function of wavelength of the 500 W Xe/Hg light source used in this work. The measurement is carried out at the distance of 5.5 cm with the liquid filter on. The inset highlights the spectral region relevant for the hydrogen evolution catalysed by the MOFs. The dashed lines denote cut-off wavelengths for each catalyst as determined from *Tauc* plot.

Results and discussion

Catalysts characterization

In this work $\text{NH}_2\text{-MIL-125(Ti)}$, further denoted as Ti, was synthesized by the protocol reported elsewhere²⁷ and described in the Experimental part. The synthesis yielded a material with high crystallinity and total pore volume⁷ (Table 3.1,

Figure 3.3). Among different kinds of metal-organic frameworks the UiO-type materials are particularly known for possessing structural defects. They account for the non-stoichiometric ratios of metal : linker observed by several groups experimentally. The missing linkers are often seen being compensated by formates,³⁵ oxygen, hydroxide, water²⁸ and/or chloride,²⁹ however a comprehensive structural information is missing. The influence of these structural defects on gas sorption was documented by Snurr *et al.*³⁶ and Zhou *et al.*³⁷ Notably, recent results by Yaghi *et al.* demonstrate that in the case of UiO-66(Zr) the missing linkers are replaced by water molecules with the charge being compensated by OH^- .³⁸

In order to consider the influence of the defects on the electronic and photocatalytic properties of $\text{NH}_2\text{-UiO-66(X)}$ materials, two synthetic protocols were followed in this work. The first method yields highly defective structure as documented by Farha and co-workers whereas the second approach was claimed to produce nearly stoichiometric UiO crystals.

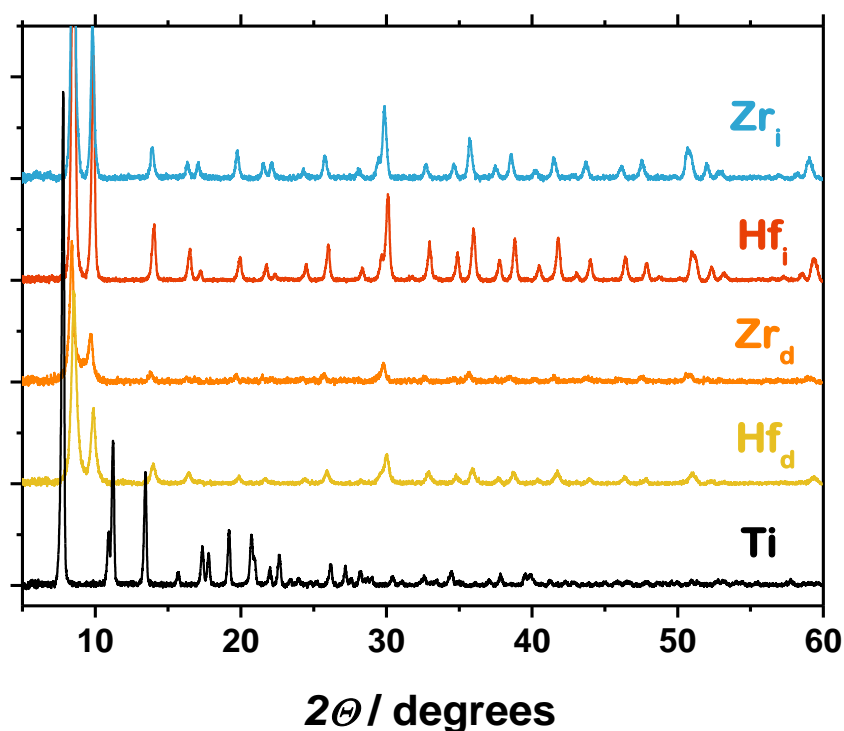


Figure 3.3. Powder X-Ray diffraction patterns of the catalysts used in this work: ideal $\text{NH}_2\text{-UiO-66}(\text{Zr})$ (blue), ideal $\text{NH}_2\text{-UiO-66}(\text{Hf})$ (red), defective $\text{NH}_2\text{-UiO-66}(\text{Zr})$ (orange), defective $\text{NH}_2\text{-UiO-66}(\text{Hf})$ (yellow), $\text{NH}_2\text{-MIL-125}(\text{Ti})$ (black).

These two types of crystals are denoted X_d and X_i ($X = \text{Zr}$ or Hf) and referred to as ‘defective’ and ‘ideal’ respectively. Well in line with the previous reports, the low-temperature protocol results in a defective structure as can be concluded from the BET surface area exceeding the theoretical prediction for $\text{NH}_2\text{-UiO-66}(\text{Zr})$ (see Table 3.1). The area is slightly higher than the predicted value for the case of 8 linkers per node instead of the stoichiometric 12 (1285 vs. 1150 m^2/g).

Table 3.1. Textural properties of the MOFs employed in this work.

Notation	MOF	$S_{\text{BET}} / \text{m}^2 \text{g}^{-1}$	$V_p / \text{cm}^3 \text{g}^{-1}$	Comment
Ti	$\text{NH}_2\text{-MIL-125}(\text{Ti})$	1500	0.61	
Zr_i	$\text{NH}_2\text{-UiO-66}(\text{Zr})$	959/700 ^a /830 ^d	0.41	‘ideal crystals’
Hf_i	$\text{NH}_2\text{-UiO-66}(\text{Hf})$	706	0.31	‘ideal crystals’
Zr_d	$\text{NH}_2\text{-UiO-66}(\text{Zr})$	1285/1150 ^b /1200 ^c	0.54	‘defective crystals’
Hf_d	$\text{NH}_2\text{-UiO-66}(\text{Hf})$	789	0.35	‘defective crystals’

a: calculated BET area for the stoichiometric crystal (12 linkers per node)

b: calculated BET area for the defective crystal (8 linkers per node) both adopted from Farha et al.²⁸

c: experimental BET area reported by Farha et al.²⁸

d: experimental BET area reported by Farha et al. for the HCl-free synthesis²⁸

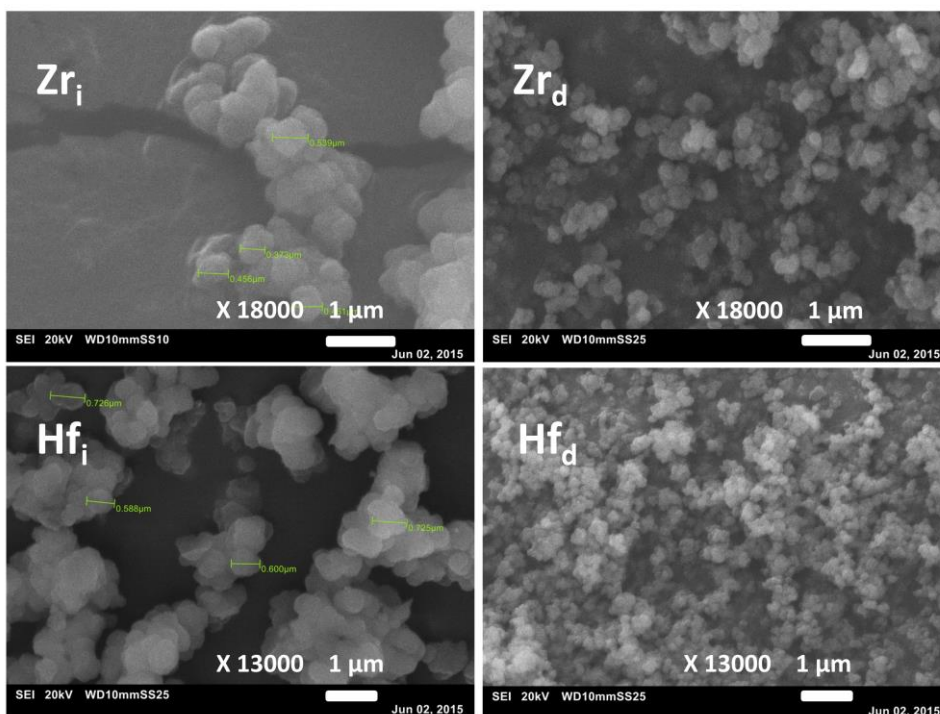


Figure 3.4. SEM micrographs of the UiO solids utilized in this work. ideal $\text{NH}_2\text{-UiO-66(Zr)}$ (top left), defective $\text{NH}_2\text{-UiO-66(Zr)}$ (top right), ideal $\text{NH}_2\text{-UiO-66(Hf)}$ (bottom left), defective $\text{NH}_2\text{-UiO-66(Hf)}$ (bottom right). The micrographs recorded at 18000 magnification (top) and 13000 (bottom).

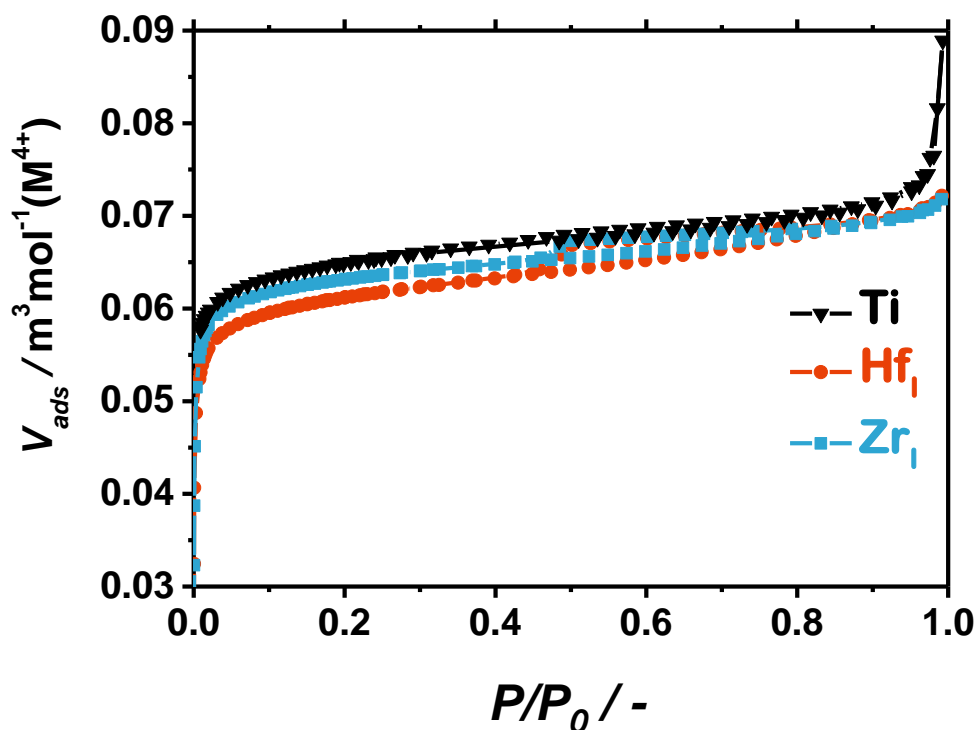


Figure 3.5. Nitrogen physisorption isotherms for the catalysts used in this work normalized to the mass of metal constituting the MOFs. Top to bottom: $\text{NH}_2\text{-MIL-125(Ti)}$ (black triangles), ideal $\text{NH}_2\text{-UiO-66(Zr)}$ (blue squares), ideal $\text{NH}_2\text{-UiO-66(Hf)}$ (red spheres) .

The structural defects in Zr_d are also reflected by the poor crystallinity of the solid as well as the small particle size as is evident from the broadening of the Bragg reflections (

Figure 3.3). Scanning electron microscopy confirms these observations as depicted in Figure 3.4. At the same time the high-temperature synthetic route yields NH_2 -UiO-66(Zr) material, Zr_i , possessing high crystallinity, better-distinguishable crystal shape and the surface area closely matching the predicted value for an ideal structure. The observations for the case of NH_2 -UiO-66(Hf) are similar, yet less prominent. The crystallinity of Hf_d is heavily affected by the synthesis procedure. However, the difference in textural properties of Hf_d and Hf_i is less dramatic than in the case of Zr-based MOFs. Figure 3.5 illustrates the N_2 adsorption isotherms for Ti, Zr_i and Hf_i per mol of the corresponding metal and shows the similarity of the three structures, two of which adopt the same topology (UiO).

Additional investigation of the defects within the UiO MOFs was carried out using thermogravimetric analysis (TGA). The TGA profiles are depicted in Figure 3.6. Similarly to the report of Lillerud *et al.*,²⁹ TGA profiles of the catalysts utilized in this work were normalized with respect to the remaining corresponding oxides. To describe the thermal decomposition of the MOFs used in this study in air we used the following equations:



The weights of the materials at 750 °C were converted to 100%. The dashed lines in Figure 1 of the main text represent the weight difference between the oxides and the anhydrous MOFs for the case of stoichiometric crystals. Such differences were calculated assuming that the combustion processes proceed via the reactions (eq. 5) - (eq. 7) and the only remaining solid products are ZrO_2 , HfO_2 and TiO_2 . In this case the nitrogen is accounted for in the form of NO_2 . An example of such calculation is given below:



According to (eq. 6), $v_{MOF} : v_{ZrO_2} = 1 : 6$

$$M_{MOF} = 1718.12 \text{ g} \cdot \text{mol}^{-1}$$

$$M_{ZrO_2} = 123.22 \text{ g} \cdot \text{mol}^{-1}$$

For the case of stoichiometric crystal

$$\frac{m_{MOF}}{m_{ZrO_2}} = \frac{v_{MOF} \cdot M_{MOF}}{v_{ZrO_2} \cdot M_{ZrO_2}} = \frac{1 \cdot 1718.12}{6 \cdot 123.22} = 2.32 = 232\% \quad (\text{eq. 8})$$

This means that if the mass of the remaining ZrO_2 is assumed to be 100%, the anhydrous stoichiometric NH_2 -UiO-66(Zr) must be positioned at 232% of weight loss

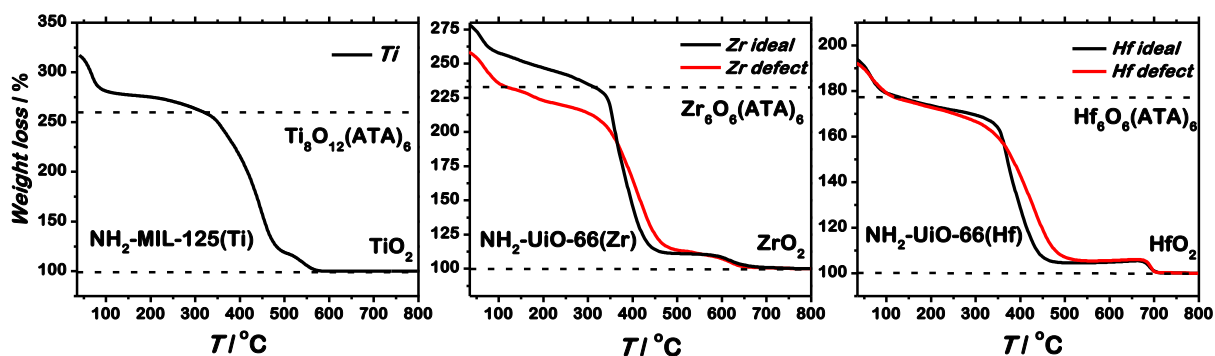


Figure 3.6. TGA profiles of $\text{NH}_2\text{-MIL-125(Ti)}$ (left), $\text{NH}_2\text{-UiO-66(Zr)}$ (center) and $\text{NH}_2\text{-UiO-66(Hf)}$ (right). The analysis is carried out in air. The profiles were normalized with respect to the remaining oxide (corresponds to 100% weight loss). The dashed lines represent the anhydrous MOF (top) and the remaining MO_2 (bottom).

scale. The same reasoning was used for calculating the expected weight losses for Ti and Hf.

While no clear plateau was observed for UiO-66(Zr) derivatives including $\text{NH}_2\text{-UiO-66(Zr)}^{28}$, our experiments allowed for a quantitative TGA analysis. The first weight loss observed up to 110 °C is associated with the solvent removal from the pores of the framework. The second step is the gradual dehydroxylation of the framework, giving rise to $\text{Zr}_6\text{O}_6(\text{ATA})_6$ followed by the loss at around 400 °C that corresponds to the destruction of the MOF. The decomposition of the ideal sample starts at the predicted weigh loss value of 232% with respect to the pure oxide (Figure 3.6 centre), whereas in the defective MOF the amount of organics is lower. In view of these results, we can conclude that the low temperature synthesis of $\text{NH}_2\text{-UiO-66(Hf)}$ does not yield MOF crystals completely free of defects, yet the plateau of the ideal sample is higher, in line with N_2 physisorption results. The presence of structural defects is also typical for Hf-based frameworks of the UiO family.^{39, 40} The weight of $\text{NH}_2\text{-MIL-125(Ti)}$ sample before the full destruction of the framework begins (ca. 350 °C) corresponds well to the theoretical expectations thus suggesting nearly ideal structure of the MOF. The influence of structural defects in $\text{NH}_2\text{-MIL-125(Ti)}$ on the photocatalytic performance as well as on electronic properties is beyond the scope of this work, yet is of great interest.

Optical properties of the synthesized Ti-, Zr- and Hf-based MOFs were investigated by diffuse reflectance UV-Vis spectroscopy. The reflectance spectra are displayed in Figure 3.7. In line with the previous reports, $\text{NH}_2\text{-MIL-125(Ti)}$ possesses two absorption bands with the maxima at 280 and 382 nm.^{7, 15, 41} The lowest in energy absorption band tails up to 475 nm, covering a fraction of the visible part of the electromagnetic spectrum. This transition is ascribed to LMCT. The spectra of $\text{Zr}_{i/d}$ and $\text{Hf}_{i/d}$ are blue shifted as compared to that of Ti while still exhibit a similar spectral profile with two distinct absorption bands $\lambda_{max} = 255$ and 370 nm. Li and co-workers attributed the 370 nm absorption band to LMCT analogously to the case of $\text{NH}_2\text{-MIL-125(Ti)}$.²³ They reported that this absorption band can be ascribed to $n\text{-}\pi^*$ transition

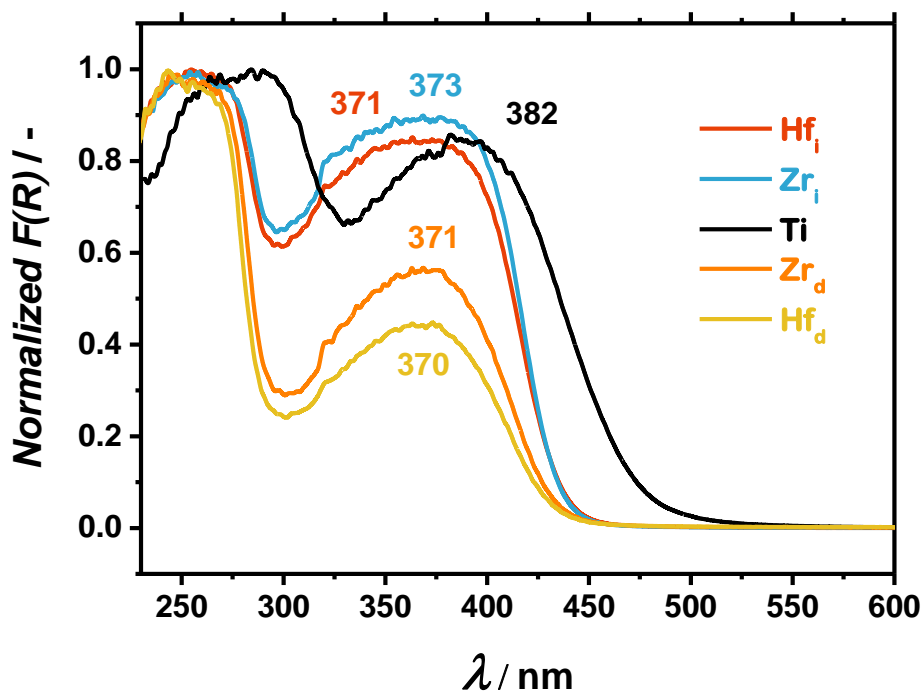


Figure 3.7. Diffuse reflectance UV-Vis spectra of catalysts studied in Kubelka-Munk representation. NH₂-MIL-125(Ti) (*black*), defective NH₂-UiO-66(Zr) (*orange*), ideal NH₂-UiO-66(Zr) (*blue*), defective NH₂-UiO-66(Hf) (*yellow*), ideal NH₂-UiO-66(Hf) (*red*).

of the linker and such excitation is followed by electron injection from a π^* orbital to the zirconium core, in contrast to the claims of Matsuoka.¹⁷

Noteworthy, the absorption maxima of the ideal and defective samples are at nearly the same position, although there is a slight blue shift (*ca.* 7 nm) of the absorption onset in the case of Zr_d and Hf_d. Another difference derived by the presence of structural defects is the reduced intensity of the lowest energy absorption band when compared against the other transition. Since this band is ascribed to the linker, a different linker to metal ratio in the structure could account for the difference in relative intensities. More importantly, the optical spectra of the ideal Zr and Hf MOF pair and those of the defective pair are nearly identical. HOCO-LUCO gaps for these solids were obtained from the *Tauc* (Figure 3.8). The experimental gap for MIL-125 is 2.75 eV, in good agreement with previous reports.^{7, 21, 41} On the other hand, the HOCO-LUCO gaps of Zr_i and Hf_i are identical and equal to 2.92 eV. Zr_d is at 2.95 eV and the largest in energy gap corresponds to Hf_d (2.97 eV). While the HOCO-LUCO gaps of photocatalysts define the operation regime *i.e.* wavelength of light that can be utilized for chemical transformations, the absolute positions of HOCO and LUCO determine the thermodynamic feasibility of certain oxidations and reductions respectively.

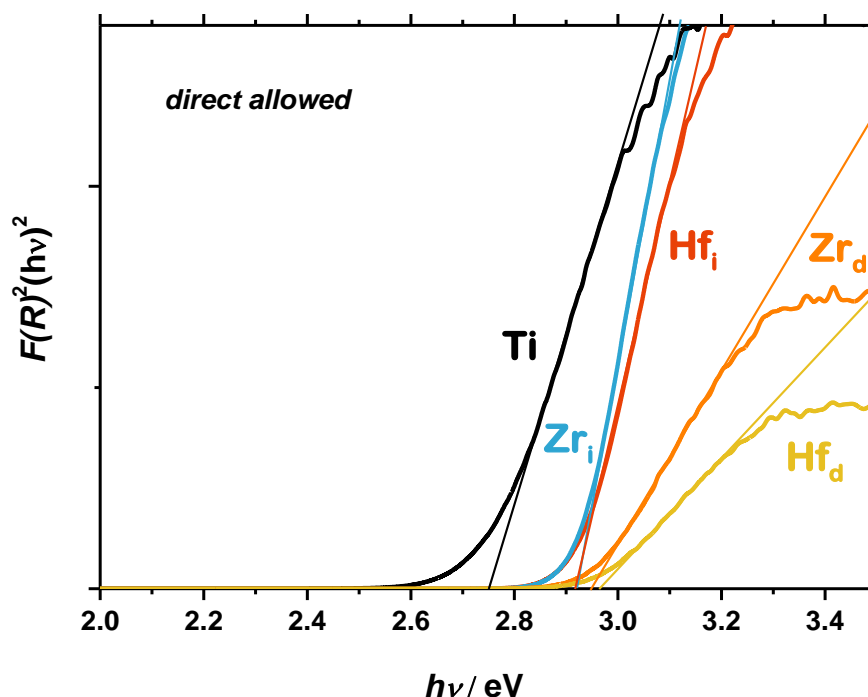


Figure 3.8. Tauc plot for the MOFs utilized in this work: NH₂-MIL-125(Ti) (*black*), defective NH₂-UiO-66(Zr) (*orange*), ideal NH₂-UiO-66(Zr) (*blue*), defective NH₂-UiO-66(Hf) (*yellow*), ideal NH₂-UiO-66(Hf) (*red*). The curves are obtained under the allowed direct transition assumption.

Computational results

Estimation of the heterogeneous H₂ redox potential is challenging, but applying the values determined in the solvated phase, we know this energy is near the vacuum level (*ca.* 4.4 eV). Consideration of only the energies of the frontier bands of the heterogeneous catalyst is not enough to predict the efficiency and activity of the material in H₂ evolution reaction. From a purely thermodynamic perspective, the lower the electron affinity the greater the HER turnover should be. Thus, considering our computational findings explained in the Experimental part and depicted in Figure 3.9, we would anticipate that the Zr- and Hf- MOFs should perform better than the Ti-material. However, we must also consider the identity of the orbitals that contribute to the frontier bands.

Indeed, Figure 3.9 shows that the LUCO for the MIL-125 structure is centred on the TiO₂ (inorganic) region, whilst the two UiO- materials have a different electronic structure. Both the Zr- and Hf- materials have organic defined frontier band extrema. DFT infers that the single electron excited state of NH₂-MIL-125 should result in the formation of a delocalised Ti³⁺ species (which can localise by protonating a bridging oxide).²⁰ In the case of the UiO series of materials, organic-centred excitons are typically short-lived, although still some catalytic activity could be expected, since the thermodynamic energy level alignment is in favour of reducing H₂.⁴² More importantly, this difference in the LUCO structure originates from the fact that the *d*-

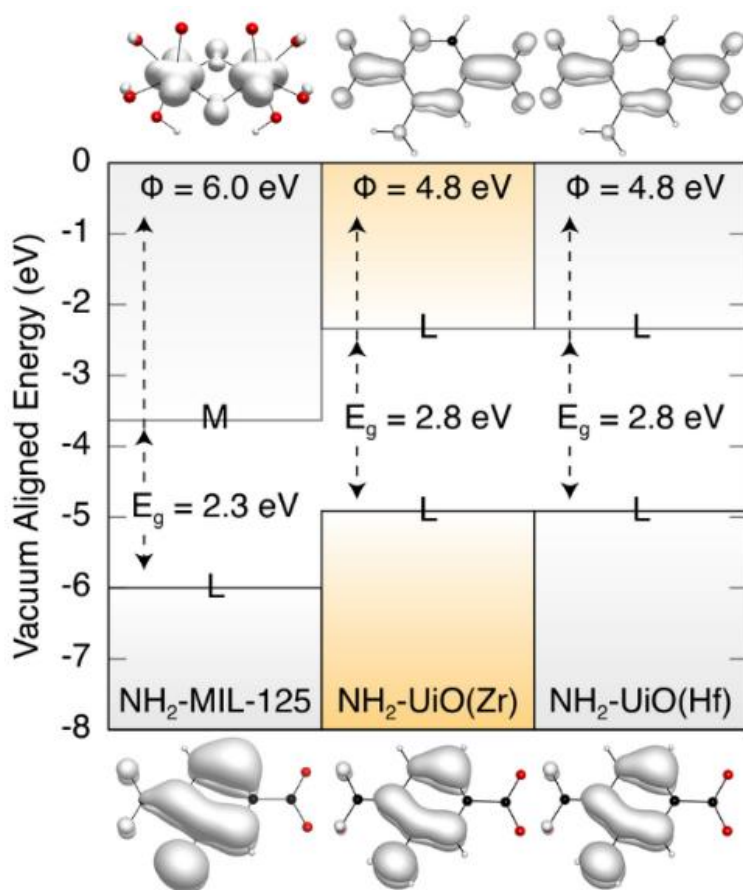


Figure 3.9. The band alignment relative to the vacuum level of the three MOFs considered here. Shown above and below are the orbitals contributing to the HOCO (*lower*) and LUCO (*upper*). M and L correspond to the localization of these orbitals on metal or ligand, respectively.

orbitals of Zr and Hf are too far in energy and thus cannot overlap with the π^* orbital of the ligand despite the suitability of the geometrical arrangement of the orbitals. At the same time the d -orbitals of Ti fulfil both the spatial and energetic requirements, allowing for the efficient overlap.

Electron paramagnetic resonance

In order to investigate the nature of excited states within the photocatalytic metal-organic frameworks we carried out electron paramagnetic resonance spectroscopy (EPR), shown in Figure 3.10. The MOFs were subjected to conditions similar to those during photocatalytic reaction as described in the experimental part. In line with the previous reports,^{17, 18} illuminating $\text{NH}_2\text{-MIL-125}(\text{Ti})$ with light of the energy corresponding to the HOCO-LUCO transition leads to the appearance of an intense paramagnetic signal ascribed to Ti^{3+} .^{13, 17, 18} Most importantly, $\text{NH}_2\text{-UiO-66}(\text{Zr})$ and $\text{NH}_2\text{-UiO-66}(\text{Hf})$ exposed to the same conditions did not develop any additional paramagnetic features upon illumination. This result is in agreement with the data reported by Matsuoka and colleagues.¹⁷ Most likely, if any paramagnetic species evolve as a result of irradiating the $\text{NH}_2\text{-UiO-66}(\text{X})$ solids, their lifetimes are too short for detection in the chosen experimental fashion.

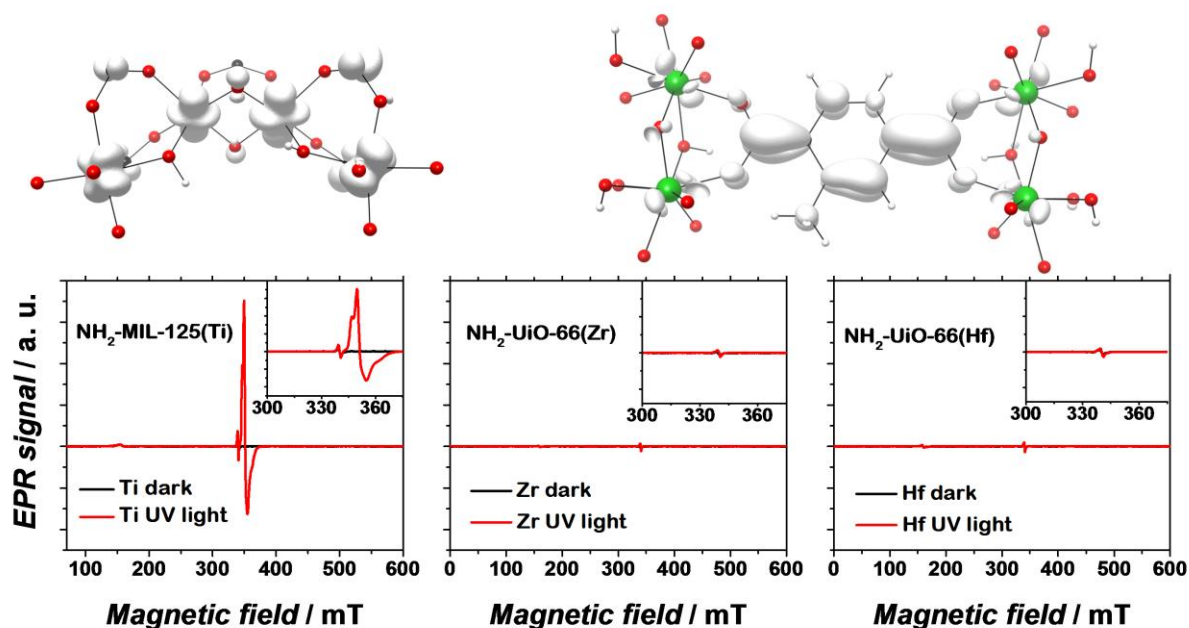


Figure 3.10. EPR spectra of dark (*black*) and UV-illuminated (*red*) MOFs: NH₂-MIL-125(Ti) (*left*), ‘ideal’ NH₂-UiO-66(Zr) (*center*) and NH₂-UiO-66(Hf) (*right*). The photoexcited electron is primarily Ti-centred in the case of NH₂-MIL-125, whereas in the UiO-type materials, the electron resides on the organic linker.

Photocatalytic performance

In summary, all MOFs subjected to the investigations have LUCO positions suitable to drive hydrogen evolution. In fact, the computational findings dictate that Zr and Hf, when excited, possess an even greater thermodynamic driving force for accomplishing the desired reduction, however, reduction of the metal node only takes place in case of the Ti MOF. The photocatalytic activity of the frameworks was assessed in visible light-driven hydrogen evolution. NH₂-MIL-125(Ti) clearly outperforms defective NH₂-UiO-66(Zr) and NH₂-UiO-66(Hf) (

Figure 3.11). The latter two have practically the same photocatalytic activity that is *ca.* 30 times lower than the one of Ti. The rates of hydrogen evolution under visible light were determined by linear fittings of the experimental $C(t)$ vs. *time* and found to be 1.48, 0.03, 0.02, 0.05 and 0.05 $\mu\text{mol}\cdot\text{h}^{-1}$ for Ti, Zr_i, Hf_i, Zr_d and Hf_d, respectively. Interestingly, the defective solids exhibit an activity twice as high as the one of ideal crystals. We speculate that this difference in photocatalytic performance may originate from: (i) the defective solids have a substantially smaller particle size and thus larger fraction of external surface; (ii) the defective solids have a greater total pore volume; (iii) the presence of structural defects has a positive influence on the rate of photocatalysis.

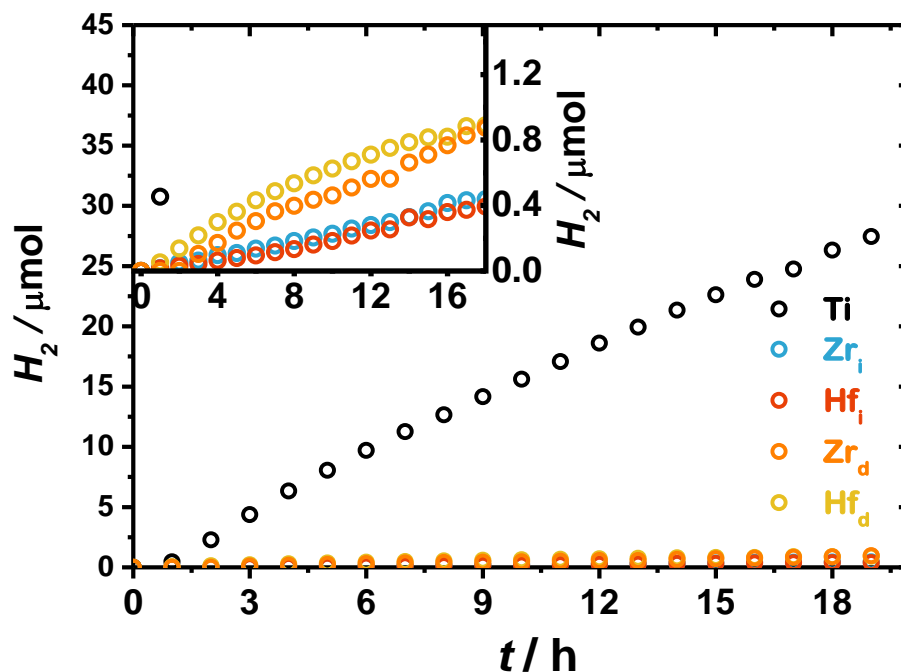


Figure 3.11. Photocatalytic performance of the MOF catalysts in hydrogen evolution: NH₂-MIL-125(Ti) (*black*), defective NH₂-UiO-66(Zr) (*orange*), ideal NH₂-UiO-66(Zr) (*blue*), defective NH₂-UiO-66(Hf) (*yellow*), ideal NH₂-UiO-66(Hf) (*red*). 500 W Xe/Hg light source, > 385 nm. The inset magnifies the region of interest for the UiO-type catalysts.

The first reasoning is particularly important in the case of dense oxides where chemical reactions can only occur at the surface of photocatalyst particles. However, we expect that in the case of MOFs this argument is of minor importance unless bulky substrates are subjected to photocatalysis. At first sight the second scenario seems the most logical: the surface area of the defective catalysts is much larger than the one of ideal MOFs. While this is definitely true for Zr_d vs. Zr_i, the case of NH₂-UiO-66(Hf) suggests that the main contribution to the catalytic performance is not due to the difference in surface areas. The total pore volumes of Hf_d and Hf_i are 0.35 and 0.31 cm³ g⁻¹, respectively. Such minor difference in surface areas should not account for doubling the catalytic rate. The difference in optical properties is also fairly negligible when speaking of such rate enhancement. In fact, the external quantum efficiencies of defective solids are twice as high as the ones of ideal MOFs as summarized in **Error! Not a valid bookmark self-reference.** This suggests that the structural defects within the UiO-type solids improve the hydrogen evolution rate.

Kinetics of photoexcited states assessed by transient absorption spectroscopy

As already anticipated, the observed difference in activity between the Ti and Hf and Zr catalysts can only be explained by the location of the LUCO at the inorganic node in case of NH₂-MIL-125(Ti). Indeed, even taking into account the difference in optical properties, NH₂-MIL-125(Ti) achieves an external quantum efficiency (EQE) ca. 13

Table 3.2. Catalytic performance.

Sample	HOCO-LUCO gap / eV	Hydrogen evolution rate / $\mu\text{mol}\cdot\text{h}^{-1}$	External quantum efficiency / %
Ti	2.75	1.48	0.022
Zr _i	2.92	0.03	0.0009
Hf _i	2.92	0.03	0.0009
Zr _d	2.95	0.05	0.0016
Hf _d	2.97	0.05	0.0016

times larger than the one of defective NH₂-UiO-66(Zr) (The first reasoning is particularly important in the case of dense oxides where chemical reactions can only occur at the surface of photocatalyst particles. However, we expect that in the case of MOFs this argument is of minor importance unless bulky substrates are subjected to photocatalysis. At first sight the second scenario seems the most logical: the surface area of the defective catalysts is much larger than the one of ideal MOFs. While this is definitely true for Zr_d vs. Zr_i, the case of NH₂-UiO-66(Hf) suggests that the main contribution to the catalytic performance is not due to the difference in surface areas. The total pore volumes of Hf_d and Hf_i are 0.35 and 0.31 cm³ g⁻¹, respectively. Such minor difference in surface areas should not account for doubling the catalytic rate. The difference in optical properties is also fairly negligible when speaking of such rate enhancement. In fact, the external quantum efficiencies of defective solids are twice as high as the ones of ideal MOFs as summarized in **Error! Not a valid bookmark self-reference.** This suggests that the structural defects within the UiO-type solids improve the hydrogen evolution rate.

Kinetics of photoexcited states assessed by transient absorption spectroscopy

As already anticipated, the observed difference in activity between the Ti and Hf and Zr catalysts can only be explained by the location of the LUCO at the inorganic node in case of NH₂-MIL-125(Ti). Indeed, even taking into account the difference in optical properties, NH₂-MIL-125(Ti) achieves an external quantum efficiency (EQE) ca. 13

Table 3.2). In order to further prove this hypothesis, we performed transient absorption spectroscopy (TAS) to study the lifetime of the excited states in these solids.

Results are presented in Figure 3.12. The MOFs were excited at the wavelengths corresponding to their respective absorption maxima. Excitation of NH₂-MIL-125(Ti) results in an intense transient signal with a maximum at 560 and 600 nm, and a very broad peak from < 500nm till over 860 nm. A kinetic model with three transient

consecutive states was necessary to obtain a reasonable fit for the experimental data.³² The third state then goes to the ground state. The third transient state has a moderately long lifetime of up to 9 ns (Table 3.3). Details of the fitting and the evolution associated difference spectra (EADS) are given in the Appendix 2.

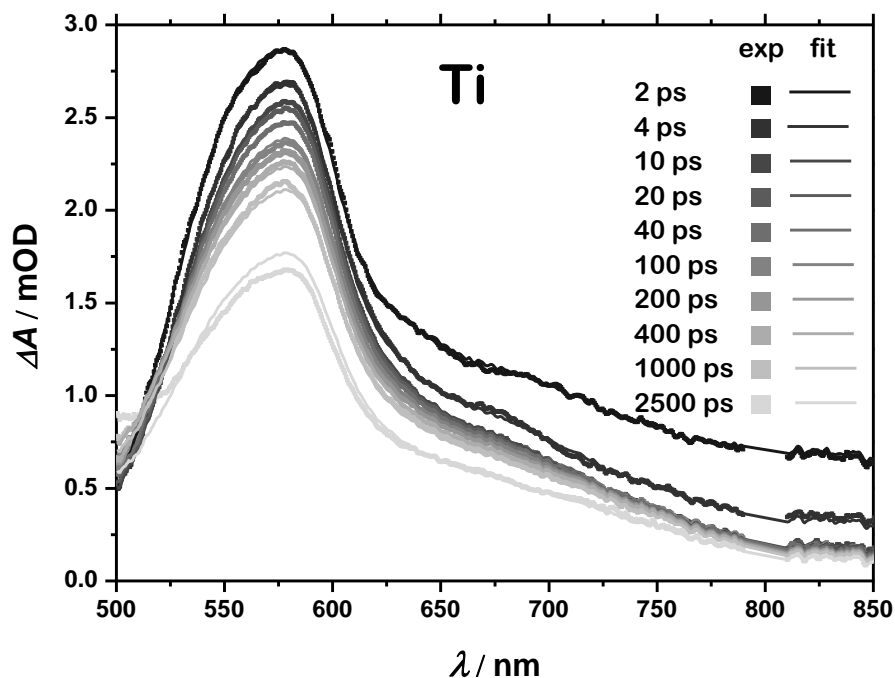


Figure 3.12. Differential transient absorption spectra for NH₂-MIL-125(Ti) upon excitation at 400 nm. Experimental data and the fittings.

Table 3.3. Fitting parameters of the TAS signals for the MOF-catalysts.

Sample	Lifetime of transient signal / ps		
Ti	1.6	80	9·10 ³
Hf _d	2.4	20	190
Zr _d	1.6	10	130
Hf _i	1.4	-	-
Zr _i	1.5	-	-

The transient spectra of NH₂-UiO-66(Zr) and NH₂-UiO-66(Hf) are markedly different from the one of Ti. The transient signals of Zr_i and Hf_i are nearly identical in terms of both kinetics of the decay and the spectral signatures. Right after the laser pulse, a broad transient signal emerges at 750 nm and decays rapidly to the ground state. The lifetime of this signal is 1.5 ps in both cases.

The defective solids exhibit a different behaviour. First of all, a kinetic model with three transient consecutive states was necessary to obtain a reasonable fit for the experimental data (see Appendix 2).³² The last state decays to the ground state. Moreover, the transient absorption band is shifted to shorter wavelengths compared

to the ones of Zr_i and Hf_i . The excited state of Hf_d and Zr_d has a significantly longer lifetime up to 190 and 130 ps. These species now have distinct properties with respect to Zr_i and Hf_i . In addition to the rapid decay pathway that is also registered in the case of ideal crystals, the defective Zr_d and Hf_d undergo a relaxation pathway with longer lifetimes, yet still several orders of magnitude shorter than the ones of Ti (Table 3.3).

Based on the EPR data and the computational results, the transient signals in the case of Hf and Zr structures can be assigned to the HOCO-LUCO transition of the NH_2 -UiO-66(X) framework. This transition is purely ligand-based and is independent of the metal ion employed. In contrast, in the Ti MOF, as established by EPR, Ti^{3+} is generated upon illumination. The main difference between the Zr/Hf and the Ti transient spectra, is the occurrence of absorption bands at much lower wavelengths in NH_2 -MIL-125(Ti), namely 560 and 600 nm, assigned to the stabilisation of the hole over the organic linker.

These results are in line with the photocatalytic experiments. Indeed, a more efficient photocatalysis is expected when photo-excited charges have a longer lifetime. The longer lifetime for the NH_2 -MIL-125(Ti) with respect to the NH_2 -UiO-66(Zr) and NH_2 -UiO-66(Hf) is also in accordance with the EPR and DFT calculations. For MOFs where the HOMO-LUMO transition resides purely at the organic linker, as opposed to a LMCT, lifetime of excited states is too short to allow for efficient utilization of the generated electrons.

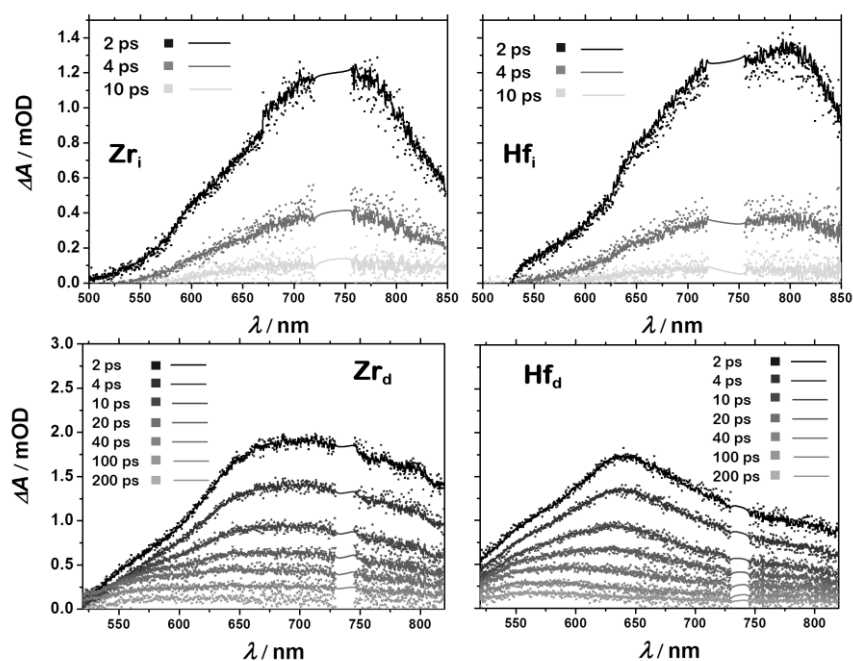


Figure 3.13. Differential transient absorption spectra for 'ideal' (*top*) and 'defective' (*bottom*) NH_2 -UiO-66(Zr) (*left*) and NH_2 -UiO-66(Hf) (*right*) upon excitation at 370 nm. Experimental data and the fittings (for more details on the fitting see Appendix 2).

Conclusions

In this work we explored the photocatalytic potential of d^0 metal-based metal-organic frameworks: NH₂-MIL-125(Ti), NH₂-UiO-66(Zr) and NH₂-UiO-66(Hf). First-principles electronic structure theory indicates that each of these MOFs has a LUCO position suitable for driving the hydrogen evolution reaction. However, experimentally the visible light photocatalytic activity of NH₂-MIL-125(Ti) is much higher than that of the UiO MOFs. This remarkable difference can be understood in terms of the kinetics of the corresponding photoexcited states. While the LMCT excited state of NH₂-MIL-125(Ti) is stabilized by the formation of Ti³⁺, excitation of NH₂-UiO-66(Zr) and NH₂-UiO-66(Hf) does not promote the formation of corresponding M³⁺ as is evident from the DFT and EPR studies. In contrast to NH₂-MIL-125(Ti), the lowest in energy transitions of NH₂-UiO-66(Zr) and -(Hf) are purely ligand-based and have a short lifetime accounting for the poor catalytic performance. The latter is due to the fact that the d -orbitals of Zr and Hf are too close to the vacuum level (low electron affinity) and thus cannot overlap with the π^* orbital of the ligand despite their geometrical suitability. The influence of structural defects on the photocatalytic activity of the UiO MOFs results in twice higher catalytic rates due to the longer lifetime of the photoexcited states, as suggested by transient absorption spectroscopy.

This work signifies the importance of the identity of orbitals defining the band extrema. The LMCT excited state of NH₂-MIL-125(Ti) has a superior lifetime as compared to the organic-based states of the UiOs. The design of MOF for photocatalysts should focus on sufficiently long excited state lifetimes, thus improving catalytic activity.

References

1. T. Rodenas, I. Luz, G. Prieto, B. Seoane, H. Miro, A. Corma, F. Kapteijn, F. X. Llabrés i Xamena and J. Gascon, *Nat Mater*, 2015, **14**, 48-55.
2. B. Seoane, J. Coronas, I. Gascon, M. E. Benavides, O. Karvan, J. Caro, F. Kapteijn and J. Gascon, *Chemical Society Reviews*, 2015, **44**, 2421-2454.
3. J. Gascon, A. Corma, F. Kapteijn and F. X. Llabrés i Xamena, *ACS Catalysis*, 2014, **4**, 361-378.
4. K. T. Butler, C. H. Hendon and A. Walsh, *ACS Applied Materials & Interfaces*, 2014, **6**, 22044-22050.
5. F. X. Llabrés i Xamena, A. Corma and H. Garcia, *The Journal of Physical Chemistry C*, 2006, **111**, 80-85.
6. M. Alvaro, E. Carbonell, B. Ferrer, F. X. Llabrés I Xamena and H. Garcia, *Chemistry - A European Journal*, 2007, **13**, 5106-5112.
7. M. A. Nasalevich, M. G. Goesten, T. J. Savenije, F. Kapteijn and J. Gascon, *Chemical Communications*, 2013, **49**, 10575-10577.
8. T. Zhang and W. Lin, *Chemical Society Reviews*, 2014, **43**, 5982-5993.
9. J. Long, S. Wang, Z. Ding, S. Wang, Y. Zhou, L. Huang and X. Wang, *Chemical Communications*, 2012, **48**, 11656-11658.
10. C.-C. Wang, J.-R. Li, X.-L. Lv, Y.-Q. Zhang and G. Guo, *Energy & Environmental Science*, 2014, **7**, 2831-2867.
11. L. Shen, S. Liang, W. Wu, R. Liang and L. Wu, *Dalton Transactions*, 2013, **42**, 13649-13657.
12. J. L. Wang, C. Wang and W. Lin, *ACS Catalysis*, 2012, **2**, 2630-2640.
13. M. Dan-Hardi, C. Serre, T. Frot, L. Rozes, G. Maurin, C. Sanchez and G. Férey, *Journal of the American Chemical Society*, 2009, **131**, 10857-10859.
14. J. H. Cavka, S. Jakobsen, U. Olsbye, N. Guillou, C. Lamberti, S. Bordiga and K. P. Lillerud, *Journal of the American Chemical Society*, 2008, **130**, 13850-13851.
15. Y. Fu, D. Sun, Y. Chen, R. Huang, Z. Ding, X. Fu and Z. Li, *Angewandte Chemie - International Edition*, 2012, **51**, 3364-3367.
16. M. Nasalevich, M. A. van der Veen, F. Kapteijn and J. Gascon, *CrystEngComm*, 2014, DOI: 10.1039/C4CE00032C.

17. Y. Horiuchi, T. Toyao, M. Saito, K. Mochizuki, M. Iwata, H. Higashimura, M. Anpo and M. Matsuoka, *Journal of Physical Chemistry C*, 2012, **116**, 20848-20853.
18. M. A. Nasalevich, R. Becker, E. V. Ramos-Fernandez, S. Castellanos, S. L. Veber, M. V. Fedin, F. Kapteijn, J. N. H. Reek, J. I. van der Vlugt and J. Gascon, *Energy & Environmental Science*, 2015, **8**, 364-375.
19. M. De Miguel, F. Ragon, T. Devic, C. Serre, P. Horcajada and H. García, *ChemPhysChem*, 2012, **13**, 3651-3654.
20. A. Walsh and C. R. A. Catlow, *ChemPhysChem*, 2010, **11**, 2341-2344.
21. C. H. Hendon, D. Tiana, M. Fontecave, C. Sanchez, L. D'arras, C. Sassoie, L. Rozes, C. Mellot-Draznieks and A. Walsh, *Journal of the American Chemical Society*, 2013, DOI: 10.1021/ja405350u.
22. C. G. Silva, I. Luz, F. X. Llabrés I Xamena, A. Corma and H. García, *Chemistry - A European Journal*, 2010, **16**, 11133-11138.
23. D. Sun, Y. Fu, W. Liu, L. Ye, D. Wang, L. Yang, X. Fu and Z. Li, *Chemistry – A European Journal*, 2013, **19**, 14279-14285.
24. D. Sun, W. Liu, M. Qiu, Y. Zhang and Z. Li, *Chemical Communications*, 2015, **51**, 2056-2059.
25. K. T. Butler, C. H. Hendon and A. Walsh, *Journal of the American Chemical Society*, 2014, **136**, 2703-2706.
26. L. P. Hammett, *Journal of the American Chemical Society*, 1937, **59**, 96-103.
27. M. A. Moreira, J. C. Santos, A. F. P. Ferreira, J. M. Loureiro, F. Ragon, P. Horcajada, P. G. Yot, C. Serre and A. E. Rodrigues, *Microporous and Mesoporous Materials*, 2012, **158**, 229-234.
28. M. J. Katz, Z. J. Brown, Y. J. Colon, P. W. Siu, K. A. Scheidt, R. Q. Snurr, J. T. Hupp and O. K. Farha, *Chemical Communications*, 2013, **49**, 9449-9451.
29. G. C. Shearer, S. Chavan, J. Ethiraj, J. G. Vitillo, S. Svelle, U. Olsbye, C. Lamberti, S. Bordiga and K. P. Lillerud, *Chemistry of Materials*, 2014, **26**, 4068-4071.
30. M. F. De Lange, T. J. H. Vlugt, J. Gascon and F. Kapteijn, *Microporous and Mesoporous Materials*, 2014, **200**, 199-215.
31. I. H. M. van Stokkum, D. S. Larsen and R. van Grondelle, *Biochimica et Biophysica Acta (BBA) - Bioenergetics*, 2004, **1658**, 262.
32. J. Hunger, T. Sonnleitner, L. Liu, R. Buchner, M. Bonn and H. J. Bakker, *The Journal of Physical Chemistry Letters*, 2012, **3**, 3034-3038.
33. G. Kresse and J. Furthmüller, *Physical Review B*, 1996, **54**, 11169-11186.
34. K. Momma and F. Izumi, *Journal of Applied Crystallography*, 2011, **44**, 1272-1276.
35. H. Furukawa, F. Gándara, Y.-B. Zhang, J. Jiang, W. L. Queen, M. R. Hudson and O. M. Yaghi, *Journal of the American Chemical Society*, 2014, **136**, 4369-4381.
36. P. Ghosh, Y. J. Colon and R. Q. Snurr, *Chemical Communications*, 2014, **50**, 11329-11331.
37. H. Wu, Y. S. Chua, V. Krungleviciute, M. Tyagi, P. Chen, T. Yildirim and W. Zhou, *Journal of the American Chemical Society*, 2013, **135**, 10525-10532.
38. C. A. Trickett, K. J. Gagnon, S. Lee, F. Gándara, H.-B. Bürgi and O. M. Yaghi, *Angewandte Chemie International Edition*, 2015, DOI: 10.1002/anie.201505461, n/a-n/a.
39. M. J. Cliffe, W. Wan, X. Zou, P. A. Chater, A. K. Kleppe, M. G. Tucker, H. Wilhelm, N. P. Funnell, F.-X. Coudert and A. L. Goodwin, *Nat Commun*, 2014, **5**.
40. M. J. Cliffe, J. A. Hill, C. A. Murray, F.-X. Coudert and A. L. Goodwin, *Physical Chemistry Chemical Physics*, 2015, **17**, 11586-11592.
41. M. A. Nasalevich, M. G. Goesten, T. J. Savenije, F. Kapteijn and J. Gascon, *Chemical Communications*, 2015, **51**, 961-962.
42. C. H. Hendon and A. Walsh, *Chemical Science*, 2015, **6**, 3674-3683.

Appendix 2

Transient absorption spectroscopy

When only single photon absorption processes occur, a linear correlation between the pump power and the change in absorption should be registered. In order to determine whether multiple photons absorption processes are being observed, a region of the data is selected for every measurement. This region contains the data at the highest intensity; it is averaged for each pump power and then fitted with a linear fit. The resulting relations are referred to as linearity checks and are given below alongside the evolution-associated difference spectra (EADS) and characteristic decays of photoexcited states.

We model the experimental data using a four-state kinetic model. In this model the excited state population decays with a characteristic time constant, τ_1 . This relaxation leads to a transient population of an intermediate state (0^*), which relaxes with a characteristic time τ_2 to lower energy levels ($0'$). Further thermalization dynamics with an equilibration time τ_3 result in the fully equilibrated state $0''$ (ground state).³²

$$dN(t)/dt = -N(t)/\tau_1 \quad (\text{eq. 9})$$

$$dN^*(t)/dt = +N(t)/\tau_1 - N^*(t)/\tau_2 \quad (\text{eq. 10})$$

$$dN'(t)/dt = +N^*(t)/\tau_2 - N'(t)/\tau_3 \quad (\text{eq. 11})$$

$$dN''(t)/dt = +N'(t)/\tau_3 \quad (\text{eq. 12})$$

NH₂-MIL-125(Ti)

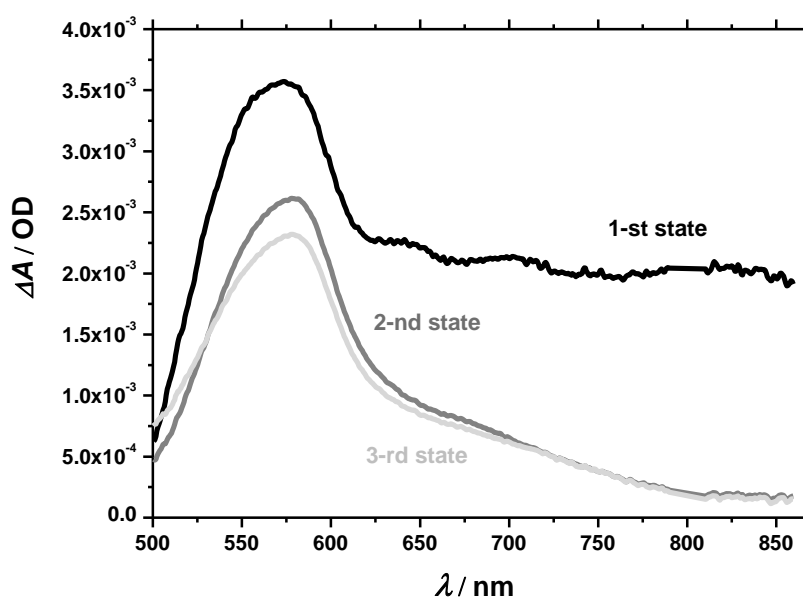


Figure A3.14. Evolution-associated difference spectra of *NH₂-MIL-125(Ti)* upon 400 nm excitation. The kinetic model exploits three transient consecutive states followed by a forced decay to the ground state.

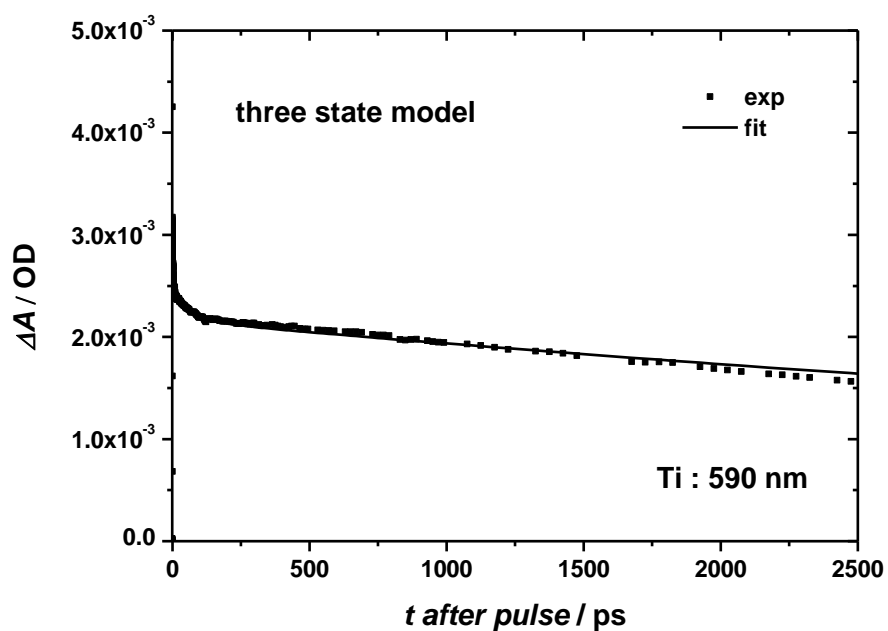


Figure A3.15. Representative time traces of NH₂-MIL-125 recorded at 590 nm upon excitation at 400 nm with excitation power of 10.1 mW: experimental data (*squares*) and fitting (*black line*). The kinetic model exploits three transient consecutive states followed by a decay to the ground state.

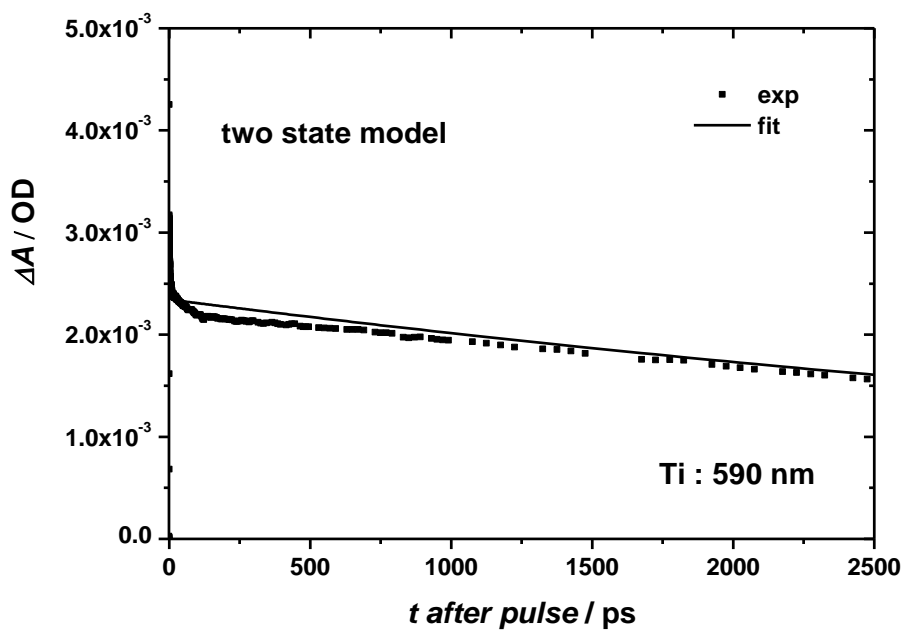


Figure A3.16. Representative time traces of NH₂-MIL-125(Ti) recorded at 590 nm upon excitation at 400 nm with excitation power of 10.1 mW: experimental data (*squares*) and fitting (*black line*). The fit is obtained by using a two-state model that is forced to decay to the ground state. The figure highlights the necessity of employing the three-state model.

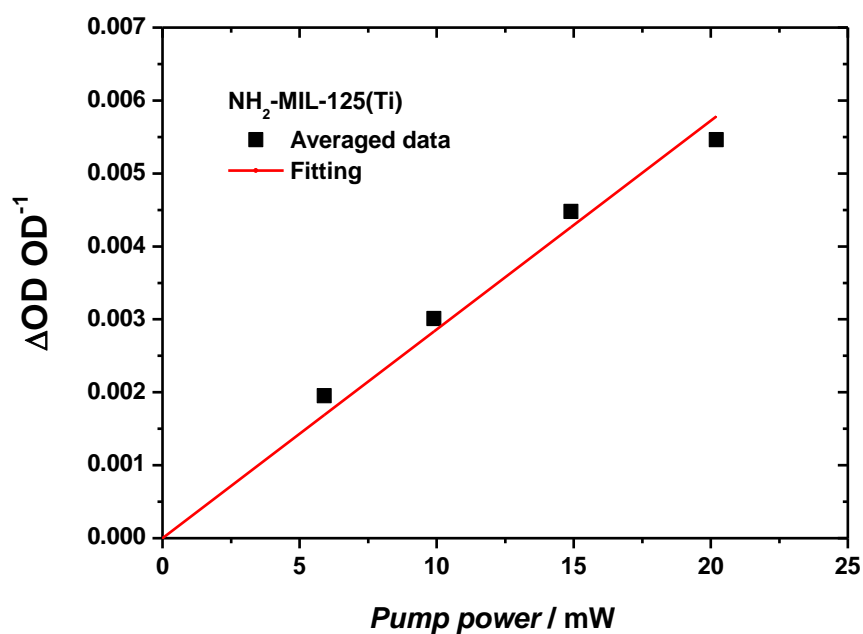


Figure A3.17. Linearity check for NH_2 -MIL-125(Ti).

NH_2 -UiO-66(Zr) 'ideal'

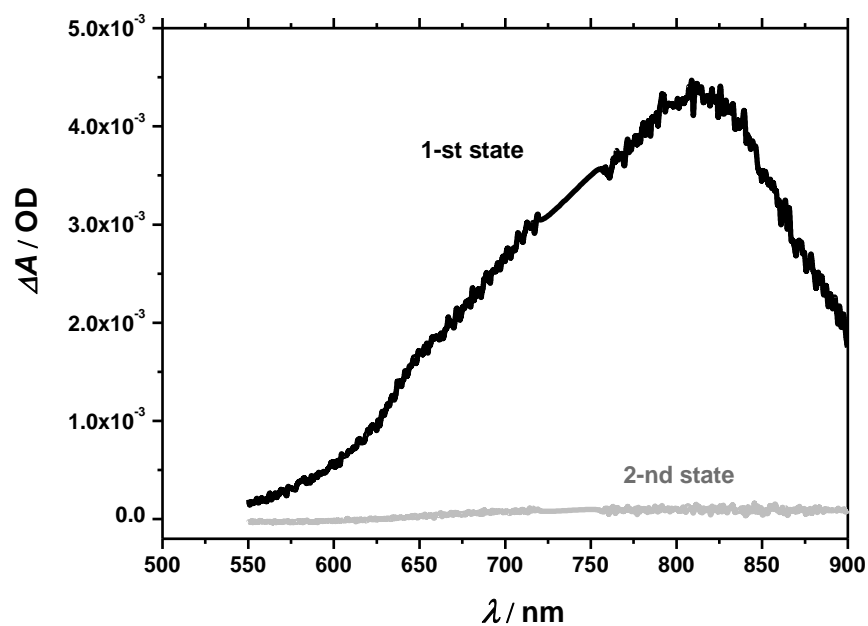


Figure A3.18. Evolution-associated difference spectra of NH_2 -UiO-66(Zr) 'ideal' upon 370 nm excitation. The kinetic model exploits two transient consecutive states. As the 2-nd transient state is practically 0, it was assumed to be the ground state, no extra constraints were added.

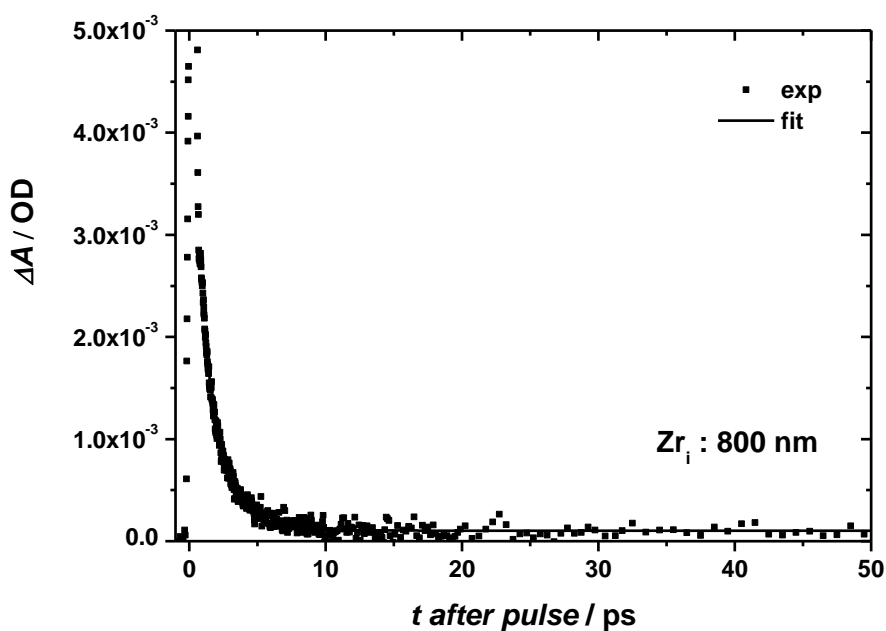


Figure A3.19. Representative time traces of $\text{NH}_2\text{-UiO-66(Zr)}$ 'ideal' recorded at 800 nm upon excitation at 370 nm with excitation power of 26.9 mW: experimental data (*squares*) and fitting (*black line*). The kinetic model exploits two transient consecutive states. As the 2-nd transient state is practically 0, it was assumed to be the ground state, no extra constraints added.

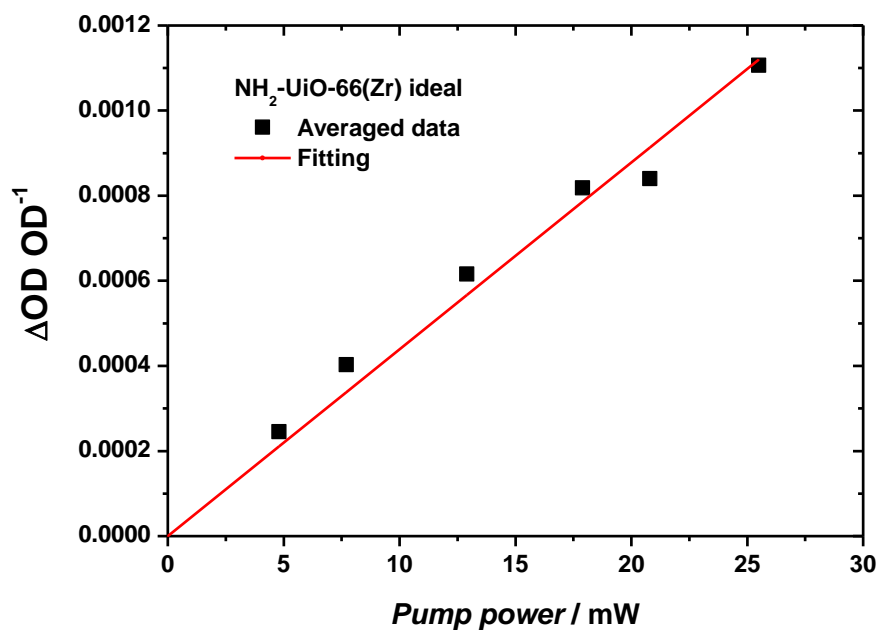


Figure A3.20. Linearity check for $\text{NH}_2\text{-UiO-66(Zr)}$ 'ideal'.

NH₂-UiO-66(Hf) 'ideal'

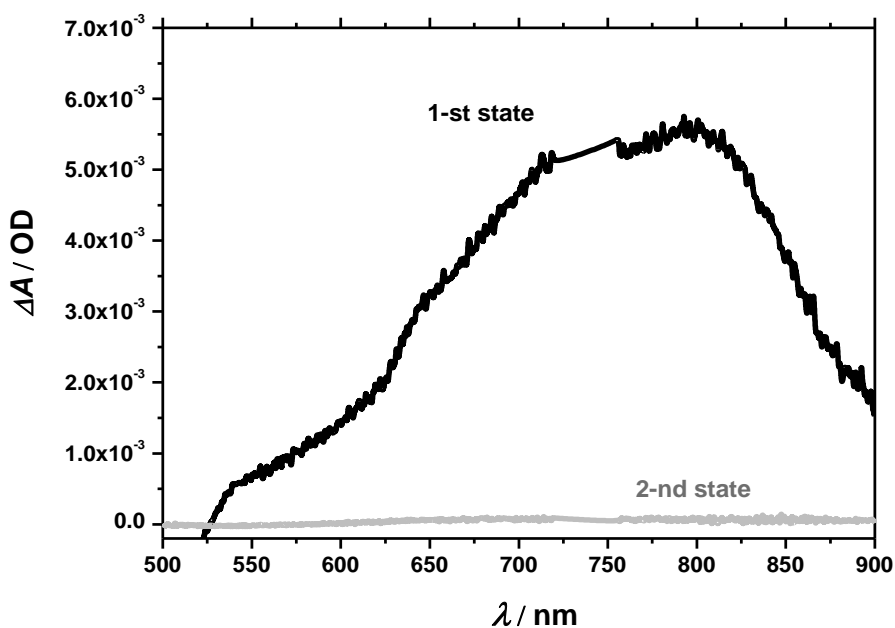


Figure A3.21. Evolution-associated difference spectra of NH₂-UiO-66(Hf) 'ideal' upon 370 nm excitation. The kinetic model exploits two transient consecutive states. As the 2-nd transient state is practically 0, it was assumed to be the ground state, no extra constraints added.

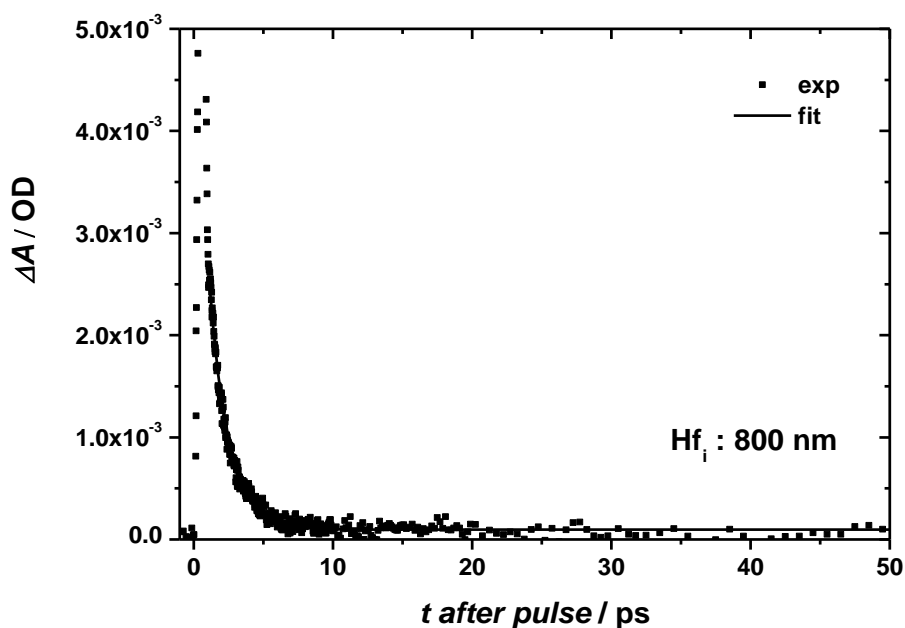


Figure A3.22. Representative time traces of NH₂-UiO-66(Hf) 'ideal' recorded at 800 nm upon excitation at 370 nm with excitation power of 26.3 mW: experimental data (*squares*) and fitting (*black line*). The kinetic model exploits two transient consecutive states. As the 2-nd transient state is practically 0, it was assumed to be the ground state, no extra constraints were added.

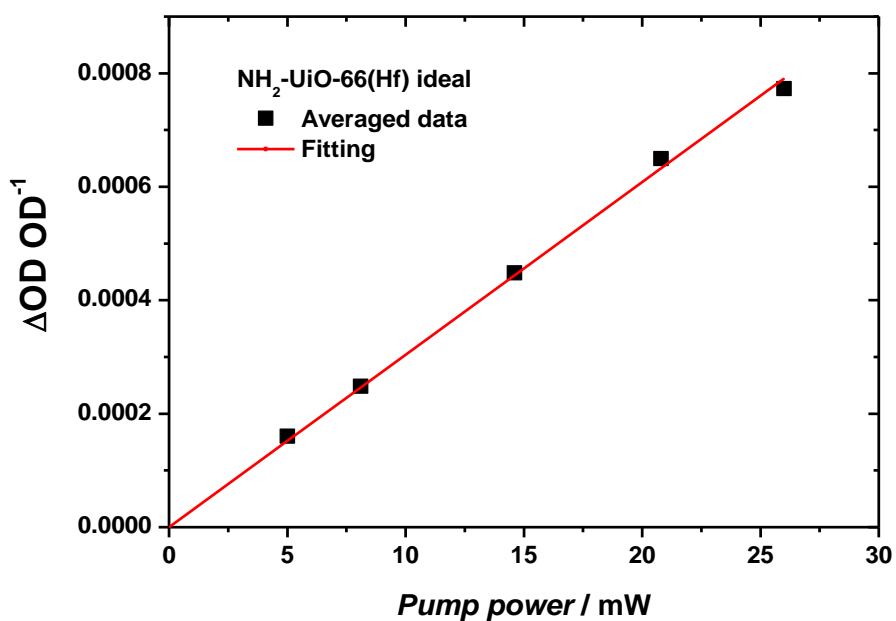


Figure A3.23. Linearity check for $\text{NH}_2\text{-UiO-66(Hf)}$ 'ideal'.

$\text{NH}_2\text{-UiO-66(Zr)}$ 'defective'

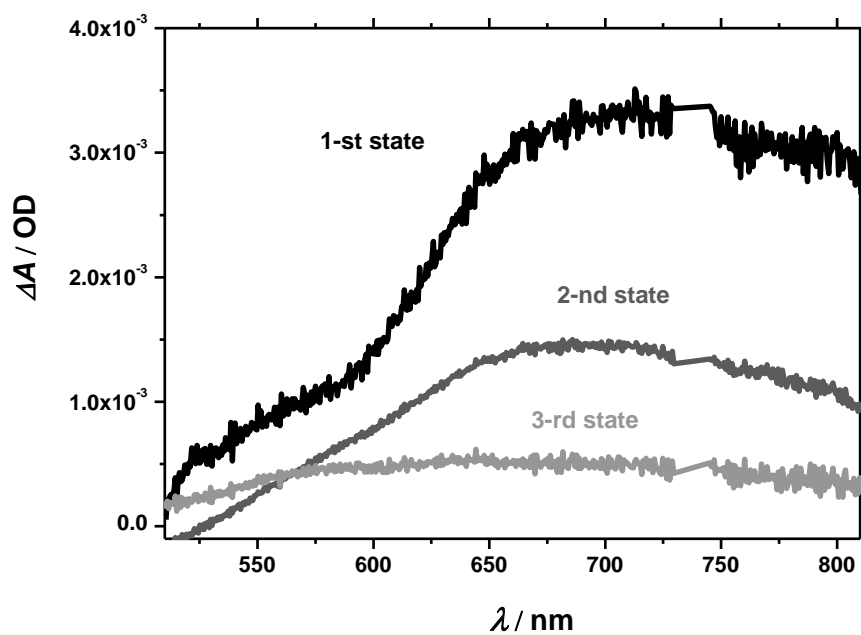


Figure A3.24. Evolution-associated difference spectra of $\text{NH}_2\text{-UiO-66(Zr)}$ 'defective' upon 370 nm excitation. The kinetic model exploits three transient consecutive states followed by a forced decay to the ground state.

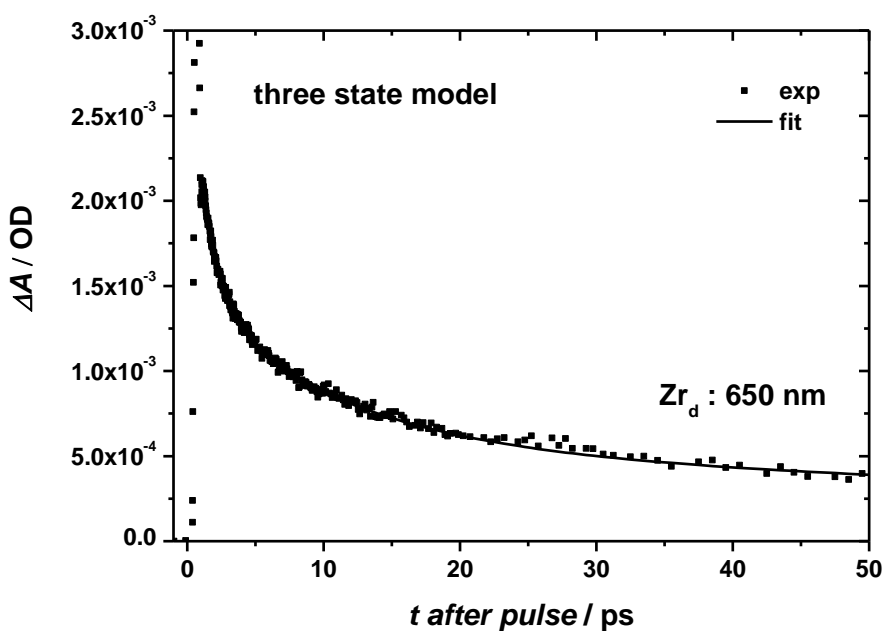


Figure A3.25. Representative time traces of NH₂-UiO-66(Zr) 'defective' recorded at 650 nm upon excitation at 370 nm with excitation power of 10.8 mW: experimental data (*squares*) and fitting (*black line*). The kinetic model exploits three transient consecutive states followed by a forced decay to the ground state.

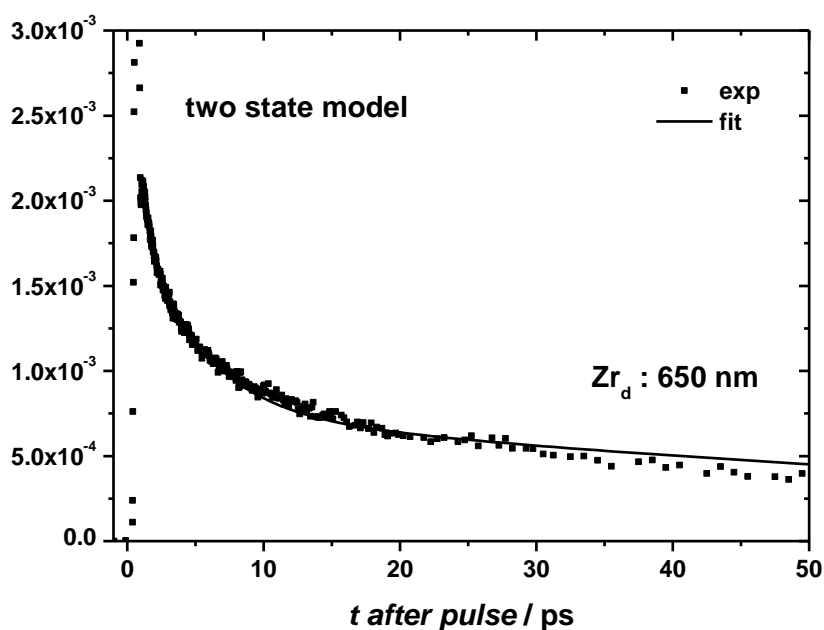


Figure A3.26. Representative time traces of NH₂-UiO-66(Zr) 'defective' recorded at 650 nm upon excitation at 370 nm with excitation power of 10.8 mW: experimental data (*squares*) and fitting (*black line*). The kinetic model exploits two transient consecutive states followed by a forced decay to the ground state. The figure highlights the necessity of employing the three-state model.

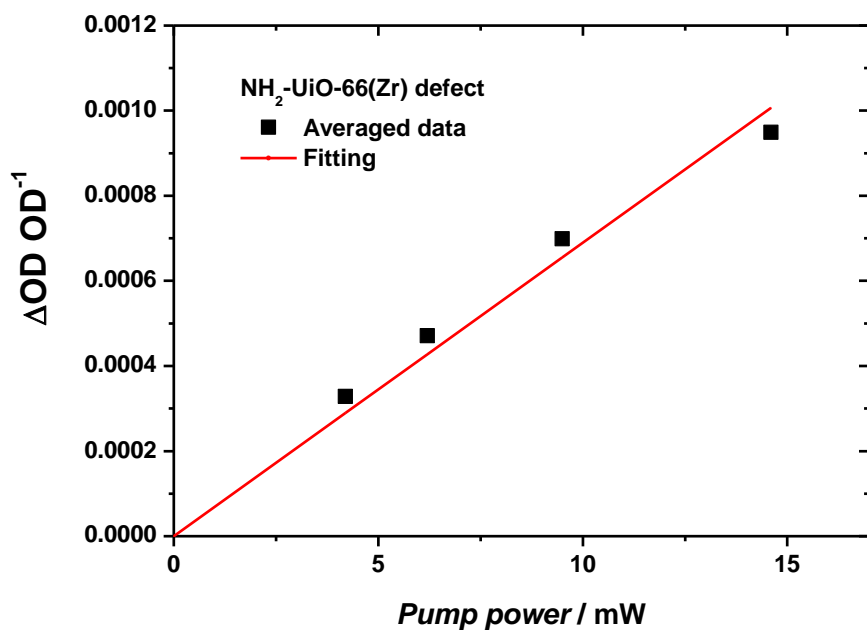


Figure A3.27. Linearity check for NH_2 -UiO-66(Zr) 'defective'.

NH_2 -UiO-66(Hf) 'defective'

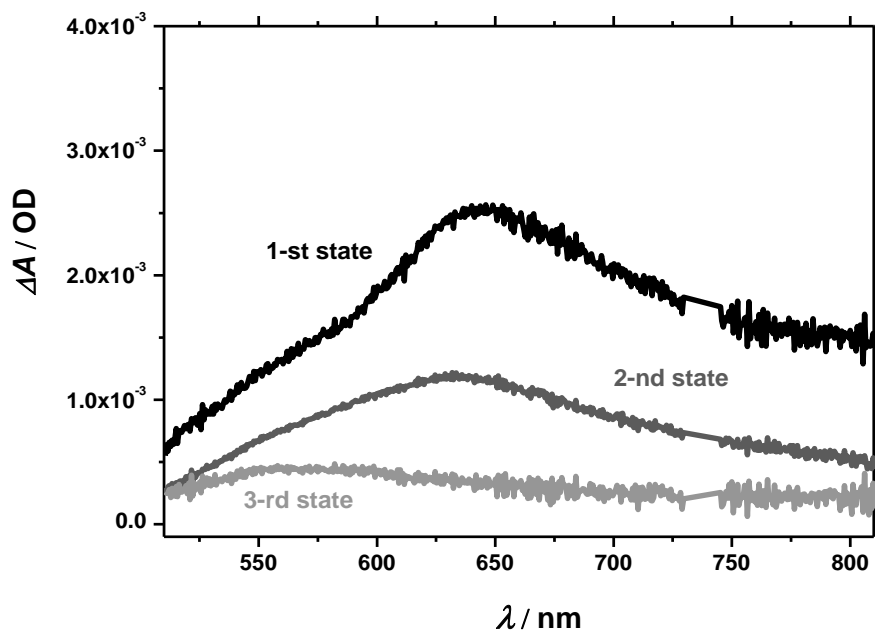


Figure A3.28. Evolution-associated difference spectra of NH_2 -UiO-66(Hf) 'defective' upon 370 nm excitation. The kinetic model exploits three transient consecutive states followed by a forced decay to the ground state.

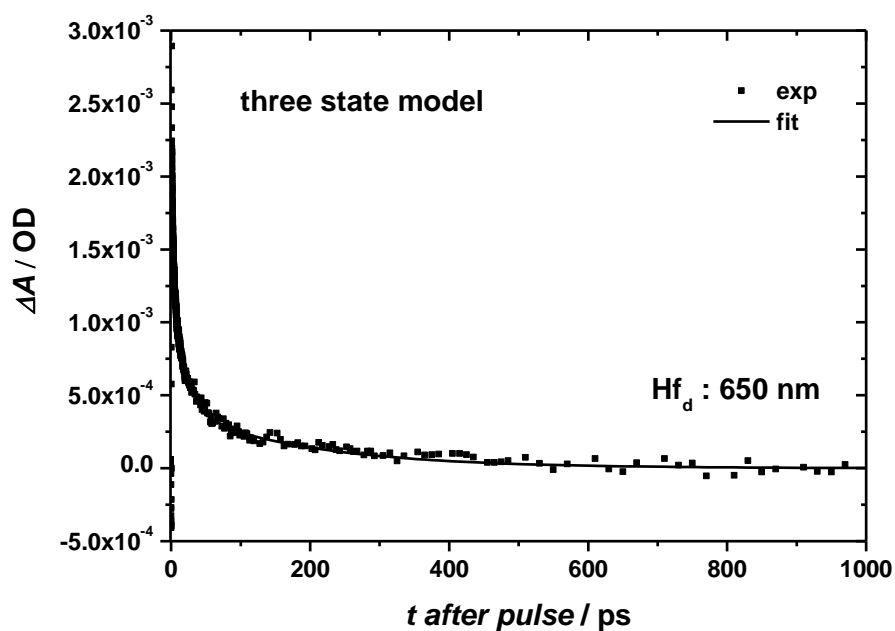


Figure A3.29. Representative time traces of NH₂-UiO-66(Hf) 'defective' recorded at 650 nm upon excitation at 370 nm with excitation power of 10.8 mW: experimental data (*squares*) and fitting (*black line*). The kinetic model exploits three transient consecutive states followed by a forced decay to the ground state.

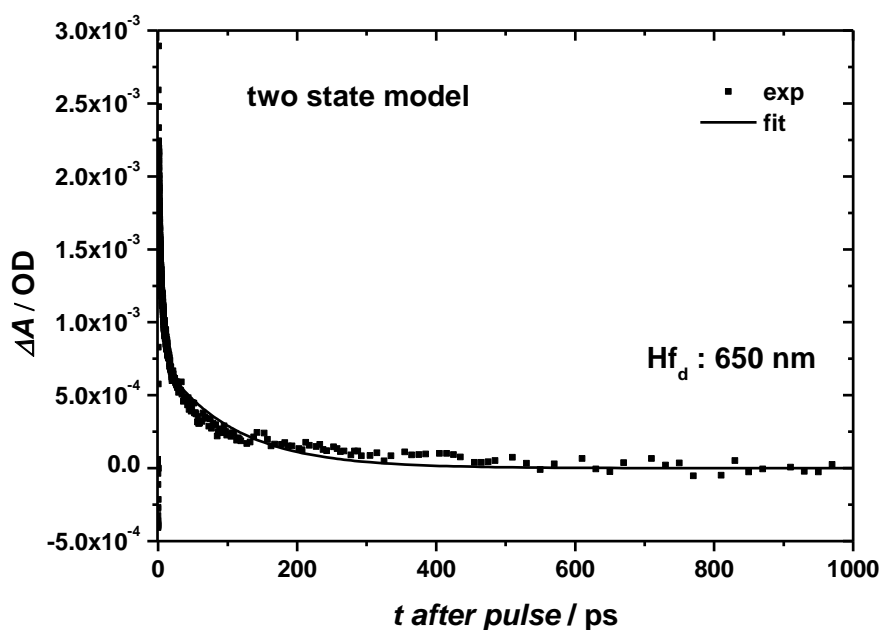


Figure A3.30. Representative time traces of NH₂-UiO-66(Hf) 'defective' recorded at 650 nm upon excitation at 370 nm with excitation power of 10.8 mW: experimental data (*squares*) and fitting (*black line*). The kinetic model exploits two transient consecutive states followed by a forced decay to the ground state. The figure highlights the necessity of employing the three-state model.

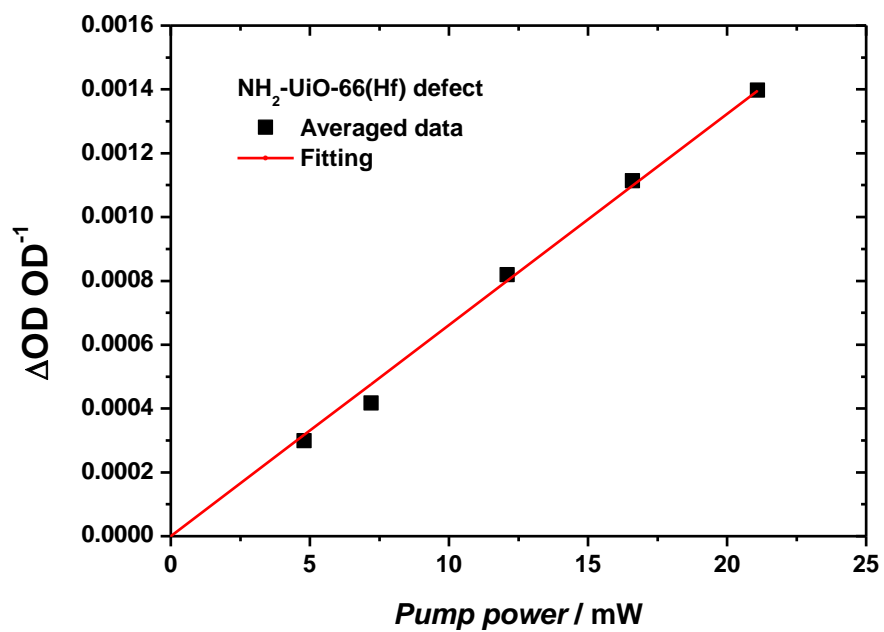


Figure A3.31. Linearity check for NH₂-UiO-66(Hf) 'defective'

Revisiting the incorporation of Ti(IV) in UiO-type metal-organic frameworks: metal exchange versus grafting and their implications for photocatalysis

The inclusion of Ti(IV) in water-stable metal-organic frameworks has been proposed as a strategy for the generation of high surface area heterogeneous photocatalysts, with UiO-66 being a promising candidate. We find that the site of Ti(IV) binding is at linker defect sites and not incorporated into the inorganic secondary building unit through metal exchange. We also demonstrate that the choice of the titanium source is critical in the generation of an active hydrogen evolution catalyst. Furthermore, we interpret the observed activity using density functional theory calculations. This also enables rational design of future Ti(IV) coordination environments in MOF catalysts.

This chapter is based on the following publication:

Revisiting the incorporation of Ti(IV) in UiO-type metal-organic frameworks: metal exchange versus grafting and their implications for photocatalysis

J. G. Santaclara, A. I. Olivos-Suarez, A. Gonzalez-Nelson, D. Osadchii, M. A. Nasalevich, M. A. van der Veen, F. Kapteijn, A. M. Sheveleva, S. L. Veber, M. V. Fedin, A. T. Murray, C. H. Hendon, A. Walsh and J. Gascon (submitted)

Introduction

The generation of hydrogen from water (hydrogen evolution reaction – HER) mediated by sunlight is a key challenge in the design of new energy conversion paradigms.¹ While there are many classes of materials that will promote this reaction, metal-organic frameworks (MOFs) have emerged as promising platforms, owing to their high surface area, structural diversity and late-stage tunability.² However, most MOFs suffer from hydrolytic instability, limiting their application in aqueous HER photocatalytic systems.^{3, 4} MOFs of the UiO series possess good water and thermal stability and opportunities for post-synthetic modification.^{5, 6}

Common strategies for functionalisation of Zr-UiO-type materials include linker modification and metal incorporation.⁷⁻⁹ The former has been extensively studied in both UiO- and MIL-125-type materials through utilisation of functionalised linkers.¹⁰⁻¹² For example, amination of the terephthalic acid linker in MIL-125 has been shown to close the band gap, redshifting from the UV and thus enabling visible light photocatalysis. In the case of UiO-66, the inclusion of photocatalytic moieties by addition of Ti(IV) has been extensively studied because of its photoaccessible unoccupied Ti(III) state, but nevertheless the structural characterisation of these materials remains largely unknown.¹³⁻¹⁹

The two hypotheses for how incorporation of Ti into UiO-66 occurs are either through metal exchange into the inorganic secondary building unit (SBU), or grafting of the Ti(IV) onto the surface of this node at a linker vacancy site (Figure 1).²⁰ Metal exchange has been attempted primarily with $\text{TiCl}_4 \cdot 2\text{THF}$ as a Ti(IV) source, but the nature of this exchange is inconclusive.^{9, 14, 21-24}

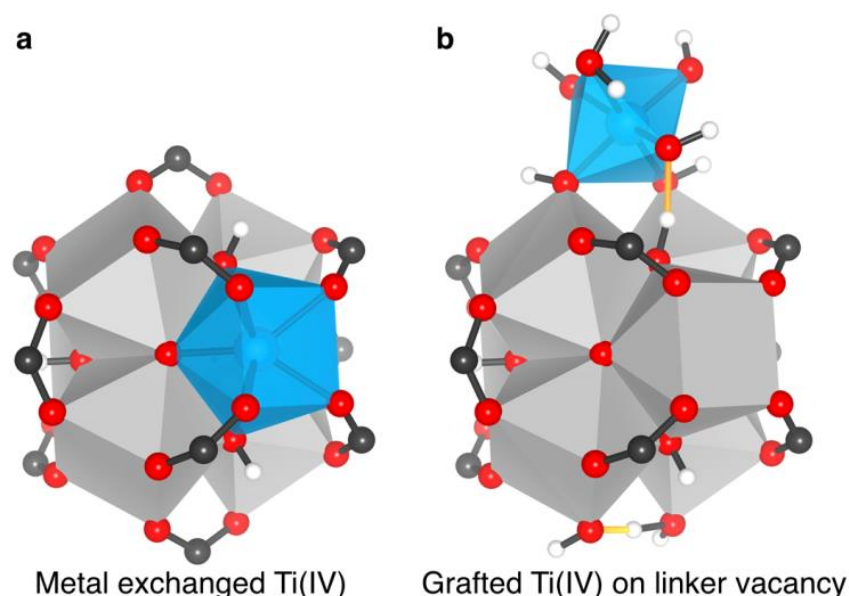


Figure 1. Proposed coordination sites of Ti in UiO-type materials. (a) The inclusion of Ti(IV) in the cluster through metal exchange. (b) The appendage of Ti(IV) to the surface of the cluster at a linker vacancy defect site.

A major impediment to the understanding of metal inclusion in UiO-type materials, either as ion exchange or metal appendage, is that, while Ti(IV) can also be conjectured to occupy linker vacancy sites, until recently the nature of these vacancies was poorly understood.^{25, 26} However, recent advances in the characterisation of UiO defect chemistry have revealed up to 33% linker vacancies,²⁷⁻³³ and the nature of these vacancies has been systematically explored in the related NU-1000 MOF and the MOF-801 series.^{20, 34, 35}

Experimental

Materials and reagents

All chemicals were purchased from Sigma Aldrich and used without further purification. Methanol and dimethylformamide (DMF) were additionally dried over molecular sieve (zeolite 5Å).

Synthesis

NH₂-UiO-66(Zr) (1). The parent NH₂-UiO-66(Zr) was synthesised by a protocol reported elsewhere,³⁶ which is an adaptation of the method reported by the group of Lillerud for the synthesis of non-functionalised “ideal” UiO-66.²⁷ “Ideal” NH₂-UiO-66(Zr) was synthesised by first mixing 24.4 mL DMF with 0.7 mL 37 wt% HCl. 1.467 g 2-Aminoterephthalic acid was added and sonicated for 10 min, followed by the addition of 0.945 g ZrCl₄. The mixture was heated at 220 °C for 20 h in an autoclave equipped with a 30 mL Teflon liner. The resulting pale yellow powder was filtered and suspended with fresh DMF in the autoclave to be washed at 100 °C for 10 h to remove possible free linker molecules from inside the pores. This DMF washing was performed twice. Subsequently, the solids were filtered and two rounds of methanol washing at 80°C for 10 h followed. Lastly, the MOF was dried for 4 h under air at 160°C in order to remove residual solvent from the pores.

Synthesis of 1’. The Ti(IV) precursor TiCl₄(THF)₂ was used, following a post-synthetic metal exchange method reported by Cohen *et al.*¹³ The procedure was scaled 8-fold up. Under inert atmosphere, 0.267 g TiCl₄(THF)₂ were dissolved in 16 mL DMF in an autoclave equipped with a clean 30 mL Teflon liner. 0.234 g dry NH₂-UiO-66(Zr) were then added. The mixture was incubated at 85°C for 5 days. After cooling, solids were isolated by centrifugation and washed with DMF (3x10 mL), followed by soaking in MeOH for 3 days at room temperature, replacing the solvent every 24 h. The washed solids were isolated by centrifugation and then dried under air at 160°C for 4 h.

Synthesis of 2. Ti(O^tBu)₄ was used, following an adapted procedure reported by Wang *et al.*¹⁶ 0.160 g NH₂-UiO-66(Zr) were suspended in 10 mL DMF inside an autoclave equipped with a clean 30 mL Teflon liner. Then 0.09 mL Ti(O^tBu)₄ were added, and the mixture was incubated at 100°C for 24 h. The solids were subsequently isolated by centrifugation and washed with DMF (3x10 mL), followed by

soaking in MeOH for 3 days at RT, replacing the solvent every 24 h. Finally, the powder was filtered and dried at 160°C for 4 h.

Characterization and methods

Powder X-Ray diffraction patterns were recorded using Bruker-AXS D5005 with CoK α radiation.

N₂-physisorption measurements were performed in a Tristar II 3020 Micromeritics unit at liquid nitrogen temperature (77 K). Prior to the experiment the samples were degassed for 16 h at 150 °C under vacuum. The BET areas were calculated using intervals allowing positive BET constants. The total pore volumes were calculated at 0.9 relative pressure.

Scanning electron microscopy (SEM). Scanning electron microscopy (SEM) was carried out using a JEOL JSM-6010LA InTouchScope microscope.

Thermogravimetric analysis was performed by means of Mettler Toledo TGA/SDTA851e, under an air flow of 60 ml min⁻¹ at heating rates of 10 K min⁻¹ up to 1073 K.

Diffuse Reflectance Infrared Fourier Transform Spectroscopy (DRIFTS) studies were performed with a Nicolet 8700, using a deuterated triglycine sulfate (DTGS) detector. KBr was used as a blank, on top of which a small amount of sample is placed (~1 mg). All spectra were obtained under He flow at 30–50 °C, preceded by an initial heating to 150 °C for 30 min to remove the majority of adsorbed water.

Diffuse reflectance UV/Vis spectra were collected using a Perkin–Elmer Lambda 900 spectrophotometer equipped with an integrating sphere (“Labsphere”) in the 200–800 nm range. BaSO₄ was used as a white standard.

EPR spectroscopy. CW and pulse EPR spectra were measured at X/Q-band (9/34 GHz) using commercial EPR spectrometer Bruker Elexsys E580 equipped with Oxford Instruments temperature control system (ER 4112HV with helium cryostat ER 4118CF-O). For X-band measurements standard Bruker MD-5 resonator was used. Modulation amplitude was 0.3 mT, mw frequency ~9.7 GHz, mw power ~ 6 mW. Transverse relaxation (phase memory time) measurements were done using two-pulse echo sequence ($\pi/2$ - τ - π - τ -echo) by incrementing time delay τ . Longitudinal relaxation measurements were done using inversion-recovery sequence (π - T - $\pi/2$ - τ - π - τ -echo) by incrementing time delay T and keeping τ constant. The integration window was 60 ns. The microwave pulse lengths were 12 and 24 ns, with the microwave power adjusted to provide $\pi/2$ and π -pulses, respectively. In all cases the relaxation time measurements were taken at global maximum of Ti(III) spectrum. For Q-band measurements Bruker ER5106QT resonator was used. Modulation amplitude was 2 mT, mw frequency ~33.5 GHz, mw power ~ 2 mW. All simulations were done using the EasySpin toolbox for Matlab.7 The sample was suspended in a mixture of acetonitrile, triethylamine and water (5 : 1 : 0.1 v/v), deoxygenated, sealed off in a quartz tube and exposed to light illumination. Light excitation was performed

using diode light with 360 nm wavelength and incident light power ~30 mW. Sample was exposed for roughly 4 minutes with continuous stirring.

X- and Q-band EPR spectra of photoinduced Ti(III) signals in three studied samples – NH₂-UiO-66(Zr) treated with Ti(O^tBu)₄, with TiCl₄, and of NH₂-MIL-125(Ti) for comparison. All compounds were studied in the reaction mixture of CH₃CN/Et₃N/H₂O, irradiated for ca. 4 minutes (experimentally adjusted to reach maximum Ti(III) generation possible for each compound), then shock-frozen in liquid nitrogen, placed into the probe of EPR spectrometer at 80 K and measured. In all cases, we attempted to simulate the spectra of each compound in two microwave bands using the same set of parameters. For *g*-tensors we have obtained reasonably close values $g = [1.970 \ 1.935 \ 1.905]$ for NH₂-UiO-66(Zr) treated with Ti(O^tBu)₄, $g = [1.976 \ 1.945 \ 1.925]$ for NH₂-UiO-66(Zr) treated with TiCl₄, and $g = [1.965 \ 1.945 \ 1.880]$ for NH₂-MIL-125(Ti). In all cases we could not closely reproduce the high-field shoulder of the spectrum showing the strongest broadening; note that similar problem was addressed in other EPR studies on Ti(III) previously.³⁷

Femtosecond Transient Absorption Spectroscopy. Samples for visible (Vis)-pump visible-probe measurements were excited using 180 fs pulses at 400 nm generated in a YKGBW oscillator (Light Conversion, Pharos SP) at 1028 nm through nonlinear frequency mixing in an OPA and second harmonics module (Light Conversion, Orpheus). A small fraction of the 1028 nm fundamental beam was split off to generate the broadband probe spectrum in a sapphire (500 – 1600 nm) crystal. The probe pulse was delayed relative to the pump using a delay stage with maximum delay of 3 ns. The pump and probe pulses overlap on the sample position under an angle of ~8 degrees, after which the probe light is led to a detector suitable for the probe spectrum selected (Ultrafast Systems, Helios). In order to prevent multiple photons absorption processes, the pump fluence was set sufficiently low, allowing us to study single exciton dynamics. In a typical experiment 3 mg of a MOF were dispersed in the solvent (3 mL) and sonicated for 30 min. In order to separate large particles (> 100 nm), the suspension was then centrifuged for 8 min at 10000 rpm. The supernatant was placed in a 2 mm stirred quartz cuvette for the measurements.

Computational Methods

Beginning with the experimentally determined pristine UiO-66(Zr) material the atomic positions and lattice parameters were relaxed using GGA/PBEsol, a 500 eV planewave cut-off, and a Gamma-only k-grid, as implemented in VASP. The convergence criteria were sufficient to 0.005 eV/atom, and the lattice parameters were within 2% of the experimental values. Then, amine substitutions were made to the ligands and a similar optimisation process was performed. The primitive computational cell contains six unique ligands, and one inorganic node. Thus, mono amination results in approximately 16% ligand concentration. More accurate electronic structure was then obtained by performing a single point calculation with the HSE06 functional, using the same basis and *k*-grid. The density of states and

electron energies were then aligned to the vacuum level using an internal vacuum for the reference potential.

Ti inclusion was performed by simple substitution of Zr for Ti, and optimization through a similar procedure as detailed above.

Linker vacancy defects were modelled by removal of a single ligand, resulting in two linker vacancy sites on the inorganic node. The node was charge balanced and passivated using two hydroxides and a H-bonded proton shared between the terminal hydroxides. Appendage of Ti and associated ligands was then performed by manual construction of relevant Ti-coordination environments (-Cl, -OH and -OMe), and for charge neutrality a pendant H₂O. The resultant structures were then optimised using the procedure detailed above.

The pseudo-excited state calculation was performed by forcing the triplet state and performing the same optimization as detailed above.

Photocatalysis

Photocatalytic experiments were carried out using a home-built set-up equipped with a 500 W Xe/Hg lamp (66983, Newport). It consists of a custom-made Pyrex-glass reactor, a CP 9001 gas chromatograph (Chrompack) for analysis of the headspace, a KSLA gas pump and the light source. Light intensity was measured with AvaSpec-3648-2-USB2 (Avantes, the Netherlands). The reactor has a volume of 42.1 mL and is equipped with a water jacket to allow for precise temperature control. The light emitted by the lamp passes through a lens assembly (77330, Newport) focusing the beam on the reactor window, an H₂O filter (61945, Newport) and a 385 nm cut-off optical filter. A KSLA gas pump is applied to ensure a sufficient mixing of gases in the headspace of the reactor and the stainless-steel tubes (2.5 mL·min⁻¹ continuous operation). Every 60 min a probe of the headspace is analysed by the GC. In a typical experiment 30 mg MOF were suspended in 23.5 mL CH₃CN, 4.7 mL TEA and 0.5 mL H₂O. The suspension was then placed in the reactor and deoxygenated by an argon flow of 30 mL·min⁻¹ applied for 30 min at 25 °C. The oxygen concentration was monitored by the GC analysis. Once the system is free of oxygen, the illumination is turned on with concomitant GC analysis (CP 9001 gas chromatograph, Chrompack). All the visible light photocatalytic experiments were carried out at 40 °C as monitored by a thermocouple. The heat was supplied in order to maximize the hydrogen production allowing the detection of H₂ gas in the case of samples with the lowest activity.

External quantum efficiencies (EQE)

External quantum efficiencies of catalysts employed in this work were calculated using the following equation:

$$\Phi = \frac{E(t)}{P(t)} \quad (\text{eq. 1})$$

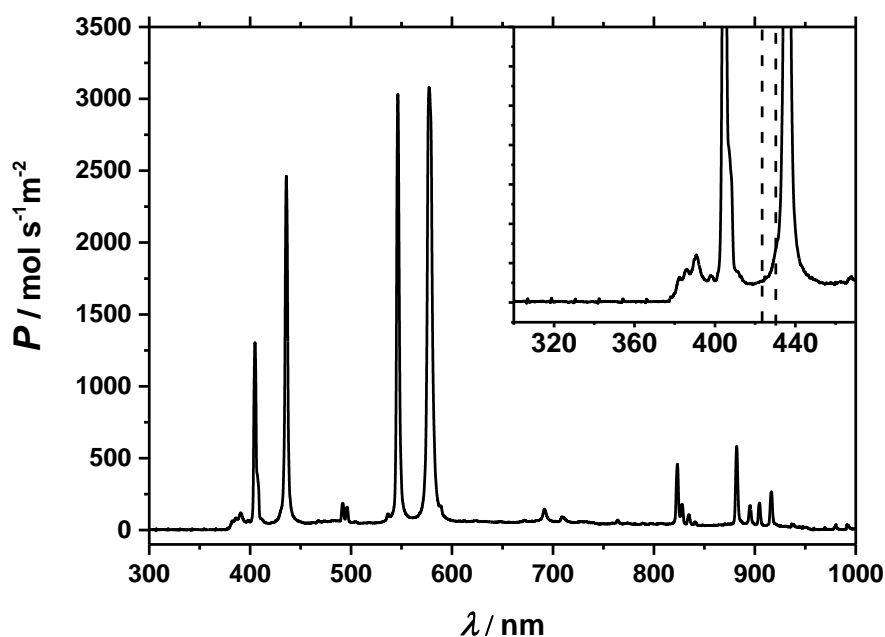


Figure 2. Incident photon flux as a function of wavelength of the 500 W Xe/Hg light source used in this work. The measurement is carried out at the distance of 5.5 cm with the liquid filter on and the 385 nm cut off filter. The inset highlights the spectral region relevant for the hydrogen evolution catalyzed by the MOFs. The dashed lines denote cut-off wavelengths for each catalyst as determined from *Tauc* plot (Figure 8).

where $E(t)$ is the number of electrons carrying out a redox reaction per unit of time; $P(t)$ is a photon flux per unit of time.

The incident photon flux was determined with the help of the photon counter as specified in the experimental part. The spectrum was taken at the conditions of the photocatalytic reactions: 385 nm cut-off filter, liquid filter on, the distance 5.5 cm. Then the curve was integrated with the lower boundary being 350 nm, where the flux goes to 0. The upper boundary for the integration was determined by using the energy gap (from *Tauc* plot). The integration yielded the following photon fluxes: $6839 \mu\text{mol}(\text{photons}) \cdot \text{s}^{-1} \text{m}^{-2}$ for **1** and $7231 \mu\text{mol}(\text{photons}) \cdot \text{s}^{-1} \text{m}^{-2}$ for **1'** and **2**. The spot size of the beam reaching the reactor window was 2.27 cm^2 . Details of the calculation for the case of **1** ($\text{NH}_2\text{-UiO-66}(\text{Zr})$) are given below:

$$P_{Ti}(t) = \int_{350}^{425} P(t, \lambda) d\lambda \cdot 0.000227 \text{ m}^2 = 6839 \mu\text{mol}(\text{photons}) \cdot \text{s}^{-1} \text{m}^{-2} \cdot 0.000227 \text{ m}^2 = \quad (\text{eq. 2})$$

$$= 1.846 \mu\text{mol}(\text{photons}) \cdot \text{s}^{-1}$$

To account for the number of photons required to assemble one hydrogen molecule (**2**) the reaction rates must be multiplied by 2 and converted to appropriate units to obtain the number of electrons:

$$E(t) = r(\text{H}_2) \cdot 2 = 0.017 \mu\text{mol} \cdot \text{h}^{-1} \cdot 2 = 0.034 \mu\text{mol} \cdot \text{h}^{-1} = 9.44 \cdot 10^{-6} \mu\text{mol} \cdot \text{s}^{-1} \quad (\text{eq. 3})$$

$$\Phi_{Ti} = \frac{E(t)}{P(t)} = \frac{9.44 \cdot 10^{-6} \mu\text{mol} \cdot \text{s}^{-1}}{1.846 \mu\text{mol} \cdot \text{s}^{-1}} = 5.12 \cdot 10^{-6} = 0.0005 \% \quad (\text{eq. 4})$$

All the other EQEs were calculated in the same manner.

Results and discussion

An ideal Ti-based photocatalyst features low energy unoccupied Ti(IV) orbitals that allow facile electron occupation of the Ti(III) state upon photoirradiation, and a local electron-rich ligand environment that can transiently stabilise a proton (e.g. a bridging oxo as found in MIL-125, or a pendant hydroxy/alkoxy motif).^{38, 39} DFT calculations are able to systematically elucidate the nature of the frontier bands for different Ti coordination environments in UiO-66. The UiO-66 material's frontier orbitals are defined by a ligand-ligand transition (Figure 3).⁴⁰ Amination of the linker (*i.e.* NH₂-UiO-66(Zr), **1**) yields an occupied midgap state, albeit still with a ligand-based transition (Figure 3).³⁶ We then investigated the energies of Ti both in the cluster (metal exchange) and on a defect site (metal appendage), in both the aminated and native frameworks. When Ti is incorporated in the cluster, the valence bands are unaltered and the conduction bands do not feature Ti orbitals at the frontier; rather, Ti orbitals are found at marginally higher energies but nevertheless should be

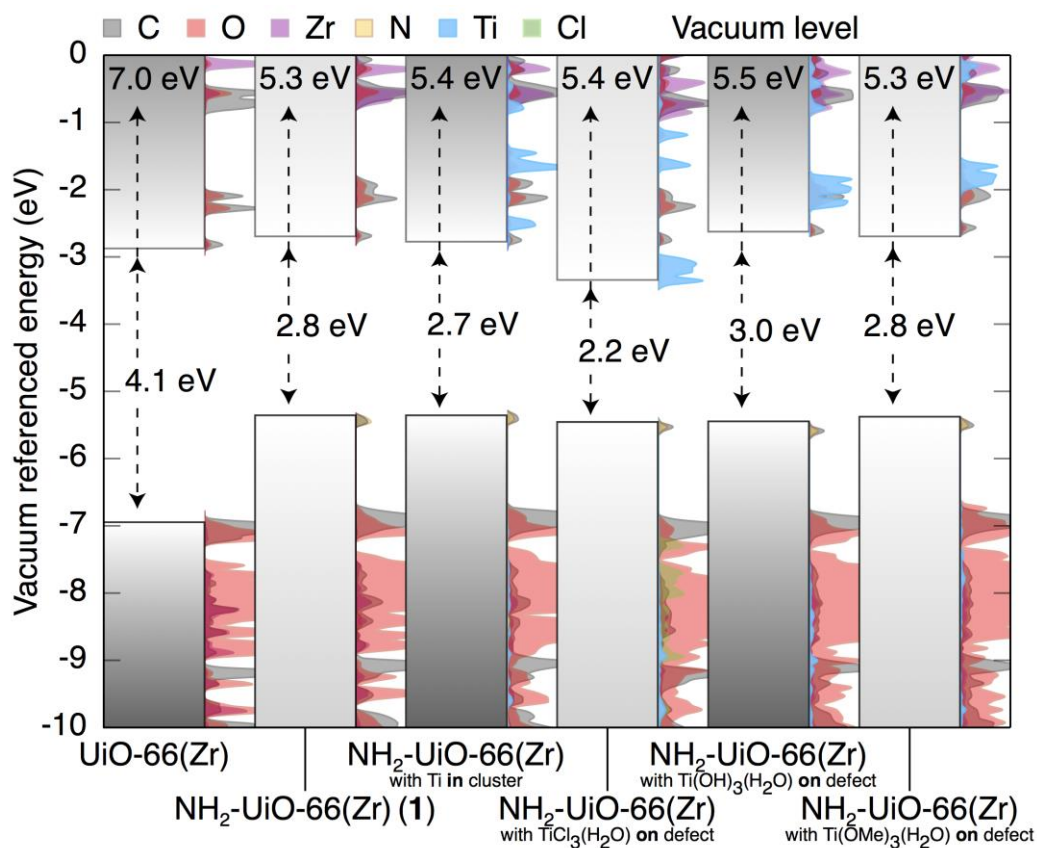


Figure 3. The density of states (DOS) and band alignment of native Zr-UiO-66, the 16%-NH₂-UiO-66(Zr) (**1**), compared to the models with Ti(IV) inside the SBU, or appended to the linker defect site

and passivated with Cl^- , OH^- or OMe^- . A single H_2O is included to complete the octahedral coordination sphere. DOS at ~ 5.4 eV and ~ 2.9 eV have amino-benzene parentage.

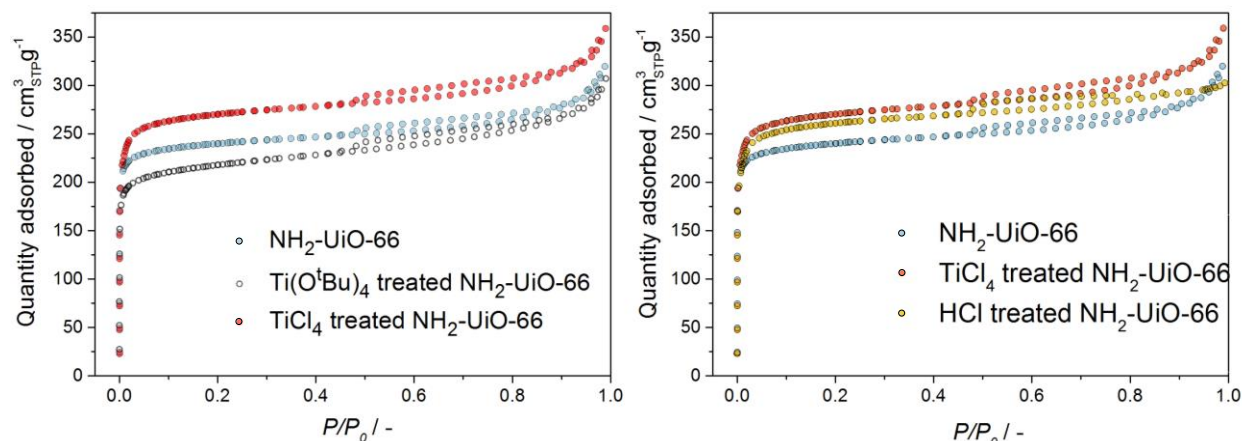


Figure 4. (left) N_2 physisorption isotherms of $\text{NH}_2\text{-UiO-66(Zr)}$ (blue) and its Ti-incorporated derivatives (black: $\text{Ti}(\text{O}^t\text{Bu})_4$; red: $\text{TiCl}_4 \cdot 2\text{THF}$). (right) N_2 physisorption was performed on $\text{NH}_2\text{-UiO-66}$ treated with HCl under Ti-incorporation conditions. N_2 physisorption isotherms of $\text{NH}_2\text{-UiO-66}$ (blue), $\text{TiCl}_4 \cdot 2\text{THF}$ treated $\text{NH}_2\text{-UiO-66}$ (red), and HCl treated $\text{NH}_2\text{-UiO-66}$ (yellow). The respective BET areas are shown in Table 1.

photoaccessible. Likewise, with Ti appended on defect sites the conduction band is not defined primarily by Ti orbitals.

These calculations assume that additional ligands on titanium are hydroxyl groups. With a weaker-field ligand such as Cl^- the Ti(IV) unoccupied state is stabilised thus bringing Ti orbitals to the frontier (Figure 3). Therefore, the ligand set as well as the titanium site occupancy should be paramount in generating an active photocatalyst.

As our goal was to generate a visible-light active photocatalyst we used the aminated precursor, **1**. Initially, we attempted to functionalise **1** using $\text{TiCl}_4 \cdot 2\text{THF}$ following a method previously reported.⁹ However, the material formed under these conditions, **1'**, simply featured an increase of linker vacancies as observed by an increase in the BET adsorption isotherm and the increased infrared O-H stretching anisotropy (Figure 4 and 5, respectively).

Table 1. Textural properties of the MOFs studied in this work.

MOF	$S_{\text{BET}} / \text{m}^2 \text{g}^{-1}$	$V_p / \text{cm}^3 \text{g}^{-1}$
$\text{NH}_2\text{-UiO-66(Zr)}$	961	0.45
$\text{Ti}(\text{O}^t\text{Bu})_4$ treated $\text{NH}_2\text{-UiO-66(Zr)}$	853	0.43
$\text{TiCl}_4 \cdot 2\text{THF}$ treated $\text{NH}_2\text{-UiO-66(Zr)}$	1082	0.50
HCl treated $\text{NH}_2\text{-UiO-66(Zr)}$	1045	0.49

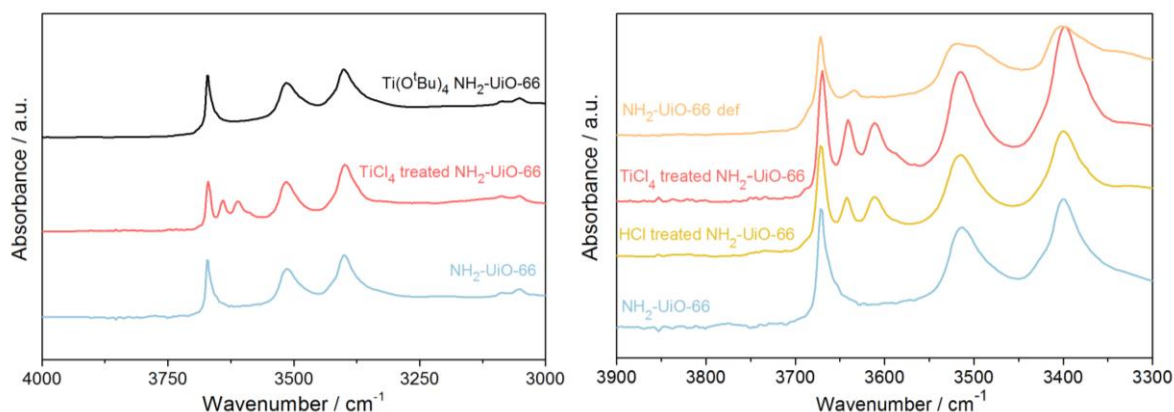


Figure 5. (left) DRIFTS spectra of $\text{NH}_2\text{-UiO-66(Zr)}$ (blue) and its Ti-incorporated derivatives (black: $\text{Ti}(\text{O}^t\text{Bu})_4$; red: $\text{TiCl}_4 \cdot 2\text{THF}$). The spectra have been normalised individually to their highest absorbance value (absorbance at 1383 cm^{-1}). (right) DRIFTS was performed on $\text{NH}_2\text{-UiO-66(Zr)}$ treated with HCl under Ti-incorporation conditions. The result was secondary $\nu(\text{O-H})$ bands analogous to those observed for $\text{TiCl}_4 \cdot 2\text{THF}$. $\nu(\text{O-H})$ and $\nu(\text{N-H})$ region of the DRIFTS spectra of $\text{NH}_2\text{-UiO-66(Zr)}$ (blue), $\text{NH}_2\text{-UiO-66(Zr)}$ treated with $\text{TiCl}_4 \cdot 2\text{THF}$ (red), and HCl (yellow), and a “defective” $\text{NH}_2\text{-UiO-66(Zr)}$ (orange) following a synthesis protocol reported elsewhere.

Additionally, we see both Ti and Cl inclusion by TEM/EDX (transmission electron microscopy/ energy dispersive X-Ray analysis, Figure 6). Given the propensity of Ti-Cl bonds to hydrolyse under the synthetic conditions (three days in methanol), we instead suspect Cl-termination of zirconium clusters and formation of $\text{Ti}(\text{OR})_x$ -type species in the pore.

Table 2. Titanium and chlorine loading in the different Ti-functionalised MOF samples based on elemental analysis^a and TEM-EDS mapping^b.

Sample	Ti/Zr atom ratio	Cl/Ti atom ratio
$\text{Ti}(\text{O}^t\text{Bu})_4$ treated $\text{NH}_2\text{-UiO-66(Zr)}$	0.1 ^b	-
$\text{TiCl}_4 \cdot 2\text{THF}$ treated $\text{NH}_2\text{-UiO-66(Zr)}$	0.05 ^a / 0.1 ^b	2.21 ^b

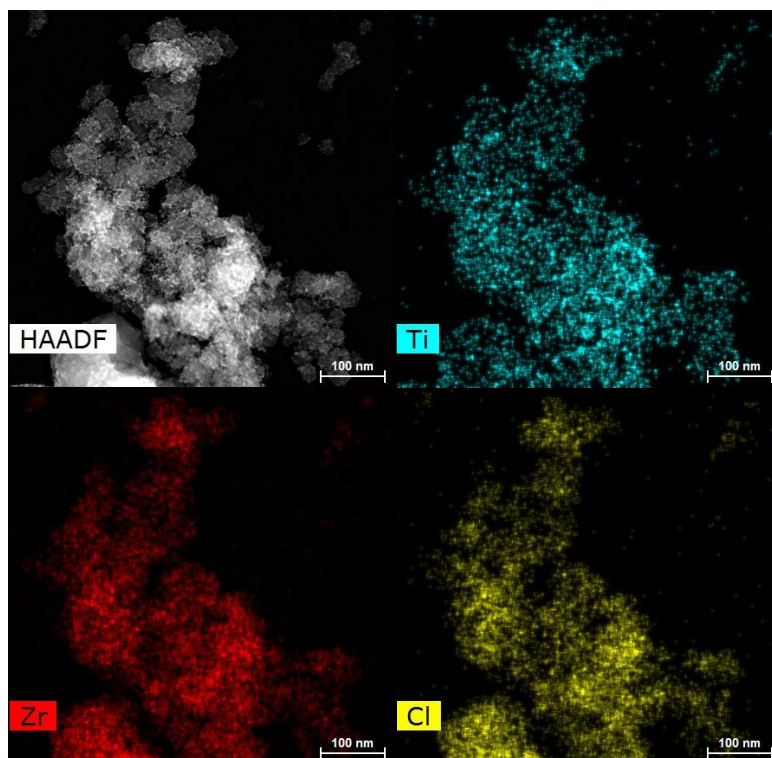


Figure 6. TEM mapping images of $\text{TiCl}_4 \cdot 2\text{THF}$ treated $\text{NH}_2\text{-UiO-66(Zr)}$

Upon photoexcitation of **1'**, X/Q-band EPR (9/34 GHz) indicates electron transfer with a formation of Ti(III) in an octahedral coordination environment, similar to $\text{NH}_2\text{-MIL-125}$ (Figure 11). However, the observation of sharp peaks with well resolved g -tensor components $g = [1.976 \ 1.945 \ 1.925]$ is more consistent with a single Ti environment (e.g. Ti(OR)_x) rather than with the superposition of environments anticipated if Ti would reside at the defect sites (*vide infra*).

The photocatalytic hydrogen evolution activity of **1'** was found to be 1.5x greater than native **1** (Figure 7). Indeed, this HER activity is in line with previously reported results for the defect-laden version of this material (data of the deliberately defective $\text{NH}_2\text{-UiO-66(Zr)}$ showed a 1.7x increase in photocatalytic activity, with approximately 30% linker vacancies).³⁶ From this data, we propose that Ti is not primarily responsible for the activity of this catalyst. Therefore, we developed a new synthetic route to minimise new linker vacancies formed during the metal inclusion.

Table 3. Catalytic performance.

Sample	Energy gap / eV	Hydrogen evolution rate / $\mu\text{mol}\cdot\text{h}^{-1}$	EQE / %
1	2.93	0.017	0.0005
1'	2.88	0.025	0.0007
2	2.88	0.192	0.0055

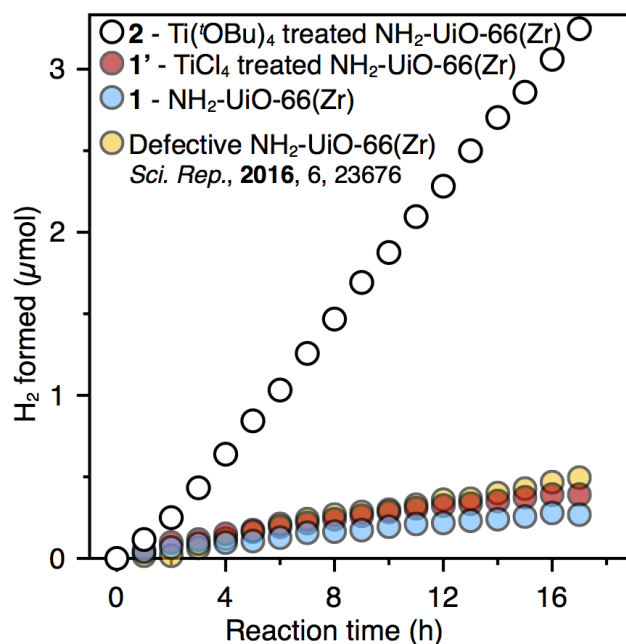


Figure 7. Photocatalytic activity of native NH₂-UiO-66(Zr) (**1**, *blue*) and a deliberately defective analogue (*yellow*) compared to the TiCl₄-treated NH₂-UiO-66(Zr) (**1'**, *red*), and Ti(O^tBu)₄-treated NH₂-UiO-66(Zr) (**2**, *white*). Deliberately defective NH₂-UiO-66 was synthesized using the method presented in Ref 36.

The most frequently proposed defect passivation of the zirconia SBUs is through termination with pendant –OH groups that share a bridging H-bonded proton (depicted at the bottom of Figure 1b). We propose that a more basic Ti salt could deprotonate the defect site and thus enhance grafting of Ti onto the inorganic SBU. Thus, we selected Ti(O^tBu)₄ as the Ti(IV) source for post-synthetic modification of **1** to form a presumably Ti-grafted product (referred to as **2**, Figure 1b). Given the reaction conditions, a representative model of the Ti coordination sphere is likely octahedral Ti(IV) associated with either hydroxides or alkoxides. The electronic structure of both systems is presented in Figure 3. **2** demonstrates the expected

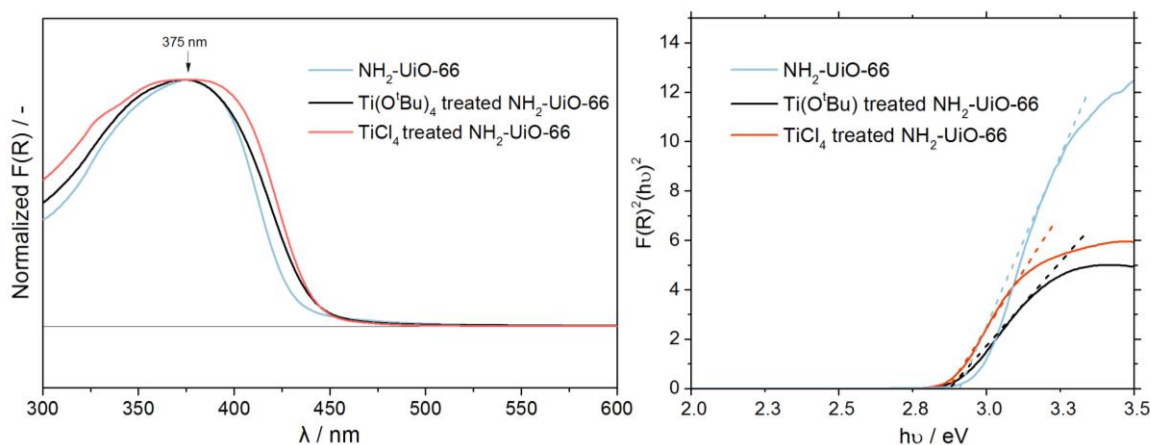


Figure 8. (*left*) Diffuse reflectance UV-Vis spectra of NH₂-UiO-66(Zr) (*blue*) and its Ti-incorporated derivatives (*black*: Ti(O^tBu)₄; *red*: TiCl₄) in Kubelka-Munk representation; (*right*) Tauc plot of these catalysts,

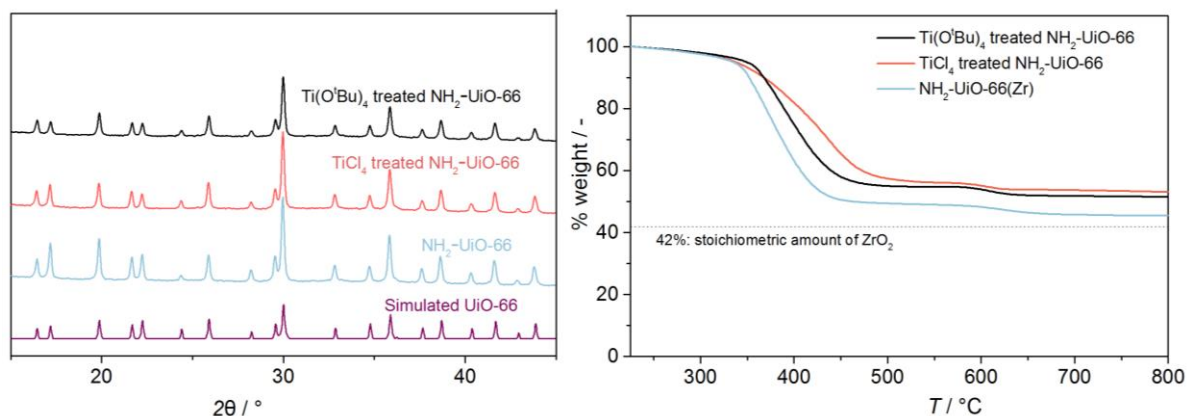


Figure 9. (left) Powder X-Ray diffraction patterns and (right) TGA profiles of NH₂-UiO-66(Zr) (blue) and its Ti-incorporated derivatives (black: Ti(OⁱBu)₄; red: TiCl₄), compared with the simulated UiO-66(Zr) (purple), calculated from crystal structure coordinates reported elsewhere.⁴¹ TGA curves are normalised with respect to the sample weight at 225 °C, and the dotted line shows the expected final weight % for a stoichiometrically ideal NH₂-UiO-66.

decrease in BET area, associated with the grafting of the Ti(IV) to the surface of the SBU, a single IR O-H stretching resonance, and a higher proportion of remaining residues of metal oxides observed by TGA (Figures 4, 5, 9, respectively) corresponding to the appendage of a metal with no concurrent increase in site vacancies. Importantly, if metal exchange were occurring into the SBU, we would expect no decrease in the surface area.

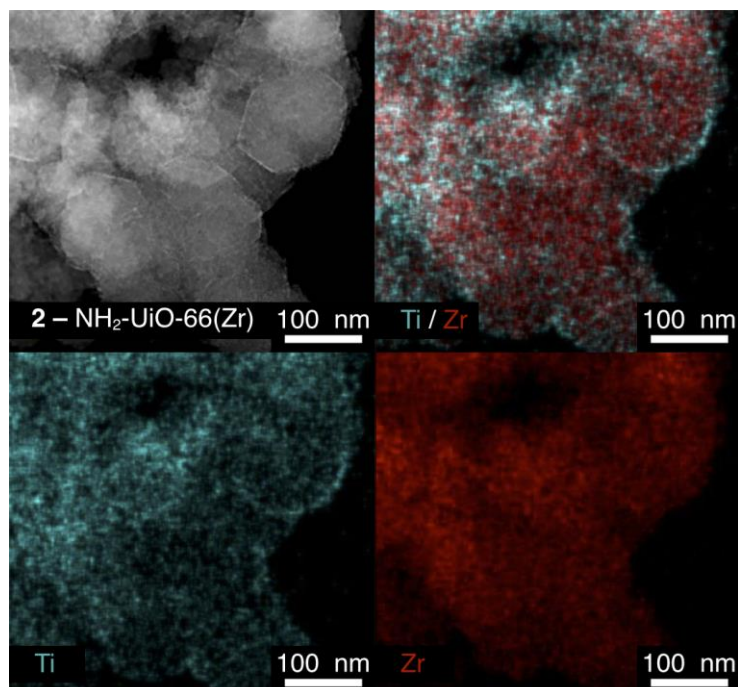


Figure 10. Transmission electron microscopy / energy dispersive X-ray spectroscopy images of NH₂-UiO-66(Zr) (2). Ti(IV) is present throughout the crystal, with highest concentrations found on the crystal edges.

TEM/EDS mapping of Ti shows good dispersion of Ti(IV) (Figure 10), with some preference for surface functionalisation, as it is expected given that a majority of defects are at surface termini. EPR of the photoexcited material (X/Q-band) in this case shows a more diffuse Ti(III) signal relative to **1'** (Figure 11 and 13), indicative of a broader distribution of g -tensor components and suggesting a number of possible combinations of Ti-containing linker defects on Zr SBUs. Noteworthy, measurements of the T_1 and T_2 relaxation times of **2** vs. NH₂-MIL-125(Ti) are in good agreement for highly dispersed Ti(IV) through the UiO-66 lattice in **2** (Figure 13) and suggest that Ti is atomically dispersed. Long-range crystallinity appeared to be maintained as observed by PXRD (Figure 9, *left*).

Most importantly, the grafted material **2** demonstrates significantly improved photocatalysis compared to the other materials considered here. Upon irradiation in CH₃CN/Et₃N/H₂O, hydrogen was evolved from water with a rate of 0.2 $\mu\text{mol h}^{-1}$, attributed to photocatalysis occurring at the Ti(III) sites, (Figure 7 and Table 3). This corresponds to a rate 11x greater than either native NH₂-UiO-66(Zr) (**1**) or the material formed by Ti incorporation through treatment of **1** with TiCl₄.2THF (**1'**). Indeed, upon photoirradiation of **2** at 370 nm, a new transient absorption (TA) band centred at around 750 nm was observed (Figure 14), which, in agreement with EPR, likely corresponds to a Ti(III) excitation.⁴²⁻⁴⁵

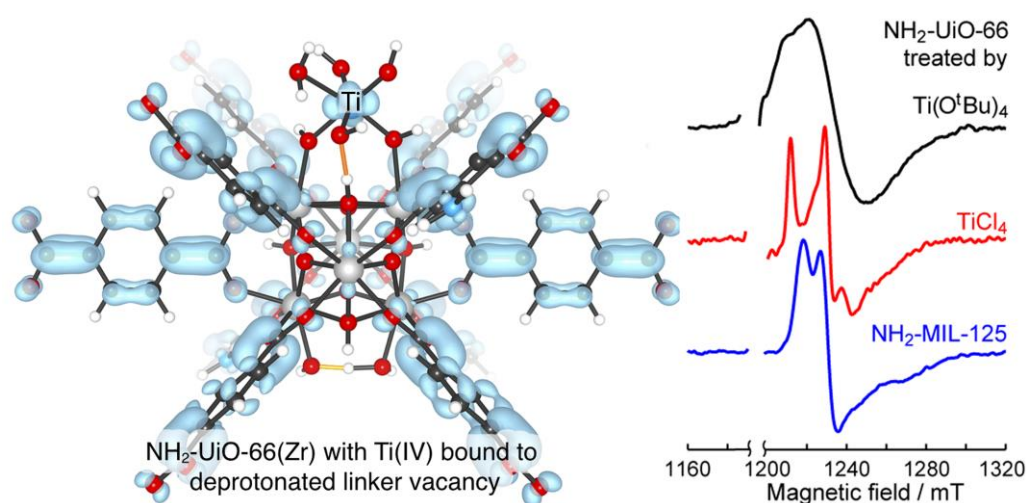


Figure 11. (*left*) The spin density of the pseudoexcited state of **2** shows a majority of spin contribution on the organic linker but, importantly a minor contribution from a Ti(III) d -orbital. (*right*) Q-band continuous wave EPR spectra (≈ 33.5 GHz) of photoexcited NH₂-MIL-125(Ti), **1'** and **2** in CH₃CN/Et₃N/H₂O.

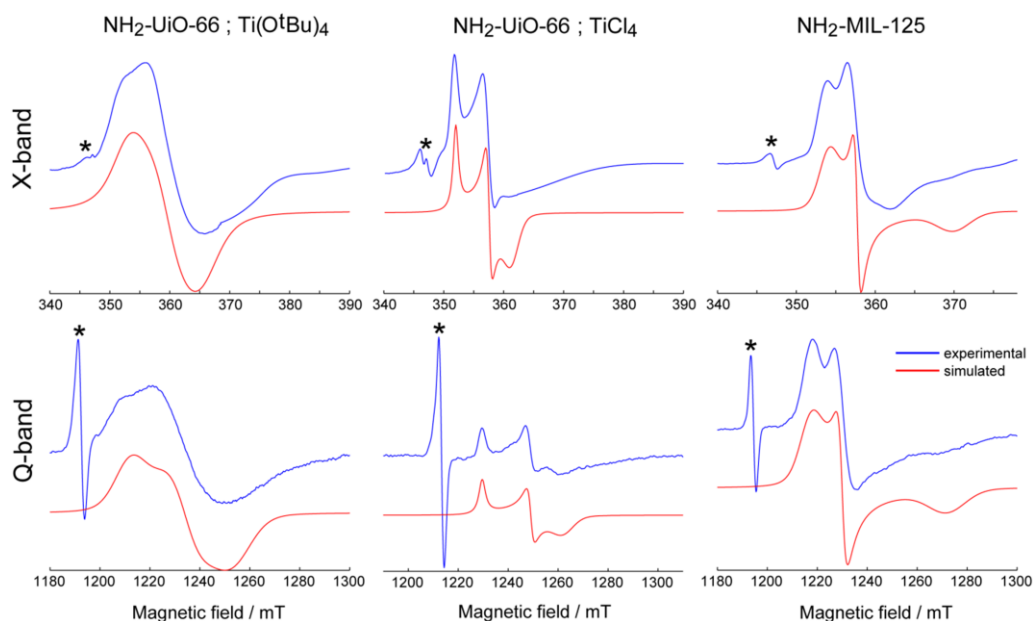


Figure 12. X- and Q-band EPR spectra of photoinduced Ti(III) signals in (*left*) NH₂-UiO-66(Zr) treated with Ti(O^tBu)₄, (*middle*) NH₂-UiO-66(Zr) treated with TiCl₄, and (*right*) NH₂-MIL-125(Ti) for comparison (80 K). Experiment (*blue*) and simulation (*red*). The radical defects' signals are marked with a star. Simulations qualitatively support that large g-strain (~0.02 for each component) imposed on the spectrum of **2** allows reasonable agreement between theory and experiment. The broadening is not caused by faster electron relaxation in **2** compared to the two other samples, since the relaxation times are slower for **2** than those for NH₂-MIL-125(Ti) (Figure 13).

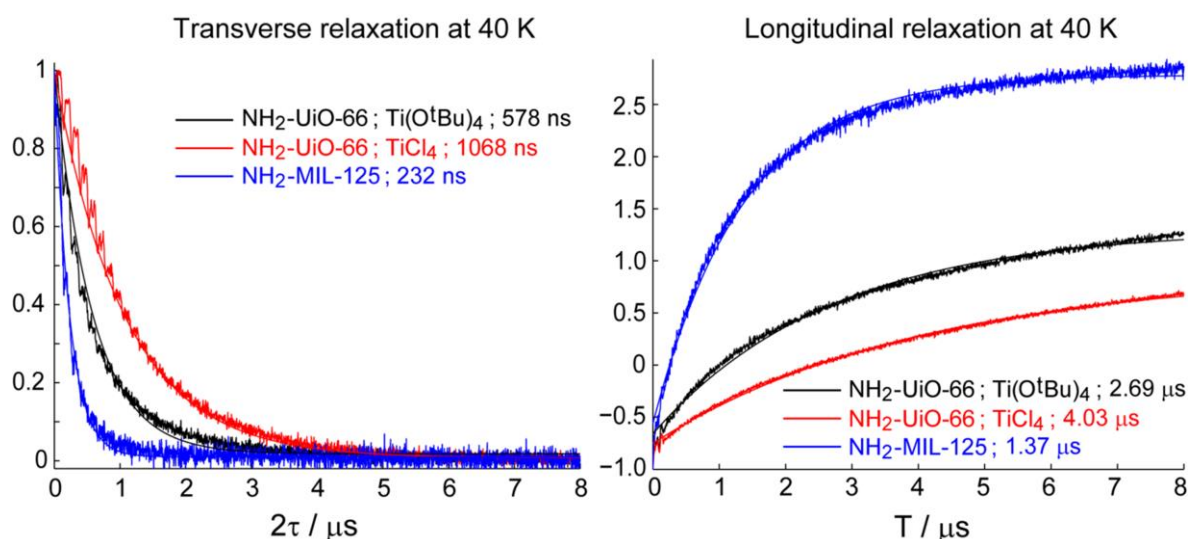


Figure 13. Transverse (T_2) and longitudinal (T_1) relaxation times measurements on photoinduced Ti(III) signals in (i) NH₂-UiO-66(Zr) treated with Ti(O^tBu)₄, (ii) NH₂-UiO-66(Zr) treated with TiCl₄, and (iii) NH₂-MIL-125(Ti) for comparison (X-band, 40 K). Solid lines show the result of monoexponential approximation, and the corresponding characteristic decay times are given in each graph.

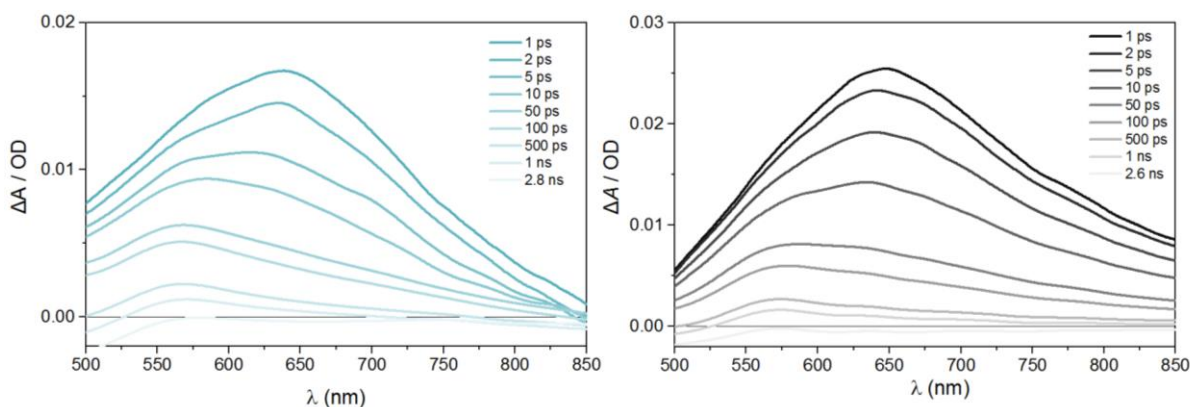


Figure 14. Differential TA spectra for on $\text{NH}_2\text{-UiO-66(Zr)}$ (*blue*) and $\text{Ti}(\text{O}^t\text{Bu})_4$ treated $\text{NH}_2\text{-UiO-66(Zr)}$ (*black*) upon excitation at 370 nm. For $\text{NH}_2\text{-UiO-66(Zr)}$ there are two clear contributions. One at 550 nm that corresponds to the hole on the linker.^{36, 46} Since this is a ligand-to-ligand transition, a second peak at 650 nm most likely corresponds to the photogenerated electron on the organic linker. In contrast, when Ti(IV) is incorporated in the $\text{NH}_2\text{-UiO-66(Zr)}$, a broad shoulder can be noticed that goes beyond 800 nm, most likely arising from Ti(III).

From direct comparison of the 2-Ti-Cl , -Ti-OH and -Ti-OMe structures we see that the electron density of the ligand determines the extent of Ti contribution to the conduction band. Whilst Ti-Cl termination is electronically the most favourable, it is unlikely that such ligand environments persist under relevant reaction conditions. Despite both Ti-OH and Ti-OMe terminated models suggest minimal Ti d orbital contributions to their conduction band minima, the ground-state DFT calculation is not the most informative representation of the orbital density upon photoexcitation. Thus, we constructed a model of triplet 2-Ti-OH and found that indeed most of the band is defined by the linkers, but there is additional highly localised titanium d character as a minor component (emphasised in Figure 11). Two conclusions can be drawn from this calculation: i) the titanium density of states will increase proportionally with the increased loading of Ti in the MOF, and ii) titanium density will increase proportionally to linker vacancies (either by increased loading of Ti-sites, or by decreased linker contribution to the frontier bands).

Conclusions

We have found that upon titanium incorporation into the MOF UiO-66, Ti incorporation occurs via its appendage to a linker vacancy rather than replacement of zirconium in the SBU. Careful choice of titanium source in the post-synthetic modification of this MOF determines the extent of covalent interaction between the MOF and Ti. Furthermore, the appendage of Ti(IV) to the surface of SUB in the MOF yields a moderately active HER photocatalyst. More active catalysts will likely spawn from the engineering of the Ti-bound ligand set to achieve persistence under the reaction conditions whilst being weakly electron donating (to lower the Ti(III) band deeper into the electronic band gap). Therefore, we have shown that in MOF catalyst design both the defect environment and external ligand field are equally important to further improve the activity of this class of materials in photocatalysis.

References

1. Y. Tachibana, L. Vayssieres and J. R. Durrant, *Nat Photon*, 2012, **6**, 511-518.
2. T. Zhang and W. Lin, *Chemical Society Reviews*, 2014, **43**, 5982-5993.
3. M. A. Nasalevich, M. van der Veen, F. Kapteijn and J. Gascon, *CrystEngComm*, 2014, **16**, 4919-4926.
4. J. G. Santaclara, F. Kapteijn, J. Gascon and M. A. van der Veen, *CrystEngComm*, 2017, DOI: 10.1039/C7CE00006E.
5. J. H. Cavka, S. Jakobsen, U. Olsbye, N. Guillou, C. Lamberti, S. Bordiga and K. P. Lillerud, *Journal of the American Chemical Society*, 2008, **130**, 13850-13851.
6. C. Gomes Silva, I. Luz, F. X. Llabrés i Xamena, A. Corma and H. García, *Chemistry – A European Journal*, 2010, **16**, 11133-11138.
7. R. J. Marshall and R. S. Forgan, *European Journal of Inorganic Chemistry*, 2016, **2016**, 4310-4331.
8. K. Hendrickx, D. E. P. Vanpoucke, K. Leus, K. Lejaeghere, A. Van Yperen-De Deyne, V. Van Speybroeck, P. Van Der Voort and K. Hemelsoet, *Inorganic Chemistry*, 2015, **54**, 10701-10710.
9. M. Kim, J. F. Cahill, H. Fei, K. A. Prather and S. M. Cohen, *Journal of the American Chemical Society*, 2012, **134**, 18082-18088.
10. S. M. Chavan, G. C. Shearer, S. Svelle, U. Olsbye, F. Bonino, J. Ethiraj, K. P. Lillerud and S. Bordiga, *Inorganic Chemistry*, 2014, **53**, 9509-9515.
11. C. H. Hendon, D. Tiana, M. Fontecave, C. Sanchez, L. D'Arras, C. Sassoeye, L. Rozes, C. Mellot-Draznieks and A. Walsh, *J. Am. Chem. Soc.*, 2013, **135**, 10942-10945.
12. M. A. Nasalevich, M. G. Goesten, T. J. Savenije, F. Kapteijn and J. Gascon, *Chem. Commun.*, 2013, **49**, 10575-10577.
13. Y. Lee, S. Kim, J. K. Kang and S. M. Cohen, *Chemical Communications*, 2015, **51**, 5735-5738.
14. A. S. Yasin, J. Li, N. Wu and T. Musho, *Physical Chemistry Chemical Physics*, 2016, **18**, 12748-12754.
15. D. Sun, W. Liu, M. Qiu, Y. Zhang and Z. Li, *Chemical Communications*, 2015, **51**, 2056-2059.
16. A. Wang, Y. Zhou, Z. Wang, M. Chen, L. Sun and X. Liu, *RSC Advances*, 2016, **6**, 3671-3679.
17. C. K. Brozek and M. Dinca, *Chemical Society Reviews*, 2014, **43**, 5456-5467.
18. M. Lalonde, W. Bury, O. Karagiari, Z. Brown, J. T. Hupp and O. K. Farha, *Journal of Materials Chemistry A*, 2013, **1**, 5453-5468.
19. J. Tu, X. Zeng, F. Xu, X. Wu, Y. Tian, X. Hou and Z. Long, *Chemical Communications*, 2017, **53**, 3361-3364.
20. R. C. Klet, S. Tussupbayev, J. Borycz, J. R. Gallagher, M. M. Stalzer, J. T. Miller, L. Gagliardi, J. T. Hupp, T. J. Marks, C. J. Cramer, M. Delferro and O. K. Farha, *Journal of the American Chemical Society*, 2015, **137**, 15680-15683.
21. S. J. D. Smith, B. P. Ladewig, A. J. Hill, C. H. Lau and M. R. Hill, *Scientific Reports*, 2015, **5**, 7823.
22. C. Hon Lau, R. Babarao and M. R. Hill, *Chemical Communications*, 2013, **49**, 3634-3636.
23. H. G. T. Nguyen, L. Mao, A. W. Peters, C. O. Audu, Z. J. Brown, O. K. Farha, J. T. Hupp and S. T. Nguyen, *Catalysis Science & Technology*, 2015, **5**, 4444-4451.
24. A. Santiago Portillo, H. G. Baldoví, M. T. García Fernandez, S. Navalón, P. Atienzar, B. Ferrer, M. Alvaro, H. Garcia and Z. Li, *The Journal of Physical Chemistry C*, 2017, **121**, 7015-7024.
25. M. J. Cliffe, W. Wan, X. Zou, P. A. Chater, A. K. Kleppe, M. G. Tucker, H. Wilhelm, N. P. Funnell, F.-X. Coudert and A. L. Goodwin, *Nat Commun*, 2014, **5**.
26. M. R. DeStefano, T. Islamoglu, S. J. Garibay, J. T. Hupp and O. K. Farha, *Chemistry of Materials*, 2017, **29**, 1357-1361.
27. G. C. Shearer, S. Chavan, J. Ethiraj, J. G. Vitillo, S. Svelle, U. Olsbye, C. Lamberti, S. Bordiga and K. P. Lillerud, *Chemistry of Materials*, 2014, **26**, 4068-4071.
28. Z. Fang, B. Bueken, D. E. De Vos and R. A. Fischer, *Angewandte Chemie International Edition*, 2015, **54**, 7234-7254.
29. S. Ling and B. Slater, *Chemical Science*, 2016, **7**, 4706-4712.
30. C. A. Trickett, K. J. Gagnon, S. Lee, F. Gándara, H.-B. Bürgi and O. M. Yaghi, *Angewandte Chemie International Edition*, 2015, **54**, 11162-11167.

31. G. C. Shearer, J. G. Vitillo, S. Bordiga, S. Svelle, U. Olsbye and K. P. Lillerud, *Chemistry of Materials*, 2016, **28**, 7190-7193.
32. J. K. Bristow, K. L. Svane, D. Tiana, J. M. Skelton, J. D. Gale and A. Walsh, *The Journal of Physical Chemistry. C, Nanomaterials and Interfaces*, 2016, **120**, 9276-9281.
33. M. J. Katz, Z. J. Brown, Y. J. Colon, P. W. Siu, K. A. Scheidt, R. Q. Snurr, J. T. Hupp and O. K. Farha, *Chemical Communications*, 2013, **49**, 9449-9451.
34. D. Yang, S. O. Odoh, T. C. Wang, O. K. Farha, J. T. Hupp, C. J. Cramer, L. Gagliardi and B. C. Gates, *Journal of the American Chemical Society*, 2015, **137**, 7391-7396.
35. H. Furukawa, F. Gándara, Y.-B. Zhang, J. Jiang, W. L. Queen, M. R. Hudson and O. M. Yaghi, *Journal of the American Chemical Society*, 2014, **136**, 4369-4381.
36. M. A. Nasalevich, C. H. Hendon, J. G. Santaclara, K. Svane, B. van der Linden, S. L. Veber, M. V. Fedin, A. J. Houtepen, M. A. van der Veen, F. Kapteijn, A. Walsh and J. Gascon, *Scientific Reports*, 2016, **6**, 23676.
37. S. Maurelli, E. Morra, S. Van Doorslaer, V. Busico and M. Chiesa, *Physical Chemistry Chemical Physics*, 2014, **16**, 19625-19633.
38. M. Kapilashrami, Y. Zhang, Y.-S. Liu, A. Hagfeldt and J. Guo, *Chemical Reviews*, 2014, **114**, 9662-9707.
39. D. O. Scanlon, C. W. Dunnill, J. Buckeridge, S. A. Shevlin, A. J. Logsdail, S. M. Woodley, C. R. A. Catlow, M. J. Powell, R. G. Palgrave, I. P. Parkin, G. W. Watson, T. W. Keal, P. Sherwood, A. Walsh and A. A. Sokol, *Nat Mater*, 2013, **12**, 798-801.
40. A. Walsh, K. T. Butler and C. H. Hendon, *MRS Bulletin*, 2016, **41**, 870-876.
41. S. Øien, D. Wragg, H. Reinsch, S. Svelle, S. Bordiga, C. Lamberti and K. P. Lillerud, *Crystal Growth & Design*, 2014, **14**, 5370-5372.
42. J. N. Schrauben, R. Hayoun, C. N. Valdez, M. Braten, L. Fridley and J. M. Mayer, *Science*, 2012, **336**, 1298.
43. M. Dan-Hardi, C. Serre, T. Frot, L. Rozes, G. Maurin, C. Sanchez and G. Férey, *Journal of the American Chemical Society*, 2009, **131**, 10857-10859.
44. A. I. Kuznetsov, O. Kameneva, N. Bityurin, L. Rozes, C. Sanchez and A. Kanaev, *Physical Chemistry Chemical Physics*, 2009, **11**, 1248-1257.
45. G. K. Ramesha, J. F. Brennecke and P. V. Kamat, *ACS Catalysis*, 2014, **4**, 3249-3254.
46. J. G. Santaclara, M. A. Nasalevich, S. Castellanos, W. H. Evers, F. C. M. Spoor, K. Rock, L. D. A. Siebbeles, F. Kapteijn, F. Grozema, A. Houtepen, J. Gascon, J. Hunger and M. A. van der Veen, *ChemSusChem*, 2016, **9**, 388-395.

Harvesting the photoexcited holes in a photocatalytic proton reduction metal-organic framework

The highly porous titanium based metal-organic framework NH₂-MIL-125(Ti) has recently attracted significant attention in the field of photocatalysis as a promising material for H⁺ reduction. This work reveals charge transfer upon visible light illumination from this MOF to two different charge acceptors, as alternative to sacrificial electron donors. Charge transfer is demonstrated through a combined spectroscopic study between this MOF and: 1) 2-(1H-Pyrazol-3-yl)phenol, a molecule that functionally mimics the tyrosine-histidine pair, responsible to shuttle the holes to the oxygen evolving centre in natural photosynthesis, and 2) TEMPO, a well-known and stable radical. Charge transfer of the holes from the MOF to these occluded molecules takes place on the time scale of picoseconds. This work suggests that, by coupling a stable and recyclable charge acceptor to the photogenerated holes, the charges can be utilised for oxidation reactions and, thus, link the reduction to the oxidation reactions in water splitting.

This chapter is based on the following publication:

Harvesting the photoexcited holes on a photocatalytic proton reduction metal-organic framework
J. G. Santaclara, A. I. Olivos-Suarez, I. du Fossé, A. Houtepen, J. Hunger, F. Kapteijn, J. Gascon, M. A. van der Veen, Faraday Discuss. 2017 (accepted manuscript), DOI 10.1039/C7FD00029D

Introduction

The demand for renewable energy sources that harvest solar energy is greater than ever.¹ Using the sun, the largest exploitable resource, as a power source is a sustainable and clean alternative to fossil fuels. Thus, the production of solar fuels by artificial photosynthesis has attracted a great deal of attention.² The first example in which water was split under UV radiation using TiO_2 as catalyst was reported by Fujishima and Honda in 1972.³ Using the photosynthetic blueprint, many different materials and devices have been reported since then, yet there is no efficient, cheap and stable system to achieve the desired light-driven water splitting for the production of solar fuels.⁴

The challenge to implement water splitting is the coupling of the oxidation and the reduction half reactions. This 4-electron reaction requires the adequate light induced separation of charges to harvest light (4 photons), but also that the charges, with adequate redox potential, are transferred to the respective catalytic sites.⁵ Ideally, both the reduction and oxidation half reactions are spatially separated, and only interconnected via the light harvesting component to avoid the undesired back electron transfer.⁶ Inspired by natural photosynthesis, researchers have focussed on developing multicomponent relay systems, where different components aid to the spatial separation and electron transfer rates are adequately matched.⁶⁻⁹

In nature, the ratio between forward and backward reactions rates is controlled *via* molecular redox relays. Here, the tyrosine-histidine pair (Tyr/His in Figure 5.1) is a key component of Photosystem II (PS II) that mediates electron transfer between the photoexcited primary electron donor (P680^+) and the Mn-containing oxygen evolving complex (OEC).¹⁰⁻¹² In this pair, the one electron oxidised alcohol group is stabilised by an adequately positioned basic histidine residue. Implementation of similar recyclable charge carriers in an artificial photosynthetic system can be done via recyclable electron donors that provide the coupling between the catalytic centres for the hydrogen evolving and the water oxidation half reactions, in a Z-scheme.¹³⁻¹⁵

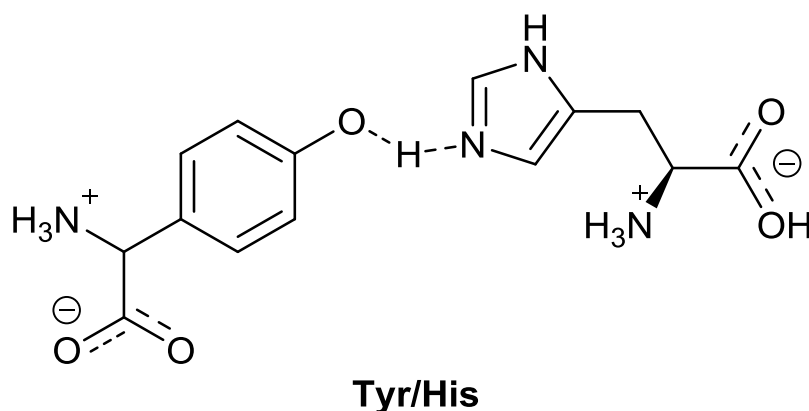


Figure 5.1. Scheme of tyrosine/histidine pair in PS II.

Metal organic frameworks (MOFs) have been recently applied to study and design artificial photosynthetic systems.⁴ The modular structure that MOFs provide is one of the most attractive features to integrate the three fundamental steps of artificial photosynthesis into a single material: 1) light harvesting, 2) charge separation; and 3) controlled arrangement of the individual components to favour the utilization of charges in redox reactions.

Although many frameworks have been reported to be able to evolve H₂, reduce CO₂ and perform organic oxidations, both the fundamentals behind the photocatalytic reactions are still elusive,¹⁶⁻¹⁸ and there has only been focus on the reductive half reaction. Recent studies of the photoexcitation processes of MIL-125(Ti) demonstrates that functionalities, such as the amino group in the NH₂-MIL-125(Ti), have an enhancement towards visible range light absorption, and more importantly, help to separate charges (beyond 10 ns) featuring ligand-to-metal charge transfer (LMCT).¹⁹ Moreover, the comparison during photoexcitation of NH₂-MIL-125(Ti) with other *d*⁰-based transition metal frameworks, such as NH₂-UiO-66(Zr/Hf), highlights the importance of a good overlap between metal and ligand orbitals for efficient separation of photoexcited charges (lifetimes of only 1-100 ps for Zr/Hf MOFs).²⁰ However, the slow decay kinetics of NH₂-MIL-125(Ti) alone do not guarantee highly efficient photocatalytic performance. A well-known problem in molecular artificial photosynthesis is the back-electron transfer after photoinduced charge separation.²¹

It is not surprising, as mention above, that only the reduction side (H₂ evolving and CO₂ reduction reaction) has been reported for MOFs mediated photocatalysis, since MOFs are build up from carboxylate linkers that do not possess the oxidative power to run the water oxidation half reaction.²² This means that these MOFs need to be coupled to an adequate water oxidation catalyst via e.g. a recyclable charge carrier.

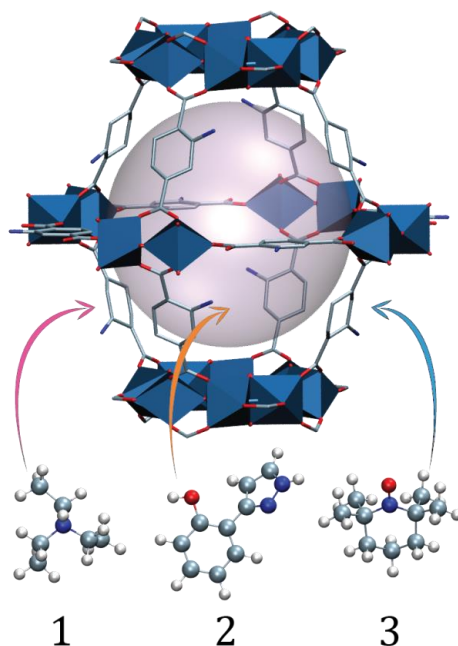


Figure 5.2. Schematic (ball and stick and polyhedra) representation of molecules **1**, **2** and **3** occluded in a large NH₂-MIL125 cage. Light pink ball represents the pore volume.

In this work, we aim to i) improve the fundamental understanding and ii) implement charge transfer to recyclable charge carriers. Thus, we demonstrate charge transfer from the visible-light absorbing NH₂-MIL-125(Ti) framework, a hydrogen evolving reaction (HER) photocatalyst, to charge-acceptor molecules incorporated in the pores (Figure 5.2). By substituting traditional *sacrificial agents* for more stable electron donors, we are able to mimic the charge shuttle tyrosine-histidine pair that natural photosynthesis uses. By a combined study of the multicomponent oxidation potentials and the dynamics at ultrafast time scales, we demonstrate charge transfer from the hole in NH₂-MIL-125(Ti) to the occluded molecules, and highlight the importance of efficient electron transfer in stabilizing the photo-induced charge separated state.

Experimental

Materials and reagents

All chemicals were purchased from Sigma Aldrich and used without further purification.

Synthesis

NH₂-MIL-125(Ti) was synthesized using a protocol reported by Walsh and co-workers.²² Typically, 2-aminoterephthalic acid (0.5 g, 2.76 mmol) was dissolved in a mixture anhydrous DMF (16 mL) and anhydrous methanol (4 mL) at RT in a glovebox. Titanium isopropoxide (0.55 mL, 1.93 mmol) was added, and the mixture was placed in a teflon liner. The autoclave was sealed and heated for 72 h at 110 °C. The obtained yellow solid was collected by filtration, dispersed in fresh DMF, and heated at 110 °C overnight to remove residual linker. Then, the same procedure was repeated using methanol for 6 h at 80 °C. Finally, the solid was dried in air at 80 °C. After synthesis, the following characterization techniques were used in order to determine purity of the MOF:

Powder X-Ray diffraction patterns were recorded using Bruker-AXS D5005 with CoK α radiation.

Nitrogen physisorption measurements were performed by using a Tristar II 3020 Micromeritics unit at 77 K. Before the experiment, the samples were degassed for 16 h at 423 K under vacuum. The BET areas were calculated using intervals to allow positive BET constants.²³ The total pore volumes were calculated at a relative pressure of 0.9.

Thermogravimetric analysis (TGA) was performed by using a Mettler Toledo TGA/SDTA851 system under an air flow (60 mL min⁻¹) at a heating rate of 10 K min⁻¹ to 1073 K.

Characterization and methods

Electrochemistry. All electrochemical experiments were performed with a platinum counter electrode (CE), a glassy carbon working electrode (WE) and an Ag/AgCl

reference electrode (RE). An Autolab PGSTAT3-2N was used as potentiostat. Between experiments, argon was bubbled through the solution for approximately 10 min. In addition, the WE was cleaned by rinsing with water and polishing with 1 μm diamond polish. For each experiment, a solution was made of analyte (10^{-3} M) and an aqueous buffer solution was used as electrolyte. Fc/Fc⁺ pair was always used for calibration before each experiment.

Spectroelectrochemistry. The optical setup comprised a Deuterium-Halogen lamp DH-2000 as light source, a USB2000 UV-VIS Spectrometer and a NIRQUEST NIR spectrometer, all components from Ocean Optics Inc. The potential was applied using CH Instruments Analyser CHI832B as potentiostat. For the measurements, a quartz cell was used. This cell comprised a platinum CE and an Ag wire as pseudo-RE. Translucent plates of glass coated with indium tin oxide (ITO) were used as WE. The SEC setup was always calibrated with Fc/Fc⁺ before each experiment. Moreover, the electrolyte was bubbled through with argon to remove any oxygen in the solution. LiClO₄ in acetonitrile (0.1 M) was used as electrolyte.

Composite preparation: 50 mg MOF was dispersed in a solution that contains the electron donor (0.024 M, 14 mL) and sonicated for 30 min. To remove large particles (> 100 nm) that cause too much light scattering, the suspension was then centrifuged for 30 min at 6000 rpm. The supernatant was placed in a cuvette for the different measurements. The resulting composites of molecules occluded in the MOF are referred in this work as: **1**@NH₂-MIL-125(Ti), **2**@NH₂-MIL-125(Ti), and **3**@NH₂-MIL-125(Ti).

Transmittance UV/VIS spectra were collected using a Perkin-Elmer Lambda 40 spectrophotometer. Liquid samples and composites (**2**@NH₂-MIL-125 and **3**@NH₂-MIL-125) were studied in Hellma 110-QS cuvettes with 2 mm optical path length.

Photoluminescence. Steady-state emission spectra were acquired using a QuantaMaster QM-1 (PTI). A 100 W Xenon arc lamp (200–900 nm) was used as a light source equipped with 121A excitation double monochromators. A Model MP-1 sample compartment, a 101A emission monochromator, and a model 710 photon counting detector PMT (185–900 nm) completed the experimental setup. The slit in all measurements was 10 nm. Fluorescence lifetime measurements were carried out using a LifeSpec-ps by Edinburgh Instruments equipped with a 405 nm laser diode emitting pulses with a 80 ps duration. The lifetimes were acquired using standard 1 cm optical path length cuvettes. The experiments were performed on suspensions of NH₂-MIL-125 (in water), and composites **1**@NH₂-MIL-125 (in acetonitrile), **2**@NH₂-MIL-125 (in DMF) and **3**@NH₂-MIL-125 (in water).

Femtosecond transient absorption spectroscopy. Samples for visible (Vis)-pump visible-probe measurements were excited using 180 fs pulses at 400 nm generated in a YKGBW oscillator (Light Conversion, Pharos SP) at 1028 nm through nonlinear frequency mixing in an OPA and second harmonics module (Light Conversion, Orpheus). A small fraction of the 1028 nm fundamental beam was split off to

generate the broadband probe spectrum (500 – 1600 nm) in a sapphire crystal. The probe pulse was delayed relative to the pump using a delay stage with maximum delay of 3 ns. The pump and probe pulses overlap on the sample position under an angle of ~8 degrees, after which the probe light is led to a detector suitable for the probe spectrum selected (Ultrafast Systems, Helios). In order to prevent multiple photon absorption processes, the pump fluence was set sufficiently low, allowing us to study single exciton dynamics. In a typical experiment 50 mg MOF was dispersed in a solution that contains the electron donor (0.024 M, 14 mL) and sonicated for 30 min. In order to remove large particles (> 100 nm) that cause too much light scattering, the suspension was then centrifuged for 30 min at 6000 rpm. The supernatant was placed in a 2 mm stirred quartz cuvette for the measurements.

The Vis-pump infrared (IR)-probe experiments were based on a regenerative Ti:Sapphire amplified laser system (Spitfire Ace, Spectra Physics), providing pulses at 800 nm with a duration of 35 fs and a pulse energy of 5 mJ at a repetition rate of 1 kHz. A commercial optical parametric amplifier (TOPAS-Prime, Light Conversion) was pumped with 1.5 mJ of the 800 nm pulses. The signal and idler pulses from one TOPAS-Prime were used in a difference frequency mixing process in a silver gallium disulphide (AgGaS₂) crystal, resulting in ~8 μJ tuneable IR pulses with a FWHM of 300 cm⁻¹. A wedged CaF₂ window was used to generate a probe and a reference pulse from the IR pulse, with the reflection of the front side used as the probe pulse and the back-reflection used as a reference pulse. A second portion of the 800 nm pulses was frequency-doubled in a beta-barium borate crystal, yielding visible pump pulses with 400 nm central wavelength. A translational stage was used to control the timing of the Vis pump-pulses relative to the IR probe-pulses. A mechanical chopper was used to block every second pump pulse, which allows for active background subtraction. The pump, probe, and reference pulses were focused onto the sample and the pump and the probe pulses were spatially overlapped. The probe and the reference pulses were recollimated and spectrally dispersed with an imaging spectrograph (Horiba Triax 180). The intensities, *I*, were detected on two separate lines of a 2x32 pixel mercury-cadmium-telluride (MCT, Infrared Associates) detector. The pump-induced absorption changes were thus given as $\Delta A = -\ln[I_{probe}/I_{reference,0}/(I_{probe,0}/I_{reference})]$, where subscript '0' refers to the IR intensities recorded without pump excitation. For all the measurements 40 mg NH₂-MIL-125(Ti) was dried overnight at 423 K, then dispersed in 800 μL solvent containing **2** (24 mg) and sonicated for 15 min.

Photocatalytic tests

Photocatalytic experiments were carried out using a home-built set-up equipped with a 500 W Xe/Hg lamp (66983, Newport). It consists of a custom-made stirred Pyrex-glass reactor, which has a volume of 42.1 mL and is equipped with a water jacket to allow for precise temperature control. Light intensity from the light source was measured with AvaSpec-3648-2-USB2 (Avantes, the Netherlands). The light emitted by the lamp passes through a lens assembly (77330, Newport) focussing the beam

on the reactor window, an H₂O filter (61945, Newport) and a 385 nm cut-off optical filter. A CP 9001 gas chromatograph (Chrompack) analyzes the headspace on-line, using a diaphragm gas pump (KNF, type NMP830 / KTDC24VDC) to ensure a sufficient mixing of gases in the headspace of the reactor and the stainless steel tubes (2.5 mL/min continuous operation). Every 60 min a probe of the headspace is analyzed by the GC.

Hydrogen evolution. In a typical experiment 30 mg of a MOF were suspended in 23.5 mL of CH₃CN, 0.5 mL of H₂O, and different amounts of electron donor (**1** and **3**). The suspension was then placed in the reactor and deoxygenated by an argon flow of 30 mL/min applied for 30 min at 25 °C. The oxygen concentration was monitored by the GC analysis. Once the system became free of oxygen, the illumination was applied followed by the GC analysis. All the visible light photocatalytic experiments were carried out at 40 °C monitored by a thermocouple. The heat was supplied in order to maximize the hydrogen production allowing the detection of H₂ gas in the case of samples with the lowest activity. A CP 9001 gas chromatograph (Chrompack) for on-line analysis of the headspace was used, and a KSLA gas pump. The pump is applied to ensure a sufficient mixing of gases in the headspace of the reactor and the stainless steel tubes (2.5 mL/min continuous operation). Every 60 min a probe of the headspace is analyzed by the GC.

Benzaldehyde production. 35 mg of NH₂-MIL-125(Ti) were suspended in 35 mL acetonitrile, 0.31 mL 1,2-dichlorobenzene (as internal standard), 0.58 mL benzyl alcohol, and electron donor was added (49 mg of **2** and 37 mg of **3**). The suspension was then placed in the reactor and stirred at a rate of ~800 min⁻¹. The system was saturated with oxygen by purging through it with a mixture of 20% O₂ and 80% He at 30 mL/min for 30 min. After that, the purge port was sealed off and the mixture was illuminated with a 500 W Xe/Hg lamp with a 385 nm optical filter. Samples were always taken directly before and after the purging through the purge-port. The obtained samples were filtrated and then analysed with gas chromatography. For this, three calibration curves were made: for the benzyl alcohol, the benzaldehyde and **3**. Here, 1,2-dichlorobenzene was used as an internal standard. No calibration curves were made for molecule **2** and benzoic acid as these did not appear in the chromatograms.

Results and discussion

The NH₂-MIL-125(Ti) framework is capable of separating charges, featuring LMCT transition upon visible light irradiation and producing enough reducing power for the hydrogen evolution reaction (HER). The LMCT efficiency of this system produces long-lived charge separated states (up to 10 ns).^{19, 20} An extensive spectroscopic characterization has pictured the nature of the separated charges and pointed to a nitrogen centred localized hole and an electron that is delocalised at the Ti₈O₈ ring in the MOF (see Figure 5.3b).¹⁹ On the acceptor side, the electron transfer to a Co-based catalyst has been evidenced by the increase of the photocatalytic HER efficiency.²⁴ On the donor side, however, *sacrificial* electron donors are still a

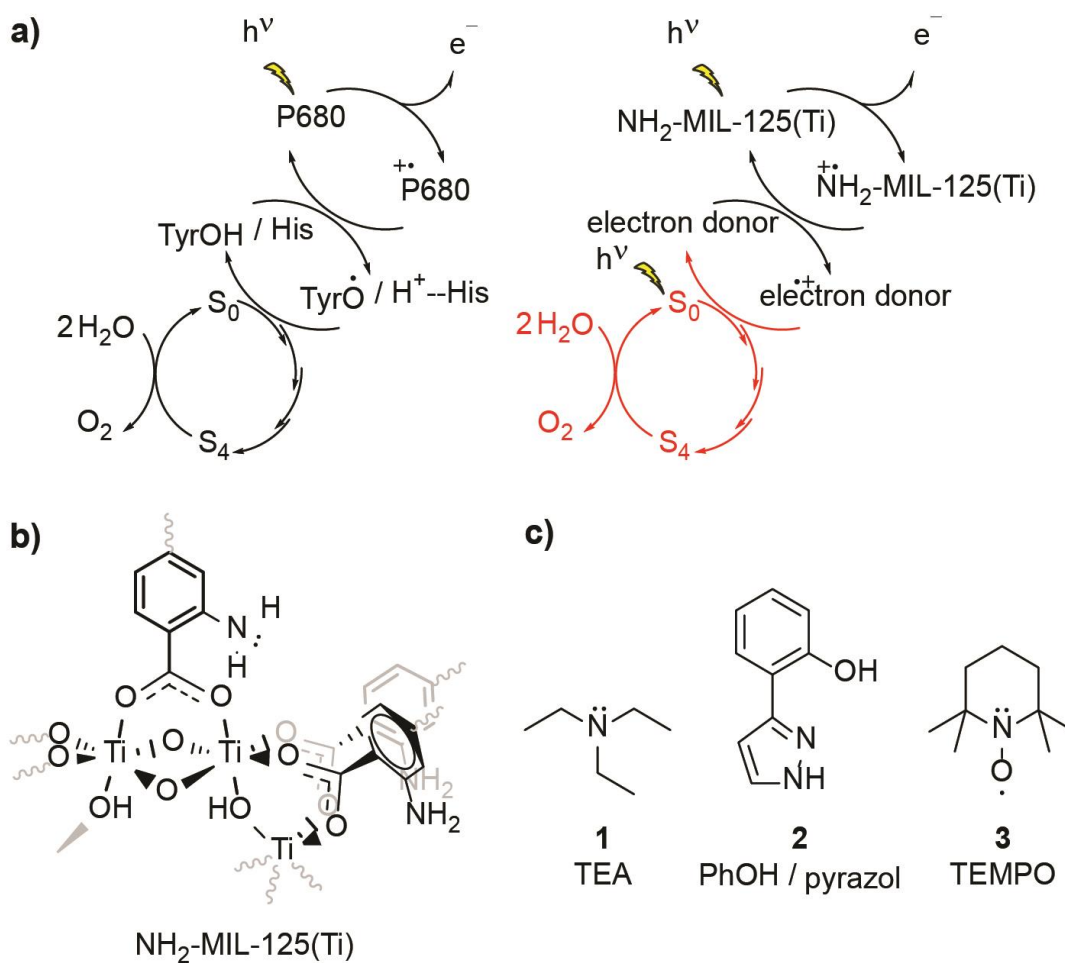


Figure 5.3. a) Schematic representation of the electron transfer reactions in PSII and in the photocatalytic MOF system (in red is shown the desired oxidation half reaction coupled to a Z-scheme), b) scheme of $\text{NH}_2\text{-MIL-125(Ti)}$, and c) compound **1-3** used as electron donors in this work.

requirement to provide the necessary electrons and complete the cycle. In spite of the slow decay kinetics observed in $\text{NH}_2\text{-MIL-125}$ that prevents fast recombination and renders the reduction half reaction, the integration of this system with an additional component that can act as electron donor and, at the same time, interconnect the charge transfer between this reductive catalytic system and an additional water oxidation catalytic system is still desired (Figure 5.3a, *right*).

We chose three charge carrier molecules that are small enough to readily diffuse (see section 4 in SI) through the cages of $\text{NH}_2\text{-MIL-125}$ with a free diameter of 4.7 and 10.7 Å and with large cage windows with a free diameter of 7 Å.^{25, 26}

Triethylamine is widely used as a hole harvester for proton reduction in order to facilitate fundamental studies of this half reaction. However, its oxidation leads to a decomposition of the positive amine radicals, making it unsustainable for a technological application.^{27, 28} Implementation of a charge carrier with functional

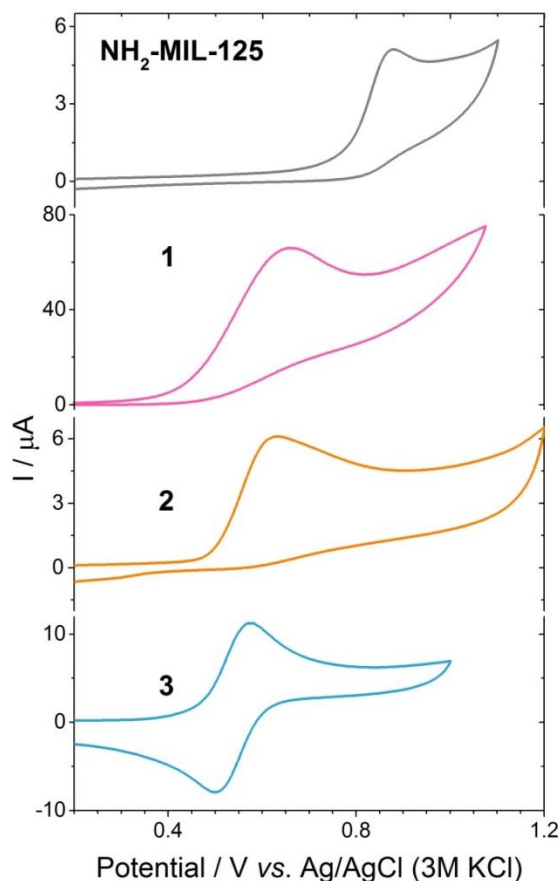


Figure 5.4. Cyclic voltammetry at 50 mV/s of $\text{NH}_2\text{-MIL-125(Ti)}$, **1**, **2** (phosphate buffer, pH 7) and **3** (0.1 M LiClO_4) in water as it is the only medium that allowed for electrochemical measurements of the MOF.

groups that can mimic the Tyr/His pair is attractive.^{29, 30} Efforts have been made on protecting phenolic analogues to the Tyr/His pair with bulky groups and make them more stable as charge carriers, but this leads to bulky molecules that are incompatible with porous hosts.³¹ Thus, we chose the unsubstituted 2-(1H-Pyrazol-3-yl)phenol (**2**) as a hole harvester (Figure 5.3c, *middle*), because it contains the phenolic group and, as proton acceptor, the basic pyrazol group, mimicking thus the Tyr/His component of the PSII. In the case of molecule **2**, it does not present an entirely under neutral conditions the oxidation potential of the hole at the linker in the MOF ($E_p = 0.85 \text{ V vs. Ag/AgCl}$, $\text{PO}_4^{3-}/\text{HPO}_4^{2-}$ in water) has a higher oxidation potential than **2** ($E_p = 0.65 \text{ V vs. Ag/AgCl}$, $\text{PO}_4^{3-}/\text{HPO}_4^{2-}$ in water), suggesting that **2** may be a suitable candidate to carry the positive charges for the oxidation reaction, although not in a reversible fashion. Interestingly, the oxidation potential of the MOF is lower than that of water, confirming that the MOF is incapable of the water oxidation half reaction, and that hence a Z-scheme would be necessary for achieving overall water splitting in this system (Figure 5.3a, *red*).

TEMPO is a well-known radical scavenger that has been successfully applied as (catalytic) oxidant in its oxidized form.³² This compound provides an oxidation

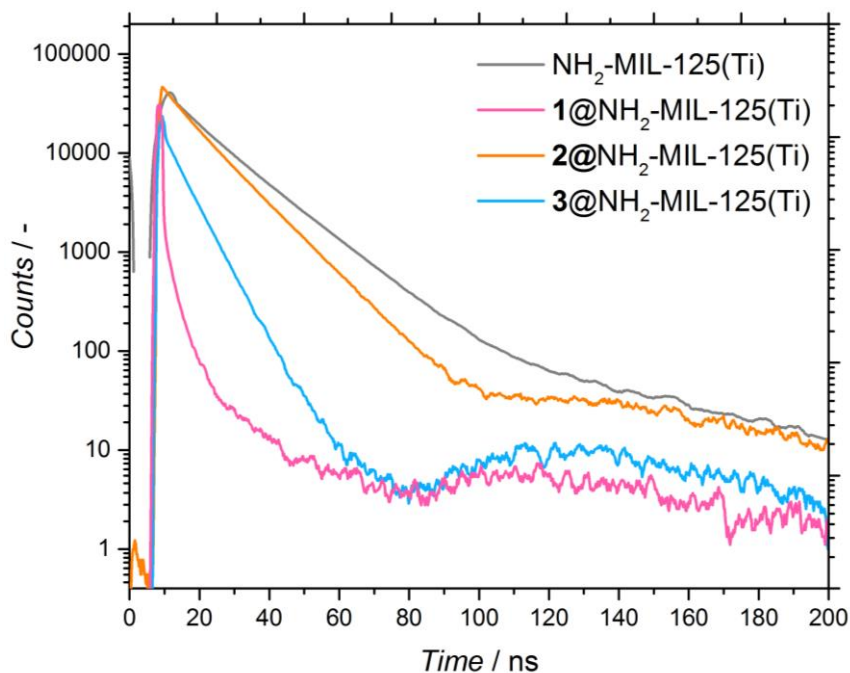


Figure 5.5. Time resolved fluorescence of $\text{NH}_2\text{-MIL-125(Ti)}$ in water (grey), $1@ \text{NH}_2\text{-MIL-125(Ti)}$ in acetonitrile (pink), $2@ \text{NH}_2\text{-MIL-125(Ti)}$ in DMF (orange) and $3@ \text{NH}_2\text{-MIL-125(Ti)}$ in water (blue). The suspensions were excited by a 404 nm laser. The decrease in fluorescence over time was measured at a wavelength of 430 nm.

potential suitable to carry the positive charge ($E_P = 0.57 \text{ V vs. Ag/AgCl, PO}_4^{3-}/\text{HPO}_4^{2-}$ in water) and, moreover, its oxidation wave is fully reversible (see Figure 5.4, bottom) to warrant the availability of oxidation power and connect the reduction with the oxidation half reactions (Figure 5.3a).

Noteworthy, the amount of occluded electron donor varied for the three different composites (and was directly correlated to the diffusion limitations of each molecule in terms of size and affinity for the pore, section 4 SI). To assess whether the adsorbed molecules interact with the photoexcited MOF and have the possibility to undergo charge transfer, time-resolved photoluminescence (PL) studies were performed on the $\text{NH}_2\text{-MIL-125(Ti)}$ and composites (Figure 5.5). Figure 5.5 shows that, when the molecules are present, there is a faster decay in all the composites compared to the pristine MOF, being the decay of the photoluminescence much faster when **1** and **3** are present than when **2** is occluded in the MOF.²⁴ To detect if there is any influence by the solvent, we also performed all measurements in acetonitrile, observing the same trend (Figure A5.19). These results point towards a different photoexcitation and/or recombination to ground state mechanism compared to the pristine MOF. However, the time resolution of the measurements (limited to 50 ps), cannot distinguish processes that might already occur on shorter time scales. Thus, further studies with subpicosecond time resolution were carried out with transient absorption (TA) spectroscopy.

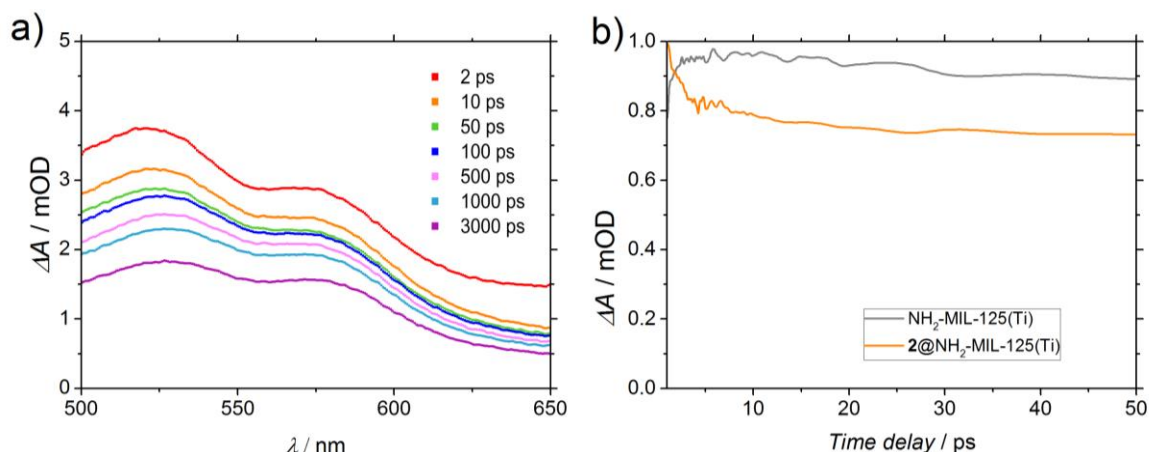


Figure 5.6. a) Differential transient spectra of **2**@NH₂-MIL-125(Ti) in DMF upon excitation at 400 nm. b) Comparison of the time traces of NH₂-MIL-125(Ti) and **2** occluded in NH₂-MIL-125(Ti) at 540 nm in DMF.

In the case of the pristine MOF, the photoexcitation with a VIS-pump (400 nm) results in an intense induced absorbance ($\lambda_{max} = 570$ nm with a shoulder at 530 nm) that can be assigned to the holes on the NH₂. An additional broad induced absorbance of lower intensity is present from 500 nm, extending beyond 750 nm, which is characteristic for the electron on the Ti⁺³ (Figure A5.21).¹⁹ We have previously shown that the kinetics and, to a large degree, the shape of the transient absorbance spectra are solvent independent.¹⁹

Figure 5.6a shows the TA spectrum of **2**@NH₂-MIL-125(Ti) in dimethylformamide (DMF) upon 400 nm excitation. Despite the fact that the shape of this spectrum is very similar to the original from solely the MOF (Figure A5.21), the decay of the induced absorbance attributed to the photogenerated holes (at $\lambda = 570$ nm) on the MOF and on **2**@NH₂-MIL-125(Ti) is remarkably different. Clearly, there is a faster decay for **2**@NH₂-MIL-125(Ti) compared to the pristine MOF. From Figure 5.6b, we see for **2**@NH₂-MIL-125(Ti) a decay of 25% of the band associated with the hole within 10 ps, in contrast to no decay for the pristine MOF, indicating that a fraction of holes at the MOF are most likely transferred to compound **2**. To further gain insight into the charge transfer process, we studied the structural changes on the functional organic groups during the photoexcitation of the composite by transient IR absorption spectroscopy. Whereas for the pristine MOF the transient IR-signals equilibrate after excitation,¹⁹ we observed for **2**@NH₂-MIL-125(Ti) transient positive and negative signals, which grow in amplitude with increasing of the delay time.

The transient spectrum (Figure 5.7) in DMF at long delay times shows two negative ΔA peaks (spectral bleaches) with two adjacent peaks with positive ΔA (induced absorbance). Such combinations of a bleach and an induced absorption can be assigned to vibrational peaks that are red-shifted upon excitation with the visible

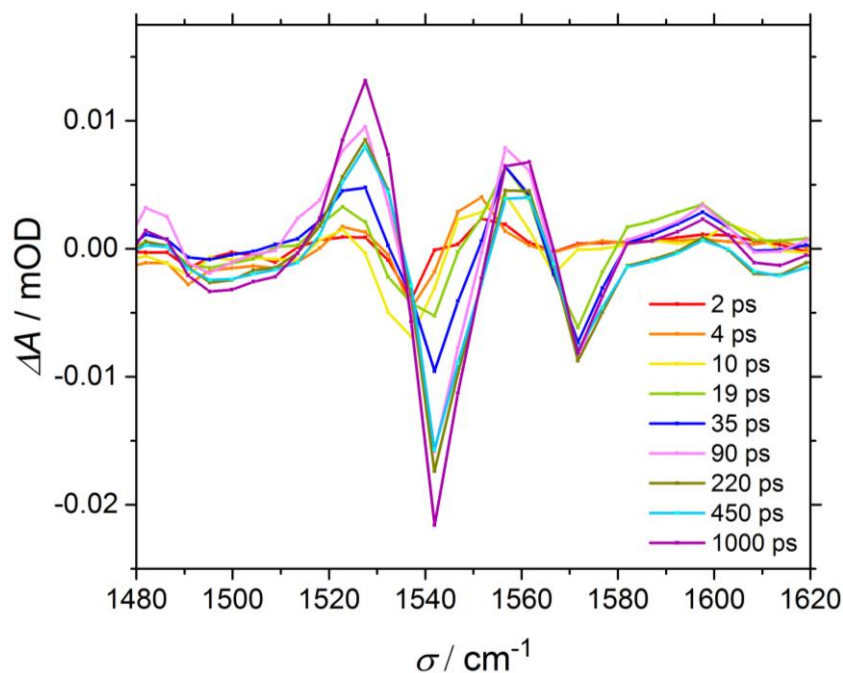


Figure 5.7. Differential transient absorption mid-IR spectra for **2**@NH₂-MIL-125(Ti) in DMF as solvent upon excitation at 400 nm

pump pulse: The photo-conversion leads to a depletion of the starting materials (MOF or **2**, see below), reflected in a reduced absorption of the molecular vibrations (spectral bleach). Simultaneously, the photo-product with red-shifted (relative to the initial bands) vibrational band is generated, which results in the observed induced absorption. Two such pairs of a spectral bleach and an adjacent induced absorption appear with increasing delay time (e.g. 1540 shifts to 1520 cm⁻¹, and 1580 shifts to 1560 cm⁻¹). As both the MOF and **2** have weak bands in IR absorption spectra in this frequency range (Figure A5.26), these transient shifts may be due to photo-oxidation of **2** or reduction of the MOF. DMF was chosen as solvent for a better comparison with TA and PL results, however, it is not IR transparent in the region of the amino group C-N vibration in the MOF (~1257 cm⁻¹). Studies with more transparent solvents (tetrachloroethane, 1210-1310 cm⁻¹ range) show similar dynamics as in DMF (new spectral features appearing, Figure A5.27). These observations mean that the N-centred holes from the MOF are transferred to compound **2**, leading to spectra arising from a photoadduct (that can be either the now negatively charged MOF or oxidised **2**). In fact, the time dynamics of the appearance of these new spectra and the faster decay detected in **2**@NH₂-MIL-125(Ti) by a Vis-probe (compared to the MOF, Figure 5.6) are very similar (see Figure 5.8). Indeed, the transient visible spectra can be fitted to a sum of exponentials, where an initial exponential decay (with a time constant of 1 ps, attributed to vibrational cooling), is followed by a decay with a time constant of 14 ps, which is comparable to the exponential growth observed in the mid-IR-probe spectra, where a characteristic time constant of 10 ps

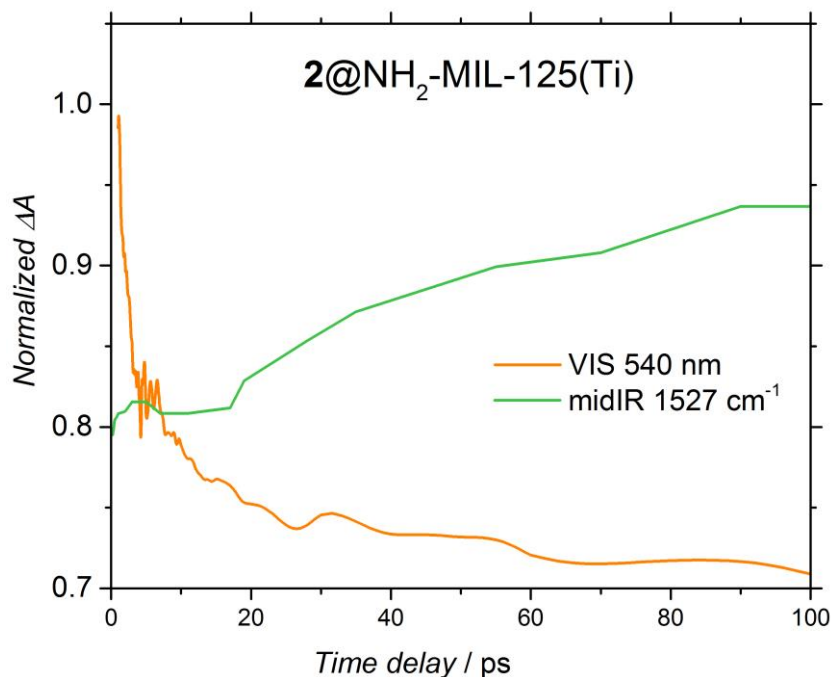


Figure 5.8. Representative time traces of **2@NH₂-MIL-125(Ti)** upon excitation at 400 nm in DMF recorded at 1527 cm⁻¹ (*green*). The orange line (corresponding to the left axes) represents the time traces at 540 nm in DMF (from Figure 5.6).

was found (Figure 5.8, determined as the time when $1/e \approx 36.8$ % of the signal has decayed), suggesting that both spectra are related to the transfer of holes.

Even though fast charge transfer occurs between **2** and MOF, only 48% of the signal assigned to the holes (at 570 nm, Figure 5.6a) has decayed after 3 ns, the time window of the Vis-probe experiment (*vs.* 46% observed in the case of the pristine MOF). Intriguingly, when the TA is performed in acetonitrile (Figure A5.22), we observe decay dynamics for composite **2@NH₂-MIL-125(Ti)** similar as for the pristine MOF, indicating that charge transfer does not take place, and it is solvent dependent. As **2** is not soluble in water, unfortunately, we could not perform these experiments in water, the most relevant solvent for water splitting.

In contrast, in the transient spectra of **3@NH₂-MIL-125(Ti)** in water (Figure 5.9b) the signal attributed to the holes (at $\lambda = 570$ nm) is not even observed. This indicates that within the time resolution of the experiment (considering that before 1 ps the spectrum is dominated by the coherent artefact) charge transfer of the holes to occluded **3** has already taken place. In acetonitrile, the charge transfer from the MOF to **3** still takes place, albeit with slower kinetics (Figure A5.23), despite *de facto* that the concentration of **3** in the composite **3@NH₂-MIL-125(Ti)** is higher in this solvent (6 and 2 molecules per large NH₂-MIL-125(Ti) cage in acetonitrile and in water, respectively, see Appendix 3, Table A5.2).

Interestingly, as in the case of **3@NH₂-MIL-125(Ti)** in water, the signal attributed to the holes in **1@NH₂-MIL-125(Ti)** in acetonitrile is also absent in the transient spectra.

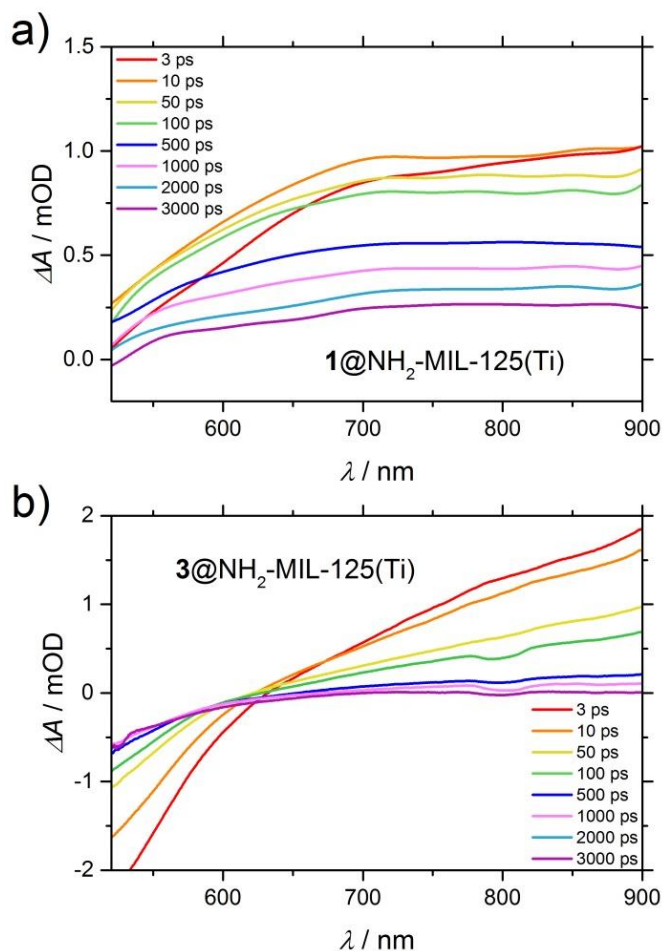


Figure 5.9. Difference transient spectra of: a) $1@NH_2\text{-MIL-125(Ti)}$ in acetonitrile and b) $3@NH_2\text{-MIL-125(Ti)}$ in water upon excitation at 400 nm.

In both cases (Figure 5.9 a and b), the lower or even negative induced absorbance towards lower wavelengths is caused by stimulated emission, that is redshifted from the ground state depletion (centred at the pump wavelength of 400 nm) that now dominates this range of the spectrum. In Figure 5.9a, the stimulated emission is present as the superposition of a negative peak (up to 700 nm at 3 ps) with a very broad positive absorbance, alike in shape and wavelength to the UV generated (pump at $\lambda = 315 \text{ nm}$) Ti^{3+} excited state in the non-functionalized MIL-125(Ti) (Figure A5.20). Since the accessibility of the photoexcited state in $NH_2\text{-MIL-125(Ti)}$ is only possible under visible light because of the participation of the amino group, and because this charge separation is necessary to be able to observe Ti^{3+} , the transient spectra must be composed of the photogenerated electrons on the Ti^{3+} and the absence of a hole due to its scavenging by the guest molecule **1** or **3**. Moreover, the fact that the electronic spectrum of the composite $3@NH_2\text{-MIL-125(Ti)}$ is clearly a superposition of the MOF and **3**, shows that there is no complexation of the two components (Figure A5.16). Additionally, spectroelectrochemistry of **3** shows no induced absorbance in the visible range upon oxidation (Figure A5.28) and visible TA spectra of **3** shows also no change in absorption upon excitation at 400 nm -

Table 5.1. Catalytic performance in HER

Electron donor ^a	Hydrogen evolution after 18 h / μmol
600 eq. 1	26.47
60 eq. 1	7.35
60 eq. 3	0
17 eq. 3	0.27
60 eq. 1 , 60 eq. 3	0.018

a: Calculated equivalents of electron donor (eq) for the stoichiometry of the reaction (the electron donor transfers one electron to the MOF, and 2 electrons are needed to produce H₂)

(Figure A5.23), meaning that the broad induced absorbance extending into the near IR observed in Figure 5.6b can be attributed to the photogenerated Ti³⁺ on the MOF. Interestingly, the spectral band attributed to Ti³⁺ decays faster for **3**@NH₂-MIL-125(Ti) than for **1**@NH₂-MIL-125(Ti). In the case of **3**@NH₂-MIL-125(Ti), this signal fully decays after 2 ns. This is in contrast to the case of **1**@NH₂-MIL-125(Ti), where there is still 30% induced absorbance remaining after 3 ns.

To understand the different decay of the Ti³⁺ spectral features observed in TA between composites **1** and **3**, and the implications on the reduction half reaction of the water-splitting reaction, we performed HER (Figure A5.31). **3**@NH₂-MIL-125(Ti) as donor/catalyst pair shows no H₂ evolution when using an excess of **3** (60 equivalents respect to the expected H₂ from MOF), whereas the activity of the MOF is partially restored when using only 17 equivalents of **3**. In contrast, the efficiency in HER (μmol H₂ produced during the reaction time) is significantly greater when **1** is added compared to the addition of **3** (see Table 1). In this case, a decreased concentration of sacrificial electron donor **1** shows a lower activity using **1**@NH₂-MIL-125(Ti) as catalyst. An additional experiment with a mixture of the two donors (**1** and **3**) showed a further decrement of activity in comparison with any of the concentrations of **1** here studied (Table 1).

Based on its reduction potential, compound **3** can also be reduced and react with the photogenerated electron on Ti³⁺ species (Figure A5.29). This is a reactivity that compound **1** does not show (probably due to its irreversible oxidation).²⁷ If we combine this information with the TA spectroscopic results that showed a faster decay of the signal attributed to Ti³⁺ for **3**@NH₂-MIL-125(Ti) than for **1**@NH₂-MIL-125(Ti), it becomes very likely that reverse electron transfer is taking place for **3**@NH₂-MIL-125(Ti) (Figure A5.30).⁷

In summary, charge transfer is observed for the three studied compounds with notable differences in the charge transfer rates that show solvent dependency. Since acetonitrile is our base solvent, only molecule **1** shows charge transfer. For molecule **2**, we observed that acetonitrile was not suitable as solvent, and, we chose DMF for our studies (**2** is not soluble in aqueous media). In the case of molecule **3**, charge transfer in water showed to be more efficient than in acetonitrile.

Due to the irreversible oxidation of **1** and **2**, the availability of the holes for oxidation reaction ceases. In contrast, the reversible oxidation of **3** results in the availability of the positive charges. Indeed, when using benzyl alcohol oxidation as probe reaction, we observe an increase of activity in presence of **3** (Figure A5.32).

Conclusions

In this work, we have demonstrated charge transfer from NH₂-MIL-125(Ti), a visible-light absorbing Ti-based MOF, to molecules occluded in its pores. We have confirmed by a combination of ultrafast spectroscopic techniques, a fast charge transfer from the MOF to **2**, a molecule that mimics the Tyr/His pair in PS II. Considering the structural changes observed in the mid-IR-probe (and in agreement with **2** irreversible oxidation wave), we propose that the oxidation of **2** results in a chemically different species after charge transfer, thus formally quenching the hole in NH₂-MIL-125(Ti), and inhibiting further the utilization of these positive charges in an oxidation reaction (similarly to the case of **1**). When charge transfer occurs at higher rates to a reversible species such as compound **3**, the hole is formally transferred, and it is still available for oxidation, as demonstrated by the enhanced catalytic oxidation activity of the **3**@NH₂-MIL-125(Ti) pair compared to the pristine MOF. We conclude that **3**⁺@NH₂-MIL-125(Ti³⁺) is effectively favouring the stabilization of the photogenerated positive charges. However, we have proven that charge transfer in the composite **3**@NH₂-MIL-125(Ti) leads to reverse electron transfer, a drawback that still has to be solved.

Our findings suggest that combining a recyclable redox shuttle, e.g. TEMPO (**3**), or reversibly oxidisable molecules inspired by the photosynthetic blueprint, with an efficient H⁺ catalytic reduction site, might indeed enable artificial photosynthetic hydrogen production combined with a water oxidation catalyst in a Z-scheme. Finding this reversible molecule that allows for spatial separation and avoids quenching of the produced charges is still an enduring great challenge.

References

1. J. Barber, *Chemical Society Reviews*, 2009, **38**, 185-196.
2. N. S. Lewis and D. G. Nocera, *Proceedings of the National Academy of Sciences*, 2006, **103**, 15729-15735.
3. A. Fujishima and K. Honda, *Nature*, 1972, **238**, 37-38.
4. T. Zhang and W. Lin, *Chemical Society Reviews*, 2014, **43**, 5982-5993.
5. B. Kok, B. Forbush and M. McGloin, *Photochem Photobiol*, 1970, **11**, 457-8.
6. L. Hammarstrom and S. Styring, *Energy & Environmental Science*, 2011, **4**, 2379-2388.
7. L. Hammarström, L. Sun, B. Åkermark and S. Styring, *Biochimica et Biophysica Acta (BBA) - Bioenergetics*, 1998, **1365**, 193-199.
8. R. E. Blankenship, D. M. Tiede, J. Barber, G. W. Brudvig, G. Fleming, M. Ghirardi, M. R. Gunner, W. Junge, D. M. Kramer, A. Melis, T. A. Moore, C. C. Moser, D. G. Nocera, A. J. Nozik, D. R. Ort, W. W. Parson, R. C. Prince and R. T. Sayre, *Science* 2011, **332**, 805-809.
9. Y. Tachibana, L. Vayssieres and J. R. Durrant, *Nat Photon*, 2012, **6**, 511-518.
10. A. R. Holzwarth, M. G. Mueller, M. Reus, M. Nowaczyk, J. Sander and M. Roegner, *Proc. Natl. Acad. Sci. U. S. A.*, 2006, **103**, 6895-6900.

11. J. Barber, *Philosophical transactions. Series A, Mathematical, physical, and engineering sciences*, 2007, **365**, 1007-1023.
12. L. Kalman, R. LoBrutto, J. P. Allen and J. C. Williams, *Nature*, 1999, **402**, 696-699.
13. Y. Zhao, J. R. Swierk, J. D. Megiatto, B. Sherman, W. J. Youngblood, D. Qin, D. M. Lentz, A. L. Moore, T. A. Moore, D. Gust and T. E. Mallouk, *Proceedings of the National Academy of Sciences*, 2012, **109**, 15612-15616.
14. B. Sherman, M. Vaughn, J. Bergkamp, D. Gust, A. Moore and T. Moore, *Photosynth Res*, 2014, **120**, 59-70.
15. K. Maeda, R. Abe and K. Domen, 2010.
16. C. Wang, Z. Xie, K. E. deKrafft and W. Lin, *Journal of the American Chemical Society*, 2011, **133**, 13445-13454.
17. Y. Fu, D. Sun, Y. Chen, R. Huang, Z. Ding, X. Fu and Z. Li, *Angewandte Chemie - International Edition*, 2012, **51**, 3364-3367.
18. M. A. Nasalevich, M. G. Goesten, T. J. Savenije, F. Kapteijn and J. Gascon, *Chemical Communications*, 2013, **49**, 10575-10577.
19. J. G. Santaclara, M. A. Nasalevich, S. Castellanos, W. H. Evers, F. C. M. Spoor, K. Rock, L. D. A. Siebbeles, F. Kapteijn, F. Grozema, A. Houtepen, J. Gascon, J. Hunger and M. A. van der Veen, *ChemSusChem*, 2016, **9**, 388-395.
20. M. A. Nasalevich, C. H. Hendon, J. G. Santaclara, K. Svane, B. van der Linden, S. L. Veber, M. V. Fedin, A. J. Houtepen, M. A. van der Veen, F. Kapteijn, A. Walsh and J. Gascon, *Scientific Reports*, 2016, **6**, 23676.
21. J. D. Megiatto, A. Antoniuk-Pablant, B. D. Sherman, G. Kodis, M. Gervaldo, T. A. Moore, A. L. Moore and D. Gust, *Proceedings of the National Academy of Sciences*, 2012, **109**, 15578-15583.
22. C. H. Hendon, D. Tiana, M. Fontecave, C. Sanchez, L. D'Arras, C. Sassoeye, L. Rozes, C. Mellot-Draznieks and A. Walsh, *J. Am. Chem. Soc.*, 2013, **135**, 10942-10945.
23. M. F. De Lange, T. J. H. Vlugt, J. Gascon and F. Kapteijn, *Microporous and Mesoporous Materials*, 2014, **200**, 199-215.
24. M. A. Nasalevich, R. Becker, E. V. Ramos-Fernandez, S. Castellanos, S. L. Veber, M. V. Fedin, F. Kapteijn, J. N. H. Reek, J. I. van der Vlugt and J. Gascon, *Energy & Environmental Science*, 2015, **8**, 364-375.
25. S. Hu, M. Liu, K. Li, Y. Zuo, A. Zhang, C. Song, G. Zhang and X. Guo, *CrystEngComm*, 2014, **16**, 9645-9650.
26. S. Vaesen, V. Guillermin, Q. Yang, A. D. Wiersum, B. Marszalek, B. Gil, A. Vimont, M. Daturi, T. Devic, P. L. Llewellyn, C. Serre, G. Maurin and G. De Weireld, *Chemical Communications*, 2013, **49**, 10082-10084.
27. M. Masui, H. Sayo and Y. Tsuda, *Journal of the Chemical Society B: Physical Organic*, 1968, DOI: 10.1039/J29680000973, 973-976.
28. J. Hu, J. Wang, T. H. Nguyen and N. Zheng, *Beilstein Journal of Organic Chemistry*, 2013, **9**, 1977-2001.
29. R. D. Richardson, E. J. Holland and B. K. Carpenter, *Nat Chem*, 2011, **3**, 301-303.
30. B. C. M. Martindale, E. Joliat, C. Bachmann, R. Alberto and E. Reisner, *Angewandte Chemie International Edition*, 2016, **55**, 9402-9406.
31. G. F. Moore, M. Hamburger, M. Gervaldo, O. G. Poluektov, T. Rajh, D. Gust, T. A. Moore and A. L. Moore, *Journal of the American Chemical Society*, 2008, **130**, 10466-10467.
32. R. A. Sheldon and I. W. C. E. Arends, *Advanced Synthesis & Catalysis*, 2004, **346**, 1051-1071.
33. S. K. Bharti and R. Roy, *TrAC Trends in Analytical Chemistry*, 2012, **35**, 5-26.

Appendix 3

Nitrogen physisorption

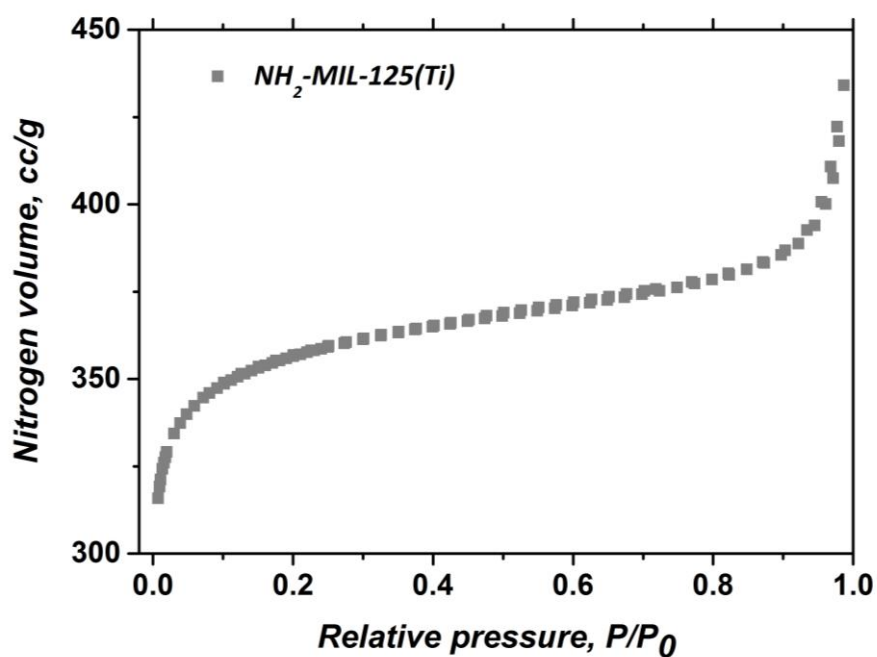


Figure A5.10. Nitrogen physisorption isotherm at 77 K for NH_2 -MIL-125(Ti).

Powder X-Ray diffraction

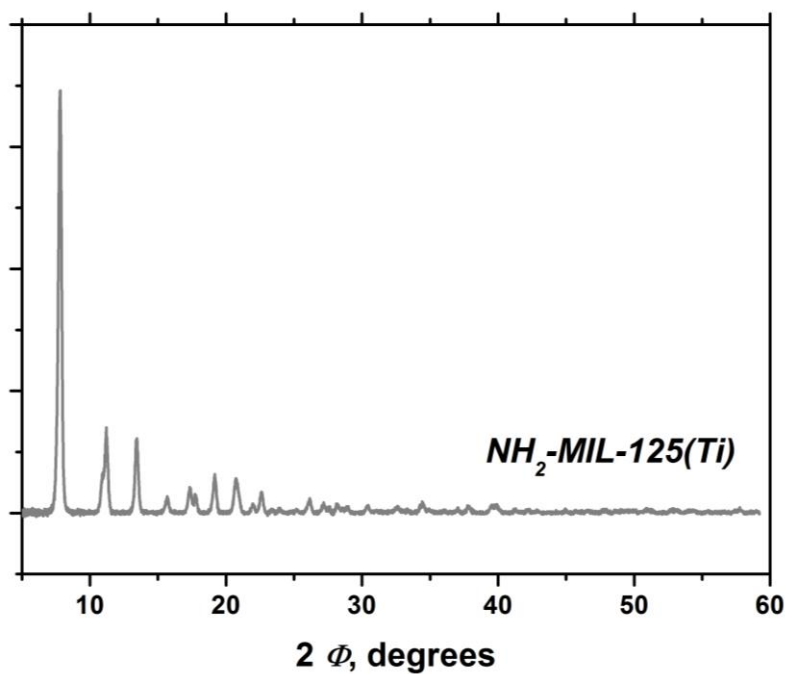


Figure A5.11. Powder X-Ray diffraction pattern of NH_2 -MIL-125(Ti).

Thermo Gravimetric Analysis (TGA)

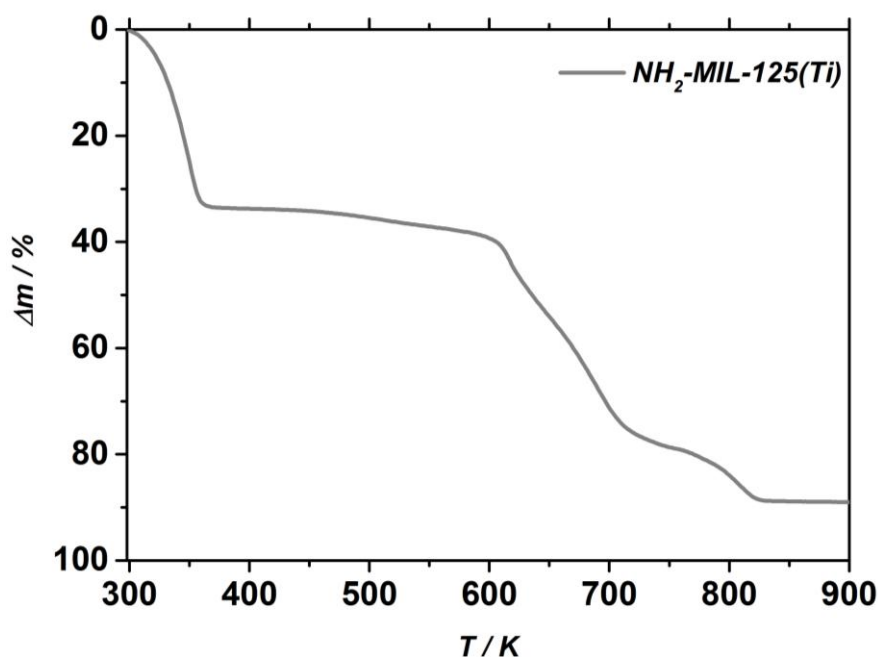


Figure A5.12. TGA pattern of NH₂-MIL-125(Ti). The 10 mg of sample was heated under air flow at a heating rate of 10 K min⁻¹.

Electron donor occlusion

Quantification for the amount of occluded molecules 1, 2, and 3 prepared in acetonitrile

NMR quantification. An internal standard method is used to determine concentration on the liquid and determine the total amount of molecule that is not adsorbed. To adsorb the molecules in the pore we add ~0.7 ml of acetonitrile-d₃ the desired amount of molecule and MOF. The resulting suspension is sonicated during 30 minutes and centrifuged to recover the supernatant. An aliquot of 0.5 ml is taken and a nmr standards is added (Maleic acid -d₂ for **1** and TEMPO and DMSO₂, Aldrich TraceCERT for the **2**). The final solution is then measured by ¹H-NMR spectroscopy in an Agilent-400 MR DD2 NMR spectrometer. For trimethylamine the signal at δ=1.24 ppm, t 9H was integrated together with that of maleic acid (δ=6.36 ppm, 2H) and the concentration of the amine was directly correlated to that of the standard. For **2** the signal at δ=7.75 ppm, d 1H and δ=7.68 ppm, dd 1H arising from the **2** were integrated together and directly correlated to that of DMSO₂ (δ=2.91 ppm, 6 H). For **3** the signals at δ=1.35 and 1.39 ppm arising from the 4 methyl groups, s 12H were integrated and correlated to that of maleic acid (δ=6.36 ppm, 2H). TMS was used for referencing the spectra.³³

The concentration of molecules in the composite obtained by NMR, and the corresponding average number of molecules per cage in the MOF, are given in Table 2:

Table 2. Quantification of molecules in the composites by NMR.

Molecule	mmol /g MOF	Molecules/cage
1	0.005	2
2	0.002	1
3	0.013	6

Quantification for the amount of occluded molecule 3 prepared in water

For **3**, in contrast to UV-VIS transparent **1** and **2**, the quantification can also be done by the more accessible UV-VIS absorption spectroscopy.

50 mg MOF was dispersed in an aqueous solution that contains the electron donor (0.024 M, 14 mL) and sonicated for 30 min. After filtration, the amount of **3** in the liquid was determined by UV-VIS spectroscopy, and by subtracting it from the initial amount of **3** added, the concentration of **3** in the composite was determined.

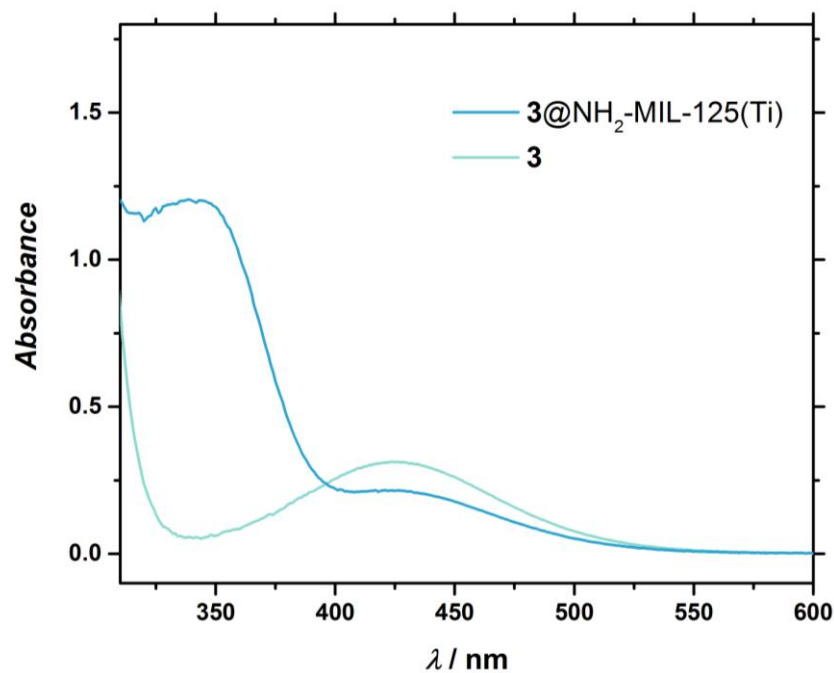


Figure A5.13. UV-VIS absorption spectra of **3** (maximum absorption at 426 nm) and composite **3@NH₂-MIL-125(Ti)** in water. From the difference between both spectra at 426 nm the amount of **3** occluded in the pores of the MOF was determined.

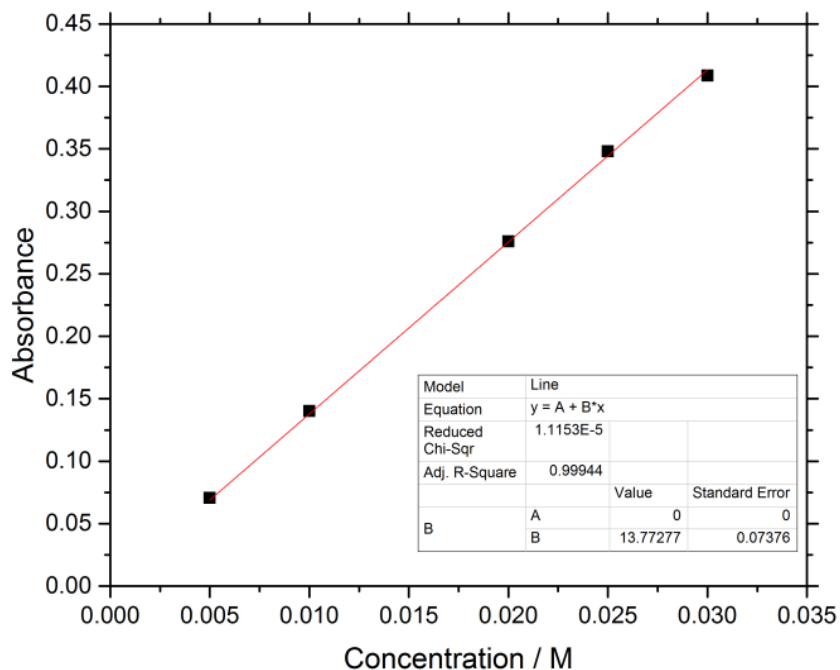


Figure A5.14. Calibration curve of **3** in water. The formula of the linear fit through the origin, $y=13.773x$, was used to calculate concentrations from the measured absorbance. This relation, along with its coefficient of determination can be found in the lower right corner.

By this quantification method, we obtained 0.0022 mmol/g_{MOF}, corresponding to one molecule **2** per cage.

UV/VIS spectroscopy

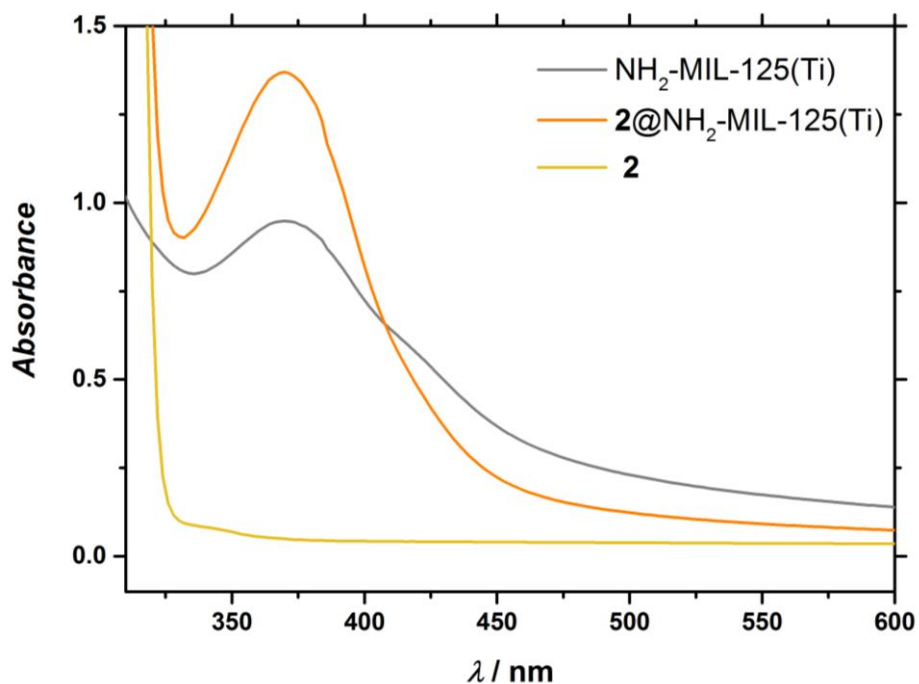


Figure A5.15. UV/VIS spectra of NH₂-MIL-125(Ti) (grey), **2**@NH₂-MIL-125(Ti) (orange) and **2** (yellow) in DMF.

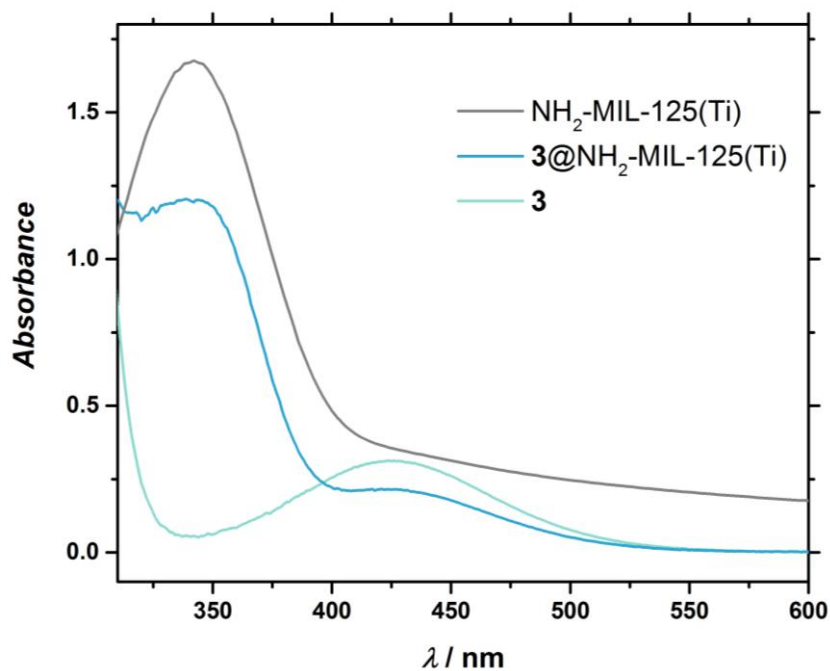


Figure A5.16. UV/VIS spectra of $\text{NH}_2\text{-MIL-125(Ti)}$ (grey), $3@\text{NH}_2\text{-MIL-125(Ti)}$ (blue) and **3** (light blue) in water.

Photoluminescence

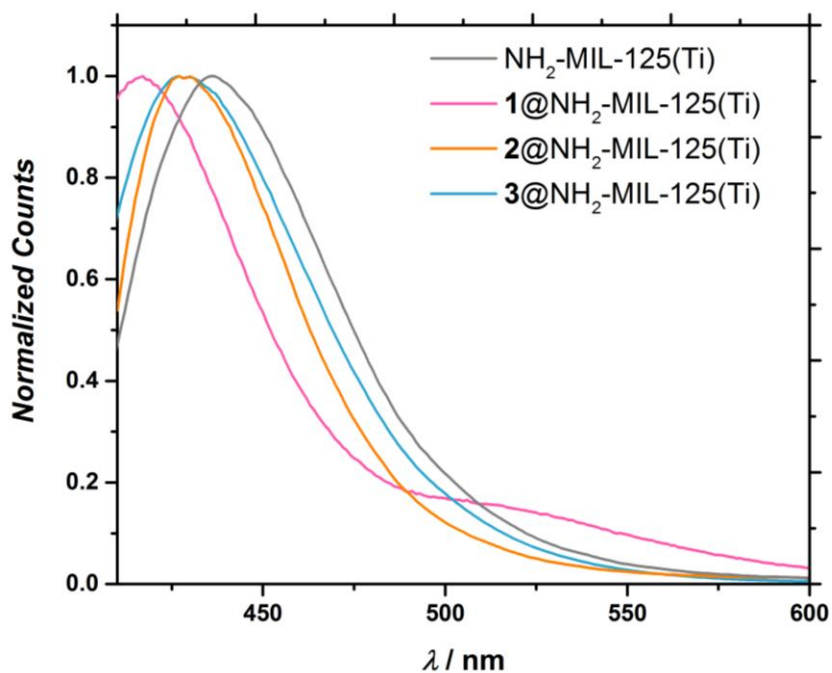


Figure A5.17. Photoluminescence spectra of $\text{NH}_2\text{-MIL-125(Ti)}$ in water (grey), $1@\text{NH}_2\text{-MIL-125(Ti)}$ in acetonitrile (pink), $2@\text{NH}_2\text{-MIL-125(Ti)}$ in DMF (orange) and $3@\text{NH}_2\text{-MIL-125(Ti)}$ in water (blue). The suspensions of $\text{NH}_2\text{-MIL-125(Ti)}$ and $3@\text{NH}_2\text{-MIL-125(Ti)}$ in water were excited by a 360 nm laser, $1@\text{NH}_2\text{-MIL-125(Ti)}$ in acetonitrile at 370 nm and $2@\text{NH}_2\text{-MIL-125(Ti)}$ in DMF at 400 nm for a better quality of the data.

Time resolved photoluminescence

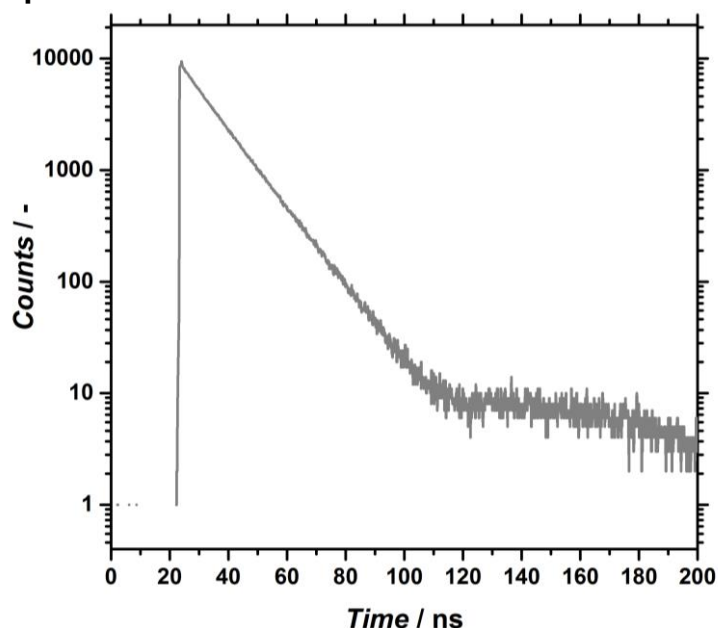


Figure A5.18. Time resolved photoluminescence spectra of $\text{NH}_2\text{-MIL-125(Ti)}$ in DMF.

The photoluminescence decay was also investigated for $\text{NH}_2\text{-MIL-125(Ti)}$ in DMF (Figure A5.18, characteristic decay time, $\tau = 12$ ns), and previously reported for powder and acetonitrile suspension ($\tau = 11.3$ ns and $\tau = 16.5$ ns, respectively).²⁴

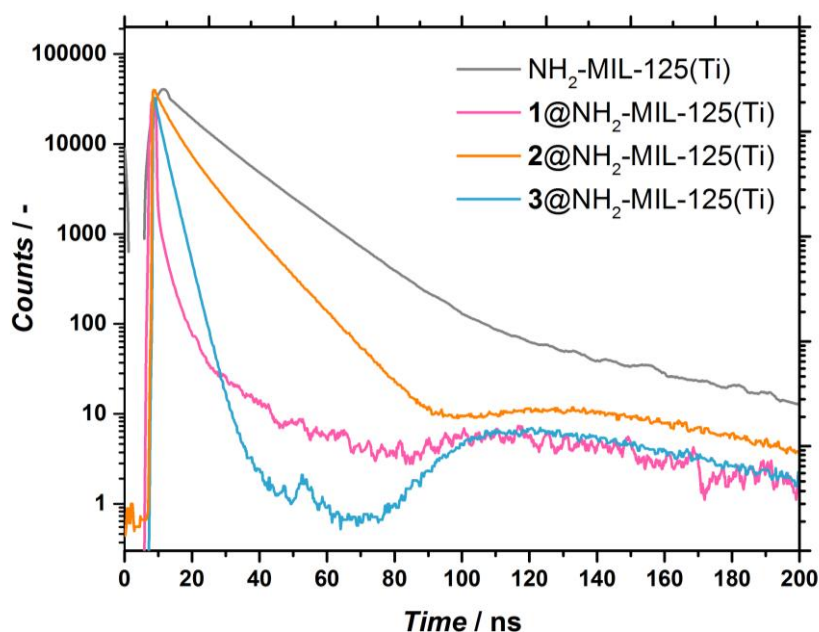


Figure A5.19. Time resolved photoluminescence spectra of $\text{NH}_2\text{-MIL-125(Ti)}$ and composites in acetonitrile.

Figure A5.19, in combination with Figure 5.5, suggests charge transfer from the MOF to molecules **1** and **2**, since energy transfer processes are then excluded due to the light absorption properties of **1** and **2** (they do not absorb visible light). For composite **3**, both charge transfer and energy transfer could be an explanation for the faster decay of MOF photoluminescence.

Vis pump-Vis probe spectroscopy

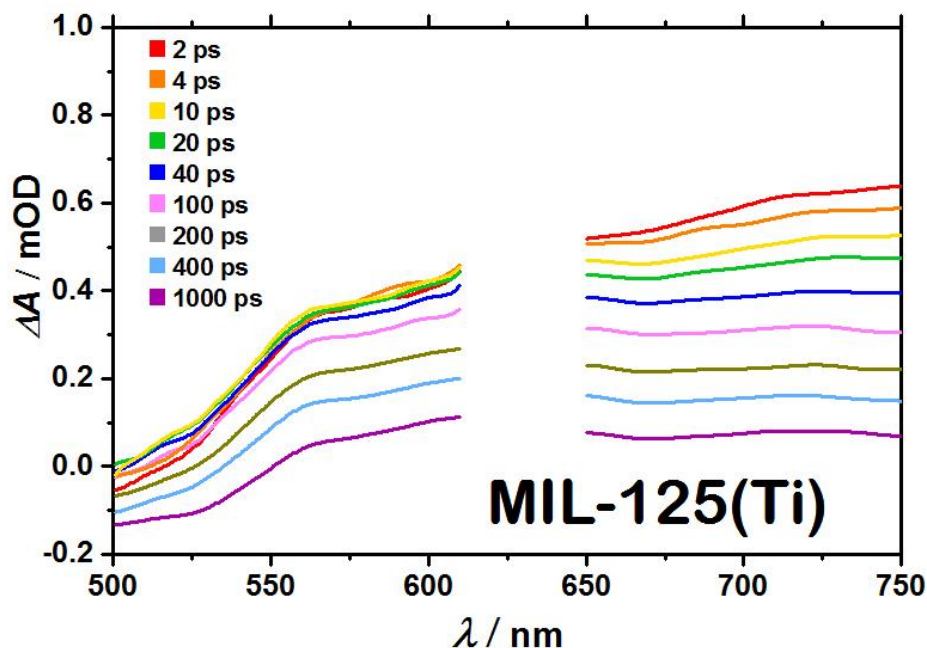


Figure A5.20. Differential transient absorption spectra for a suspension of MIL-125(Ti) in water upon excitation at 315 nm. The remnant of the 630 nm light used to generate 315 nm light via second-harmonic generation in the pump beam results on a signal between 610-650 nm that overwhelms transient spectra, hence this part of the spectra is omitted.

In the case of **2**@NH₂-MIL-125(Ti), charge transfer does not appear to happen using acetonitrile as solvent (Figure A5.22), obtaining very similar decay dynamics as using the unloaded MOF.⁴

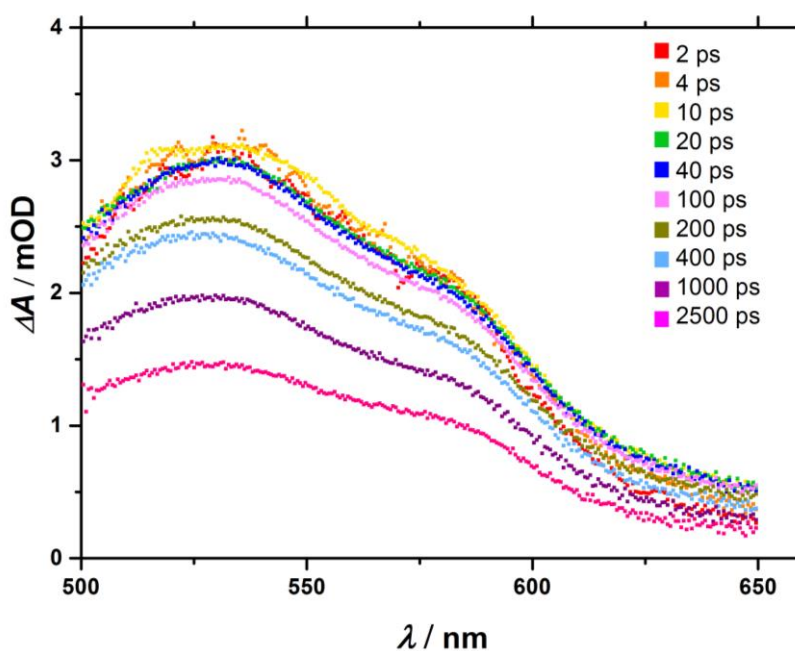


Figure A5.21. Differential transient absorption spectra for a suspension of NH₂-MIL-125(Ti) in DMF upon excitation at 400 nm

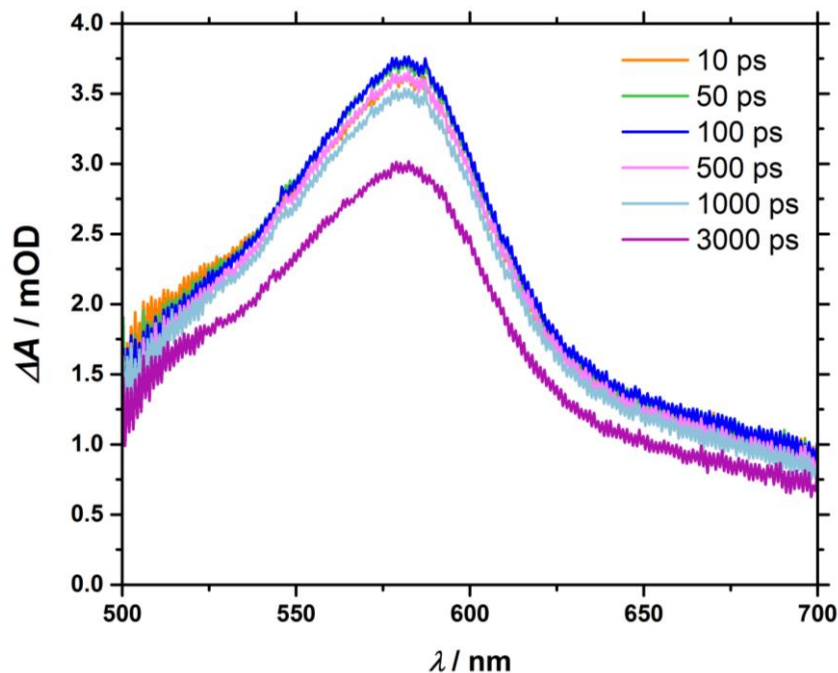


Figure A5.22. Differential transient absorption spectra for a suspension of **2**@NH₂-MIL-125(Ti) in acetonitrile upon excitation at 400 nm

For composite **3**@NH₂-MIL-125(Ti), charge transfer in acetonitrile occurs in a less efficient manner: the signal attributed to the photogenerated holes decays much faster than in the MOF. Again, we see the fast decay of the signal assigned to the electron on the Ti⁺³, showing reversible electron transfer (as it was observed in water). The decays have been calculated by the equation of exponential decays: $N(t) = N_0 e^{-t/\tau}$.

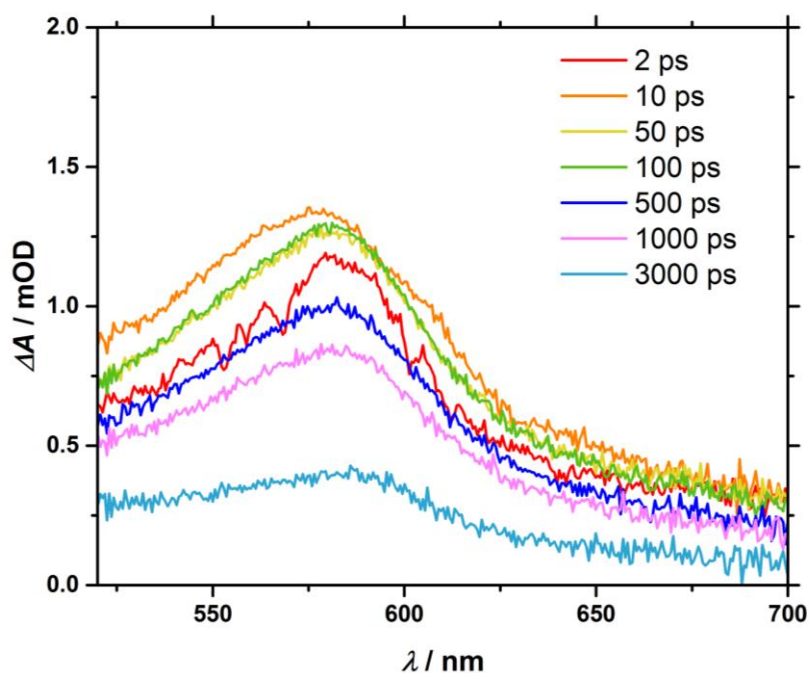


Figure A5.23. Differential transient absorption spectra for a suspension of **3**@NH₂-MIL-125(Ti) in acetonitrile upon excitation at 400 nm

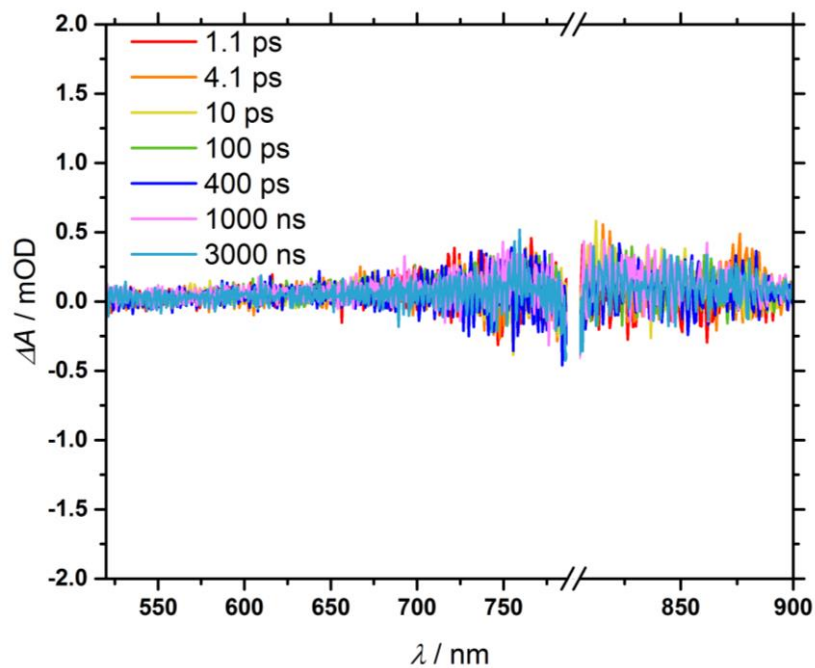


Figure A5.24. Differential transient absorption spectra for **3** in water upon excitation at 400 nm. No transient signal (only noise) is observed.

Steady state IR spectra

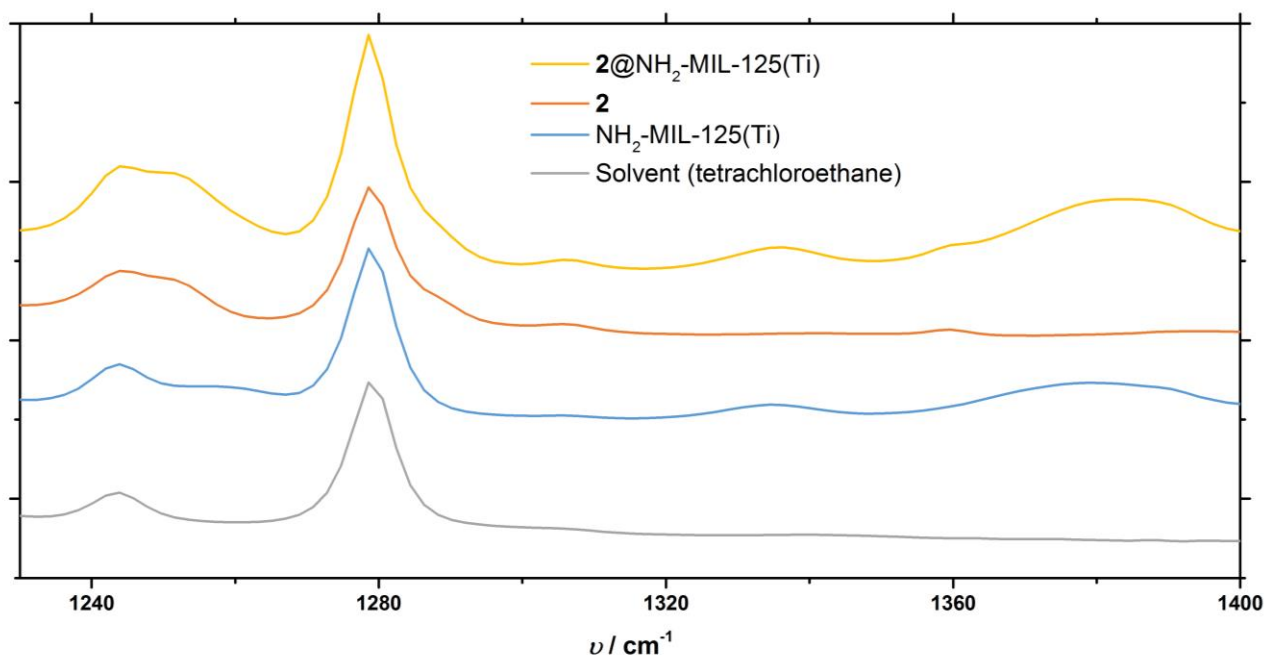


Figure A5.25. Mid-IR spectra for a suspension of **2@NH₂-MIL-125(Ti)** in tetrachloroethane

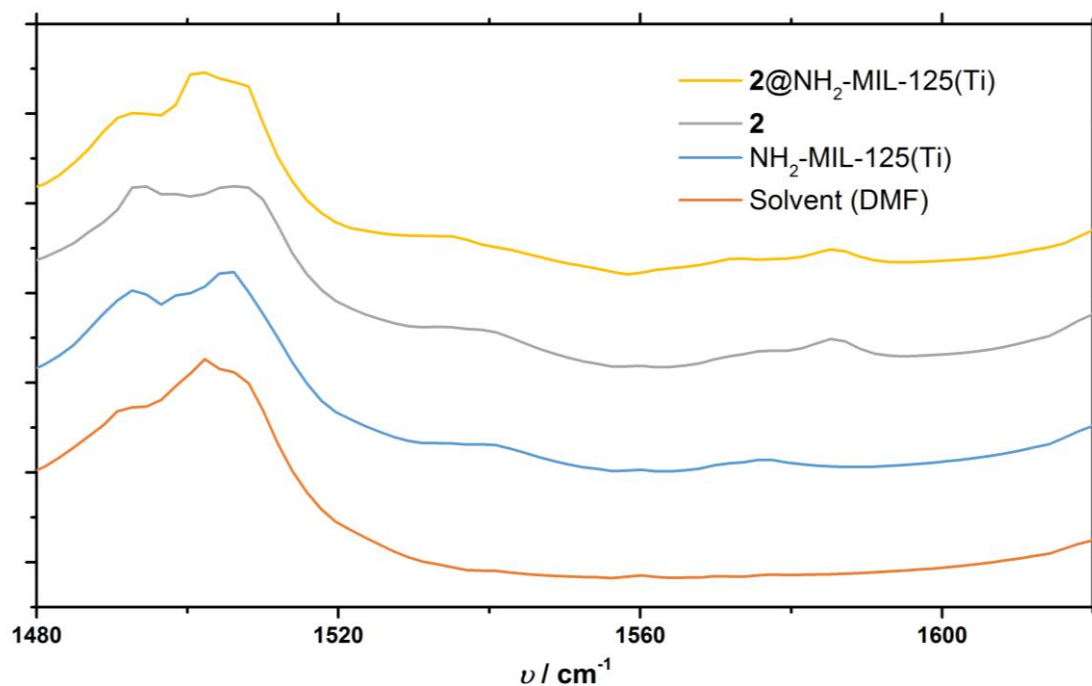


Figure A5.26. Mid-IR spectra for a suspension of **2**@NH₂-MIL-125(Ti) in DMF

Vis pump-mid-IR probe spectroscopy

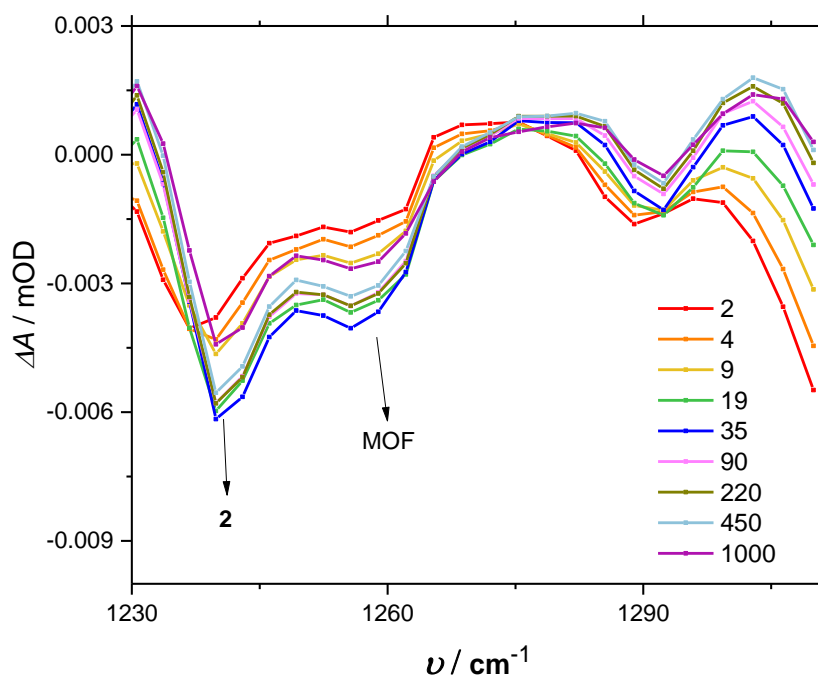


Figure A5.27. Differential transient absorption mid-IR spectra for a suspension of **2**@NH₂-MIL-125(Ti) in tetrachloroethane upon excitation at 400 nm (range 1210-1310 cm⁻¹).

Spectroelectrochemistry (SEC)

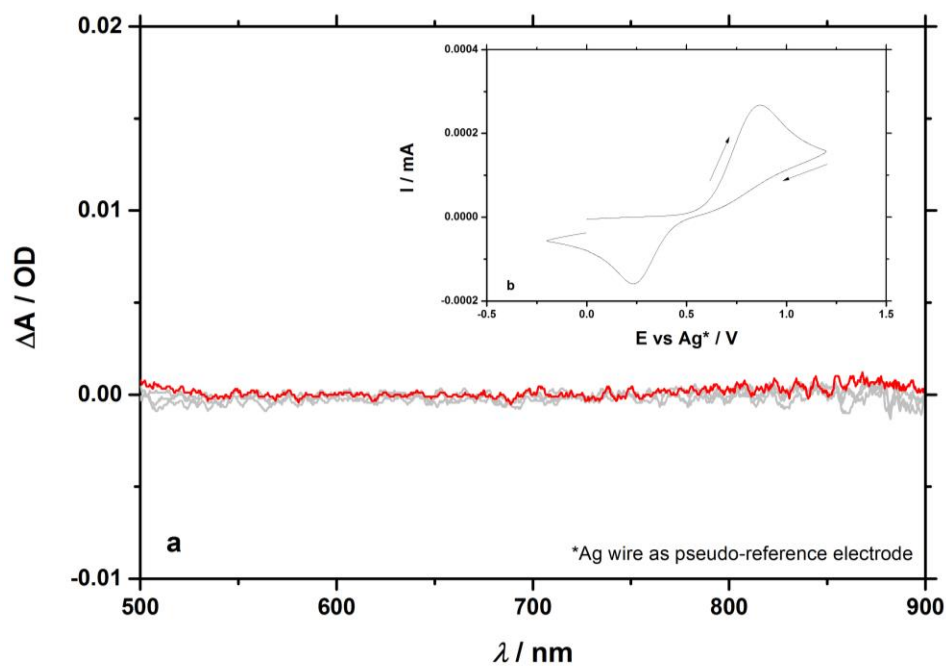


Figure A5.28. Absorption spectral changes of **3** (TEMPO) in acetonitrile ($1 \cdot 10^{-3}$ M) upon closure of the oxidation cycle. Inset (panel b) displays the registered cyclic voltammogram. Panel a shows that no change in absorbance was measured while applying positive bias. The arrows indicate the scan direction. The scan rate was 50 mV/s.

Reactivity

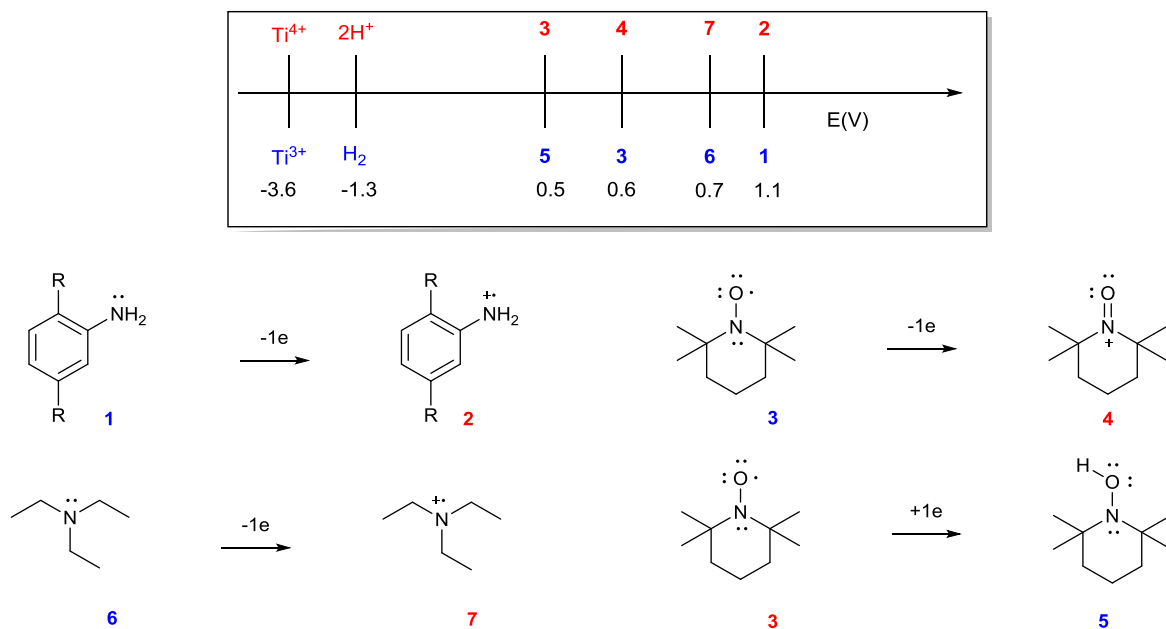


Figure A5.29. Scheme of the relative redox potentials of the compounds here studied (*top*). Oxidation or reduction half reactions of compounds **1**, **2**, and **3**.

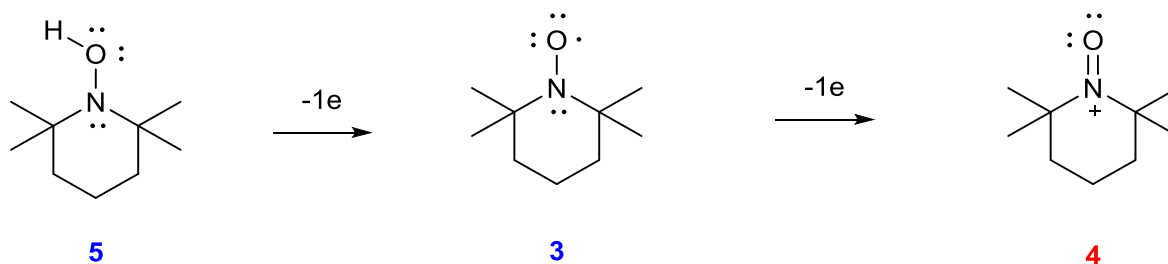


Figure A5.30. Reactivity of compound **3** (TEMPO). This indicates that either the one-electron oxidised **3** is reduced again via interaction with Ti^{3+} , or neutral **3** is directly reduced by Ti^{3+} . The proton source is water impurity from the solvent.

Photocatalytic hydrogen evolution

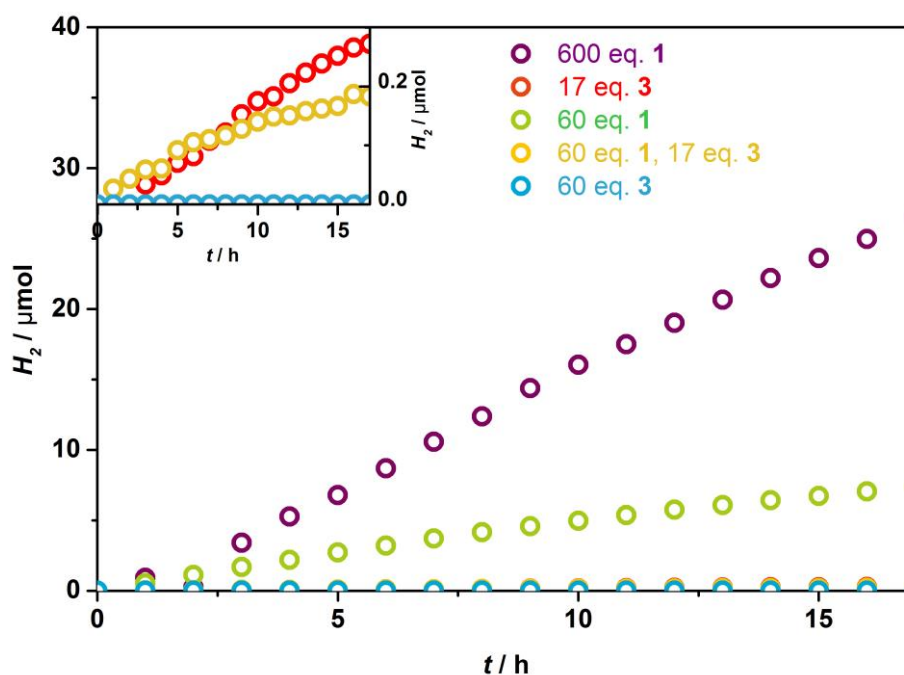


Figure A5.31. Photocatalytic hydrogen evolution under illumination at >385 nm light. 23.5 mL acetonitrile, 0.5 mL water, 30 mg $\text{NH}_2\text{-MIL-125}$ and 600 eq. (4.7 mL) **1** (purple), 17 eq. (150 mg) **3** (red), 60 eq. (0.5 mL) **1** (green), 60 eq. **1** and 17 eq. **3** (0.5 mL **1**+150 mg **3**) (yellow), and 60 eq. (500 mg) **3** (blue).

Photocatalytic benzaldehyde evolution

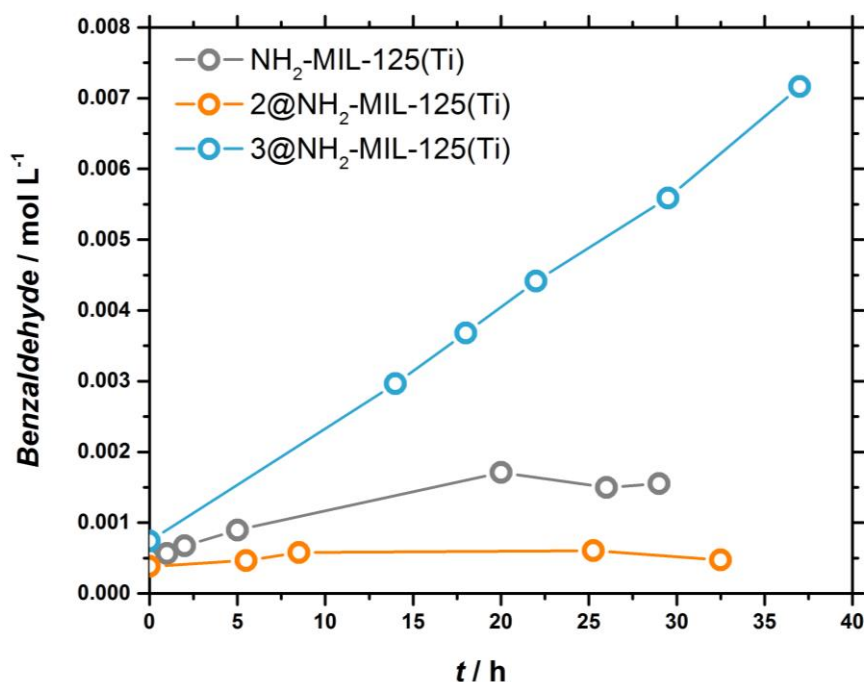


Figure A5.32. Photocatalytic benzaldehyde evolution. NH₂-MIL-125(Ti) (grey), 2@NH₂-MIL-125(Ti) (orange) and 3@NH₂-MIL-125(Ti) (blue). 35 mL acetonitrile, 0.31 mL 1,2-dichlorobenzene, 0.58 mL benzyl alcohol, 35 mg NH₂-MIL-125(Ti), 38 mg of 2 and 37 mg of 3.

TEMPO has already been applied for oxidation catalysis. The oxoammonium cation TEMPO⁺ (oxidized TEMPO) is a relatively strong oxidant ($E^0 = 0.53\text{V}$). For its application, an extra oxidant compound must be used (*m*-chloroperbenzoic acid, sodium bromide, sodium hypochlorite, among others) in order to apply TEMPO as co-catalyst.³² The stoichiometric application of TEMPO as oxidant is only possible for systems with pH lower than 3, where TEMPO is disproportionate and the effective oxidant is produced without the aid of the additional oxidant. To probe the charge transfer from 3@N⁻H₂-MIL-125(Ti³⁺) → 3⁻@NH₂-MIL-125(Ti³⁺), we performed catalytic oxidation tests using benzyl alcohol as substrate. The photo-oxidation activity using the pristine NH₂-MIL-125(Ti) as catalyst and O₂ as end oxidant is low. When using the 3@NH₂-MIL-125(Ti) pair, the catalytic activity clearly increases. In contrast, when using 2@NH₂-MIL-125(Ti), the catalytic activity is negligible.

Summary

The supply of water, food and energy is the most important challenge to sustain humankind development in the 21st century. Focusing on energy, fossil fuels are excellent energy sources for transportation and generation of heat and electricity, but they are finite natural resources, and we are depleting them at a rapid rate. While it is estimated that the fossil fuel reserves (in terms of coal, natural gas and crude) are sufficient for centuries, the effect of diminishing them will be felt considerably sooner, due to the more challenging and expensive unconventional extraction process. Moreover, it is well-known that their use impairs global warming. Inspired by natural photosynthesis as the greatest chemical factory of mother Earth, photocatalysis has been studied by several generations of scientists as a promising method for green energy production.

The research strategy followed in this thesis was the production of solar fuels using metal-organic frameworks (MOFs) as light-harvesting mimics of the natural blueprint (chapter 1). Many attempts have been made to push MOFs' light absorption into the visible region of the spectrum targeting efficient solar energy utilization. Since one of the most appealing properties of MOFs for photocatalysis is the easy tuneability of their light harvesting properties, ligand engineering has been intensively used to alter their electronic structure by modifying the orbital composition (chapter 1). However, enhancing sunlight uptake is only worth when the photogenerated charges meet two fundamental requirements: 1) possessing sufficient redox potentials (HOCO and LUCO positions) for driving the desired chemistry and 2) located on atoms or molecule fragments that facilitate the charge transfer. In this context, chapter 1 stresses the potential of advanced spectroscopic techniques to gain structural and mechanistic insight, and hence supporting future development of MOFs to harvest and store solar energy.

Apart from the thermodynamic requirement that implies that LUCO and HOCO level positions need to be suitable in order to run the desired redox half reaction, the kinetics of the photoexcited states critically influence efficiency in photocatalysis. Accordingly, the lifetime of the charge separated state(s) is of paramount importance, since it needs to be sufficiently long, such that catalytic conversion can compete with the charge separated state decay (chapter 2). In order to capture the entire extent of the photoexcited state decays and the fast dynamics of photocatalytic systems, sub-picosecond time resolution is needed. Ultrafast pump-probe spectroscopies allows us to get direct information on the MOFs excited redox-active states and to study their decay profiles from sub-picoseconds up to several nanoseconds time resolution. In chapter 2, the kinetics of the photoexcitation process were elucidated for two titanium based MOFs, MIL-125(Ti) and NH₂-MIL-125(Ti). Even though both MOFs exhibit a ligand to metal charge transfer transition, it was found that NH₂-MIL-125(Ti) has a remarkably longer lifetime due to the electron-donating primary amine on the benzene ring. In addition to the charge recombination rates, the localization of

photogenerated electrons and holes is critical for the design of reduction and oxidation catalysts, respectively. Indeed these charges need to be easily transferrable to reactants in order to achieve catalytic conversion. The most unambiguous way to assess this issue experimentally in MOFs photocatalytic systems is by spectro-electrochemistry (SEC). SEC analysis gave strong evidence for the LMCT character of the NH₂-MIL-125(Ti) photoexcited state, through the detection of the absorption fingerprints of linker radical cation and reduced Ti-oxocluster (chapter 2). A more elaborate way to precisely localize the photoexcited charges is by employing VIS-pump mid-IR-probe spectroscopy. By using this ultrafast technique electrons and holes can be traced through the different organic groups of the framework. This measurements revealed that the photogenerated hole resides on the amino group in NH₂-MIL-125(Ti) (chapter 2).

Chapter 3 provides a photophysical understanding of the electronic properties of *d*⁰ MOFs based on Ti⁴⁺, Zr⁴⁺ and Hf⁴⁺. In general, MOFs featuring ligand-to-metal charge transfer (LMCT) as the lowest energy electronic transition are desired for photocatalysis. MIL-125(Ti)-type materials are a well-known example, where LMCT has been clearly demonstrated by EPR, flash photolysis, theory and ultrafast spectroscopy combined with spectroelectrochemistry (chapter 2 of this thesis). However, demonstrating LMCT in photoactive MOFs is often overlooked and the mechanism behind light-excitation in the case of UiO-66(Zr) has been debated by several researchers. In chapter 3, with the help of DFT and EPR spectroscopy, it was found that both the HOCO and the LUCO are defined by organic orbitals, and that this framework does not feature LMCT, since there is no contribution during photoexcitation from the metal (both for Zr and Hf-based NH₂-UiO-66). The fact that this transition is solely ligand based, results in a short lifetime of excited state and, therefore, a poor photocatalytic performance for hydrogen production.

Inspired by titanium's renowned status in photocatalytic materials, yet elusive nature as building component for stable MOFs, chapter 4 treats with the creation of mid-gap metal-centred states by post-synthetic metal incorporation of Ti⁴⁺ in the NH₂-UiO-66 framework. Although titanium exchange in UiO-66 framework has been reported, the integration of these small Ti⁴⁺ metal cations appears somehow doubtful when it comes to incorporating them into structures that require high coordination numbers, such as the UiO-66 cluster. Current knowledge in the field of cation exchange in MOFs indicated that Ti⁴⁺ substitution in UiO-66's Zr-oxoclusters is not an entirely feasible process; as observed by Dincă and coworkers, cation exchange is not favoured in metal nodes containing coordinatively saturated cations, clearly the case for UiO-66. Farha's and Hupp's groups also noted from extensive empirical evidence that exchange tends to be unfavourable when the involved cations have dissimilar radii, and when the framework has small pore diameters and poor flexibility. With the aim to distinguish the real contribution of titanium functionalization in NH₂-UiO-66(Zr), we explored different strategies for Ti inclusion in the framework. By a combined experimental and theoretical study, we found that Ti incorporation occurs via its appendage to a linker vacancy rather than replacement of zirconium in the SBU.

Additionally, careful choice of titanium source in the post-synthetic modification of this MOF determines the extent of covalent interaction between the MOF and Ti. Furthermore, the appendage of Ti(IV) to the surface of SUB in the MOF yields a moderately active hydrogen evolution reaction (HER) photocatalyst, obtaining a 11-fold increase in hydrogen evolved compared to the parent MOF. Chapter 4 demonstrates that in MOF catalyst design both the defect environment and external ligand field are equally important to further improve the activity of this class of materials in photocatalysis.

Chapter 5 treats one of the most challenging problems in artificial photosynthetic systems: the coupling of water oxidation and reductive half reactions into the Z-scheme. Sacrificial electron donors (and acceptors) are generally extensively used to isolate the half reactions in photocatalytic processes, with MOFs systems not being an exception. Chapter 5 focusses on the understanding of the role of these sacrificial electron donors, such that we can replace them by recyclable ones. Through a combined study of multicomponent oxidation potentials and the dynamics at ultrafast time scales, charge transfer from the excited $\text{NH}_2\text{-MIL-125(Ti)}$ to three different candidate charge acceptors is revealed: 1) trimethylamine (TEA), one of the most commonly used sacrificial electron donors, 2) 2-(1H-Pyrazol-3-yl)phenol, a molecule that functionally mimics the tyrosine-histidine pair, responsible to shuttle the holes to the oxygen evolving centre in natural photosynthesis, and 3) TEMPO, a well-known and stable radical. Chapter 5 suggests that, by coupling a stable and recyclable charge acceptor to the photogenerated holes, the charges can be utilised for oxidation reactions and, thus, link the reduction to the oxidation reactions in water splitting.

Outlook

MOFs provide an attractive matrix to achieve solar energy conversion by hierarchically organizing light-harvesting antennae and catalytic centres. Nonetheless so far, photocatalytic MOFs also show several drawbacks. Indeed, it is fair to admit that, despite some advances in the field during the last years, photocatalytic MOF performance is still far from the state of the art, compare to, for example, the highest solar-to-hydrogen efficiencies (STH) obtained in semiconductor-based photoelectrochemical cells (PEC), which exceed 10%. Future endeavours to further exploit the promise that MOFs hold for application in photocatalysis should focus on the understanding of their electronic properties.

It is noteworthy that while most reports focus on the hydrogen evolution or the CO_2 reduction reaction, there are only few MOF examples on water oxidation. This is not surprising, since most MOFs are built up from carboxylate linkers, and typically do not possess enough oxidation power to perform water oxidation. Moreover, the use

of buffer solutions (in most examples, pH varies from 4 to 8) and strong oxidants typically used for water oxidation (e.g. cerium ammonium nitrate, and sodium peroxodisulfate) results in extreme environments where MOFs are unstable. Consequently, every study focusses on hydrogen evolution by means of a sacrificial electron donor (usually triethanolamine or trimethylamine) to provide an oxidative half reaction to close the catalytic cycle. However, finding a suitable charge acceptor that generates an oxidized product that is stable and innocent, causing no adverse effects on the components of the system, is still a challenge (chapter 5).

Low charge mobility is another limitation in most photocatalytic MOFs. Thus, conducting properties are very attractive for improved efficiencies, potentially allowing for higher electron/hole separation, and for physical separation of charges (in photo-electrochemical cells, PEC). Despite the fact that an exciting new field on conductor MOFs has emerged, insights in the electronic transport properties of MOFs are still lacking. Moreover, the application of conductive MOFs in photocatalysis for solar fuels generation should be encouraged.

We have emphasized that strong visible light absorption, long lifetime of excited states and high yield of charge-separated states are the main requirements for an excellent photocatalyst. Accordingly, matching reactant conversion times with the lifetime of photogenerated charges is the key for minimizing charge recombination and maximizing the energy utilized for the photochemical reaction. We believe that the combination of innovative spectroscopic techniques and the appropriate photocatalytic testing will advance this field greatly.

Even when achieving a high quantum yield is the ultimate goal, the future growth of MOF-based photocatalysts requires deeper understanding of the operation of current systems and their advantages over other photocatalytic materials. Ultrafast spectroscopies are highly powerful tools to unravel MOFs functioning and to develop design guidelines for these materials in photocatalysis.